Characterisation Techniques for Temporally Structured Pulses in High-Repetition-Rate Laser-Plasma Wakefield Accelerators



Wei-Ting Wang
Jesus College
University of Oxford

A thesis submitted for the degree of
Doctor of Philosophy

Trinity 2024

Abstract

Multi-pulse laser-plasma wakefield accelerators (MP-LWFA) provide an alternative way towards compact and multi-kilohertz operation of GeV-scale laser-electron accelerators for advanced light sources and future particle accelerators. However, an appropriate pulse characterisation technique has not been developed for examining and optimising temporal structures of multi-pulse trains in MP-LWFA. The aim of this research is to understand whether the spectral and temporal structures of ps-long pulse trains with fine structures on the fs-scale can be characterised with a frequency-resolved optical gating (FROG) technique. A FROG device with a single-shot beam geometry was developed to measure various pulse train structures generated by the temporal interference of two chirped pulses. It was experimentally demonstrated that the single-shot FROG device, using the extended ptychographic iterative engine phase retrieval algorithm, could retrieve pulse trains with 11 pulses, a time-bandwidth-product of (16 $\pm$ 1), average pulse spacing of (232 $\pm$ 7) fs, and local pulse spacing increment of (27 $\pm$ 7) fs. The results indicate that the single-shot FROG technique could characterise pulse trains with various temporal structures. Therefore, this framework, accompanied by cross-referenced spectral interferometry, can be employed for the complete pulse characterisation of pulse trains in a novel electron acceleration scheme known as plasma-modulated plasma accelerators.

Acknowledgements

First and foremost, I would like to express my deepest gratitude to my parents. I could not have undertaken this journey without their support from every aspect outside of my academic research. Despite the COVID-19 pandemic disrupting a period in my PhD career, their encouragement gave me the strength to maintain resilience and overcome challenges.

After finishing my research career at Oxford, I want to express my appreciation to my supervisor, Professor Simon Hooker, for his professional suggestions about my thesis summarising four-year research work. The quality of my thesis writing was significantly improved following his advice. I am also thankful to my college advisor, Professor Philip Burrows, for his kind support outside of my academic life.

Having more than four years of PhD research career, I am grateful to Dr. Linus Feder for his participation in my research project about pulse train measurement. Without his suggestion about building an imaging spectrometer, I could not have proceeded with my experimental work and succeeded in the project. I want to sincerely thank Dr. James Chappell for participating in the pulse measurement experiments and helpful suggestions in electron spectrometry. Many thanks to both of them for providing me with professional guidance in my research career at Oxford.

Based on my experience working with junior PhD students, I want to acknowledge Johannes Van De Wetering for his explanation of the plasma-modulated plasma accelerators. I appreciate our discussions during several lunchtimes in the Beecroft Building. I enjoyed working with David McMahon, a friendly and passionate young scientist. His sincerity showed me respect when we discussed his research about plasma channels.

Lastly, I would be remiss in not mentioning Emily Archer for her help in the 2023 Gemini Campaign. Thanks to her for sharing the experimental layout of the campaign. I want to thank Darren Chan for his honest comments on my presentations for the JAI Fest. Many thanks to this young gentleman.

晨光

觀物有感

金草碧葉遠陽天
晨風垂柳雁自閒
清河浮舟雀聲耳
朝想白雲夕聽川

民國一零九年
於英國牛津城
王維廷

Contents

List of Figures **ix**

List of Tables **xiii**

List of Abbreviations **xiv**

List of Symbols **xvi**

1 Introduction **1**
1.1 Discovery of fundamental particles 1
1.2 Conventional particle accelerators 2
1.3 Conventional laser-plasma accelerators 4
1.4 Motivation 5
1.5 Author's role 5
1.6 Thesis outline 6

2 Theory of laser-plasma wakefield accelerators **8**
2.1 Waves in a plasma 9
2.1.1 Plasma properties 9
2.1.2 Governing equations 9
2.1.3 Plasma oscillation 10
2.1.4 Ponderomotive force 10
2.1.5 Propagation of electromagnetic waves in a plasma 11
2.1.6 Excitation of plasma waves 12
2.1.7 Wake-breaking limit of plasma waves 14
2.2 Laser-plasma wakefield accelerators 15
2.2.1 Electron trapping 15
2.2.2 Electron acceleration 16
2.2.3 Plasma beat-wave accelerators 18
2.2.4 Laser-plasma wakefield accelerators 19
2.2.5 Self-modulated laser-plasma wakefield accelerators 21
2.2.6 Multi-pulse laser-plasma wakefield accelerators 22
2.3 Limitations and solutions 24

2.3.1 Laser diffraction . . . 24
2.3.2 Dephasing lengths . . . 25
2.3.3 Pump depletion . . . 25
2.3.4 Laser systems . . . 25

3 Theory of multi-pulse train characterisation 28
3.1 Introduction . . . 29
3.2 Theory of multi-pulse trains . . . 29
3.2.1 Interference of chirped pulses . . . 29
3.2.2 Generation of multi-pulse trains . . . 32
3.2.3 Representation of multi-pulse trains . . . 35
3.3 Measurement of multi-pulse trains . . . 36
3.3.1 Auto-correlation of multi-pulse trains . . . 36
3.3.2 Fundamentals of frequency-resolved optical gating . . . 41
3.3.3 Beam geometries of FROG . . . 44
3.3.4 Non-collinear second-harmonic generation . . . 51
3.3.5 Single-shot beam geometry in SHG FROG . . . 52
3.4 Phase retrieval algorithms in FROG . . . 53
3.4.1 Iterative Fourier transform algorithms . . . 53
3.4.2 Principle component general projections algorithms . . . 55
3.4.3 Ptychographic iterative engine algorithms . . . 57
3.5 Time-frequency joint information . . . 60
3.5.1 Time directions . . . 60
3.5.2 Direct spectral phase information . . . 62
3.6 Conclusions . . . 63

4 Simulation of multi-pulse train characterisation 65
4.1 Introduction . . . 66
4.2 Simulation of multi-pulse train generation . . . 66
4.2.1 Generation of real multi-pulse trains . . . 66
4.2.2 Non-uniformity of pulse trains . . . 70
4.2.3 Influence of adopting grating pair compressors . . . 71
4.2.4 Error analysis of multi-pulse train generation . . . 73
4.3 Phase retrieval of multi-pulse trains . . . 75
4.3.1 Selection of FROG algorithms . . . 75
4.3.2 Influence of bandpass filters . . . 79
4.3.3 Influence of noise . . . 82
4.3.4 Retrieval of nonuniform pulse trains . . . 87
4.4 Optical systems . . . 90
4.4.1 Phase-matching angles and temporal window sizes . . . 90

4.4.2 Phase-matching bandwidths and spectral window sizes 92
4.4.3 Temporal and spectral resolution of FROG traces 95
4.4.4 Design of imaging spectrometers in FROG 97
4.5 Conclusions 101

5 Implementation of multi-pulse train characterisation 102
5.1 Introduction 103
5.2 Development of a single-shot FROG device 103
5.2.1 Design of the single-shot FROG device 103
5.2.2 Specification of the single-shot FROG device 106
5.3 Measurement of multi-pulse trains in OPAL 112
5.3.1 Experimental setup 112
5.3.2 Data analysis procedure 113
5.3.3 Pulse measurement results 118
5.3.4 Diagnosis of nonuniform pulse spacing 124
5.4 Measurement of multi-pulse trains in Gemini TA3 125
5.4.1 Introduction 125
5.4.2 Experimental setup 127
5.4.3 Procedure of pulse retrieval and data analysis 132
5.4.4 Pulse measurement results 134
5.5 Conclusions 138

6 Pulse characterisation of plasma-modulated pulse trains 140
6.1 Introduction 141
6.2 Theory 141
6.2.1 Plasma-modulated laser pulses 141
6.2.2 Generation of P-MoPA pulse trains 144
6.2.3 Representation of P-MoPA pulse trains 145
6.2.4 Frequency-resolved optical gating (revisited) 147
6.2.5 Self-referenced spectral interferometry 148
6.2.6 Cross-referenced spectral interferometry 150
6.3 Simulation 152
6.3.1 Simulation conditions 152
6.3.2 Characterisation of reference pulses 155
6.3.3 Characterisation of plasma-modulated laser pulses 158
6.4 Experiment 162
6.4.1 Design considerations of the pulse measurement device 162
6.4.2 Optical layout of the pulse measurement device 163
6.5 Conclusions 165

7 Conclusions **169**
7.1 Author's contributions 169
7.2 Summary 170
7.3 Limitations 172
7.4 Outlook 174

Appendices

A Supplemental material for the pulse train generation **179**
A.1 Michelson interferometer 179
A.2 Grating-pair compressor 181

B Computer codes for the pulse train characterisation **184**
B.1 Generation of multi-pulse trains 184
B.2 Generation of P-MoPA pulse trains 191
B.3 The ePIE algorithm 198
B.4 The SSA algorithm 206

References **215**

List of Figures

2.1 Example of plasma wakefield excited by a squared laser pulse 13
2.2 Example of the phase space of the electron motion 16
2.3 Example of plasma wakefield excited a beat wave in a plasma beat-wave accelerator 19
2.4 Example of plasma wakefield excited by an intense ultra-short laser pulse in the LWFA 20
2.5 Example of plasma wakefield excited by a train of low-energy ultra-short laser pulses in MP-LWFA 23

3.1 Schematic of pulse train generation 33
3.2 Representation of pulse train in the spectral and temporal domains . . . 36
3.3 Schematics of an electric field auto-correlator and intensity fringe averaged auto-correlator 38
3.4 Schematics of a collinear SHG auto-correlator and a non-collinear SHG fringe-resolved auto-correlator 39
3.5 Examples of an input pulse train with a uniform pulse spacing and its SHG-AC signal 40
3.6 Examples of an input pulse train with a nonuniform pulse spacing and its SHG-AC signal 40
3.7 Intensity interferometric auto-correlation of the multi-pulse train 42
3.8 Examples of 1- and 2-D STFT. 44
3.9 Schematic of a non-collinear FROG 44
3.10 Temporal and spectral intensity of a pulse train with 5 pulses and a 200-fs pulse spacing 45
3.11 Comparison of FROG techniques and corresponding FROG traces 47
3.12 Beam geometries of TG FROG and modern FROG techniques 50
3.13 Non-collinear beam geometry of the SHG process and single shot geometry of in a uni-axial crystal 52
3.14 Schematic of a basic FROG algorithm 54
3.15 Schematic of the PCGP algorithm 55
3.16 Schematic of the ePIE algorithm 59

4.1 Procedures of simulating multi-pulse trains 67

4.2 Real spectra of laser pulses and Pulse trains with T_m of 200 fs and N_p of 10 68
4.3 Example of simulated pulse train and standard error of the simulated pulse spacings in different pulse trains 69
4.4 Strategy of adjusting T_m and N_p by changing ψ_2 and τ 69
4.5 Variation of T_m and N_p with τ in a pulse train 70
4.6 Intensity of pulse trains and pulse spacing variation of pulse trains affected by ψ_3 70
4.7 s_0 and s_1 versus ψ_3 71
4.8 ΔL_s and ΔL_m versus T_m ranging from 150 fs to 250 fs for pulse trains with $N_p = 6$, 10, and 15 72
4.9 ψ_3 and s_1 versus T_m 73
4.10 δT_m versus δL_m and δL_s 74
4.11 δT_m versus $\delta\theta_i$ and δf 75
4.12 Comparison of the convergence rate of FROG algorithms for different pulse trains 77
4.13 Retrieval results for $N_p = 5$ and $T_m = 200$ fs. The grey and red curves show the input pulse train and retrieved pulse train. 78
4.14 Retrieval results for $N_p = 10$. The definitions of coloured curves follows ones in Figure 4.13. 78
4.15 Retrieval results for $N_p = 15$ 78
4.16 Probe and gate pulses forming the SHG FROG traces with the insertion of a bandpass filter whose $\Delta\lambda = 10$ nm 80
4.17 SHG FROG traces with and without the insertion of a bandpass filter. . 80
4.18 GDD versus spectral bandwidth of a filter and pulse spacing. 81
4.19 Retrieval results of FROG traces with Poisson noise 84
4.20 Retrieved temporal and spectral intensity of a pulse train with Poisson noise 85
4.21 Retrieval results of FROG traces with Gaussian noise 86
4.22 Retrieved temporal and spectral intensity of a pulse train with Gaussian noise 87
4.23 FROG error, G_{FROG}, and RMS intensity error, σ_I, versus SNR for the Poisson and Gaussian noise 88
4.24 FROG traces influenced by GDD = $11,570$ fs^2 and TOD. 89
4.25 s_1 versus TOD and RMS error versus SNR of Gaussian noise 89
4.26 Variation of θ_p and Δt_d versus θ_{cut} 91
4.27 $\eta_{SHG}(\lambda, \theta_p)$ of four nonlinear crystals. 92
4.28 η_{SHG} versus λ at θ_p in $\theta_{cut} = 60^\circ$ and $L_s = 100\mu$m. 93
4.29 Illustration of insufficently wide $\Delta\Lambda$ and $\Delta\Lambda$ versus L_s 94

4.30 Phase-matching curves at which the phase-matching angles are shifted by 1° and normalised power of the SH spectrum versus deviation of phase-matching angle . . . 94
4.31 Variation of spectral resolution and number of grid points versus TBP for the pulse train measurement . . . 96
4.32 TBP versus N_p in pulse trains with a constant Δt_{rms} . . . 97
4.33 Schematic of a grating spectrometer . . . 98
4.34 Littrow angle and focal length versus groove density . . . 99

5.1 Optical layout of an 800-nm FROG device with a single-shot beam geometry 104
5.2 Experimental setup of the 800-nm FROG device. . . . 106
5.3 Resolution testing result . . . 107
5.4 Definition of the spatial resolution R_s and optical contrast versus the group element . . . 107
5.5 Spectral lines and FWHM spectral bandwidth . . . 108
5.6 SSA signal versus pixel number and temporal calibration curve . . . 110
5.7 FROG trace and auto-convolution signal for the spectral calibration . . . 110
5.8 Spatial frequency of the auto-convolution signal and spectral calibration curve . . . 111
5.9 Schematic of multi-pulse train measurement. . . . 112
5.10 Schematic of data analysis procedure for pulse train measurement . . . 113
5.11 Histogram of background noise and corresponding FROG trace images . 115
5.12 Temporal and spectral calibration of the FROG device . . . 116
5.13 Retrieval result of a 343-fs short pulse . . . 119
5.14 Retrieval results of a short pulse passing through a block of 105-mm SF-10 glass . . . 120
5.15 Retrieval results of a pulse train with a positive chirp, $\Delta\tau_{\mathrm{rms}} = 1.4$ ps and TBP = 14.1 . . . 122
5.16 Retrieval results of pulse train with a negative chirp, $\Delta\tau_{\mathrm{rms}} = 1.6$ ps and TBP = 16.1 . . . 123
5.17 Retrieved pulse trains with average T_m of 198 and 232 fs . . . 124
5.18 Experimental layout of the 2023 experiment to demonstrate the RDI in a MP-LWFA in Gemini TA3 at RAL . . . 129
5.19 Beam path of the pulse train measurement in the 2023 RDI-in-MP-LWFA experiment. . . . 131
5.20 Experimental setup of the single-shot FROG device used in the 2023 RDI in MP-LWFA experiment . . . 131
5.21 Procedure of pulse train reconstruction for the 2023 Gemini experiment. 132
5.22 Calibration of FROG images for the 2023 RDI experiment . . . 134
5.23 Retrieval results for a pulse train with a 153-fs pulse spacing . . . 135

5.24 Retrieval results for a pulse train with a 124-fs pulse spacing 137

6.1 Schematic of the pulse train generation process in the P-MoPA 142
6.2 Examples of a plasma wakefield excited by a seed pulse and spectral intensity of the plasma-modulated drive pulse 144
6.3 Examples of compressed drive pulse in the temporal and spectral domains 145
6.4 Examples of P-MoPA pulse train structures in the temporal and spectral domains 146
6.5 Schematic of a SPIDER setup 148
6.6 Schematic of an FTSI algorithm used in SPIDER 149
6.7 Schematic of a SEA-TADPOLE setup 151
6.8 Schematic of an FTSI algorithm in SEA-TADPOLE 152
6.9 Input spectra and pulses in the simulation of P-MoPA pulse train measurement. 153
6.10 Simulated spectra and intensity of plasma-modulated pulses before and after pulse compression. 154
6.11 Blind and cross-correlation FROG traces in the P-MoPA. 156
6.12 Retrieved spectral phase of the seed pulse. 157
6.13 SEA-TADPOLE traces of the plasma-modulated drive pulse. 160
6.14 Fourier-transformed SEA-TADPOLE traces of the plasma-modulated drive pulse. 160
6.15 Retrieved spectra of the plasma-modulated drive pulse. 161
6.16 Retrieved plasma-modulated drive pulses. 161
6.17 Schematic of the pulse measurement device. 164
6.18 Experimental setup of the 1030-nm cross-correlation FROG device. . . . 165

A.1 Schematic of a Michelson interferometer. BS—beam splitter; and M—mirror; 180
A.2 Schematic of a grating-pair compressor 183

List of Tables

2.1 $\gamma_{\min}$ and $\gamma_{\max}$ of trapped electrons in a plasma wakefield [57], where $\Delta\Phi = E_{\max} - E_{\min}$. 16

4.1 Error sources of pulse trains with $N_p = 10$ and $T_m = 150$, 200, and 250 fs. 75
4.2 Comparison of calculated GDD obtained from $\langle\tau\rangle_\omega$ and the input GDD for different numbers of pulses in pulse trains. 81
4.3 Crystal specification of BBO for the measurement of pulse trains 98
4.4 Specification of imaging spectrometer 100

5.1 Specification of the 800-nm single-shot SHG FROG 112
5.2 Dispersion of materials in the 800-nm single-shot SHG FROG device. . . 116

6.1 Phase retrieval results for characterising the seed pulse. 158

List of Abbreviations

AC . . . . . auto-correlation

BBO . . . . . beta barium borate

CCD . . . . . charged coupled device

CPA . . . . . chirped pulse amplification

CMOS . . . . . complementary metal-oxide-silicon

ePIE . . . . . extended ptychographic iterative engine

XPW . . . . . cross-polarised wave

FFT . . . . . fast Fourier transform

FEL . . . . . free electron laser

FTSI . . . . . Fourier-transform spectral interferometry

FROG . . . . . frequency-resolved optical gating

FWHM . . . . . full width half maximum

GD . . . . . group dispersion

GDD . . . . . group delay dispersion

GVD . . . . . group velocity dispersion

GP . . . . . general projection

GS . . . . . Gerchberg-Saxton

IAC . . . . . interferometric autocorrelation

iFFT . . . . . inverse fast Fourier transform

KDP . . . . . potassium dideuterium phosphate

LWFA . . . . . laser-plasma wakefield accelerators

$LiIO_3$ . . . . . lithium iodate

LBO . . . . . lithium triborate

MP-LWFA . . . . . multi-pulse laser-plasma wakefield accelerators

Nb:YAG . . . . . neodymium:yttrium–aluminium–garnet

NA . . . . . numerical aperture

1-D . . . . . one-dimensional

PBWA . . . . . plasma beat-wave accelerators

P-MoPA . . . . . plasma-modulated plasma accelerators

PCGP . . . . . principle component generalised projections

PIE . . . . . ptychographic iterative engine

RMS . . . . . root-mean-square

SHG . . . . . second harmonic generation

SM-LWFA . . . . . self-modulated laser-plasma wakefield accelerators

SNR . . . . . signal-to-noise ratio

SI . . . . . spectral interferometry

STC . . . . . space-time coupling

STFT . . . . . short-time Fourier transform

STRUT . . . . . spectral and temporally resolved up conversion technique

SEA . . . . . spatially-encoded arrangement

SPIDER . . . . . spectral phase interferometry for direct electric-field reconstruction

SVD . . . . . singular value decomposition

SEA-TADPOLE . . . . spatially-encoded arrangement temporal analysis by dispersing a pair of light E-fields

TBP . . . . . time-bandwidth product

TOD . . . . . third-order dispersion

Ti:sa . . . . . titanium sapphire

3-D . . . . . three-dimensional

2-D . . . . . two-dimensional

UV . . . . . ultraviolet

Yb:YAG . . . . . ytterbium:yttrium–aluminium–garnet

List of Symbols

p . . . momentum

c . . . speed of light in vacuum

h . . . Plank constant

λ_r . . . resonant wavelength of the cavity

D_c . . diameter of the cavity

ΔU . . energy gain inside the cavity

K . . . correction factor of the energy gain inside the cavity

P_{rf} . . radio frequency power

L_{ca} . . length of the cavity

P_k . . output power of klystrons

r_s . . . the shunt impedance

η_k . . . efficiency of klystrons

I_b . . . beam current in klystrons

λ_D . . Debye length

ϵ_0 . . . vacuum permeability

n_0 . . . plasma density

T_e . . . electron temperature

k_B . . Boltzmann constant

q . . . charge of particle

n_p . . . number density of particles

ρ . . . charge density

μ_0 . . . vacuum permeability

t . . . time

T_e . . . electron temperature

B . . . magnetic flux density

v . . . velocity

E . . . electric field

f . . . frequency

ω . . . angular frequency

λ . . . wavelength

ω_p . . plasma angular frequency

f_p . . . plasma frequency

λ_p . . . plasma wavelength

λ_0 . . . centre laser wavelength

$\gamma_\perp$ . . transverse Lorentz factor

a_0 . . . normalised field amplitude

I_0 . . . laser intensity

Φ_{pond} . ponderomotive potential

F_{pond} . ponderomotive force

σ . . . conductivity

n_c . . . critical plasma density

v_p . . . phase velocity

v_g . . . group velocity

n_i . . . number density of charged ions

δn . . perturbed electron density

E_z . . longitudinal electric field

E_{wb} . . wave-breaking electric field

L_r . . laser spot size

E_r . . radial electric field

v_i . . . initial velocity of an electron

v_f . . . final velocity of an electron

m_e . . mass of electron

γ_e . . . Lorentz factor of electron

H . . . hamiltonian function

k_p . . . wave vector of plasma wakefield

L_d . . dephasing length

T_p . . . plasma period

$\Delta\omega_b$. beat wave frequency

z_R . . Rayleigh length

σ_E . . energy spread of electron bunch

L_{pd} . . pump depletion length

$\Delta\omega$ . . spectral bandwidth

ψ . . . spectral phase

ϕ . . . temporal phase

ψ_n . . n^{th}-order spectral phase

T_m . . pulse spacing in pulse train

N_p . . number of pulses in pulse train

τ . . . time delay between two pulses

ΔL_m . displacement of the Michelson arm

ΔL_s . slant distance of a two-pass grating pair compressor

λ_g . . . grating period

I_{IAC} . interferometric autocorrelation trace

I_{FROG} FROG trace

E_{sig} . . FROG kernel

G_{FROG} FROG trace error

η_{SHG} . SHG efficiency

L_c . . crystal thickness

θ_{p} . . . phase matching angle

θ_{cut} . . cut angle of nonlinear crystal

$\langle\tau\rangle_\omega$. mean conditional delay

n_{or} . . refractive index of ordinary wave

n_{ex} . . refractive index of extraordinary wave

σ_t . . . RMS temporal intensity error

σ_ω . . RMS spectral intensity error

σ_ϕ . . RMS intensity-weighted temporal phase error

σ_ψ . . RMS intensity-weighted spectral phase error

N_{PE} . photoelectron

S_{non} . nonuniformity pulse train

s_n . . . nth order nonuniformity of pulse train

T_{trace} . temporal window of FROG trace

F_{trace} . spectral window of FROG trace

$\Delta\nu_{\mathrm{rms}}$. RMS spectral bandwidth

$\Delta\tau_{\mathrm{rms}}$. RMS pulse duration

N_{grid} . grid size of FROG trace

δf . . spectral resolution

δt . . . temporal resolution

L_p . . length of plasma channels

Scientists have become the bearers of the torch of discovery in our quest for knowledge.

— Stephen W. Hawking, English scientist,
1942 - 2018 [1]

1 Introduction

Contents

1.1 Discovery of fundamental particles 1
1.2 Conventional particle accelerators 2
1.3 Conventional laser-plasma accelerators 4
1.4 Motivation 5
1.5 Author's role 5
1.6 Thesis outline 6

1.1 Discovery of fundamental particles

Understanding the composition of the universe is just the beginning of a philosophical journey in a human's limited life span. Answering all the scientific questions eventually guides humans to confront the ultimate question: why do we exist in such a complex and mysterious spacetime? The answer to this question depends on how humans perceive this world and how they interpret all the natural phenomena that have been discovered.

From the perspective of particle physicists, our world consists of 12 fundamental particles [2]. These particles are considered point-like, without any substructure, and the building blocks of matter on the scale of $\leq 10^{-15}$ m or femtometres (fm) [3]. According to the theory of the diffraction limit in optics and wave–particle duality in quantum mechanics [4, 5], a particle with energy, $pc \leq hc/d$, is required to probe structures

at scale d, where p is the momentum of the particle, c is the speed of light, and h is the Planck constant. To resolve any structure smaller than 0.1 fm, the centre-of-mass energy must be larger than 2 gigaelectronvolts (GeV).

In the development of femtoscopy for the study of the fundamental composition of the world, particle accelerators are regarded as the cornerstone of elementary particle physics. During the last several decades, physicists invented and constructed early types of particle accelerators such as electrostatic accelerators, linear accelerators, cyclotrons, betatrons, and synchrotrons [6]. Since the development of particle accelerators, 26 Nobel Prizes in Physics have been awarded for their direct and indirect contributions to outstanding research in the fields of spectrography, crystallography, radiography, atomic structures and fundamental particles [7].

In the modern era, particle accelerators have also been applied outside scientific research. A large number of particle accelerators (over 20,000) have assisted in the development of semiconductor manufacturing, mainly in ion implantation, electron beam processing and microscopes [8]. Furthermore, particle accelerators have been deployed in more than 100 medical centres and hospitals for use of the radiotherapy, hadron therapy, and medical imaging [9, 10].

To make further discovery in regard to the fundamental constituents of the universe, it is essential to understand the principles of particle accelerators and develop advanced particle acceleration concepts that can satisfy the demands of scientific research in fundamental physics for the next 50 years.

1.2 Conventional particle accelerators

In conventional particle accelerators, cylindrical resonant cavities are used to form longitudinal and time-varying electric fields to achieve high accelerating voltages [11]. The aperture sizes of these cavities are constrained by the resonant wavelength $\lambda_r = \pi D_c/2.4$, where D_c is the diameter of the cavity. The energy gain inside the cavity is $\Delta U = K\sqrt{P_{\mathrm{rf}} L_{\mathrm{ca}} r_s}$, where the correction factor $K < 1$, P_{rf} is the radio frequency (RF) power, L_{ca} is the length of the cavity, and r_s is the shunt impedance. For a 20-cell RF-cavity ($L_{\mathrm{ca}} = 20$ cm) working at 1.3 GHz, the energy gain can be up to 20 MeV [12].

Klystrons are power generators that use low-amplitude RF waves to modulate streams of constant current, which induce a bunching effect to excite intense RF fields as output. The output power of klystrons is $P_k = \eta_k U_0 I_b$, where the efficiency is η_k, the voltage supply is U_0, and the beam current is I_b. These machines are commonly used to supply high RF power (> megawatt, MW) and couple it into RF cavities with rectangular waveguides to achieve a high acceleration gradient [13]. For a commercially available klystron (E37503, Canon) [14], a peak power of 20 MW with a pulse length of 150 μs and working at 1 GHz was demonstrated for projects in the Compact Linear Collider (CLIC) [15].

RF breakdown is considered as the primary factor limiting the highest achievable acceleration gradients in a cavity. Its primary cause is believed to be the field emission at the surface protrusions of RF cavities, which induces strong local electric fields [16]. The current flow through the protrusions leads to high local temperatures and the melting of surface structures. As a consequence, the enhanced field emission causes surface ionisation or electron avalanche, which damages the inner walls of the RF cavities [17]. Under the constraint of RF breakdown, recent research has demonstrated an acceleration gradient of 190 MV/m working at an input frequency of 11.7 GHz and with an input power of 115 MW [18].

Therefore, it is necessary to combine many accelerator stages to accelerate charged particles to sufficiently high energy (hundreds of GeV). For instance, the International Linear Collider (ILC), which would be used to collide positrons and electrons, has a target centre-to-mass energy of 500 GeV. To achieve this energy level, ILC requires 16,000 RF cavities with an acceleration gradient of 35 MV/m and a total length of 22 kilometres (km) [19].

Due to the constraints of RF breakdown, future RF-based particle accelerator facilities will be on a scale of km, and their construction and operation cost will be very high. For instance, constructing the entire ILC facility requires land with a length of 31 km and was expected to cost approximately 12 billion GBP [20] in 2012.

1.3 Conventional laser-plasma accelerators

One solution to overcome the acceleration limit caused by the RF breakdown is to exploit the nature of plasma to sustain much higher electric fields than materials commonly used in conventional accelerator technologies.

In contrast to conventional particle accelerators, an equivalent electric field generated in these plasma cavities is of the order of 100 GeV/m and can accelerate electrons to hundreds of megaelectronvolts (MeV) within a few tens of micrometres (μm) [21]. This technique, named laser-plasma wakefield accelerator (LWFA), was first proposed by Tajima and Dawon [22] in 1979. The potential to accelerate electrons to high energies by using laser technologies was first demonstrated in their simulation work. The underlying physics opens the possibility of ultra-compact particle accelerators that could be applied in the fields of free-electron lasers or lepton colliders [23–26].

Generation of high energy ($\sim$ MeV) electron bunches with conventional LWFA requires laser intensity of the order of 10^{18} W/cm^2 and pulse duration of 40 fs [27]. This strategy inevitably requires a laser system with high peak power ($\sim 10^{12}$ W or TW). To date, Titanium:sapphire (Ti:Sa) laser systems are the mainstream technology providing high peak power laser pulses to generate plasma wakefields. However, the low quantum efficiency of the gain medium leads to very low wall-plug efficiencies (0.1 – 1 %) and significant heating of the amplification crystals, which require dedicated heat management systems [28].

These issues limit Ti:Sa laser systems to low repetition rate ($\sim$ Hz), which significantly lowers the average power of X-rays and event-rates of particle collisions in applications of LWFA-based free-electron lasers (FELs) and lepton colliders, respectively. Simply speaking, current LWFA systems are unable to be compatible with current accelerator technologies such as those proposed for the upgraded Linac Coherent Light Source (LCLS-II) with a MHz repetition rate [29] and the CLIC with 18,000 bunches per second [12].

To overcome the insufficiency of the conventional LWFA, advanced acceleration concepts have been proposed. Among these new concepts, Hooker et al. [28] proposed

the use of structured laser pulses to excite plasma wakefields resonantly which can enable the use of laser technologies with high wall-plug efficiencies and repetition rates.

1.4 Motivation

Proof-of-principle experiments of LWFA using structured laser pulses require accurate and precise characterisation of temporal pulse structures, since plasma wakefields excited by these complex laser pulses are sensitive to the variation of the temporal structures ($\sim$ fs) of these pulses with pulse duration on the picosecond (ps) scale.

To successfully demonstrate LWFA using structured laser pulses, reliable pulse diagnostic tools are necessary. The development and demonstration of these scientific instruments require systematic research in optical instrumentation and optical signal processing. Although ultrafast pulse measurement has been researched for decades, it is essential to choose the most suitable techniques for specific tasks according to the features of laser pulses that can be used in the experiments.

The motivation of this thesis is to clearly and systematically describe the steps of building optical instruments for the characterisation of structured pulses suitable for driving LWFA. It also aims to experimentally demonstrate that the pulse measurement devices built by the author were able to characterise temporally structured pulses on the basis of physical simulations and analysis of experimental data.

1.5 Author's role

I identified appropriate techniques for the measurement of laser pulses with complex temporal structures and for developing pulse measurement devices. Through detailed physical simulations, two dedicated pulse measurements instrument were successfully constructed. I conducted optical testing on these instruments and investigated their actual capability of pulse measurement. The experimental results show that devices were able to measure laser pulses with the required structures. These pulse measurement instruments are being used in the TW lab at the University of Oxford for research of two ground-breaking LWFA concepts proposed by Professor Simon Hooker and Professor Roman Walczak.

I have worked in the fields of laser pulse measurement and electron bunch spectrometry during my doctoral research career. My contributions to scientific research in LWFA were assisting in the diagnostics of electron spectra with magnetic dipoles for electron acceleration in optically formed plasma channels and the measurement of multi-pulse laser trains using a single-shot auto-correlator for the study of resonant excitation of plasma wakefields. In collaboration with my former and current colleagues, I have co-published two peer-reviewed scientific journals [30, 31].

1.6 Thesis outline

The research and results described in this thesis are organised into the following chapters.

Chapter 2 provides an introduction to plasma properties, wave propagation in plasmas and the theoretical background of LWFA. The limitations of LWFA and potential solutions to overcome them are briefly addressed.

Chapter 3 presents a theory of pulse train formation and an approach of generating multi-pulse trains for proof-of-principle LWFA experiments. In addition, the theoretical background of ultra-short pulse measurement for pulse trains is discussed in preparation for simulation work.

Chapter 4 describes results of simulations of multi-pulse train generation and the influence of potential experimental uncertainty. Phase retrieval algorithms suitable for the pulse measurement of multi-pulse trains are investigated, and the effects of potential experimental conditions on the pulse measurement are discussed. On the basis of the simulated performance of optical components, the design of a pulse measurement instrument is described.

Chapter 5 discusses procedures for implementing a provisional pulse measurement device. According to the results of optical testing, a specification of the pulse measurement device is provided. Using the developed optical systems, a thorough analysis of the experimental data collected in two major experiments is presented for the demonstration of the pulse measurement system.

Chapter 6 introduces a different type of laser pulse trains generated by plasma modulation and pulse compression. Theoretical background of this type of pulse trains is summarised based on the research conducted by the author's colleagues, and appropriate pulse characterisation type is discussed. Preliminary simulation work is presented to guide the design and construction of a new pulse measurement device.

Chapter 7 summaries all the research work described in previous chapters and discusses their limitations. Finally, proposals of the future work are presented.

Now, that this whiteness is a Mixture of the severally colour'd rays, falling confusedly on the paper, I see no reason to doubt of.

— Sir Isaac Newton, English scientist, 1642 - 1727 [32]

2

Theory of laser-plasma wakefield accelerators

Contents

2.1 Waves in a plasma 9
2.1.1 Plasma properties 9
2.1.2 Governing equations 9
2.1.3 Plasma oscillation 10
2.1.4 Ponderomotive force 10
2.1.5 Propagation of electromagnetic waves in a plasma 11
2.1.6 Excitation of plasma waves 12
2.1.7 Wake-breaking limit of plasma waves 14
2.2 Laser-plasma wakefield accelerators 15
2.2.1 Electron trapping 15
2.2.2 Electron acceleration 16
2.2.3 Plasma beat-wave accelerators 18
2.2.4 Laser-plasma wakefield accelerators 19
2.2.5 Self-modulated laser-plasma wakefield accelerators 21
2.2.6 Multi-pulse laser-plasma wakefield accelerators 22
2.3 Limitations and solutions 24
2.3.1 Laser diffraction 24
2.3.2 Dephasing lengths 25
2.3.3 Pump depletion 25
2.3.4 Laser systems 25

2.1 Waves in a plasma

2.1.1 Plasma properties

A plasma behaves like a fluid composed of electrons, ions and neutral particles [33, 34]. Its physical behaviour is mainly governed by the Newtonian force and the electromagnetic force. In a volume of interest, a plasma typically contains a large number of particles interacting with each other. therefore, a plasma exhibits collective effects that involve simultaneous interactions between each particle.

Although plasma is formed by charged particles and neutral particles, it has the tendency to maintain charge neutrality in a macroscopic volume. Because of the Debye shielding effect, the Coulomb force can extend only about a Debye length, λ_D, defined by [35].

$$\lambda_D = \sqrt{\frac{\epsilon_0 k_B T_e}{n_0 q^2}}, \tag{2.1}$$

where ϵ_0 is the vacuum permeability; k_B is the Boltzmann constant; T_e is the electron temperature; n_0 is the plasma density; and q is the charge of particle.

For ionised gas to be regarded as a plasma in a volume scaled by a length of L_p, it requires $L_p \gg \lambda_D$. For instance, an ionised gas with the given properties, $n_0 = 2.5 \times 10^{17}$ cm^{-3}, $T_e = 11{,}605$ K, and $L_p = 100$ μm, can be regarded as a plasma because $L_p \gg \lambda_D = 15$ nm.

2.1.2 Governing equations

Equations (2.2 – 2.7) describe the motion of charged particles in a plasma. These equations are the continuity equation regulates the fluid mechanism, the Lorentz force governing the motion of charged particles, and the Maxwellian equations describing the electromagnetic forces [36].

$$\frac{\partial n}{\partial t} + \boldsymbol{\nabla} \cdot (n_p \boldsymbol{v}) = 0, \tag{2.2}$$

$$\frac{\partial \boldsymbol{p}}{\partial t} = q(\boldsymbol{E} + \boldsymbol{v} \times \boldsymbol{B}), \tag{2.3}$$

$$\boldsymbol{\nabla} \cdot \boldsymbol{E} = \frac{1}{\epsilon_0}\rho, \tag{2.4}$$

$$\boldsymbol{\nabla} \times \boldsymbol{E} = -\frac{\partial \boldsymbol{B}}{\partial t}, \tag{2.5}$$

$$\boldsymbol{\nabla} \cdot \boldsymbol{B} = 0, \tag{2.6}$$

$$\boldsymbol{\nabla} \times \boldsymbol{B} = \mu_0 \boldsymbol{J} + \mu_0 \epsilon_0 \frac{\partial \boldsymbol{E}}{\partial t}, \tag{2.7}$$

where n_p is the number density of particles; $\boldsymbol{v}$ is the velocity; $\boldsymbol{p}$ is the momentum; ρ is the charge density; μ_0 is the vacuum permeability; $\boldsymbol{E}$ is the electric field; $\boldsymbol{B}$ is the magnetic flux density; and t is time.

2.1.3 Plasma oscillation

One of the most important plasma phenomena is the plasma-electron oscillation first studied by Tonks et al. [37]. The plasma frequency, ω_p, derived from Equations (2.3) and (2.4) is given by [38]

$$\omega_p = \sqrt{\frac{e^2 n_e}{m_e \epsilon_0}}. \tag{2.8}$$

For an underdense plasma with an electron density $n_e = 1 \times 10^{17}$ cm^{-3}, the plasma frequency $f_p = \omega_p/2\pi = 18$ THz. This corresponds to a plasma wavelength $\lambda_p = \omega_p/2\pi c = 106$ μm and a plasma period $T_p = 352$ fs, where c is the speed of light in vacuum.

2.1.4 Ponderomotive force

Suppose that a nonlinear external force is a spatially varying electric field, $\boldsymbol{E}(\boldsymbol{r}) = \boldsymbol{E}_0(\boldsymbol{r})\cos(\omega_0 t)$, where $\boldsymbol{r}$ is the position and ω_0 is the centre angular frequency of an external force. Using Equation (2.3), the ponderomotive force, $\boldsymbol{F}_{\text{pond}}$, can be shown to be [39]

$$\boldsymbol{F}_{\text{pond}} = -\frac{e^2}{4 m_e \omega_0^2} \boldsymbol{\nabla} \boldsymbol{E}_0^2. \tag{2.9}$$

It is convenient to define the ponderomotive potential, Φ_{pond}, by [40]

$$\begin{aligned}\Phi_{\text{pond}} &= \frac{e^2}{4m_e\omega_0^2}\boldsymbol{E}_0^2 \\ &= \frac{e^2}{8\pi^2 m_e\epsilon_0 c^3}I_0\lambda_0^2,\end{aligned} \tag{2.10}$$

where I_0 is the laser intensity; and λ_0 is the laser wavelength.

For highly intense electric field, the relativistic effect needs to be taken into account. Therefore, it is convenient to introduce the normalised field amplitude, $a_0 = eE_0/m_e\omega_0 c$. Using the relation $\gamma_\perp = (1 + a_0^2)^{1/2}$, where $\gamma_\perp$ is the transverse Lorentz factor [41], Equation (2.9) can be rewritten as

$$\boldsymbol{F}_{\text{pond}}^{\text{rel}} = -m_e c^2 \boldsymbol{\nabla}\gamma. \tag{2.11}$$

For a laser pulse with $I_0 = 1 \times 10^{18}$ W/cm, $\lambda_0 = 1$ μm, and $a_0 = 0.85$, the non-relativistic $\Phi_{\text{pond}} = 93$ keV.

2.1.5 Propagation of electromagnetic waves in a plasma

For a monochromatic plane wave, $\boldsymbol{E} = \boldsymbol{E}_0 \exp(\boldsymbol{k}_0 \cdot \boldsymbol{r} - \omega_0 t)$, propagating in a homogenous, isotropic and non-magnetic plasma, the wave equation can be written as [42]

$$\boldsymbol{\nabla}^2\boldsymbol{E} = \mu_0\frac{\partial \boldsymbol{J}}{\partial t} + \mu_0\frac{\partial^2 \boldsymbol{D}}{\partial t^2}, \tag{2.12}$$

where $\boldsymbol{J} = \sigma\boldsymbol{E}$ is the free current density; $\boldsymbol{D} = \epsilon_0\boldsymbol{E}$ is the dielectric displacement; and σ is the conductivity.

The dispersion relation of an electromagnetic wave propagating in a plasma is given by [43, 44]

$$k_0 = \frac{1}{c}\sqrt{\omega_0^2 - \omega_p^2}. \tag{2.13}$$

The critical plasma density, n_c, is defined as $n_c = \omega_0^2\epsilon_0 m_e/e^2$ using the condition, $\omega_0 = \omega_p$. n_c defines a boundary whether a wave with ω_0 can propagate in a plasma. For an electromagnetic wave with $\lambda_0 = 1$ μm, $n_c = 1.1 \times 10^{21}$ cm^{-3}. Any wave with $\lambda_0 >$ 1 μm cannot propagate in this plasma with $n_0 = n_c$ because k_0 of the wave becomes a complex number according to Equation (2.13).

According to Equation (2.13), the phase velocity of a monochromatic wave, $v_p = \omega/k$, is given by

$$v_p = c\left[1 - \left(\frac{\omega_p}{\omega_0}\right)^2\right]^{-1/2}. \tag{2.14}$$

The group velocity of a laser pulse, $v_g = \partial\omega/\partial\omega$, is given by

$$v_g = c\left[1 - \left(\frac{\omega_p}{\omega_0}\right)^2\right]^{1/2}. \tag{2.15}$$

According to Equation (2.15), v_g of a laser pulse propagating in an underdense plasma ($n_e \ll n_c$) is always smaller than c.

2.1.6 Excitation of plasma waves

A plasma wave can be excited by the ponderomotive force in an underdense plasma. Suppose that the number density of singly-charged ions is $Zn_i = n_0$, where n_0 is the ambient plasma density, and $Z = 1$, and these ions are stationary within the time scale of interest. The number density of electrons is defined as $n_e = n_0 + \delta n$, where the perturbed electron density $\delta n \ll n_0$ [45]. The total potential in the plasma is $\Phi_{\text{tot}} = \Phi + \Phi_{\text{pond}}$, where Φ is the potential of perturbed electron density and Φ_{pond} is the potential of ponderomotive force defined in Equation (2.10).

In a one dimensional (1-D) co-moving frame in which $\xi = z - ct$ and $\tau' = t$, the quasi-static approximation gives $\partial^2/\partial t^2 = c^2\partial^2/\partial\xi^2$ and $\partial^2/\partial z^2 = \partial^2/\partial^2\xi$ [46]. The wave equation of plasma waves excited by an external force, Φ_{pond}, within the limit of the small pump strength ($a_0 \ll 1$) is

$$\frac{\partial^2\Phi}{\partial\xi^2} + k_p^2\Phi = -k_p^2\Phi_{\text{pond}}. \tag{2.16}$$

Using the Green's function to solve the non-homogeneous 2$^{\text{nd}}$-order differential equation given in Equation (2.16) [47], the solution can be written as

$$\Phi = -k_p\int_0^{\xi}\Phi_{\text{pond}}\sin\left[k_p\left(\xi - \xi'\right)\right]d\xi', \tag{2.17}$$

Suppose that a laser pulse has a rectangular ponderomotive potential along the ξ-axis. Adopting the mathematical treatment described in Gorbunov et al. [48], a

Gaussian beam profile in the r-axis as given by

$$\Phi_{\text{pond}}(\xi) = \begin{cases} -\frac{1}{4}a_0^2, & -L/2 \leq \xi \leq L/2 \\ 0, & \text{otherwise} \end{cases} \tag{2.18}$$

where L is the pulse length; and the normalised field amplitude is $a_0 = m_e\omega_p c/eE_0$.

The longitudinal electric field E_z generated in the plasma wakefield can be found from Equation (2.17) as given by

$$\begin{aligned} E_z &= -\frac{\partial \Phi}{\partial \xi} \\ &= \frac{a_0^2 k_p}{2} \sin\left(\frac{k_p L}{2}\right) \cos(k_p \xi). \end{aligned} \tag{2.19}$$

Assuming that the plasma wakefield propagates at $v_p = v_g$, the maximum field strength, $E_z^{max} = a_0^2 k_p/2$, is achieved when the pulse length $L = \lambda_p/2$. For laser pulse with other shapes, such as a sine-squared or Gaussian pulse, the optimal pulse lengths, $L = \Delta\tau c$, where $\Delta\tau$ is the laser pulse duration. The maximum electric field strength are at λ_p and $\lambda/\sqrt{2}\pi$, respectively [48, 49].

Assuming that a laser pulse has a Gaussian beam profile in a quasi three-dimensional (3-D) cylindrical coordinate, Gorbunov et al. [48] provided solutions for Equation (2.16). For a given potential $\Phi_s(\xi, r) = R(r)a_0/4$, where $R(r) = \exp(-r^2/L_r^2)$, the radial

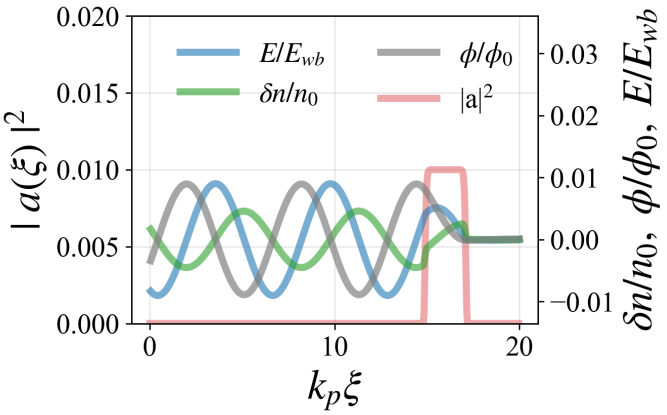


Figure 2.1: Example of plasma wakefield excited by a squared laser pulse. The red, blue, grey and green curves show the intensity of laser pulse $|a|^2(\xi)$, the amplitude of electric field E/E_{wb}, the amplitude of wakefield potential ϕ, and the amplitude of perturbed plasma density $\delta n/n_0$ normalised to n_0, respectively.

electric field of a wakefield, E_r, is given by

$$\begin{aligned} E_r &= -\frac{\partial \Phi_s}{\partial r} \\ &= -\frac{a_0^2 r}{L_r^2} \exp\left(-\frac{r^2}{L_r^2}\right) \sin(k_p \xi). \end{aligned} \tag{2.20}$$

where the spot size $L_r \gg 1/k_p$.

According to Equation (2.20), E_r generates a focusing and defocusing force depending on ξ. Compared to Equation (2.19), E_r has a $\pi/4$-phase shift with respect to E_z.

For arbitrary laser field strength, nonlinear plasma wakefields can be generated. Sprangle et al. [50, 51] developed a 1-D nonlinear theory of laser-plasma interactions using the quasistatic approximation. In the theory, the potential of plasma wakefield can be obtained by solving

$$\frac{\partial^2 \Phi}{\partial \xi^2} = k_p^2 \gamma_p^2 \left\{ \beta_p \left[1 - \frac{(1+a)^2}{\gamma_p (1+\Phi)^2} \right]^{1/2} - 1 \right\}, \tag{2.21}$$

where a is the normalised laser field strength, $\gamma_p = (1-\beta_p^2)^{1/2}$ and $\beta_p = v_p/c$.

Figure 2.1 shows the plasma wakefield excited by a rectangular pulse in the 1-D linear regime ($a0 \ll 1$), showing a sinusoidal distribution of the perturbed plasma density, $\delta n/n_0$, behind the pulse. The generated on-axis electric field, $E/E_{\rm wb}$, in the plasma wave also gives a sinusoidal distribution having peak amplitude at $\delta n/n_0 = 0$.

2.1.7 Wake-breaking limit of plasma waves

Breakdown of a plasma wakefield constrains the maximum E_z that can be coherently excited in a plasma [52]. T. Tajima et al. [22, 53] gave a physical picture of the wave-breaking limit which the oscillation length of electrons in one plasma period could not exceed the plasma wavelength. The maximum electric field in the non-relativistic cold wave-breaking limit, $E_{\rm wb}$, is given by

$$E_{\rm wb} = \frac{m_e c \omega_p}{e}. \tag{2.22}$$

For a plasma wakefield with $v_p \approx c$ or $\gamma \gg 1$, the maximum E_z can be larger than that predicted by Equation (2.22). The cold relativistic wave breaking limit, $E_{\rm wb}^{\rm R}$, generated in a plasma is given by [54]

$$E_{\rm wb}^{\rm R} = E_{\rm wb} \sqrt{2(\gamma_p - 1)}, \tag{2.23}$$

Using Equation (2.22), a laser pulse with $\lambda_0 = 1\mu$m in a plasma with $n_e = 10^{17}$ cm^{-3} can generate a plasma wakefield with $E_{\rm wb}$ of approximately 30 GV/m, which is about 300 times stronger than the electric field generated by conventional waveguide-based particle accelerators ($\sim$ 100 MV/m). For wakefield excitation in the relativistic regime, $E_{\rm wb}^{\rm R} \sim 440$ GV/m using Equation (2.23) and γ_p in Equation (2.21).

2.2 Laser-plasma wakefield accelerators

2.2.1 Electron trapping

Trapping of electrons in a plasma wakefield means that an electron with an initial velocity, v_i, has sufficient momentum, $p_e = \gamma_e m_e v_i$, so that it can move into a correct phase region where a plasma wave can accelerate it [55–57]. While the electron is being accelerated and moving with the plasma wave propagating at v_p, the final velocity of the electron, v_f, gradually approaches c such that $v_f > v_p$ before it moves into the deceleration phase. If v_i is too small, the electron will not be able to catch up with the moving plasma wave. In contrast, the electron will run out of the plasma wave too early if v_i is too large. Both cases lead to untrapped electrons.

To determine the minimum and maximum velocity of electrons for trapping and acceleration, the Hamiltonian function of the electron orbit in a plasma wakefield, H, is adopted [58] as given by

$$H \equiv -\gamma(1 - \beta_e\beta_p) - \Phi(\psi) + C_0, \tag{2.24}$$

where $\beta_e = 1/\sqrt{1 - 1/\gamma_e^2}$; $\beta_p = v_p/c$; the potential $\Phi(\psi) = A_0 \cos(\psi + \psi_0)$; the constant $C_0 = -\gamma_0(1 - \beta_0\beta_p) - A_0 \cos(\psi_0)$; γ_0 and β_0 are the initial conditions of an electron in the initial phase, ψ_0.

Figure 2.2 illustrates the phase space of electrons in a plasma wakefield. An electron is trapped in a plasma wakefield only when its motion forms a closed orbit in the phase space. The separatrix is a boundary that separates the stable and unstable regions of electron motion. Therefore, an electron cannot be trapped in a plasma wakefield when its motion in phase space falls outside the separatrix. For a sinusoidal plasma wakefield, the centre of the separatrix is located at $(k_p\lambda_p, \gamma_p)$ and the width of separatrix is $k_p\lambda_p$.

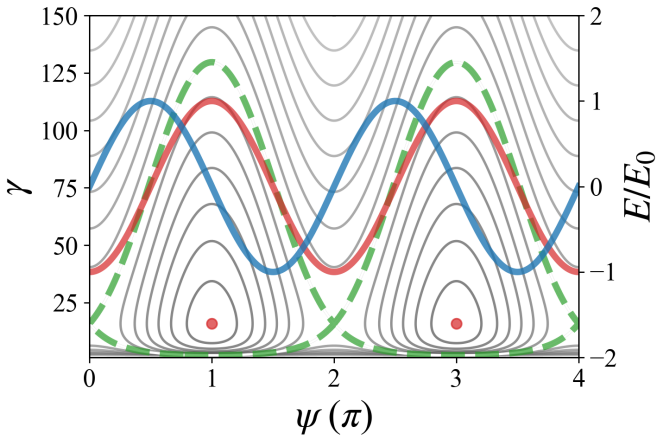


Figure 2.2: Example of the phase space of the electron motion. The grey, green-dashed, blue, and red curves show the contour of $H(\psi, \gamma)$, the separatrix, the longitudinal electric field, E_z/E_0, the radial field, E_r/E_0, respectively. The red dots locate the centre of the separatrix.

There is minimum electron energy, $\gamma_{\min}$, required to allow an electron to be trapped in a plasma wakefield. In addition, the maximum energy, $\gamma_{\max}$, that an electron can gain in a plasma wakefield is also limited. In the upper part of Figure 2.2, there are many orbits that are not closed and outside the separatrix.

According to Esarey et al. [57], the minimum and maximum energy of trapped electrons in plasma wakefields are summarised in table 2.1

2.2.2 Electron acceleration

Once electrons in a plasma wakefield have an initial energy large enough ($\gamma_e \geq \gamma_{\min}$), they can be trapped and accelerated in a plasma wakefield. Although the width of the separatrix is $k_p\lambda_p$, the actual region allowing acceleration of electrons in a plasma wakefield should take into account the longitudinal acceleration and radial focusing

	$\gamma_p\Delta\Phi \ll 1$	$\gamma_p\Delta\Phi \gg 1$	$E_0 \to E_{\text{wb}}$
$\gamma_{\min}$	$\gamma_p(1-\beta_p\sqrt{2\gamma_p\Delta\Phi})$	$\frac{\Delta\Phi}{2}+\frac{1}{2\Delta\Phi}$	γ_p
$\gamma_{\max}$	$\gamma_p(1+\beta_p\sqrt{2\gamma_p\Delta\Phi})$	$2\gamma_p^2\Delta\Phi$	$4\gamma_p^3-3\gamma_p$

Table 2.1: $\gamma_{\min}$ and $\gamma_{\max}$ of trapped electrons in a plasma wakefield [57], where $\Delta\Phi = E_{\max} - E_{\min}$.

electric fields in a plasma wakefield. Hence, the overall region that can be used to accelerate electrons in a plasma wakefield is only $k_p\lambda_p/4$.

In addition to the radial focusing force, the relativistic effect of accelerated electrons is of importance. When electrons are accelerated close to c ($v_e \rightarrow c$), a dephasing effect restricts their highest energy gain, $W_{\max}$, from the plasma wakefield. This occurs because v_p of the plasma wave is equal to v_g of the laser pulse ($v_g < c$). The accelerated electrons will eventually move to a phase of deceleration after a dephasing time, τ_d, corresponding to a dephasing length, L_d.

In the 2-D quasi-linear regime, the acceleration length, L_d, can be derived by [59]

$$\begin{aligned} L_d &= \frac{\lambda_p}{4c\left[1-\sqrt{1-(\frac{\omega_p}{\omega_0})^2}\right]} \\ &\cong \frac{\pi c^2\omega_0^2}{\omega_p^3} \end{aligned} \tag{2.25}$$

Since $\omega_p \approx n_0^{1/2}$, $L_d \propto n_0^{-2/3}$ for a given ω_0. As an example, a laser pulse with $\lambda_0 = 800$ nm excites a plasma wakefield in a plasma with $n_0 = 10^{17}$ cm^{-3}, $L_d \approx 90$ cm. In contrast, a plasma with $n_0 = 10^{18}$ cm^{-3} only gives a 3-cm dephasing length (30 times shorter than 90 cm).

Based on the discussion above, the total energy gain of electrons in the wave-breaking limit, $W_{\max}$, is given by

$$\begin{aligned} W_{\max} &= \int_0^{L_d} -eE_{\rm wb}dz \\ &= \frac{\pi m_e^2c^2\omega_0^2\epsilon_0}{e^2n_0}, \end{aligned} \tag{2.26}$$

Therefore, a single-stage electron accelerator can achieve $W_{\max} = 90$ GeV if using a plasma with $n_0 \sim 10^{17}$ cm^{-3} and its plasma wakefield is excited to $E_{\rm wb} \sim 96$ GV/m. Using Equation (2.11), it can be found that it requires a laser pulse with an intensity of 7.5×10^{18} W/cm or $a_0 = 2.3$ to achieve $E_{\rm wb} = 96$ GV/m. This creates an incentive to use a plasma channel with a low on-axis $n_0 \sim 10^{17}$ cm^{-3} to accelerate electrons in a single stage.

2.2.3 Plasma beat-wave accelerators

A plasma beat-wave accelerator (PBWA) is a type of LWFA, proposed by Tajima and Dawson in [22] 1979. Although the available laser intensity was able to achieve 10^{18} W/cm^{-2} with neodymium-doped (Nd-doped) Glass laser technologies in the 1970s, the laser pulse duration (10 ps $< \Delta\tau <$ 2 ns) was much longer than T_p for reasonable n_0, implying weak and inefficient excitation of plasma wakefields. Hence, they proposed using two laser beams with slightly different frequencies to create a beat wave that modulates the envelope of the two laser pulses [60]. The modulated laser beam was then used in the demonstration of electron acceleration in their simulation work.

Resonant excitation of plasma wakefields with the laser beat wave requires that ω_0 of co-propagating laser beams, ω_1 and ω_2, satisfy the phase matching conditions, $\omega_p = \omega_1 - \omega_2$ and $k_p = k_1 - k_2$ [61]. Once the phase matching conditions are satisfied, plasma waves can be excited by the beat wave with small pump strength ($a_0 \ll 1$) and their field amplitude grows slowly with time. Joshi et al. [61] showed that the growth rate δ is a linear function of the pump strength as given by $\delta = \omega_p a_1 a_2^*/4$, where the normalised field amplitude $a_n = eE_n/m\omega_n c$. However, the effect of relativistic detuning of plasma wavelength limits the maximum wakefield amplitude. The saturation amplitude, $E_{\rm sat} = 4\,(a_1 a_2/3)^{1/3}$, for a beat wave frequency at $\Delta\omega_b = 2\pi - 4\pi(9a_1a_2)^{2/3}$ [61, 62].

Figure 2.3 shows an example of the plasma wakefield excited by a beat wave whose modulation frequency $\Delta\omega_b = \omega_p$ in the quasi-linear regime. As can be seen, the sinusoidal plasma wakefield grew towards the back of the driver.

PBWA experiments were first conducted by the UCLA group in the late 1980s [63]. After more than a decade of efforts, the highest electron energy gain up to 38 MeV was reported [64–66] using a CO_2 laser delivering two co-propagating laser pulses with the λ_0 of 10.3 μm and 10.6 μm. The $\Delta\tau$ ranged from 100 to 400 ps. The n_0 produced in the experiment was approximately 9.4×10^{15}cm^{-3} (λ_p = 340 μm).

The latest simulation work based on PBWA shows that the relativistic detuning could be overcome by chirping the laser beat wave or creating a plasma gradient [67]. Based on the concept of auto-resonance [68, 69], Luo et al. claimed that the PBWA

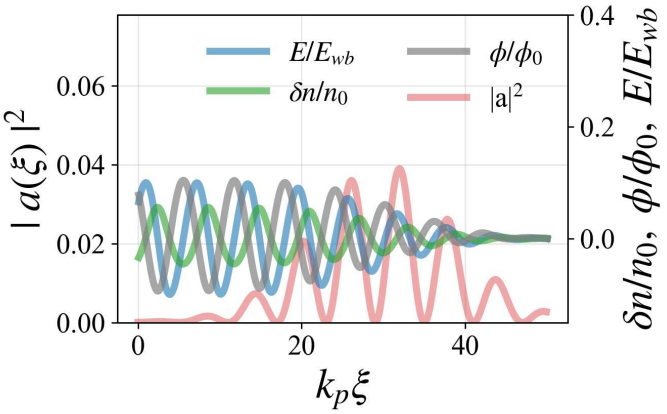


Figure 2.3: Example of plasma wakefield excited a beat wave in a PBWA. The red curve shows the intensity of laser pulse, $|a|^2$. Coloured curves are defined in Figure 2.1.

could achieve the wavebreaking limit by applying a linear frequency chirp to the input laser pulse with a pulse duration equal to 40 λ_p in the simulation.

2.2.4 Laser-plasma wakefield accelerators

A LWFA using a single short laser pulse to excite plasma wakefields, originally proposed by Tajima and Dawson in 1979, did not attract much attention until the realisation of chirped-pulse amplification (CPA) by Maine et al. [70]. Gorbunov et al. first developed a theory about the nonlinear excitation of plasma waves by a single short electromagnetic pulse with different shapes. Later, Sprangle et al. [71] proposed a LWFA adopting optical guiding for long-range electron acceleration, taking into account the latest CPA-based laser technology ($\tau_0 = 1$ ps, $E_0 = 1$ kJ) in the late 1980s.

In a LWFA, it is required that the pulse length of a laser pulse is shorter than the plasma wavelength so that the maximum amplitude of excited plasma wakefield can be reached [72]. In the linear regime ($E_{\max} \ll 2$), the maximum electron energy gain that can be achieved is $\gamma_{\max} = 4\gamma_p^2 E_{\max}$, where $E_{\max}$ is normalised to $E_{\rm wb}$ of the plasma wakefield. In contrast, the maximum electron energy gain in the nonlinear regime ($E_{\max} \gg 2$) is $\gamma_{\max} = 2\gamma_p^2 E_{\max}^2$ [57].

This scaling law has motivated the application of very high power laser pulses in driving laser-plasma accelerators. [73]. Figure 2.4 shows an example of plasma wakefields excited by a single short laser pulse in the 1-D non-linear regime. The saw-

tooth profile of the longitudinal electric field is an important feature resulting from the sharp distribution of plasma density excited by the highly intense laser driver ($a_0 = 2$).

Direct measurement of plasma waves using the femtosecond interferometry [74, 75] was reported in 1996. The acceleration of electrons with a maximum energy gain of 1.6 MeV in plasma wakefields [76] was observed in 1998. The first observation of mono-energetic electron bunches accelerated by the LWFA was reported by three different groups [77–79] in 2004. The three independent experiments used similar experimental conditions, such as $n_0 \sim 10^{19}$ cm^{-3}, $I > 10^{18}$W/cm^2, and driving plasma wakefield in the nonlinear regime. The highest electron energy observed was (170 $\pm$ 20) MeV with a charge of (0.5 $\pm$ 0.2) nC.

In the latest development of LWFAs, the highest electron energy gain of 7.8 GeV [80] was reported in 2019. In this experiment, short and intense laser pulses ($E_{\text{peak}} = 850$ TW, $\Delta\tau = 35$ fs) were guided in plasma channels and used to excite plasma wakefields in the nonlinear regime. One purpose of this experiment was to extend the electron acceleration range by plasma channels. A plasma channel, whose on-axis n_0 < off-axis n_0, can be regarded as an optical fibre commonly used to guide light through long distances ($\sim$ tens of mm). In that experiment, shallow plasma channels in 20-cm-long capillary-discharged waveguides were first formed by high-peak current pulses through magnetohydrodynamic (MHD) processes. Long laser pulses ($\sim$ 1 ns) were then send into the capillary waveguide to change the profile of the existing plasma channels by

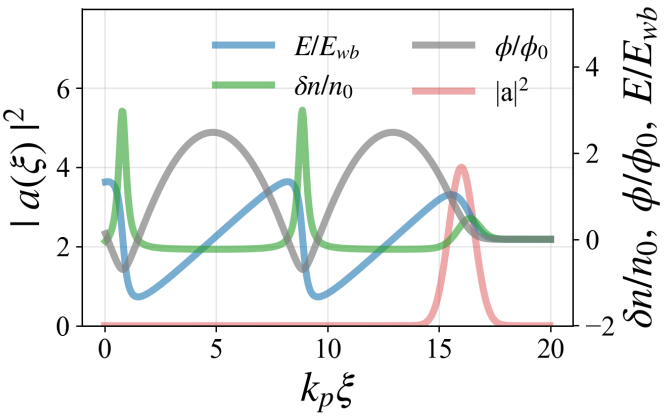


Figure 2.4: Example of plasma wakefield excited by an intense ultra-short laser pulse in a LWFA. Coloured curves are defined in Figure 2.1.

laser-induced hydrodynamic expansion in order to change the properties of the channel profile for efficient electron acceleration [81].

The LWFA using single-short pulses ($\Delta\tau \sim 40$ fs) have benefited from the development of laser mode-locking, CPA, and Ti:Sa laser systems [70, 82–84] for decades. It has become an important type of laser electron accelerators in the LWFA community [85–87].

2.2.5 Self-modulated laser-plasma wakefield accelerators

A self-modulated laser-plasma wakefield accelerator (SM-LWFA) uses a long laser pulse with high peak power to excite plasma wakefield resonantly [88, 89]. The mechanism of resonant excitation of plasma wakefield in the SM-LWFA requires: (i) the pulse length is longer than the plasma wavelength ($\Delta\tau c > \lambda_p$); and (ii) laser pulses can propagate in a plasma ($\omega_0 > \omega_p$).

Based on these conditions, a low-amplitude plasma wakefield can be created by the leading edge of the long laser pulse. The excited plasma wakefield within the long laser pulse produces a periodic variation of plasma density. This periodic plasma density interacts with the long laser pulse and hence induces the forward-Raman scattering (FRS) instability. This instability modulates the intensity of the long laser pulse so that the modulation period of the pulse is equal to the plasma period. This modulated laser pulse then drives a stronger plasma wave, in turn, leads to further modulation of the laser. This feedback mechanism leads to stronger modulation of the laser pulse, and excitation of a large amplitude plasma wave. Although SM-LWFAs have less stringent requirements on the input laser pulse duration, the electrons accelerated by SM-LWFA commonly have a very large energy spread and low beam quality. This is because the electron trapping and acceleration can happen in multiple cycles of the plasma wave.

The excitation of plasma wakefields in the high-density self-modulated regime was first observed by Darrow et al. [90] using the detection of Stokes and anti-Stokes in the spectrum of the pump laser. Accelerated electrons in an SM-LWFA were first measured by Nakajima et al. [91], using laser pulses ($\delta\tau = 1$ ps, $P_0 = 3$ TW) and plasma density $n_0 = 10^{19}$ cm^{-3}. Recent research has experimentally investigated electron acceleration mechanism involved in direct laser acceleration (DLA) in SM-LWFA [92–94]. DLA is

a mechanism which the transverse momentum of electron trapped in the off-axis is transferred into increased longitudinal momentum by the $\mathbf{v} \times \mathbf{B}$ force of the laser driver [93]. The experimental work in the low-density regime of SM-LWFA ($\omega_p \ll \omega_0$) by King et al. [94] ($\Delta t \sim 700$ fs, $n_0 \sim 3 \times 10^{17}$ cm^{-3}) suggested that the accelerated electrons at low energy (< 60 MeV) was produced via SM-LWFA and the higher energy gain (> 60 MeV) was caused by DLA.

2.2.6 Multi-pulse laser-plasma wakefield accelerators

A multi-pulse Laser-plasma wakefield accelerator (MP-LWFA) uses a sequence of low-energy laser pulses to excite plasma wakefield resonantly. In contrast to the PBWA, the temporal intensity of the pulse train in MP-LWFA is not restricted to a cosine-squared modulation. In principle, the duration, separation, and intensity of each pulse in the pulse train can be adjusted following the local plasma density variation. Robust theories about MP-LWFA [95–99] were developed in the 1990s, using the 1-D cold plasma model of nonlinear plasma wakefield excitation [51].

Based on the theory of MP-LWFA [99], the pulse front of each pulse in a train of multi-pulse should be placed at which $E_z = 0$ in each cycle of the plasma wakefield so that the maximum E_z for the next cycle can be generated. In other words, the optimal pulse spacing between the (n + 1) th pulse and the nth pulse $\Delta T_p = \lambda_n/c$, where n = 1, 3, 5, $\cdots$.

According to the theory [99], the nonlinear wavelength λ_n and the optimal pulse length L_n are given by $L_n = \frac{2}{k_p} E_n^{\frac{1}{2}} \kappa(\rho)$ and $\lambda_n = \frac{4}{k_p} E_n^{\frac{1}{2}} \kappa(\varrho)$, where k_p is the plasma wavelength seen by the first pulse, E_n is the maximum longitudinal electric field generated by the nth pulse, κ is the elliptic integral of the second kind, $\rho = \sqrt{1 - \gamma_n^2 E_n^{-2}}$ and $\varrho = \sqrt{1 - E_n^{-2}}$.

Umstadter et al. [97] showed that the longitudinal electric field, E_z, could be generated more efficiently by a train of multiple pulses compared to the same E_z generated by a single pulse in the simulation work. The efficiency means using less total pulse energy to excite an equivalent amplitude of E_z. In one of their examples, a single pulse ($\delta\tau = 120$ fs, $I_0 = 1.8 \times 10^{19}$ W $\cdot$ cm^{-2}, $a_0 = 5.2$) could generate $E_z = 0.34$ GV/cm in a plasma ($n_0 = 6.4 \times 10^{17}$cm^{-3}). The same E_z could be generated

by four optimised pulses of a multi-pulse train ($a_0 = 1.2$) in a plasma ($n_0 = 10^{16}\text{cm}^{-3}$). This implied a 13-times less energy used in a multi-pulse train to drive the same E_z compared to a single intense laser pulse.

Figure 2.5 shows an example of the plasma wakefield excited by a train of pulses with optimised pulse spacing and pulse length. The excited plasma wakefield shown in the graph shows an increase of plasma wavelength after the consecutive multiple pulses. The amplitude of E/E_{wb} also grows rapidly and shows a saw-tooth profile behind the last pulse.

Due to the technical difficulty of producing tunable multi-pulse trains, or simply pulse trains, for MP-LWFA, this accelerator scheme did not gain much attention until it was revisited by Hooker et al. [28] in 2014. The motivation of adopting the MP-LWFA to accelerate electrons is to overcome the problem of low wall-plug efficiency (< 0.1 %) and low repetition rate ($\sim$ Hz) in the high power Ti:Sa laser systems. This is because the mechanism of the resonant excitation of plasma wakefields allows the use of less energy and intensity of pulses to generate the longitudinal electric field for electron acceleration.

The first observation of plasma wakefields generated by multi-pulse trains was reported by Cowley et al. [100] in 2017. The measurement of plasma wakefields was based on a technique called temporally encoded spectral shifting (TESS) [101, 102]. The observation of resonant excitation of plasma wakefield in cm-long optically formed plasma channels was reported by Ross et al. [30] in 2024. The experimental results

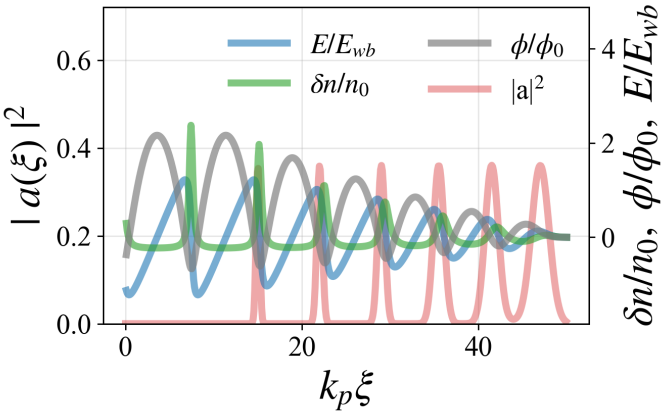


Figure 2.5: Example of plasma wakefield excited by a train of low-energy ultra-short laser pulses in MP-LWFA. Coloured curves are defined in Figure 2.1.

suggested a resonant excitation of plasma wakefield ($n_0 \sim 4.3 \times 10^{17}$ cm^{-3}) by pulse trains ($E = 2.5$mJ, 170-fs pulse spacing) reached an acceleration gradient of 3 GV/m in plasma channels with plasma channel lengths $L_p \sim 110$ mm.

2.3 Limitations and solutions

2.3.1 Laser diffraction

Laser pulses propagating in space can be often approximated by a Gaussian function, $U(r, z)$, as given by [103]

$$U(r,z) = \frac{W_0}{W(z)} \exp\left[-\frac{r^2}{W^2(z)}\right] \exp\left[-jkz - jk\frac{r^2}{2R(z)} + j\xi(z)\right], \tag{2.27}$$

where $2z_0$ is the depth of focus; $W_0 = \sqrt{\lambda_0 z_0/\pi}$ is the waist radius; $W(z) = \sqrt{1+(z/z_0)^2}$, $R(z) = z\left[1+(z/z_0)^2\right]$; and $\xi(z) = \tan^{-1}(z/z_0)$.

The beam intensity is given as $I(r,z) = P_0 \exp\left[-2r^2/W^2(z)\right]/\pi W^2(z)$, where P_0 is the total power. The spot size focused by an optic is given by $D_f = 2W_0 = 4\lambda_0 f/\pi D$, where f is the focal length, and D is the input beam aperture. The Rayleigh length, $z_R = \pi W_0^2/\lambda_0$.

According to the definition of the beam intensity, approximately 86 % of laser power can be confined in which $r \leq W(z)$. For $|z| = z_0$, the intensity drops to one-half of the intensity at $I(r,0)$. For a laser pulse with $\lambda_0 = 1$ μm and $I = 10^{18}$ W/cm^2 focused by a f/30 parabola, its spot size $2W_0 \simeq 38$ μm and $L_R \simeq 9$ mm. This effect of laser diffraction can limit the available intensity delivered on the target gas, which limits the amplitude of excited plasma wakefield and hence the energy gain of the accelerated electrons.

To extend z_R, using external optical guiding structures or relativistic self-guiding were proposed [71, 88]. Theoretical studies of the instability and wakefield structures [104–106] were published in the 1990s, showing the advantages of using external plasma channels with low on-axis plasma density to guide highly intense pulses. Experiments were conducted following promising simulation results and demonstrated high electron energy gain of up to 7.8 GeV [72, 79, 80, 107].

2.3.2 Dephasing lengths

The dephasing length, $L_d \propto n_0^{2/3}$, is a fundamental limit of the electron acceleration in LWFAs. Although the plasma density can be decreased to avoid this effect, the quality of the beam will be deteriorated in terms of the energy spread, σ_E/E, where σ_E is the RMS energy spread of the on-axis accelerated beam [108]. Hence, decreasing n_0 becomes a trade-off, which is not an optimal solution for the problem of dephasing effect.

The idea of dephasing-less LWFAs has been proposed to overcome this problem by Debus et al. [109]. By using laser pulse shaping in space and time and manipulating plasma density, several research groups have demonstrated the benefits of their advanced acceleration concepts in simulations [110, 111], but these concepts have yet to be demonstrated experimentally.

2.3.3 Pump depletion

In all types of LWFA, the driving laser plays a key role of exciting plasma wakefields in different ways. This driving laser pulse has to transfer its energy to the plasma and generate longitudinal electric fields to accelerate electrons. The process of energy transfer leads to the depletion of laser energy and hence ultimately constrains the energy gained by the accelerated electrons in a single-stage LWFA. The pump depletion length in the quasi-linear regime, L_{pd}, is given by $L_{\mathrm{pd}} = \omega_0^2\omega_p^2/c\tau_0 a_0^2$ [112].

To overcome this problem, Leemans et al. proposed the idea of using multiple stages of LWFAs to accelerate electron bunches [113]. Simulations show that an energy gain of 1000 GeV is possible using capillary-discharged wave guides or curved plasma channels in principle [25, 114].

2.3.4 Laser systems

The conventional LWFA commonly adopts single short pulses ($L_0 < \lambda_p$) to excite plasma wakefields. Since Ti:sa laser systems can generate high-power ($\sim$ J) and ultra-short pulses ($\sim$ 30 fs) from the Ti-Sapphire crystals with the chirped-pulse amplification and the mode-locking techniques, they have become the main driving laser systems in LWFA research.

However, high-peak-power Ti:sa laser systems used in LWFAs have problems involved in the heat management issues leading to the low wall-plug efficiency ($< 1\%$) and low repetition rate ($\sim$ Hz) [28, 115, 116]. These problems result from the intrinsic low quantum efficiency ($\sim 65\%$) of and the large energy ($\sim$ tens of J) stored in the Ti-Sapphire laser crystals [117].

For the future development of particle accelerators, low electron beam emittance ($\sim$ 1 μm), low electron energy spread (0.1%), high electron energy (> 1 GeV), high bunch charge ($\sim$ tens of pC), and a high repetition rate ($\sim$ kHz) are in demand [118]. These beam parameters require that the driving laser systems have high repetition rates ($\sim$ kHz), high peak power ($\sim$ PW), high average power ($\sim$ kW) and high stability [73]. Therefore, the low wall-plug efficiency of Ti:sa laser systems will become a serious issue for LWFA-based particle accelerator facilities.

To meet this challenge, different laser technologies have been considered, including thin-disk lasers and fibre lasers [28]. In addition to laser technologies, different acceleration schemes have been proposed, such as self-resonance PBWA [67] and plasma-modulated plasma accelerators (P-MoPA) [119, 120]. These advanced acceleration schemes allow the use of longer laser pulses ($\sim$ ps) produced by different laser gain media, such as neodymium:yttrium–aluminium–garnet (Nd:YAG) or Nd:glass, to be laser drivers of plasma wakefield excitation [121–123].

In P-MoPA, a seed laser pulse ($\Delta\tau \sim 40$ fs) excites plasma wakefields in a plasma channel ($L_p \sim$ tens of mm). A drive laser pulses ($\Delta\tau \sim 1$ ps, E) trailing the seed pulse experiences the excited plasma wakefield in the quasi-linear regime. Due to the gradient variation of plasma density, the localised frequency components in the drive pulse are blue- and red-shifted from a centre laser frequency and develop spectral sidebands separated by a plasma frequency, ω_p. After leaving the modulation stage, a dispersive optic can vary the spectral phase of the sidebands, or simply speaking, "compress" the drive pulse into a series of fs-short pulses. This P-MoPA pulse train then enters into another plasma channel to excite plasma wakefield and accelerates electrons to a GeV-scale according to the PIC simulation [119].

In contrast to MP-LWFA requiring pulse spacing optimised to meet the plasma resonance condition, P-MoPA has an advantage that the pulse spacing of a P-MoPA pulse train is automatically in lock with the plasma period, T_p. Hence, the entire acceleration mechanism is simpler than MP-LWFA in principle. Detailed mechanism of pulse conversion and method of pulse characterisation in the P-MoPA are discussed in Chapter 6.

The first steps in the path of discovery, and the first approximate measures, are those which add most to the existing knowledge of mankind.

—Charles Babbage, British mathematician, 1791 -1871 [124]

3 Theory of multi-pulse train characterisation

Contents

3.1 Introduction 29
3.2 Theory of multi-pulse trains 29
3.2.1 Interference of chirped pulses 29
3.2.2 Generation of multi-pulse trains 32
3.2.3 Representation of multi-pulse trains 35
3.3 Measurement of multi-pulse trains 36
3.3.1 Auto-correlation of multi-pulse trains 36
3.3.2 Fundamentals of frequency-resolved optical gating 41
3.3.3 Beam geometries of FROG 44
3.3.4 Non-collinear second-harmonic generation 51
3.3.5 Single-shot beam geometry in SHG FROG 52
3.4 Phase retrieval algorithms in FROG 53
3.4.1 Iterative Fourier transform algorithms 53
3.4.2 Principle component general projections algorithms 55
3.4.3 Ptychographic iterative engine algorithms 57
3.5 Time-frequency joint information 60
3.5.1 Time directions 60
3.5.2 Direct spectral phase information 62
3.6 Conclusions 63

3.1 Introduction

This chapter aims to provide a theoretical background supporting the simulation and experimental implementation of pulse train characterisation. The author wanted to (i) develop a theoretical model of pulse train generation, (ii) investigate proper pulse pulse measurement techniques for pulse train characterisation, and (iii) understand how to characterise pulse structures from experimental data.

This chapter is organised as follows. Section 3.2 discusses the theory of temporal interference between two pulses for supporting the simulation of pulse train generation. Section 3.3 presents investigation of different pulse characterisation techniques and related optical effects and geometries. Section 3.4 provides brief introduction to different phase retrieval algorithms supporting the pulse measurement. Section 3.5 describes time-frequency-joint information in pulse measurement that could support the characterisation of time direction in pulse train measurement.

3.2 Theory of multi-pulse trains

3.2.1 Interference of chirped pulses

This section provides a theoretical background for the pulse train generation for a proof-of-principle MP-LWFA experiment. The analytic equations provided at the end of this section were used to assist in the simulation of multi-pulse train characterisation. It should be mentioned that the procedures of mathematical derivation shown in this section follow a similar approach described by Robinson et al. [125] for generating trains of ultrashort pulses using birefringence crystal arrays.

A complex electric field of an optical pulse, $u(t)$, propagating in the time domain can be written as a slowly varying envelope function multiplied by a carrier angular frequency term, which is written as

$$u(t) = a(t)\exp(j\omega_0 t), \tag{3.1}$$

where $j = \sqrt{-1}$; t is time; $a(t)$ is the slowly varying envelope function; and ω_0 is the centre angular frequency of the optical pulse.

The slowly varying envelope, $a(t)$, in Equation 3.1 is a superposition of frequency components given by

$$a(t) = \frac{1}{2\pi}\int_{-\infty}^{\infty} A(\tilde{\omega})\exp(j\tilde{\omega}t)d\tilde{\omega}, \tag{3.2}$$

where $\tilde{\omega} = \omega - \omega_0$; and ω is the angular frequency centred at ω_0.

To describe a laser pulse passing through a dispersive optical system, the envelope function of the laser pulse, $a(t)$, in Equation (3.2) can be written as

$$a(t) = |a(t)|\exp[j\phi(t)], \tag{3.3}$$

where $|a(t)|$ is the absolute value of $a(t)$; and $\phi(t)$ is the temporal phase.

In the spectral domain, the spectral envelope function, $A(\omega)$, is given by

$$A(\tilde{\omega}) = |A(\tilde{\omega})|\exp[j\psi(\tilde{\omega})], \tag{3.4}$$

where $|A(\tilde{\omega})|$ is the absolute value of $A(\tilde{\omega})$; and $\psi(\tilde{\omega})$ is the spectral phase.

Since the temporal and spectral phases are functions of time and frequency, the two terms in Equations (3.3) and (3.4) can be written as their Taylor series expansions. The temporal phase is given by

$$\phi(t) = \sum_{n=0}^{\infty}\frac{1}{n!}\frac{\partial^n\phi(t)}{\partial t^n}t^n, \tag{3.5}$$

and the spectral phase is given by

$$\psi(\omega) = \sum_{n=0}^{\infty}\frac{1}{n!}\frac{\partial^n\psi(\tilde{\omega})}{\partial\omega^n}(\omega-\omega_0)^n. \tag{3.6}$$

The temporal phase, $\phi(t)$, contains time and frequency information which is called the instantaneous frequency, $\omega_{\text{inst}}(t)$, as defined by

$$\omega_{\text{inst}}(t) = \omega_0 + \frac{\partial\phi(t)}{\partial t}. \tag{3.7}$$

The spectral phase contains the information of frequency-dependent delay, $\Delta\tau_s(\omega)$, as given by

$$\Delta\tau_s(\omega) = -\frac{\partial\psi(\omega)}{\partial\omega}. \tag{3.8}$$

It is assumed that only the spectral phase, $\psi(\omega)$, up to the second-order is taken into account, and the spectral envelope function, $A(\omega)$, is Gaussian. The spectrum of an optical pulse, $A(\tilde{\omega})$, can be written as

$$A(\tilde{\omega}) = A_0 e^{-(\frac{\tilde{\omega}}{\Delta\omega})^2} e^{j(\psi_0+\psi_1\tilde{\omega}+\frac{1}{2}\psi_2\tilde{\omega}^2)}, \tag{3.9}$$

where A_0 is the maximum spectral amplitude; $\Delta\omega$ is the bandwidth at full width at half maximum (FWHM); ψ_0 and ψ_1 are the zeroth and first-order spectral phase defined in Equation (3.6), respectively.

The pulse amplitude, $u_{out}(t)$, can be obtained by taking the Fourier transform of Equation (3.9) described as

$$u_{out}(t) = \frac{A_0}{2\pi}\sqrt{\frac{\pi}{\frac{1}{\Delta\omega^2}+j\frac{1}{2}\psi_2}}\exp\left[\frac{-(t+\psi_1)^2}{j(\frac{4}{j\Delta\omega^2}+2\psi_2)}-j\psi_0\right]. \tag{3.10}$$

Because ψ_0 in Equation (3.10) is the absolute phase and the pulse duration of $u(t)$ is much longer than an optical cycle, it can be omitted in the pulse train model. Suppose that two pulses are separated by a time delay, τ, and ψ_2 is introduced in their spectra. Thus, their envelope functions, u_1 and u_2 can be written as

$$u_1\left(t+\frac{\tau}{2}\right) = \frac{A_0}{2\pi}\sqrt{\frac{\pi}{\frac{1}{\Delta\omega^2}+j\frac{1}{2}\psi_2}}\exp\left[\frac{-\left(t+\frac{\tau}{2}\right)^2}{j\left(\frac{4}{j\Delta\omega^2}+2\psi_2\right)}\right], \tag{3.11}$$

and

$$u_2\left(t-\frac{\tau}{2}\right) = \frac{A_0}{2\pi}\sqrt{\frac{\pi}{\frac{1}{\Delta\omega^2}+j\frac{1}{2}\psi_2}}\exp\left[\frac{-\left(t-\frac{\tau}{2}\right)^2}{j\left(\frac{4}{j\Delta\omega^2}+2\psi_2\right)}\right]. \tag{3.12}$$

Assume that the two pulses, u_1 and u_2, collinearly propagate in space and overlap in time. The intensity of the pulse, $|u_{\mathrm{tot}}(t)|^2$, formed by u_1 and u_2 can be written as

$$\begin{aligned}|u_{\mathrm{tot}}(t)|^2 &= \left|u_1(t-\frac{\tau}{2})+u_2(t+\frac{\tau}{2})\right|^2 \\ &= \alpha\left[|f_1(t)|^2+|f_2(t)|\right]^2+f_3(t),\end{aligned} \tag{3.13}$$

where

$$f_1(t) = \exp\left[X(t_1+\frac{\tau}{2})^2\right], \tag{3.14}$$

$$f_2(t) = \exp\left[X(t_2 - \frac{\tau}{2})^2\right], \tag{3.15}$$

$$f_3(t) = 2\exp\left[X(t^2 + \frac{\tau^2}{4})\right]\cos(Y\tau t), \tag{3.16}$$

and

$$\alpha = \left|\frac{A_0}{2\pi}\sqrt{\frac{\pi}{\frac{1}{\Delta\omega^2} + j\frac{1}{2}\psi_2}}\right|^2, \tag{3.17}$$

in which

$$X = \frac{-2\Delta\omega^2}{4 + {\psi_2}^2\Delta\omega^4}, \tag{3.18}$$

and

$$Y = \frac{\psi_2\Delta\omega^2}{4 + {\psi_2}^2\Delta\omega^4}. \tag{3.19}$$

It can be seen that Equation (3.16) is a function of time, t, and the frequency of intensity modulation is determined by τ, ψ_2, and $\Delta\omega$. This implies that a pulse train with a given period of modulation and pulse duration can be generated by controlling the material dispersion and time delay between two pulses with a broad bandwidth.

3.2.2 Generation of multi-pulse trains

To implement a proof-of-principle MP-LWFA experiment, Professor Simon Hooker proposed the use of a grating pair compressor and Michelson interferometer to generate controllable pulse trains from high power laser pulses with broad enough spectral bandwidth ($\sim$ 25 nm). This technique was adopted in an MP-LWFA experiment [100] implemented in 2017. This section aims to exploit the theory discussed in Section 3.2.1 to derive required τ and ψ_2 for a given pulse spacing, T_m, and the number of pulses, N_p, in a pulse train in order to assist in simulations of pulse train characterisation.

Figure 3.1 summarises the process of generating pulse trains. First, an input pulse with a spectral bandwidth of $\Delta\omega$ enters the optical system. Second, the grating-pair compressor stretches or introduces a frequency chirp to an input short pulse. Third, the Michelson interferometer splits the chirped pulse into two replicas separated by τ. Finally, a pulse train is generated by controlling ψ_2 and τ.

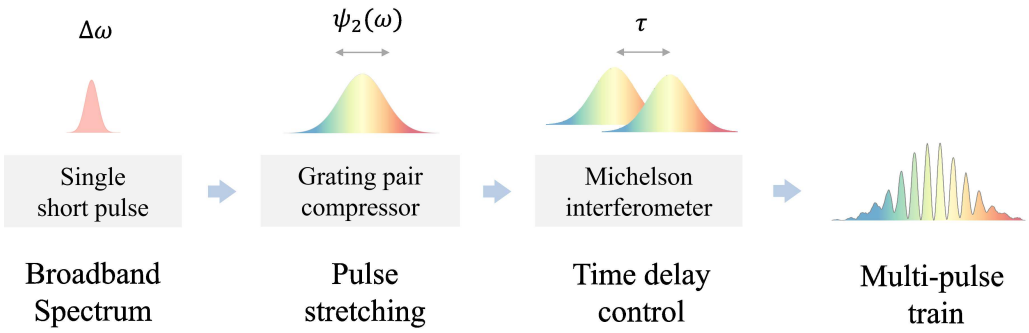


Figure 3.1: Schematic of pulse train generation with a broadband short pulse, Michelson interferometer, and grating-pair compressor.

According to Equation (3.13), it can be seen that a pulse formed by two co-propagating pulses that are separated by τ, and have the same amount of ψ_2 has a modulated intensity profile. According to Equation (3.19), the modulation frequency, f_m, is given by

$$f_m = \frac{\psi_2 \Delta\omega^4}{4 + {\psi_2}^2 \Delta\omega^4}. \tag{3.20}$$

The third term on the right-hand side in Equation (3.13) governs the structure of a pulse train only if a nonzero amount of delay time and a second-order spectral phase are introduced into the two co-propagating pulses. Thus, Equation (3.20) can be used to estimate the amount of τ and ψ_2 required to generate a pulse train with given T_m and N_p.

The angular frequency of the intensity modulation, ω_m, is defined by

$$\omega_m = 2\pi f_m = Y\tau. \tag{3.21}$$

T_m between two pulses in a pulse train is the period of the modulation, which is given by

$$T_m = \frac{2\pi}{Y\tau}. \tag{3.22}$$

Substituting Equation (3.19) into Equation (3.22), the required τ between the two co-propagating pulses can be determined by

$$\tau = \frac{8\pi + 2\pi{\psi_2}^2 \Delta\omega^4}{\psi_2 \Delta\omega^4 T_m}. \tag{3.23}$$

To define N_p in a pulse train, the pulse duration of an entire pulse train, $\Delta\tau_{\mathrm{FWHM}}$, has to be given in advance. Here, the FWHM pulse duration is used. Because the envelope

function in Equation 3.13 does not have an analytic solution, an approximation of the intensity function is introduced assuming that τ between the two co-propagating pulses is relatively small compared to the pulse duration of an entire pulse train. Therefore, the intensity function of a pulse train, $I(t)$, can be written as

$$I(t) \approx e^{-Xt^2} \cos(Y\tau t). \tag{3.24}$$

The exponential term in Equation (3.24) can be used to calculate $\Delta\tau_{\mathrm{FWHM}}$ as given by

$$\Delta\tau_{\mathrm{FWHM}} = 2\sqrt{\frac{(4 + {\psi_2}^2\Delta\omega^4)\ln(2)}{2\Delta\omega^2}}. \tag{3.25}$$

Suppose that there are N_p pulses within $\Delta\tau_{\mathrm{FWHM}}$, and T_m between each pulse is given. $\Delta\tau_{\mathrm{FWHM}}$ can be written as

$$\Delta\tau_{\mathrm{FWHM}} = N_pT_m = 2\sqrt{\frac{4 + {\psi_2}^2\Delta\omega^4}{2\Delta\omega^2}}. \tag{3.26}$$

Therefore, ψ_2 used to generate a pulse train is given by

$$\psi_2 = \pm\sqrt{\frac{(\Delta\omega N_pT_m)^2 - 8\ln(2)}{2\ln(2)\Delta\omega^4}}. \tag{3.27}$$

Using Equations (3.23) and (3.27), τ and ψ_2 can be estimated if N_p and T_m of a multi-pulse train are given.

Based on the principles of the Michelson interferometer and grating pair compressor discussed in [126] and [127], respectively, τ and ψ_2 can be related to the displacement of the Michelson arm, ΔL_m, and the grating separation or slant distance of a two-pass grating pair compressor, ΔL_s, respectively. Therefore, once the properties of a pulse train, such as T_m and N_p, are defined, and the FWHM bandwidth of the input pulse, $\Delta\omega$, is obtained from the spectrum of the input pulse, ΔL_m and ΔL_s can be estimated. As a result, ΔL_m and ΔL_s are given in Equations (3.28) and (3.29), respectively.

$$\Delta L_m = \frac{8\pi c + 2\pi c{\psi_2}^2\Delta\omega^4}{2\psi_2\Delta\omega^4T_m}, \tag{3.28}$$

where and

$$\Delta L_s = \pm\frac{2\pi c^2\lambda_g^2\cos^2\theta_d}{m^2\lambda^3}\left[\frac{(\Delta\omega N_pT_m)^2 - 8\ln(2)}{2\ln(2)\Delta\omega^4}\right]^{\frac{1}{2}}, \tag{3.29}$$

where λ_g is the grating period; θ_d is the diffraction angle; m is the diffraction order.

Using Equations (3.19), T_m in Equation (3.22) can be rewritten as

$$\begin{aligned} T_m &= \frac{2\pi\left(4+\psi_2^2\Delta\omega^4\right)}{\psi_2\Delta\omega^2\tau} \\ &\approx \frac{2\pi\psi_2\Delta\omega^2}{\tau}, \end{aligned} \tag{3.30}$$

where the approximate holds if $\psi_2\Delta\omega^2 \gg 4$, which is true for a large frequency chirp ($\psi_2 > 10,000 fs^2$) introduced in a pulse with a bandwidth larger than tens of THz.

It is worth comparing Equation (3.30) with Equation (7) in Robinson et al. [125] as given by $\Delta\tau \approx \pi\Delta/b\tau'$, where $\Delta\tau$ is the pules spacing; the difference of group delays between the ordinary wave and extraordinary waves is $\Delta v_g = 1/\beta'_{0e} - 1/\beta'_{0o}$; l is the propagation length in a birefringence crystal or wave plate; the frequency chirp is $b = b(\psi_2, \Delta\omega)$; and $\tau' = l/\Delta_{v_g}$. Comparing Equation (3.30) with Equation (7) in Robinson et al. [125], it can be observed that both equations imply that the pulse spacing, T_m or $\Delta\tau$ can be controlled by τ and ψ_2 for a given $\Delta\omega$.

3.2.3 Representation of multi-pulse trains

In MP-LWFA, it is essential to characterise the temporal structures of pulse trains. Based on the Fourier transform theorem, the temporal amplitude is the superposition of frequency components with spectral phase. Hence, understanding the spectral phase is important for pulse train characterisation because the spectral amplitude of a pulse can commonly be obtained by using an optical spectrometer. In other words, the temporal structure of a pulse can be derived from the measured spectrum of a pulse and its spectral phase obtained by another optical measurement device.

Figure 3.2a shows the spectra of an input pulse and a pulse train. The input spectrum is assumed to be Gaussian. The spectrum of the pulse train is modulated by a period, $T_\omega = 1/\tau$, after passing through a Michelson interferometer. The spectral phase has a quadratic variation with a saw-tooth structure which reveals an important feature of spectral interference.

The temporal intensity variation of the two pulse replicas and pulse train is shown in Figure 3.2b. The pulse train has a modulated intensity similar to its spectrum.

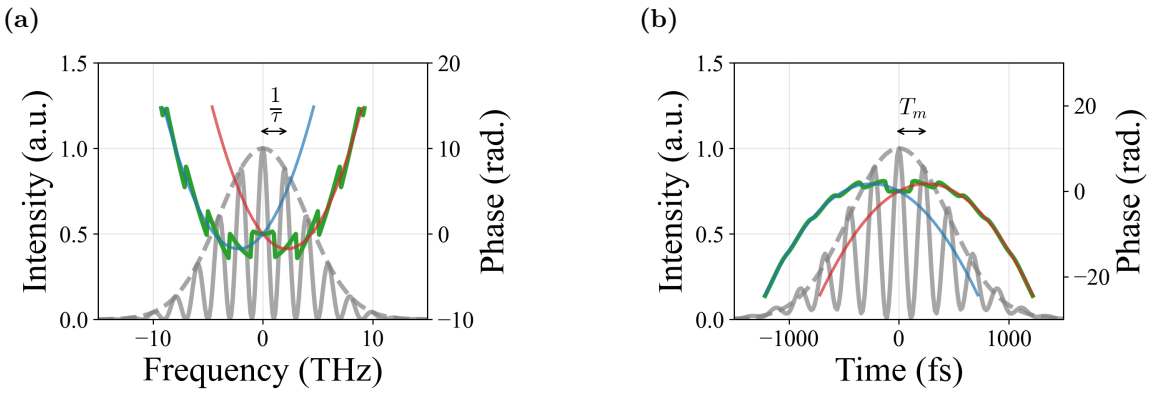


Figure 3.2: Representation of pulse train in the spectral and temporal domains. (a) Spectra of a Gaussian input pulse (dashed grey curve) and pulse train (solid grey curve). The red and blue curves represent the spectral phases of the two input pulse spectra. The green curve is the spectral phase of the pulse train. (b) Pulse (dashed grey curve) and pulse train (solid grey curve). The red and blue curves represent the temporal phases of the two stretched input pulses. The green curve shows the temporal phase of the pulse train.

The temporal phase of the pulse train has a quadratic-like variation with a saw-tooth structure similar to the one in Figure 3.2a. The modulated intensity has a value of T_m defined in Equation (3.22).

Because pulse trains have complicated temporal and spectral structures, the author adopted the root-mean-square (RMS) pulse duration, $\Delta\tau_{\text{rms}}$ and the RMS spectral bandwidth, $\Delta\nu_{\text{rms}}$, to describe the pulse duration and spectral bandwidth of pulse trains. The time-bandwidth product TBP $= \Delta\tau_{\text{rms}}\Delta\nu_{\text{rms}}$ is used to quantify the complexity of multi-pulse trains, following the definition suggested in [128, 129].

In the measurement of pulse trains, T_m, and N_p are the two most important parameters to be measured. Based on the Fourier transform theorem, the spectral phase of a pulse train accompanied by its spectrum needs to be determined so that the temporal structure of the pulse train can be characterised accurately.

3.3 Measurement of multi-pulse trains

3.3.1 Auto-correlation of multi-pulse trains

Because the time scale of pulse trains is on the order of ps and the pulse spacing is on the order of fs, it is not possible to use conventional photodiodes and oscilloscopes

to measure the pulse trains with enough temporal resolution ($\sim$ 10 fs). Therefore, self-referenced pulse measurement techniques are investigated in this section aimed at showing the investigation of auto-correlation techniques in the pulse train characterisation.

Electric field auto-correlation

Using a pulse to characterise itself can be implemented by an optical setup consisting of a Michelson interferometer and a photo-detector as shown in Figure 3.3a. The input pulse is first split into two replicas by a beam splitter. The pulses, after passing through the beamsplitter, are reflected by two mirrors, and a photo-detector measures the signal of recombined pulses.

Because a conventional photo-detector has a much slower response time compared to the oscillation period of the laser field, the signal measured by the photo-detector is a time-averaged power, which is given by [130]

$$\langle P_{\text{out}} \rangle = 2\Gamma(0) + [\Gamma(\tau) + \text{c.c.}], \tag{3.31}$$

where τ is the time delay between two input pulse replicas, and Γ is given by

$$\Gamma(\tau) = \frac{1}{T} \int_{-\frac{T}{2}}^{\frac{T}{2}} a(t) a^*(t-\tau) dt, \tag{3.32}$$

where T is the time scale that covers only a single optical pulse of interest; $a(t)$ is the amplitude of the input pulse.

Taking the Fourier transform of Equation (3.32) and letting $\tau' = t - \tau$ result in

$$\begin{aligned} \mathcal{F}\{\Gamma(\tau)\} &= \frac{1}{T} \int_{-\frac{T}{2}}^{\frac{T}{2}} dt \int_{-\infty}^{\infty} a(t) \exp(j\omega t) dt \int_{-\infty}^{\infty} a^*(\tau') \exp(j\omega\tau') d\tau' \\ &= |a(\omega)|^2. \end{aligned} \tag{3.33}$$

Equation (3.33) implies that electric field auto-correlation only provides information about the power spectral density of an input pulse with no phase information, which is not suitable for the pulse train characterisation.

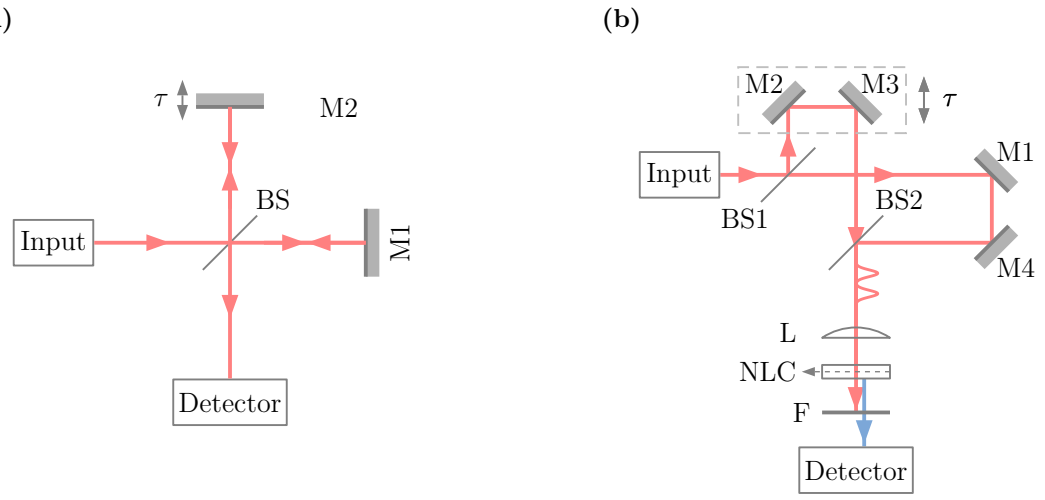


Figure 3.3: (a) Schematic of an electric field auto-correlator. BS—beam splitter; and M—mirror. (b) Schematic of an intensity fringe averaged auto-correlator. L—lens; NLC—nonlinear optical crystal; and F–filter.

Intensity fringe-averaged auto-correlation

In order to record the intensity variation of an optical pulse, using a nonlinear crystal to generate the second harmonic generation (SHG) signal of an input pulse by a Michelson interferometer was first proposed and demonstrated by Weber [131]. A simple optical setup of an intensity fringe-averaged auto-correlation is shown in Figure 3.3b. The setup is similar to the electric field auto-correlator. However, the output pulse is focused onto a nonlinear crystal by a lens to enhance the intensity so that the SHG signal can be generated with enough efficiency. A low-pass filter is used to filter out the fundamental signal. Later, it was proven that this technique could be used to estimate the pulse duration of a single pulse if an envelope distribution function of the input pulse is defined [132].

The SH signal measured by a photo-detector is given by [133]

$$\langle P_{\mathrm{SHG}}(\tau)\rangle \sim \langle |a^4(t)|\rangle + 2\langle |a^2(t)a^2(t-\tau)|\rangle. \tag{3.34}$$

In a noncollinear SHG auto-correlator shown in Figure 3.4a, an input pulse are split into two replicas by a beam splitter. The two pulse replicas cross at the nonlinear crystal. The SHG signal varying with τ between the two pulse replicas is measured by a photo-detector.

Figure 3.5a and 3.5b show an input pulse train with a uniform pulse spacing and its corresponding SHG auto-correlation (AC) signal, respectively. Because the peak-to-peak spacing in the SHG-AC signal contains information about the pulse spacing of a pulse train, this technique was adopted in a proof-of-principle MP-LWFA experiment [100]. With a computer algorithm devised by Professor Simon Hooker [134], the experimental results showed that the pulse spacing of pulse trains could be retrieved with prior knowledge about the optical system and input pulse spectra.

However, this technique, accompanied by the algorithm, is not sensitive to the variation of pulse spacing between each pulse in a pulse train. An example of a pulse train with non-uniform pulse spacing is shown in Figure 3.6a. The red curve shows the variation of T_m in contrast to the constant T_m of the pulse train shown in Figure 3.5a. Comparing the intensity of SHG-AC signal shown in Figure 3.5b and Figure 3.6b, the peak-to-peak spacings in the intensity of SHG-AC signal formed by pulse trains with uniform and non-uniform pulse spacings are similar. This is because the second term in Equation (3.34) is symmetric. Thus, the SHG auto-correlation signal provides ambiguous information about the pulse structure.

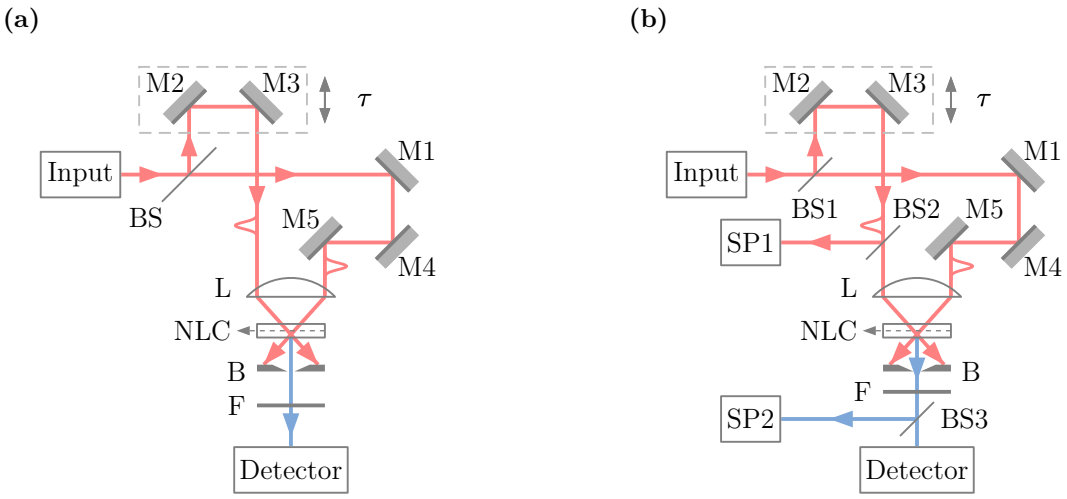


Figure 3.4: (a) Schematic of a collinear SHG auto-correlator. BS—beam splitter; M—mirror; L—lens; NLC—non-linear optical crystal; B—beam block; and F—filter. The red lines represent the fundamental frequency signal, and the blue line represents the second harmonic frequency. (b) Schematic of a non-collinear SHG fringe-resolved auto-correlator. SP—spectrometer. Other symbols and colour lines follow the definitions in (a).

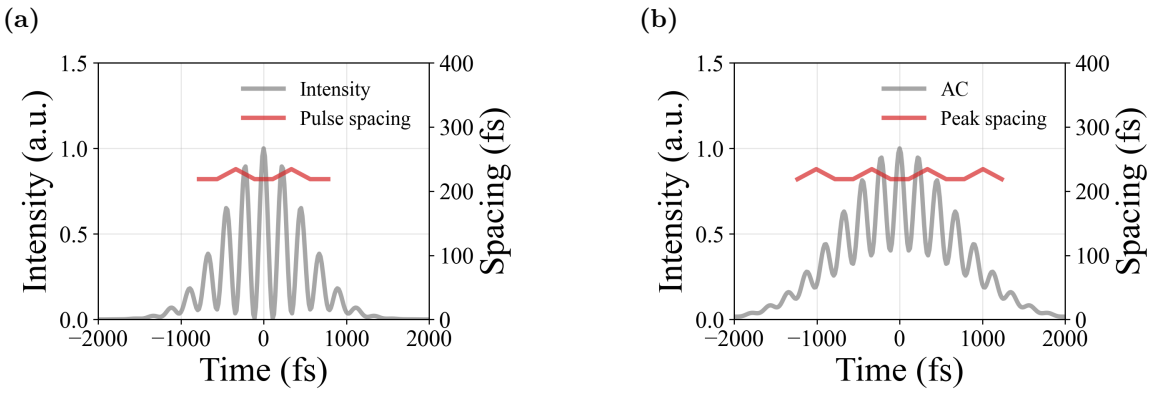


Figure 3.5: (a) Input pulse train with a uniform pulse spacing. The grey curve shows the intensity of the pulse train. The red curve represents the variation of pulse spacing. (b) SHG-AC signal of (a) The grey curve shows the SHG-AC signal. The red curve represents the spacing between each peak of AC signal

The most obvious change is the intensity contrast at the wings. However, it is difficult to correctly measure the contrast of SHG-AC signal at the wings because large systematic errors and high background noise are frequently introduced in an experimental optical setup. The author found it difficult to use the measured SHG-AC signal to detect subtle local pulse spacing variation in pulse trains generated in a real MP-LWFA experiment implemented at RAL in 2022 [30]. This is an important motivation to research a proper pulse characterisation technique in the author's research.

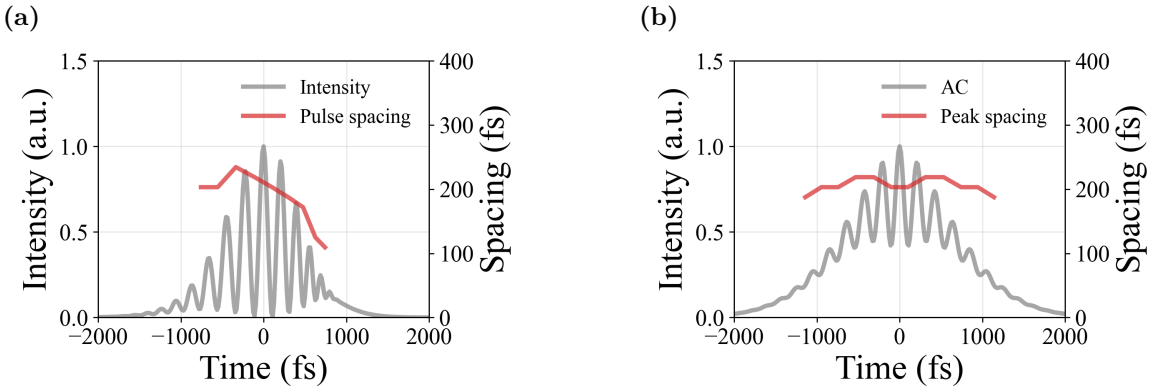


Figure 3.6: (a) Input pulse train with a nonuniform pulse spacing. (b) SHG-AC signal of (a). The definitions of coloured curves are shown in Figure 3.5

Intensity interferometric auto-correlation

An intensity interferometric auto-correlator can measure the interferometric intensity of an input pulse if the care of fine time delay resolution is taken. The interferometric intensity can be described as [135]

$$\begin{aligned} I_{\mathrm{IAC}} = &\text{ Background signal} \\ &+ \text{Interferometric term of } \omega_0 \\ &+ \text{Interferometric term of } 2\omega_0 \\ &+ \text{SHG auto-correlation signal.} \end{aligned} \tag{3.35}$$

Naganuma et al. [136] demonstrated that the envelope of an input pulse accompanied by its phase information could be retrieved by a numerical algorithm using interferometric auto-correlation traces, I_{IAC}, the fundamental spectrum and SHG spectrum of the input pulse. However, Chung et al. numerically demonstrated that the reconstructed pulse shape had inherent ambiguity, which means that this technique cannot be used to distinguish pulses with similar temporal structures [137].

In addition to this problem, an intensity interferometric auto-correlator needs to resolve the fast oscillating interferometric terms whose frequency is determined by ω_0 and $2\omega_0$. This condition requires a very fine time-delay resolution ($\sim 1/\omega_0$), which leads to very long data collection time for ps-long pulse trains. An example of the interferometric auto-correlation signal of a pulse train is shown in Figure 3.7. It can be observed that the fringes in I_{IAC} cannot be resolved. The reconstructed pulse structure cannot provide meaningful pulse measurement with these unresolvable interferometric fringes. Therefore, it can be concluded that this technique is difficult to implement for characterising ps-long pulse trains in practice.

3.3.2 Fundamentals of frequency-resolved optical gating

Although researchers had attempted to measure different types and lengths of pulses in the past [138–141], none of the methods was able to fully characterise the real temporal structures and phase of ultra-short pulses. The first technique that guaranteed the uniqueness of retrieved pulses was proposed and demonstrated later by Trebino et al.

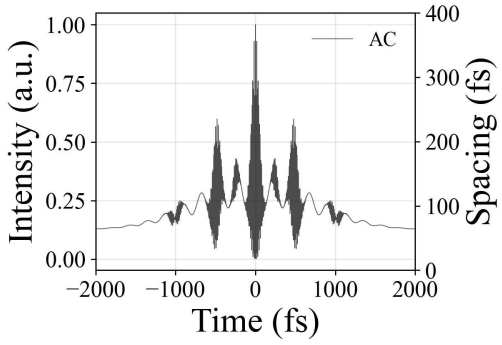


Figure 3.7: Intensity interferometric auto-correlation of the multi-pulse train shown in Figure 3.5a. Since the local intensity peaks are not resolvable, the spacing of peaks is not shown in this graph.

in 1993 [142]. This technique is known as frequency-resolved optical gating (FROG). It is a hybrid pulse measurement technique combining spectrography and auto-correlation to produce a spectrogram of an optical pulse. A spectrogram is a 2-D trace that records the variation of spectral information of signal varying with time. The spectrogram can be used to retrieve temporal and spectral properties of ultra-short pulses.

Trebino et al. thought that the auto-correlation measurement of optical pulses was equivalent to the 1-D phase retrieval problem, which was first studied by Akutowicz [143]. Later, a discussion on the uniqueness of the 1- and 2-D phase retrieval problems was published by Barakat et al. [144]. It was mathematically proven that the 1-D phase retrieval problem had multiple solutions. In contrast to the 1-D problem, a solution of the 2-D phase retrieval problem could be uniquely determined because there existed more degrees of freedom in a spectrogram. Here, the term 'degrees of freedom' refers to the spectral information of the measured signal at different time delays.

Based on Akutowicz and Barakat et al.'s findings, computer algorithms were developed by different research groups in 1970s and summarised in a review paper by Fienup [145]. The most well-known algorithm is Gerchberg-Saxton (GS) algorithm [146] which became the basis of the phase retrieval algorithm used in FROG. Before the advent of FROG, phase retrieval problems in crystallography and optical imaging had been studied [147]. Therefore, FROG can be regarded as the first application of the phase retrieval technique in the ultra-fast optics community.

In the pulse train measurement, the spectral phase of the spectra is the most important property to be characterised. By recording spectrograms of pulse trains, the temporal structures of them could be retrieved by the FROG technique. The short-time Fourier transform (STFT) is one of the proper tools to represent a time-frequency distribution of a pulse, $S(t, f)$, which can be written as [148]

$$S(\tau, \omega) = \left| \int_{-\infty}^{\infty} u(\tau) g(\tau - t) \exp(-j\omega\tau) d\tau \right|^2, \tag{3.36}$$

where $\omega = 2\pi f$; $u(t)$ is the amplitude of a pulse to be measured; and $g(\tau)$ is an observation window or a gate function with a size of T at $\tau =$ t.

Figure 3.8 provides a graphical representation of Equation (3.36). The amplitude of a pulse, $u(t)$, containing a positive frequency chirp is shown in Figure 3.8a. A gate function $g(\tau - t)$ is used to capture the information within a temporal window T at $\tau = t$. The spectrogram, $S(t, f)$, is shown in Figure 3.8b. It can be seen that the lower frequency components of the pulse arrive earlier than the higher frequency components. With the information contained in a two-dimensional time-frequency distribution, a pulse envelope can be acquired if the gate function is known.

In the FROG technique, the input pulse itself serves as a gate function. FROG relies on phase retrieval algorithms to reconstruct the temporal structure of the input pulses from their FROG traces, $I_{\mathrm{FROG}}(\tau, \omega)$, which is a kind of spectrograms containing a time-and-frequency distribution of the input pulse. This time-frequency distribution is slightly different from the STFT trace because the gate function in a FROG trace is not guaranteed to be a shorter event as required by the STFT theorem.

$I_{\mathrm{FROG}}(\tau, \omega)$ can be written as [149]

$$I_{\mathrm{FROG}}(\tau, \omega) = \left| \int_{-\infty}^{\infty} E_{\mathrm{sig}}(t, \tau) \exp(-j\omega t) dt \right|^2 \tag{3.37}$$

where $E_{\mathrm{sig}} = u(t)g(t - \tau)$ is the kernel of a FROG trace; $u(t)$ is the input pulse to be measured; and $g(t)$ is a function of $u(t)$ depending on the types of FROG.

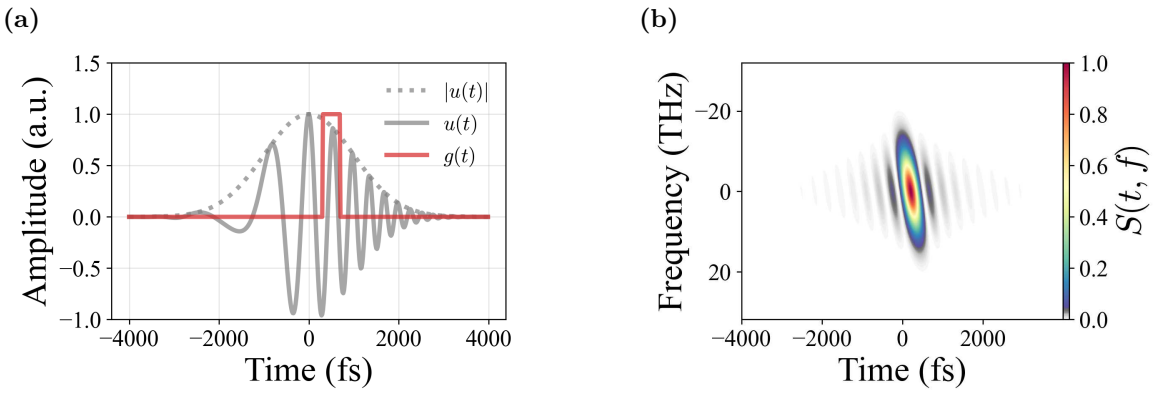


Figure 3.8: (a) One-dimensional illustration of Equation (3.36). The dotted line shows $|u(t)|$. The grey curve shows the field amplitude, $u(t)$. The red curve shows the gate function, $g(t)$. (b) Two-dimensional depiction of Equation (3.36).

3.3.3 Beam geometries of FROG

Figure 3.9 shows a simple optical setup of FROG in a non-collinear beam geometry. In this setup, an input pulse is split into two replicas by the beamsplitter and then focused by the lens into the nonlinear optical crystal. The delay stage in the dashed grey box can control the time delay between the pulse replicas to ensure they overlap in the time domain. The imaging lens is used to image the correlation signal generated in the nonlinear crystal by the two crossing beams. The spectrometer spectrally resolves correlation signal.

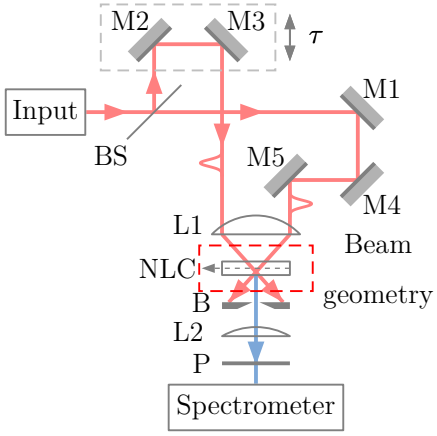


Figure 3.9: Schematic of a non-collinear FROG. P—polariser. All other symbols and colour lines follow the definitions in Figure 3.4a. The dashed red rectangle shows a region where the beam geometry can be applied in different types of FROG techniques.

Figures 3.10a and 3.10b show an input pulse train and its spectrum as examples for the following discussion about beam geometries in the FROG techniques. The input pulse train has a value of $N_p = 5$ and $T_m = 200$ fs.

Second harmonic generation FROG

The simplest beam geometry in all types of FROG is the SHG FROG, which is also a spectrally-resolved SHG auto-correlator. This beam geometry was first demonstrated by Ishida et al. [150] in 1985. The first experimental setup measuring the auto-correlation traces was developed by Watanabe et al. [151]. The theory and the first phase retrieval algorithm of the SHG FROG were later studied and developed by Delong et al. [142, 152, 153].

A general beam geometry of SHG FROG is shown in Figure 3.11a. Two input pulse replicas with the fundamental centre frequency, ω_0, cross at the nonlinear crystal by an angle, θ_p. With a time-varying delay stage, the SHG FROG trace can be produced. The SHG FROG trace is given by

$$E_{\text{sig}}(\tau, \omega) = \left| \int_{-\infty}^{\infty} E(t)E(t-\tau)\exp(j\omega t)dt \right|^2 . \tag{3.38}$$

The SHG FROG has the highest sensitivity to the input signal among all other types of FROG because it only relies on the second-order nonlinear process to generate the FROG trace. It also introduces minimum dispersion to the input pulse before arriving at

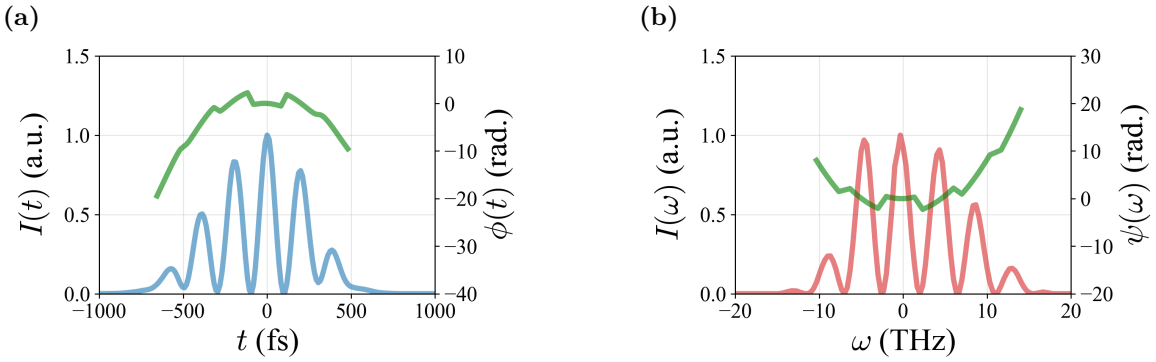


Figure 3.10: Temporal and spectral intensity of a pulse train with 5 pulses and a 200-fs pulse spacing. (a) Pulse train with 5 pulses and a 200-fs pulse spacing. The blue and the green curves are the temporal intensity profile and phase, respectively. (b) Spectrum of pulse train in (a). The red and the green curves are the spectral intensity profile and phase, respectively.

the nonlinear crystal. However, the SHG FROG trace is symmetric along the time-delay axis as shown in Figure 3.11b. This property gives a time ambiguity to the retrieved FROG trace for all types of pulses, including the pulse trains. Although several research groups devised ideas to solve this time ambiguity problem, the optical setup requires extra optical devices, limiting the use in practical applications [154–156].

Third harmonic generation FROG

Third-harmonic generation (THG) FROG was demonstrated by Tsang et al. in 1996 [157]. They adopted a non-collinear beam geometry and focused pulses from a Ti:Sa oscillator onto the surface of a glass plate to generate THG signal and the FROG traces. A collinear type of THG FROG using circularly polarised laser pulses was later demonstrated by Chadwick et al. [158].

The THG FROG, as shown in figure 3.11c, uses two input pulses crossing at an optical-Kerr medium to generate the third harmonic of the input pulses. It requires no specific crossing beam angle since the nonlinear process is the third-order optical Kerr effect [159]. The THG FROG trace is given by

$$E_{\text{sig}}(\tau,\omega) = \left| \int_{-\infty}^{\infty} E^2(t)E(t-\tau)\exp(j\omega t)dt \right|^2 . \tag{3.39}$$

The THG FROG is asymmetrical, implying no time ambiguity, as shown in Figure 3.11d. However, the low efficiency of THG leads to the use of a high numerical aperture (NA) microscope objective to focus the beam onto the Kerr-medium tightly. This results in a situation which the input pulse is influenced by the unknown dispersion of microscope objectives since the lens designs of the objectives are usually not provided by the manufacturers.

Self-diffraction FROG

The self-diffraction (SD) FROG was first demonstrated by Clement et al. in 1995 [160]. This type of FROG uses two input pulse replicas to form interference fringes spatially in an optical Kerr-medium as shown in figure 3.11e. Due to the optical Kerr effect, the refractive index of the Kerr medium varies with the intensity of the interference fringes and forms a grating-like distribution. Since the spatial interference

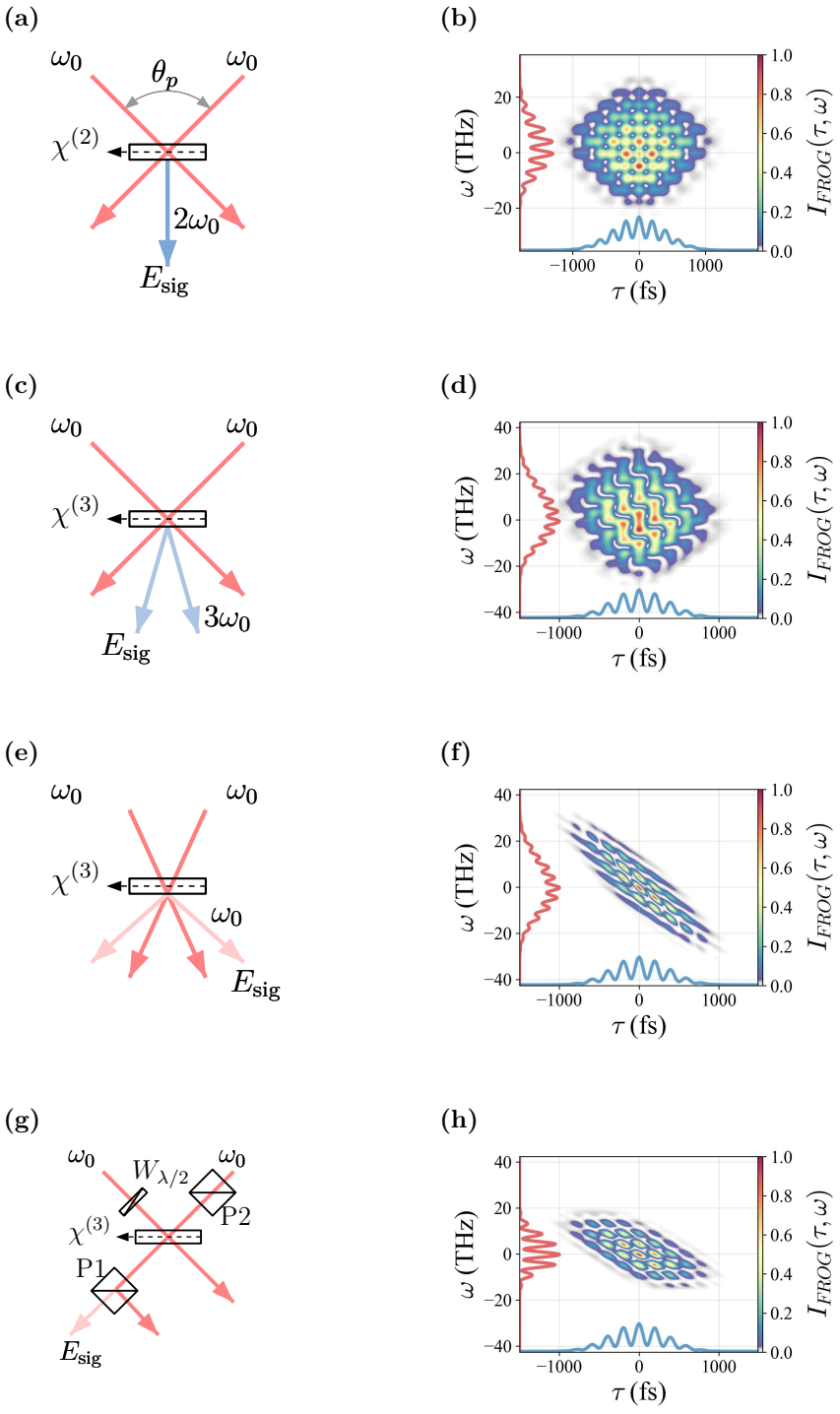


Figure 3.11: Comparison of FROG techniques and corresponding FROG traces formed by the input pulse train shown in Figure 3.10. (a) Beam geometry of SHG FROG. θ_b is the beam crossing angle. $\chi^{(2)}$—the second-order nonlinear process. (b) SHG FROG trace. (c) Beam geometry of THG FROG. $\chi^{(3)}$ represents the third order nonlinear process. (d) THG FROG trace. (e) Beam geometry of SD FROG. (f) SD FROG trace. (g) Beam geometry of PG FROG. P1—polariser; P2—Polarising beamsplitter; and $W_{\lambda/2}$—half waveplate. (h) PG FROG trace.

fringes only appear when the two pulses overlap in the time domain, the input beams are self-diffracted by the interference fringes propagating to a different direction from the input pulses. Collecting the diffracted signal at each time delay can produce the SD FROG trace which is given by

$$E_{\text{sig}}(\tau,\omega) = \left| \int_{-\infty}^{\infty} E^2(t) E^*(t-\tau) \exp(j\omega t) dt \right|^2 . \tag{3.40}$$

As shown in Figure 3.11f, the SD FROG trace is asymmetrical and has a more apparent time-frequency variation than the THG FROG trace for the same pulse train. Although it uses the third-order nonlinear effect, its signal is not directly from the third harmonic of the input pulses. This results in using common lenses as focusing optics to create the interference fringes. However, it is necessary to cross the two input pulses at a small angle (a few degrees) to avoid wavelength-dependent phase mismatching. Because of this condition, SD FROG is not suitable for pulses with large spectral bandwidths.

Polarisation gate FROG

The polarisation gate FROG is the first FROG geometry demonstrated by Kane and Trebino in 1993 [153]. It uses two input pulse replicas and the optical Kerr effect to generate the FROG trace. The optical setup, as shown in Figure 3.11g, is more complicated than the other types of FROG discussed earlier. A test pulse to be measured passes through an optical analyser formed by one polariser and a polarising beam splitter. This analyser is placed in one of the two input beam paths. The other pulse, or the gate pulse, passes through a half wave plate in order to make the pulse polarised by 45° in the other input beam path. When the two pulses overlap at a time delay, the intense intensity of the gate pulse with a 45-degree polarisation induces the optical Kerr effect at the overlapping region and slightly changes the polarisation of the test pulse due to the birefringence effect. The signal leaking through the analyser forms the PG FROG trace given by

$$E_{\text{sig}}(\tau,\omega) = \left| \int_{-\infty}^{\infty} |E(t)|^2 E(t-\tau) \exp(j\omega t) dt \right|^2 . \tag{3.41}$$

The PG FROG trace shown in Figure 3.11h is asymmetrical, which means that there is no time ambiguity. PG FROG traces can reflect intuitive time-frequency information

such as the instantaneous frequency of a pulse. This is because the absolute squared value of the input pulse in Equation (3.41) does not contain any phase to distort the PG FROG trace. In other words, the phase information of a test pulse can be directly revealed in a PG FROG trace. In addition to this advantage, PG FROG can measure pulses with very large spectral bandwidths such as pulses from supercontinuum generation [161]. The disadvantages of PG FROG are the use of extra optical components in the beam paths as well as high-quality and expensive polarising optics.

Other types of FROG

There are types of FROG based on different beam geometries and concepts. The transient-grating (TG) FROG [162] is one of the examples and its beam geometry is shown in Figure 3.12a. The TG FROG uses three replicas of the input pulse and is based on a similar effect used in the SD FROG. Two of the input beams cross at a small angle to form interference fringes. The fringes induce the optical Kerr effect, resulting in a periodic distribution of refractive index in a Kerr-medium. The third pulse replica with variable time delays is diffracted to another propagation direction after passing through the Kerr-medium. The diffracted signal is recorded as the TG FROG trace given by

$$E_{\mathrm{sig}}(\tau,\omega) = \left| \int_{-\infty}^{\infty} E_1(t)E_2(t)E_3^*(t-\tau)\exp(j\omega t)dt \right|^2 . \tag{3.42}$$

Although the TG FROG has more complicated beam geometry than the PG FROG, it can produce FROG traces similar to those in the PG FROG without using a waveplate and an analyser. This arrangement provides an almost dispersion-free optical setup and produces intuitive FROG traces.

All types of FROG invented in the 1990s measure the spectra of input pulses varying with time delay. However, other modern types of FROG have moved beyond these conventional types of spectrogram and use fairly simple beam geometries based on only one input beam, as shown in Figure 3.12b. Multi-photon intra-pulse interference phase scan (MIIPS) FROG, dispersion-scan (d-scan) FROG and vectorial FROG (V-FROG) are of this type [163–165]. They use one input beam to generate the SHG signal and measure the SHG spectra varying with other parameters such as pre-defined phase, material dispersion or polarisation states. These FROG techniques have the

simplest beam geometry and the highest sensitivity to the input pulse. The V-FROG also can even measure optical pulses with various polarisation states. However, most of these FROG techniques require scanning parameters, which prohibits the single-shot capability in the pulse measurement.

FROG geometry for pulse train characterisation

In summary, most types of FROG use two-beam geometries except for TG FROG and other modern types of FROG such as V-FROG, d-scan FROG and MIIPS FROG. FROG geometries based on the SHG process are highly sensitive to the input pulse. Most FROG techniques can support the single-shot measurement, which gives more flexibility to low repetition-rate laser sources. Although SHG FROG has high simplicity and sensitivity, its FROG traces contain time ambiguity, making analysing retrieved pulses more difficult.

The pulse train measurement has several requirements. First, it needs a single-shot ability in proof-of-principle MP-LWFA experiments. This is because pulse trains have unstable shot-to-shot energy and operate at a low repetition rate (< 1 Hz) in high-power Ti:Sa laser systems [166–168]. Second, a high signal-to-noise (SNR) ratio is necessary for the pulse train measurement to avoid any systematic error contributed from FROG trace noise contamination. Third, any dispersion introduced by optical components before the pulse arrives at the nonlinear medium in an FROG setup should be avoided. Finally, the cost and feasibility of optical setup are of importance.

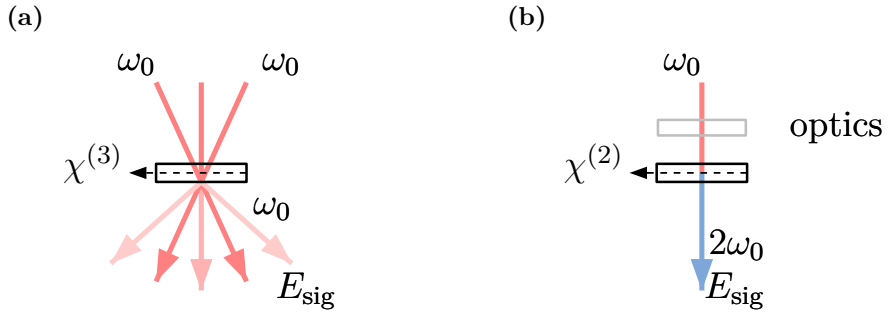


Figure 3.12: (a) Beam geometry of TG FROG. P1—polariser; P2—Polarising beam splitter. $W_{\lambda/2}$—half waveplate. (b) Beam geometry of MIIPS FROG, V-FROG and d-scan FROG. The grey rectangle shows where external optics, such as phase plates, glass wedges or waveplates, can be placed at.

Based on the requirements mentioned above, SHG FROG became the most suitable technique to investigate whether a pulse train can be fully characterised. This is because the SHG process is more efficient than the other FROG techniques based on third-order nonlinearity, and it can support the single-shot measurement. Additionally, the SHG FROG requires fewer dispersive optical components making the entire setup simpler than other counterparts.

3.3.4 Non-collinear second-harmonic generation

To generate efficient SHG from two crossing beams in a nonlinear crystal, the phase-matching conditions [169] must be satisfied, which are

$$\omega_3 = \omega_1 + \omega_2, \tag{3.43}$$

and

$$\mathbf{k}_3 = \mathbf{k}_1 + \mathbf{k}_2. \tag{3.44}$$

For a phase mismatched condition, Equation (3.44) can be written as

$$\Delta\mathbf{k} = \mathbf{k}_1 + \mathbf{k}_2 - \mathbf{k}_3. \tag{3.45}$$

The phase-mismatched SHG efficiency is given by [170]

$$\eta_{\mathrm{SHG}} \propto \frac{L_c^2 P_1}{A_{\mathrm{eff}}} \left[\frac{\sin(\Delta k L/2)}{\Delta k L/2}\right]^2, \tag{3.46}$$

where u_1 is assumed to be real; P_1 is the peak power of the input field $u_1(0)$; L_c is the thickness of the nonlinear crystal; and A_{eff} is the effective interaction area.

For the non-collinear SHG FROG technique of the pulse train measurement, the phase-matching condition in Equation (3.44) can be satisfied by crossing two input pulse replicas into a uniaxial crystal. This beam geometry and the crystal orientation are shown in Figure 3.13a.

Polarisation of the input beams with a centre frequency, ω_0, is assumed to be vertical to the y-z plane. The phase-matching condition requires that the polarisation of k_3 be parallel to the y-z plane. The refractive index, $n(\theta_{\mathrm{cut}})$, is defined as [171]

$$\frac{1}{n^2(\theta)} = \frac{\sin^2(\theta)}{n_{\mathrm{ex}}^2} + \frac{\cos^2(\theta)}{n_{\mathrm{or}}^2}, \tag{3.47}$$

where n_{or} and n_{ex} are the refractive indices of the ordinary and extraordinary waves, respectively.

Since the optic axis lies on the y-z plane, Equation (3.44) becomes

$$n(2\omega_0, \theta_{\text{cut}})\omega_3 = n_{or}(\omega_0)\omega_1 \cos\theta_{\text{p}} + n_{or}(\omega_0)\omega_2 \cos\theta_{\text{p}}. \tag{3.48}$$

Because $\omega_3 = 2\omega_0$ and $\omega_1 = \omega_2 = \omega_0$,

$$n(2\omega_0, \theta_{\text{cut}}) = n_{or}(\omega_0)\cos\theta_{\text{p}}. \tag{3.49}$$

The phase-matching angle θ_{p} inside the uniaxial crystal is

$$\theta_{\text{p}} = \cos^{-1}\left[\frac{n_{or}(\omega_0)}{n(2\omega_0, \theta_{\text{cut}})}\right]. \tag{3.50}$$

According to the Snell's law [172], the angle of input beam θ_{in} outside the crystal is given by

$$\theta_{\text{in}} = \sin^{-1}\left[n_{or}(\omega_0)\sin^{-1}\theta_{\text{p}}\right]. \tag{3.51}$$

3.3.5 Single-shot beam geometry in SHG FROG

Suppose that two input pulses propagate in the y-z plane and cross inside a uniaxial crystal by an angle, θ_{p}, as shown in Figure 3.13b. The transverse beam size of the

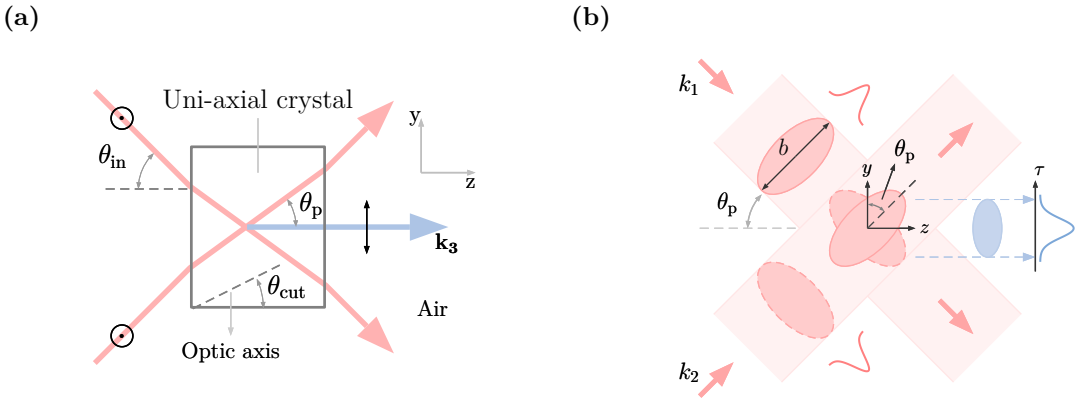


Figure 3.13: Non-collinear beam geometry of the SHG process and single shot geometry of in a uni-axial crystal. (a) Non-collinear beam geometry of the SHG process in a uniaxial crystal. The red arrows represent the input beams. The blue error represents the SHG signal. θ_{p} is the phase-matching angle. θ_{cut} is the cut angle of the crystal. (b) Single shot geometry of two crossing beams in a uni-axial crystal. Red ellipses represent the input pulses. The blue ellipse shows the generated SHG signal.

input pulse is given by b. The wave vectors of the two input pulses are given by k_1 and k_2, respectively. The origin of the coordinate is located at the centre of the crossing beams. The superposition of the two beams generating the SHG signal at plane z = 0 can be written as

$$|u_{\text{cross}}(t,\mathbf{r})|^2 = 2|u(t,\mathbf{r})|^2 + |u(t,\mathbf{r})|^2 \exp\left[j\omega_0(t - 2\frac{y}{c}\sin\theta_{\text{p}})\right] + \text{c.c.}. \tag{3.52}$$

The time delay, $\tau(y)$, mapped onto the transverse position along the y-axis at plane $z = 0$ is given by [173]

$$\tau(y) = 2\frac{y}{c}\sin\theta_{\text{p}}. \tag{3.53}$$

Since the beam projected onto the transverse position on the y-axis along its propagation direction is $y = b/\cos\theta_{\text{p}}$, the overall delay range, Δt, provided by a beam with b at θ_{p} is given by

$$\Delta t = 2\frac{b}{c}\tan\theta_{\text{p}}. \tag{3.54}$$

3.4 Phase retrieval algorithms in FROG

In this section, several important phase retrieval algorithms in FROG are reviewed for supporting the simulation of pulse train measurement discussed in Chapter 4.

3.4.1 Iterative Fourier transform algorithms

The Gerchberg-Saxton (GS) algorithm is a generalised error reduction algorithm used to solve unknown phase of signal from intensity measurement of diffraction phenomena via backward and forward Fourier transform [146, 174]. A modified version of GS algorithm was developed by R. Trebino et al. [142] to solve the phase retrieval problem in the field of pulse measurement. The numerical optimisation algorithm of retrieving an optical pulse accompanied by its phase from a FROG trace has two constraints. One is the measured FROG trace and the other is the physical formulation of the nonlinear process given by E_{sig}.

Trebino et al. defined the FROG trace error for the pulse retrieval process by [142, 175]

$$G_{\mathrm{FROG}} = \left[\frac{1}{N^2}\sum_{m=1}^{M}\sum_{n=1}^{N}\left|I_{\mathrm{FROG}}(\tau_m,\omega_n) - I_r(\tau_m,\omega_n)\right|^2\right]^{\frac{1}{2}}, \tag{3.55}$$

where I_r and I_{FROG} are the retrieved and measured FROG traces, respectively.

Figure 3.14 shows a phase retrieval algorithm developed by Trebino et al. The algorithm starts with the kth iteration. An initial guess of the electric field, $u_i(t)$, with random phase is given in the first step the algorithm for $k = 1$. In the second step, the algorithm generates $E_{\mathrm{sig}} = E(t)E(t-\tau)$. Here, the SHG nonlinear process is taken as an example. Next, the Fourier transform of E_{sig} is computed as A_{s}. In the next step, a measured FROG trace, $I_{FROG}(\omega,\tau)$, is applied as the second constraint in the algorithm. The modulus of A_{s} is then replaced with the square root of $I_{FROG}(\omega,\tau)$ and the phase of A_{s} remains unchanged. The new data trace A_{g} from this step is used to calculate the FROG error G_{FROG}.

Once the FROG error converges to a predefined value, the algorithm stops. Otherwise, the inverse Fourier transform of A_{g} is calculated for the next step. A newly generated $u(t)$ will be input into the next iteration until the value of G_{FROG} satisfies a pre-defined condition. In the basic FROG algorithm, the method for generating

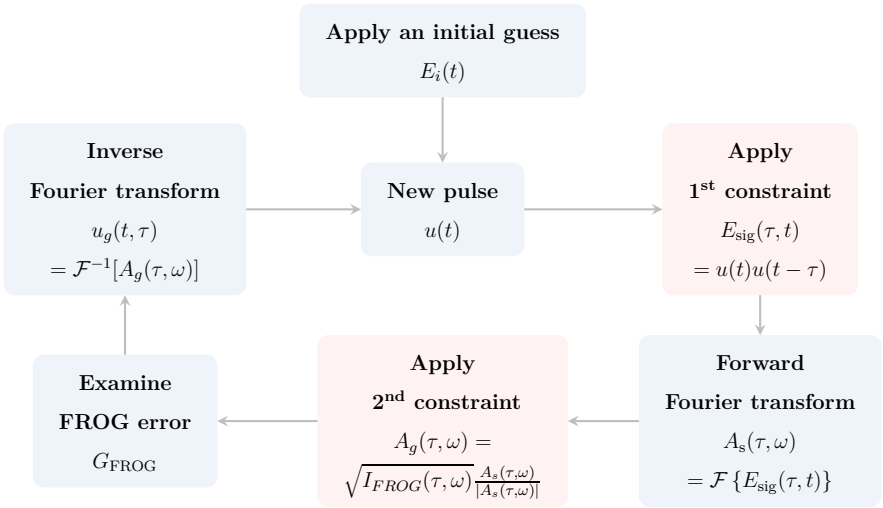


Figure 3.14: Schematic of a basic FROG algorithm.

$u^{(k+1)}(t)$ in each iteration is given by

$$u^{(k+1)}(t) = \int_{-\infty}^{\infty} A_g^{(k)}(t,\tau)d\tau, \tag{3.56}$$

where k means the k$^{\text{th}}$ iteration.

3.4.2 Principle component general projections algorithms

Another phase retrieval algorithm is the principle component generalised projections (PCGP) algorithm devised by Kane [176, 177] in 1997. This algorithm uses the singular value decomposition (SVD) and the power method in linear algebra to retrieve ultra-short pulses. It can retrieve two unknown pulses from a single FROG trace with a fast convergence rate.

Figure 3.15 shows the phase retrieval processes of the PCGP algorithm. First, An initial guess of the electric field, E_i, is given. Second, it takes the outer product of $E(t)$ and a gate pulse $G(t)$ as shown in Equation 3.57.

$$E_{\text{outer}} = E(t) \otimes G(t) \tag{3.57}$$

where E and G are defined as

$$E = [E_1, E_2, E_3, ..., E_n]^T \tag{3.58}$$

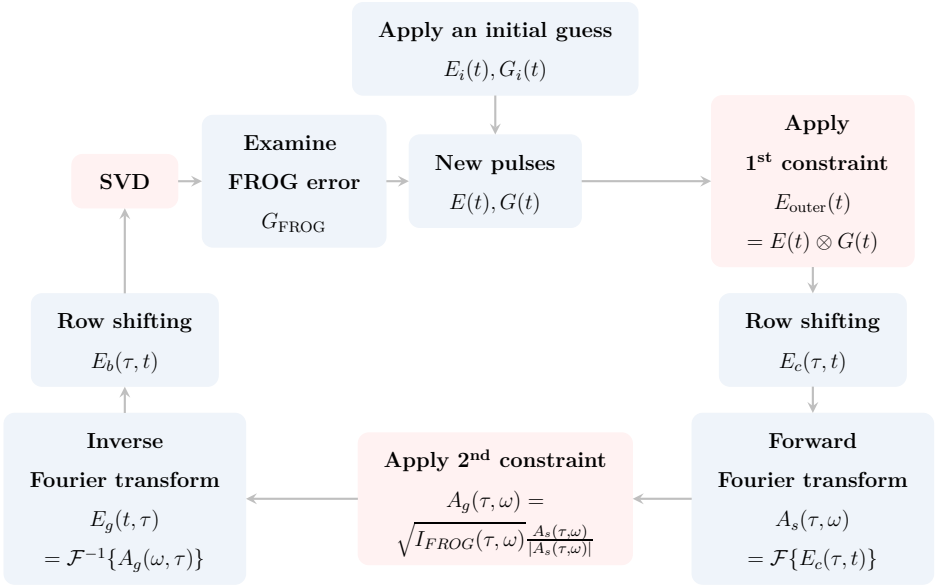


Figure 3.15: Schematic of the PCGP algorithm.

and

$$G = [G_1, G_2, G_3, ..., G_n]^T . \tag{3.59}$$

Through the forward row-shifting on matrix E_{outer}, a cross-correlation matrix, E_c, can be produced as shown in Equation 3.57. In this matrix, each column represents the cross-correlation of the probe and gate function at different time delays.

$$E_c = \begin{bmatrix} E_1G_1 & E_1G_2 & E_1G_3 & \cdots & E_1G_N \\ E_2E_2 & E_2G_3 & E_2G_4 & \cdots & E_2G_1 \\ E_3E_3 & E_3G_4 & E_3G_5 & \cdots & E_3G_2 \\ \vdots & \vdots & \vdots & \ddots & \vdots \\ E_NE_N & E_NG_1 & E_nG_2 & \cdots & E_1G_{N-1} \end{bmatrix} \tag{3.60}$$

Third, the amplitude of a newly generated $A_s(\tau, \omega)$ can be obtained by taking the Fourier transform of Equation 3.60 in each column. Fourth, the modulus of $A_s(\tau, \omega)$ is replaced with the square root of the measured FROG trace, $I_{\text{FROG}}(\tau, \omega)$. The phase of $A_s(\tau, \omega)$ is retained. This step generates a data trace, A_g, with the magnitude of the square root of $I_{FROG}(\tau, \omega)$ and the phase of $A_s(\tau, \omega)$. By taking the inverse Fourier transform of A_g in each column, a matrix, E_g, is obtained in the next step. Since the newly produced matrix, E_g, is still a cross-correlation matrix, the next step is to shift the column of E_g back to the form of E_{outer}. This new matrix is denoted by E_b.

The most crucial step in the PCGP algorithm is to solve the SVD problem by using the power method [178, 179]. This step can provide the best estimate of $E(t)$ and $G(t)$ for the next iteration. Any N-by-N symmetric matrix, **E**, can be decomposed into three matrices P, D and U^T as shown in Equation (3.61).

$$\mathbf{E} = PDU^T, \tag{3.61}$$

where N is the number of elements in an array; and T means the transpose of a matrix.

P and U are the matrices of the eigenvectors in forms of $E_bE_b^T$ and $E_b^TE_b$, respectively. D is an diagonalised singular value matrix having elements, σ_n. Its elements are weighting factors, giving information about the most dominant eigenvectors in the matrix. Orthogonal matrices, P and U, are the probe and gate matrices, respectively.

These eigenvectors with the largest eigenvalues are used as the next guess of the probe and gate functions in the next iteration.

The power method guarantees convergence if there exist eigenvectors [178]. It also provides a faster way to solve the eigenvectors in Equation (3.61). According to the theory of the power method,

$$E_b E_b^T P = \sum_{n=1}^{N} \lambda_n P_n, \tag{3.62}$$

$$E_b^T E_b U = \sum_{n=1}^{N} \Lambda_n U_n, \tag{3.63}$$

where λ_n is the eigenvalue of P_n; and Λ_n is the eigenvalue of U_n.

Taking matrix P as an example, the power method states that any nonzero vector, x_0, can be a linear combination of eigenvectors P_n given by

$$x_0 = \sum_{n=1}^{N} \alpha_n P_n, \tag{3.64}$$

where α_n are arbitrary coefficients.

Multiplying x_0 by $E_b E_b^T$ m times gives

$$(EE^T)^{(m)} x_0 = \sum_{i}^{N} \lambda_i^{(m)} \alpha_i P_i. \tag{3.65}$$

Assuming that the largest eigenvalue is λ_1, the most dominant eigenvector is approximated as $\lambda_1^{(m)} \alpha_1 P_1$. This means that multiplying the previous probe function, P, by $E_b E_b^T$ several times will automatically give the best estimate of P for the next iteration. The same procedure holds for the gate function, G. The algorithm will continue to find P and G, and then examine G_{FROG} in each iteration until its value satisfies predefined conditions.

3.4.3 Ptychographic iterative engine algorithms

Ptychography was first developed to improve the resolution of electron images of atomic structures in scanning transmission electron microscopy (STEM) [180]. This technique has been developed in the imaging community for decades and is known as the coherent diffraction imaging (CDI) technique [181]. A well-known algorithm used in the CDI community is the extended ptychographic iterative engine (ePIE) algorithm

developed by Maiden et al.[182]. The ePIE algorithm modifies the update functions of the object and probe electric fields and introduces a stochastic process of optimisation to enhance the noise immunity of the algorithm.

The PIE algorithms did not attract much attention in the ultrashort pulse measurement community until Rohwer and Spangenberg et al. [183, 184] published their paper discussing the application of the PIE algorithm in the pulse measurement. This technique is known as time domain ptychography. The superior ability of the PIE/ePIE algorithm which deals with missing data and incorporation of pulse spectra as another constraint was discussed by Sidorenko et al. [185].

Several publications have demonstrated pulse reconstruction by the time-domain ptychography for pulses with $\Delta\tau$ ranging from ps to attosecond (as) time scales [186–188]. According to Spangenberg et al. and Kane [184, 189, 190], FROG accompanied by the PIE or ePIE algorithm provides several advantages: (i) the time ambiguity of retrieved pulses can be removed from FROG traces by inserting a bandpass filter in one of the input crossing beams in a FROG device, (ii) the temporal and spectral domains of a FROG trace can be decoupled, and (iii) pulse reconstruction can be accomplished by taking only a few data sets of spectra corresponding to specific delay times.

Figure 3.16 shows the pulse reconstruction procedures of the ePIE algorithm. The initial guess of the probe pulse, $P_i(t)$, and the gate pulse , $G_i(t)$, are given at the beginning of the pulse reconstruction process. $P_i(t)$ and $G_i(t)$ are used to generate the cross-correlation signal $E_{\text{sig}}(\tau_n, t) = P(t)G(t - \tau_n)$ in the kth iteration. The subscript n means the nth time delay. In the next step, the forward Fourier transform of E_{sig} is computed as $A_s(\tau_n, \omega)$. The algorithm replaces the modulus of $A_s(\tau_n, \omega)$ with the square root of the measured FROG trace I_{FROG} and leaves the phase of $A_s(\tau_n, \omega)$ unchanged at the nth time delay. The inverse Fourier transform of $A_s(\tau_n, \omega)$ is given by $E_g(\tau_n, t)$.

The most important step in the ePIE algorithm is the update functions of the $P_i(t)$ and $G_i(t)$ for the next iteration of retrieval process. The ePIE algorithm regards the pulse retrieval as a steepest descent optimisation process [185]. The uniqueness of the solutions can be proven under certain conditions described in [191, 192]. Accordingly,

the update functions for the next probe pulse, $P'(t)$, and gate pulses, $G'(t)$, are given by

$$P'(t) = P(t) + \alpha \left[E_g(\tau_n, t) - E_{\text{sig}}(\tau_n, t)\right], \tag{3.66}$$

and

$$G'(t - \tau_n) = G(t - \tau_n) + \beta \left[(E_g(\tau_n, t) - E_{\text{sig}}(\tau_n, t)\right], \tag{3.67}$$

where

$$\alpha = \delta \frac{|G(t - \tau_n)|G^*(t - \tau_n)}{|G(t - \tau_n)|_{\max}|G(t - \tau_n)|^2}, \tag{3.68}$$

and

$$\beta = \delta \frac{|P(t)|P^*(t)}{|P(t)|_{\max}|P(t)|^2}, \tag{3.69}$$

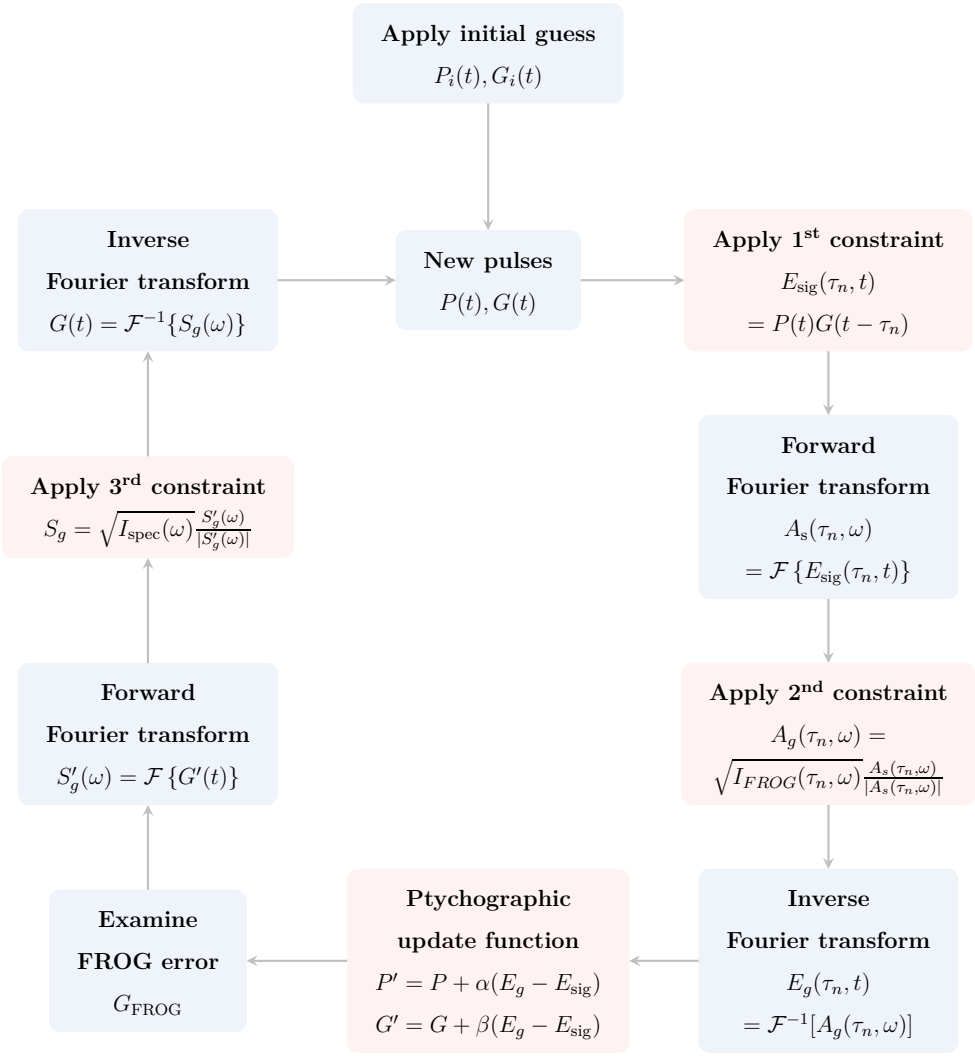


Figure 3.16: Schematic of the ePIE algorithm.

where δ is a constant.

In the ePIE algorithm, the order of updating $P'(t)$ and $G'(t-\tau_n)$ at nth time delay are randomised. Each iteration of the algorithm is not completed until the entire retrieved FROG trace at the nth time delay is calculated. After updating P' and G', the algorithm examines the FROG error G_{FROG}. If the value of G_{FROG} does not match pre-defined conditions, the algorithm goes to the step of applying the measured spectrum of the G' as the third constraint. In this step, the Fourier transform of the updated gate pulse is calculated as $S'_g(\omega)$. Next, the modulus of $S'_g(\omega)$ is replaced with the square root of the measured spectrum, $S_g(\omega)$. Finally, the inverse Fourier transform of $S'_g(\omega)$ is computed. After the last step, the newly updated P' and G' are used in the next iteration of the pulse reconstruction process.

3.5 Time-frequency joint information

3.5.1 Time directions

As discussed in Section 3.3.3, the time direction in the SHG FROG traces cannot be distinguished from an SHG FROG trace [193] if there is no prior knowledge about the laser pulse to be measured. Furthermore, SHG FROG does not provide intuitive time-frequency joint information compared to other types of FROG [194].

Two approaches have been proposed to remove the ambiguity of the time direction in an SHG FROG trace. One method suggested in Truong et al. [195] was using a specially designed etalon to generate two pulses from the input pulse. The energy of one pulse was designed to be weaker than that of the other. Since the order of two pulses passing through the etalon had been designed, the time of direction of a pulse retrieved by the algorithm could easily be determined. The other approach demonstrated in Zeek et al. [154] used a pulse shaper to directly generate a weaker pre- or post-pulse in a laser beam line so that the time of direction of the main pulse in a FROG trace could be determined. The author claimed that the shaper-assisted method was more practical than inserting a customised etalon in a laser beam line.

However, these two approaches increase the complexity and cost of a FROG device. Instead, Spangenberg et al. [184] suggested using a bandpass filter in one of the two

crossing beam paths to break the symmetry of the FROG trace. The time ambiguity can then be removed. Unfortunately, the use of a bandpass filter in SHG FROG leads to a non-symmetric blind FROG trace formed by two different pulses. According to Seifert et al. [196], blind FROG traces do not provide unique solutions to the phase retrieval process unless the algorithm has prior knowledge of the input pulse spectra.

In the following context, the origin of time direction revealed in a blind FROG trace formed by a pulse, and its spectrally filtered replica are discussed using the notations in [129]. It is assumed that a Gaussian gate pulse, $g(t)$, is generated by sending one of the Gaussian probe pulse replicas, $p(t)$, through a bandpass filter. $g(t)$ and $p(t)$ are given as

$$p(t) = e^{-a_p t^2} e^{-jb_p t^2} e^{j\omega_0 t}, \tag{3.70}$$

$$g(t) = e^{-a_g t^2} e^{-jb_g t^2} e^{j\omega_0 t}, \tag{3.71}$$

where subscript p and g represent the corresponding parameters of signal and gate pulse, respectively.

Thus, the spectral amplitude of $p(t)$ and $g(t)$ can be written as

$$S_p(t) = \sqrt{\pi(\alpha_p + j\beta_p)} e^{-\alpha_p \omega^2} e^{-j\beta_p \omega^2}, \tag{3.72}$$

$$S_g(t) = \sqrt{\pi(\alpha_g + j\beta_g)} e^{-\alpha_g \omega^2} e^{-j\beta_g \omega^2}, \tag{3.73}$$

where

$$a = \frac{\alpha}{\alpha^2 + \beta^2} \tag{3.74}$$

and

$$b = \frac{\beta}{\alpha^2 + \beta^2}. \tag{3.75}$$

The SHG FROG trace formed by $p(t)$ and $g(t)$ is given by

$$\begin{aligned} I_{\mathrm{FROG}(\tau,\omega)} &= \left| \int_{-\infty}^{\infty} p(t) g(t-\tau) \exp[(-j\omega t)] dt \right|^2 \\ &\propto \exp\left(A_1 \tau^2 + A_2 \omega \tau + A_3 \omega^2 \right), \end{aligned} \tag{3.76}$$

where

$$A_1 = \frac{(a_p + a_g)/2}{(a_p + a_g)^2 + (b_p + b_g)^2}, \tag{3.77}$$

$$A_2 = \frac{2(a_p b_g - a_g b_p)}{(a_p + a_g)^2 + (b_p + b_g)^2}, \tag{3.78}$$

and

$$A_3 = \frac{2\left[a_p(a_p^2 + b_p^2) + a_g(a_g^2 + b_g^2)\right]}{(a_p + a_g)^2 + (b_p + b_g)^2}. \tag{3.79}$$

Assuming that the bandpass filter does not introduce dispersion to $g(t)$ and $\beta_p = \beta_g$, the numerator in Equation (3.78) can be rewritten as

$$a_p b_g - a_g b_p = \frac{(\alpha_p - \alpha_g)\beta_p}{[(\alpha_p + \beta_p)^2 + (\alpha_g + \beta_g)^2]^2}. \tag{3.80}$$

Therefore, a bandpass filter inserted in one of the two cross-beam paths can remove the symmetry of an SHG FROG trace and reveal the sign of β. The FROG trace formed in such a condition is called blind FROG trace in the following context. Since the arrival time of the higher frequencies and lower frequencies in a pulse is related to the sign of β, the time direction of an input pulse can be distinguished in the non-centrosymmetric blind FROG traces.

3.5.2 Direct spectral phase information

Following the discussion in Section 3.5.1, the time-frequency-joint information can be directly revealed in a blind FROG trace. This is important for the pulse train measurement because the direct time-frequency information is helpful for extracting spectral phase without using the phase retrieval algorithm, which could be used as an estimate of initial conditions in the phase retrieval algorithm. The experimental demonstration of using a bandpass filter to measure the spectral phase of pulses was conducted by Chu et al. [197] in 1995. This technique is known as the spectrally and temporally resolved up-conversion technique (STRUT).

To understand the frequency-and-time joint information in spectrogram [129, 198], the mean conditional delay, $\langle\tau\rangle_\omega$, is defined as

$$\langle\tau\rangle_\omega = \frac{\int \tau I_{\mathrm{FROG}}(w,\tau)d\tau}{\int I_{\mathrm{FROG}}(w,\tau)d\tau}. \tag{3.81}$$

Recall Equation (3.76). $\langle\tau\rangle_\omega$ of a SHG FROG trace centre at $2\omega_0$ in the frequency domain has a form given by

$$\begin{aligned}\langle\tau\rangle_\omega &= \frac{\int \tau \exp(A_1\tau^2 + A_2\tau\omega + A_3\omega^2)d\tau}{\int \exp(A_1\tau^2 + A_2\tau\omega + A_3\omega^2)d\tau} \\ &= \frac{A_2\omega\sqrt{\frac{\pi}{4(A_1)^3}}\exp\left\{\left[\frac{(A_2\omega)^2}{4A_1}\right] - (A_3\omega)^2\right\}}{\sqrt{\frac{\pi}{A_1}}\exp\left\{\left[\frac{(A_2\omega)^2}{4A_1}\right] - (A_3\omega)^2\right\}} \\ &= \frac{(a_p b_g - a_g b_p)}{\left[a_p(a_p^2 + b_p^2) + a_g(a_g^2 + b_g^2)\right]}(\omega - \omega_0). \end{aligned} \tag{3.82}$$

According to Equation (3.6), it can be shown that $\Delta\tau_s(\omega) = -\psi_2(\omega - \omega_0)$, where ψ_2 is the second order spectral phase defined in Equation (3.6). Therefore, it can be seen that $\langle\tau\rangle_\omega$ is equivalent to $\Delta\tau_s(\omega)$. The coefficient in Equation (3.82) can be related to ψ_2 as given by

$$\psi_2 = -\frac{(a_p b_g - a_g b_p)}{\left[a_p(a_p^2 + b_p^2) + a_g(a_g^2 + b_g^2)\right]}. \tag{3.83}$$

Since the denominator of Equation (3.83) has a form similar to Equation (3.80), using a bandpass filter in the SHG FROG technique can not only remove the time ambiguity of a pulse but also directly reveal the frequency-dependent delay in the FROG trace formed by a pulse and its spectrally filtered replica.

3.6 Conclusions

In conclusion, the author has presented and reviewed the theory of pules train generation, pulse measurement techniques based on FROG, the phase retrieval algorithm and the removal of time ambiguity in SHG FROG.

Section 3.2 provided a theoretical background of the temporal interference of two chirped pulses. Based on the pulse train generation technique proposed by Professor Simon Hooker, the author derived equations that could assist in the estimation of τ and ψ_2 for generating a pulse train with given T_m and N_p. Measuring high power pulse trains from Ti:sa laser systems required retrieval of relative phase variation of the pulse train spectrum in a single shot to reduce the influence of unstable laser energy and beam pointing.

Section 3.3 presented investigation of pulse train measurement based on auto-correlation technique. It was concluded that none of them were suitable for the pulse train measurement, especially the diagnostic of nonuniform pulse trains. In addition, we reviewed the FROG techniques with different beam geometries. The SHG FROG was eventually selected by the author because this technique had high sensitivity to input pulses, simple beam geometry, and the ability of supporting single-shot measurement.

Section 3.4 gave an review of three phase retrieval algorithms used in the FROG techniques, such as PG, PCGP and ePIE algorithms. These techniques were taken into account for the simulation of pulse train characterisation.

Section 3.5 provided simple theory to explain how to remove the time ambiguity and reveal direct phase information from SHG FROG traces formed by a pulse and its spectrally filtered replica. This type of SHG FROG traces are called the blind FROG traces throughout this thesis.

According to the discussion presented in this chapter, the author decided to investigate the SHG FROG technique using a bandpass filter and the ePIE phase retrieval algorithm to implement the pulse train measurement for proof-of-principle MP-LWFA experiments.

When you can measure what you are speaking about, and express it in numbers, you know something about it; but when you cannot measure it, when you cannot express it in numbers, your knowledge is of a meagre and unsatisfactory kind: it may be the beginning of knowledge, but you have scarcely, in your thoughts, advanced to the stage of science, whatever the matter may be.

— Lord Kelvin, Scottish scientist,
1824 -1907 [199]

4

Simulations of multi-pulse train characterisation

Contents

4.1 Introduction 66
4.2 Simulation of multi-pulse train generation 66
4.2.1 Generation of real multi-pulse trains 66
4.2.2 Non-uniformity of pulse trains 70
4.2.3 Influence of adopting grating pair compressors 71
4.2.4 Error analysis of multi-pulse train generation 73
4.3 Phase retrieval of multi-pulse trains 75
4.3.1 Selection of FROG algorithms 75
4.3.2 Influence of bandpass filters 79
4.3.3 Influence of noise 82
4.3.4 Retrieval of nonuniform pulse trains 87
4.4 Optical systems 90
4.4.1 Phase-matching angles and temporal window sizes 90
4.4.2 Phase-matching bandwidths and spectral window sizes 92
4.4.3 Temporal and spectral resolution of FROG traces 95
4.4.4 Design of imaging spectrometers in FROG 97
4.5 Conclusions 101

4.1 Introduction

This chapter systematically presents simulations aimed at supporting the implementation of a pulse-train measurement instrument. The author wanted to understand (i) potential systematic errors and uncertainty in the pulse train generation technique, (ii) the ability of the phase retrieval algorithms to retrieve pulse trains under several experimental conditions, and (iii) optical constraints that can assist in the design and development of an experimental FROG device for pulse train measurement.

This chapter is organised as follows. Section 4.2 discusses the influence of real spectra, third-order spectral phase, and systematic errors on the pulse trains generated by a grating-pair compressor and a Michelson interferometer. Section 4.3 presents an investigation of the appropriate phase retrieval algorithms for pulse train measurement, the influence of a bandpass filter and different noise sources on the pulse train measurement, and the ability of the selected phase retrieval algorithm to diagnose nonuniform pulse spacing in pulse trains. Section 4.4 provides studies on the selection of nonlinear crystals, outlines criteria for measuring pulse trains, and describes the proper design of an imaging spectrometer for pulse train measurement.

4.2 Simulation of multi-pulse train generation

4.2.1 Generation of real multi-pulse trains

The theoretical model of pulse trains discussed in Section 3.2 assumes that the spectrum of an input pulse is Gaussian, which is an idealisation. Therefore, it is important to understand the influence of real spectra on pulse trains and the accuracy of T_m generated by the pulse train model. This section provides simulation results to support the implementation of a proof-of-principle MP-LWFA experiment. The strategy of adjusting the pulse spacing, T_m, and the number of pulses, N_p, in a pulse train is given in the end. It should be noted that the selection of T_m and N_p in this chapter followed the most probable combinations of parameters that could be adopted in the proof-of-principle MP-LWFA experiments. These parameters were constrained by the available

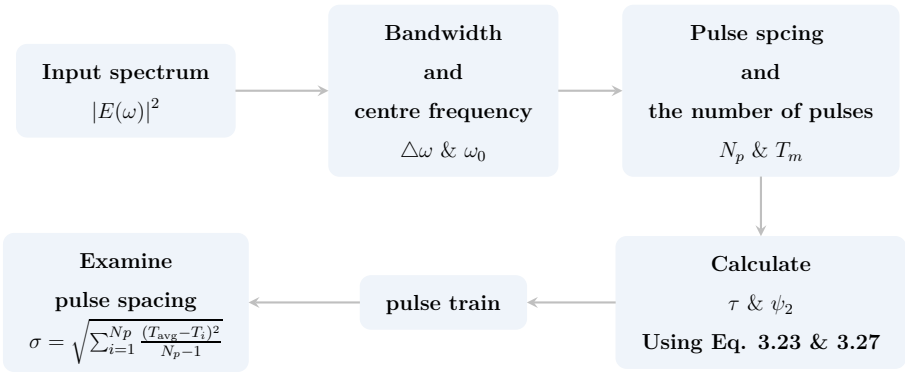


Figure 4.1: Procedures of simulating multi-pulse trains

pulse energy, generated plasma density, and exprected plasma wakefield amplitude in a provisional experimental setup.

Figure 4.1 shows the algorithm used to simulate realistic pulse trains. First, the simulation used a realistic spectrum accompanied by $\Delta\omega$ and ω_0. Second, the required T_m and N_p in a pulse train were given. The τ between the two input pulse replicas and ψ_2 could be calculated using Equations 3.23 and 3.27. A pulse train was simulated using Equations 3.23 and 3.27. Finally, the error of the simulated pulse train compared to the ideal T_m was examined.

Figure 4.2a shows the three input spectra used in this simulation. These measured spectra were generated from different Ti:sa laser systems, including the Astra and Gemini lasers of the Central Laser Facility (CLF) at Rutherford Appleton Laboratory (RAL), and the Oxford Plasma Accelerator Laboratory (OPAL). The centre wavelengths of these spectra λ_0 were assumed to be at 800 nm.

Figure 4.2b shows the normalised temporal intensity of three pulse trains generated using the input spectra shown in Figure 4.2a. In these cases, T_m and N_p were set to 200 fs and 10, respectively. The TBPs of these pulse trains were approximately 10. The real pulse trains no longer had Gaussian profiles. The relative intensity of each pulse in these pulse trains show different variation, which could excite different amplitude of plasma wakefield even though the T_m and N_p were given the same.

In an MP-LWFA, the required T_m is determined by the plasma density, n_0. The RMS error, σ, of the pulse spacing was adopted to understand the accuracy of T_m in a

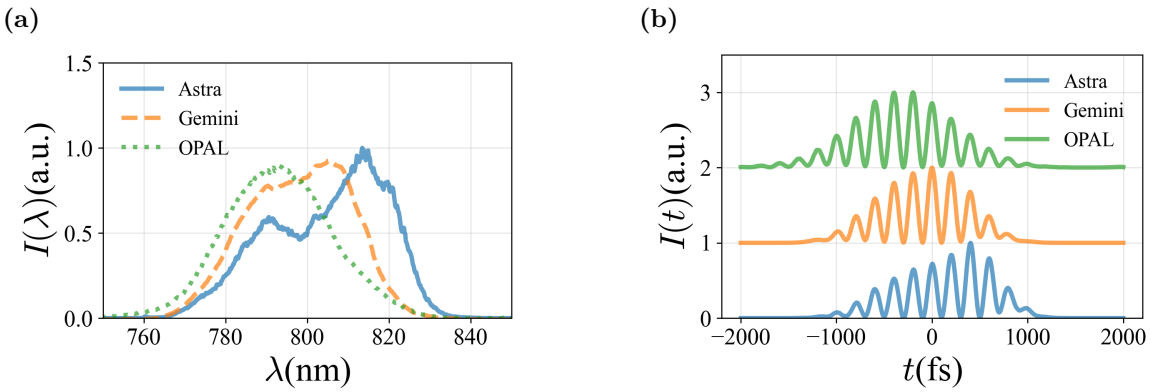


Figure 4.2: (a) Spectra of laser pulses generated from three different laser systems: TA2 (solid blue), TA3 (dashed orange), and OPAL (dotted green). (b) Pulse trains with T_m of 200 fs and N_p of 10 generated with the spectra shown in (a).

pulse train produced by the algorithm, as shown in Figure 4.1. σ is given as

$$\sigma = \sqrt{\sum_{i=1}^{N_p} \frac{(T_{\text{avg}} - T_i)^2}{N_p - 1}}, \tag{4.1}$$

where T_{avg} is the average pulse spacing; and T_i represents the ith pulse spacing in a pulse train.

Figure 4.3b shows simulated T_m for pulse trains with different N_p. The input spectrum was the Gemini spectrum shown in Figure 4.2a. The predefined T_m was 200 fs. In this simulation, the pulse train model provided the required τ and ψ_2 to simulate pulse trains with a given T_m and N_p at a certain degree of accuracy. The difference between the predefined T_m and simulated T_m decreases with the number of pulses in a pulse train. According to this example, the algorithm described in Figure 4.1 could provide reliable values of τ and ψ_2 that could be used to set up the Michelson interferometer and grating-pair compressor for pulse trains with $N_p \geq 10$ in a real experiment.

When generating pulse trains in a real experiment, it may be necessary to adjust N_p and T_m to deal with unexpected situations. Figure 4.4a shows a strategy to adjust T_m of a pulse train while keeping its N_p fixed, indicating that changing ψ_2 and fixing τ were an appropriate method to vary T_m. Figure 4.4b shows that two parameters, ψ_2 and τ, had to be adjusted simultaneously if N_p in a pulse train needed to be changed while keeping T_m fixed.

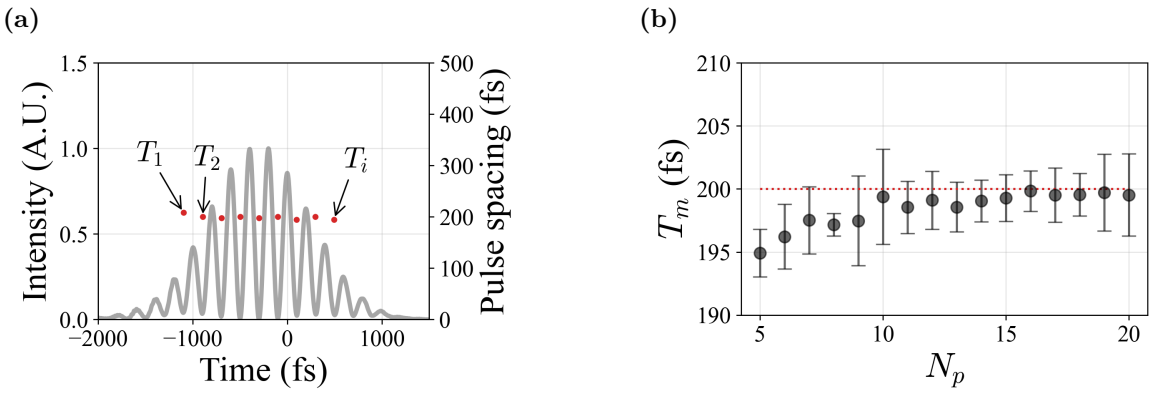


Figure 4.3: (a) Example of simulated pulse train. Red dots represent the pulse spacing. The grey curve shows the intensity profile. (b) Simulated T_m versus given N_p in pulse trains. The dashed red line, black dots, and error bars show the required $T_m = 200$ fs, simulated T_m in average, and the standard deviation of T_m calculated from 10 simulated pulse trains with fixed N_p.

During an MP-LWFA experiment [30] as discussed in Section 2.2.6, it was not possible to change ψ_2 frequently due to its involvement in the adjustment of the grating-pair compressor, which required a lot of time to realign the entire post-compressor laser beam line. A quicker way to adjust T_m was to change τ, as shown in Figure 4.5, although it also changed N_p in a pulse train. However, the simulation showed that N_p did not change significantly within a range of τ. For a case which $N_p = 8$, the T_m could be varied from 250 fs to 200 fs while varying τ. Due to time constraints in an experiment conducted at RAL, this strategy was adopted to adjust the pulse spacing of different pulse trains in the MP-LWFA experiment [30].

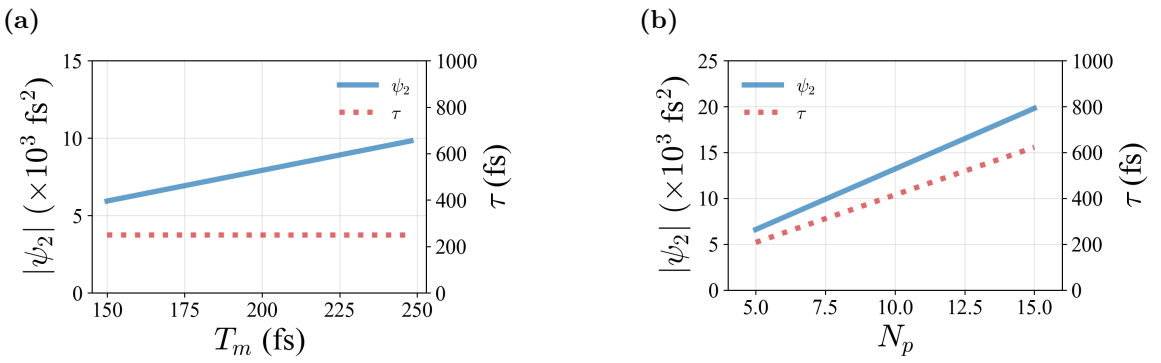


Figure 4.4: Strategy of adjusting T_m and N_p by changing ψ_2 and τ. ψ_2 and τ versus (a) T_m for a pulse train with a fixed N_p of 10; and (b) N_p for a pulse train with a fixed T_m of 200 fs.

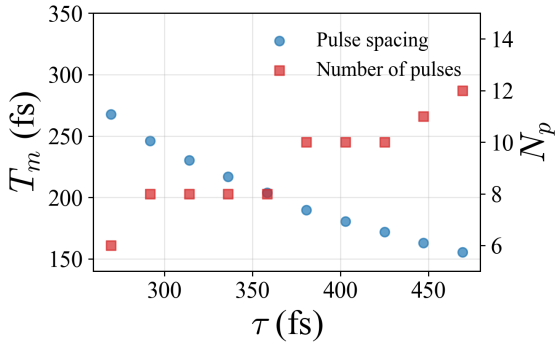


Figure 4.5: Variation of T_m and N_p with τ for a pulse train. The blue dots represent the pulse spacing and the red squares represent N_p in a pulse train.

4.2.2 Non-uniformity of pulse trains

In experiments at RAL, the only way to change ψ_2 was to adjust the grating separation of the pulse compressor, L_m. However, this also had an effect on the third-order spectral phase, ψ_3. Therefore, it is essential to understand this effect and how it affects T_m and N_p

Figures 4.6a and 4.6b show how ψ_3 affects generated pulse trains in terms of T_m. The pulse train parameters were the same as Figure 4.2 and the spectrum was the same as the one used in Figure 4.3. The sign of ψ_3 also affected the directionality of the pulse spacing variation, as shown in Figure 4.6b. This implies that ψ_3 must be kept as small as possible to ensure that resonant wakefield excitation is maintained across the whole pulse train.

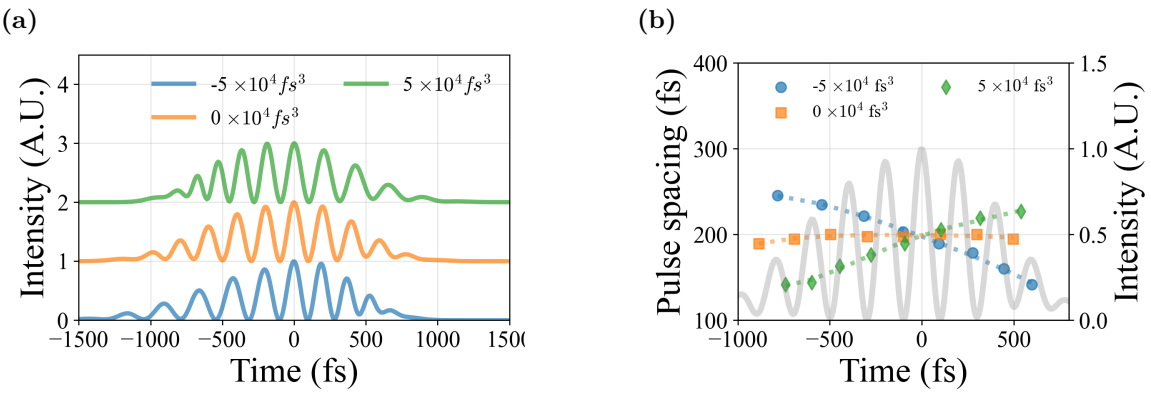


Figure 4.6: (a) Intensity of pulse trains affected by ψ_3. (b) Pulse spacing variation of pulse trains shown in (a). The coloured dots represent T_m with different ψ_3. The light grey curve shows the intensity of pulse train with zero ψ_3. The dotted lines shows the curve fit corresponding to the pulse spacing variation

A 4^{th}-order polynomial curve fitting function was used to quantify the non-uniformity of pulse spacing caused by ψ_3. The variation of pulse spacing, $S_{\text{non}}(t)$, in a pulse train is given by

$$S_{\text{non}}(t) = s_0 + s_1 t + \frac{1}{2}s_2 t^2 + \frac{1}{6}s_3 t^3 + \frac{1}{24}s_4 t^4, \tag{4.2}$$

where t is time; and the non-uniformity coefficient of pulse spacing, s_n, is the nth order derivative of $S_{\text{non}}(t)$ with respect to time;

When T_m is uniform in a pulse train, the higher-order s_n is close to zero and s_0 can be regarded as the average pulse spacing. Depending on the sign of s_1, T_m can either increase or decrease by $\delta T = s_1 \times T_m$ from one pulse to the next. For instance, the T_m of a pulse pulse train increases by $\delta T = s_0 s_1$ or 10 fs from one pulse to the next if T_m at the centre of the pulse train is 200 fs and s_1 is 0.05.

Figure 4.7 shows the variation of the coefficients, s_0 and s_1, with ψ_3 for different pulse trains with uniform T_m, indicating that the ψ_3 did not significantly affect the average T_m of pulse trains in the simulation as shown in Figure 4.7a. The greatest effect on the variation of T_m was on s_1 as shown in Figure 4.7b. Therefore, a nonzero ψ_3 could increase or decrease T_m linearly from one pulse to the next in a pulse train.

4.2.3 Influence of adopting grating pair compressors

The technique of generating pulse trains for proof-of-principle experiments in the MP-LWFA required the use of a grating-pair compressor and a Michelson interferometer

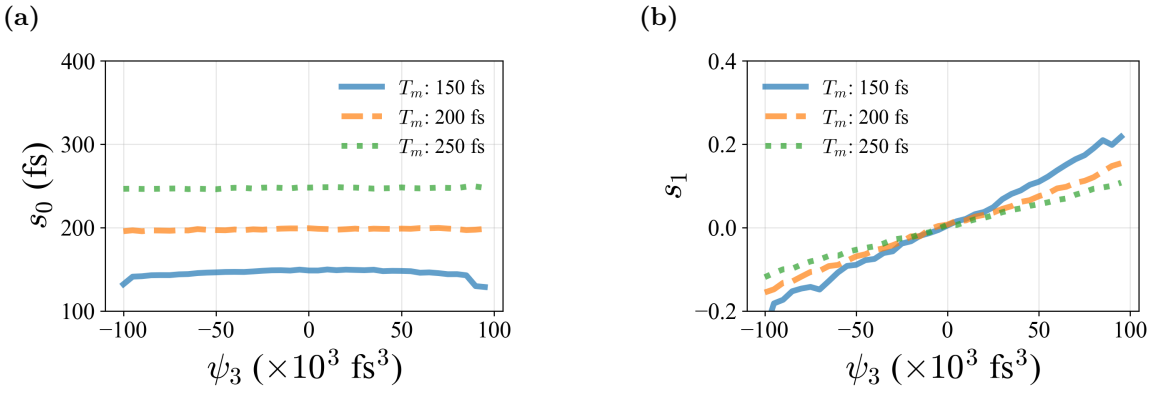


Figure 4.7: s_0 and s_1 versus ψ_3. (a) s_0 versus ψ_3 for multi-pulse trains with different initial values of T_m. (b) s_1 versus ψ_3 for pulse trains with three different initial values of T_m.

as discussed in Section 3.2.2. Equations (3.28) and (3.29) were used to calculate the required ΔL_m and ΔL_s. This section aims to investigate the uniformity of pulse spacing in pulse trains affected by the grating pair compressor.

The Gemini laser system used a two-pass grating-pair compressor. The angle of incidence, θ_i, was 36° and the grating groove density, g, was 1480 lines/mm (or l/mm). It was assumed that the centre frequency of the pulse, λ_0, was at 800 nm. ΔL_s was defined as the displacement away from the reference position providing full pulse compression. In other words, ΔL_s gave a larger grating separation from the reference position in this simulation. The input spectrum for this simulation is given by the Gemini pulse spectrum, as shown in Figure 4.2a.

Figure 4.8 shows results that could be used to assist in designing MP-LWFA experiment. For pulse trains with $6 < N_p < 15$ in the range 150 fs $< T_m <$ 250 fs, the required values of ΔL_s and ΔL_m were a few mm and within a hundred of μm, respectively.

Figure 4.9a shows the value of ψ_3 output by the same conditions of the grating-pair compressor for pulse trains as shown in Figure 4.8 while changing the grating separation ΔL_s to produce T_m ranging from 150 fs to 250 fs. The variation of s_1 of these pulse trains under the same range of T_m is shown in Figure 4.9b. These results show a severe non-uniformity of pulse spacing in the generated pulse trains. For instance, if a uniform pulse train with $N_p = 10$ and $T_m = 200$ fs had an s_1 of 0.05, the pulse spacing would increase

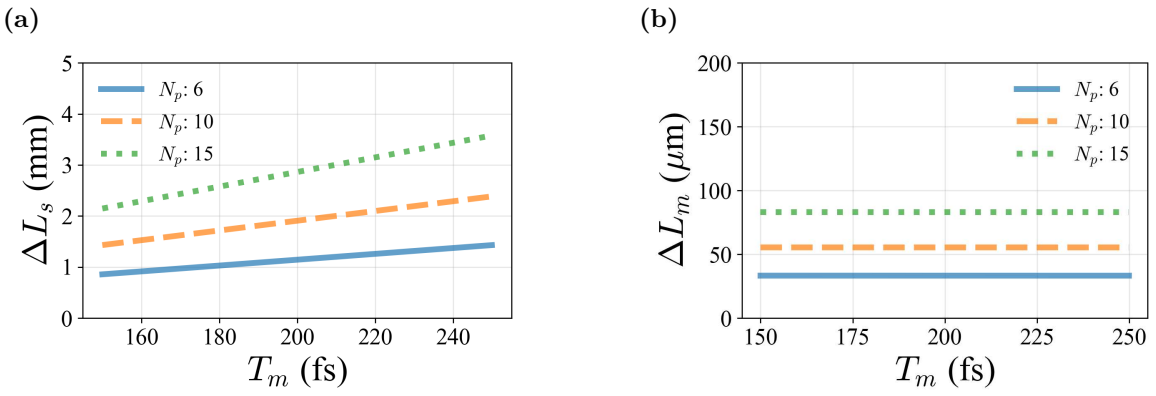


Figure 4.8: Variation of ΔL_s and ΔL_m versus T_m ranging from 150 to 250 fs for pulse trains with $N_p = 6$, 10, and 15. (a) ΔL_s versus T_m. (b) ΔL_m versus T_m.

by 10 fs from one pulse to the next. If the middle pulse spacing was 200 fs, the first pulse spacing would be 160 fs and the last pulse spacing would be 250 fs for this pulse train.

According to the discussion in Section 2.4.1 of Chris Arran's thesis [101], an accuracy of $\delta t/T_m \simeq 1/2N_p$ is required to generate a plasma wakefield with an amplitude equal to 64% of the resonant case, where $\delta t = s_1 T_m$. In other words, the amplitude of a wakefield is reduced by 36% of its resonant case for a pulse train with $N_p = 10$ and $s_1 = 0.05$. Therefore, it is necessary to use other optical devices to reduce ψ_3 of the input pulse spectrum so that the non-uniformity of a pulse train can be reduced and hence stronger plasma wakefield can be excited.

4.2.4 Error analysis of multi-pulse train generation

When using the pulse train generation technique, error analysis is important for experimental physicists to understand the performance of this optical system. This section briefly provides a method to estimate the uncertainty of T_m generated by the pulse train generation technique discussed in Section 4.2.1.

In the simulation, it was assumed that ψ_3 could be minimised so that s_1 had no effect on the variation of T_m. The simulation conditions, such as the input spectrum and compressor parameters, were assumed in Section 4.2.3. Three values of pulse spacing, 100 fs, 200 fs and 250 fs, were adopted, with TBPs of 8, 10 and 13, respectively.

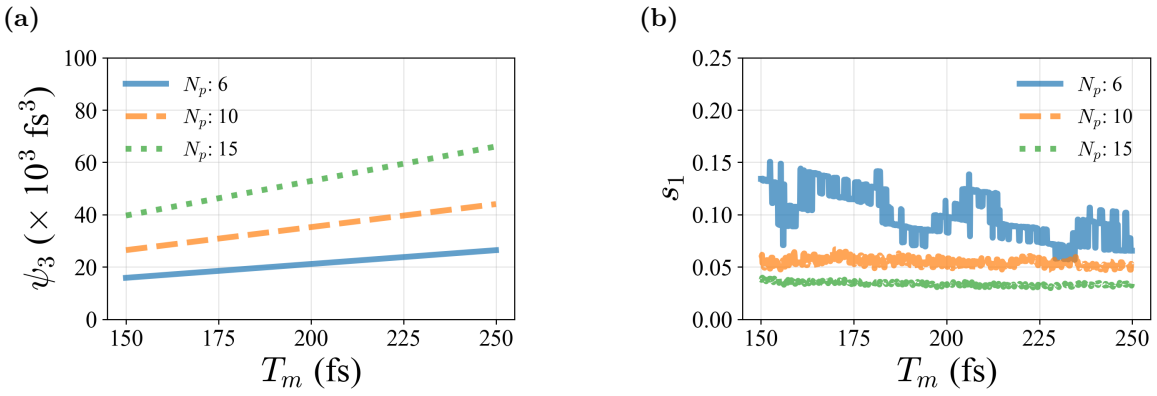


Figure 4.9: Produced ψ_3 and s_1 versus T_m ranging from 150 fs to 250 fs for pulse trains with $N_p = 6$, 10, and 10 while changing the grating separation ΔL_s. (a) ψ_3 versus T_m. (b) s_1 versus T_m.

The error of the average pulse spacing, δT_m, is defined by

$$\delta T_m = \sqrt{\sum_n \left(\frac{\partial T_m}{\partial x_n}\right)^2 {dx_n}^2}, \tag{4.3}$$

where T_m is the average pulse spacing; and x_n is the source of error.

To simplify this error analysis, only four systematic error sources were taken into account: (i) the uncertainty of the Michelson arm displacement, ΔL_m, (ii) the uncertainty of the slant distance of the grating-pair compressor, ΔL_s, (iii) the misalignment of the angle of incidence, $\delta\theta_i$, and (iv) the uncertainty of grating groove density, δg. The variation of T_m with respect to the three initial input pulse spacings was obtained by scanning the values of these four parameters, as shown in Figures 4.10 and 4.11.

A polynomial curve fitting curve-fitting routine in Python was used to find find the best fit of these curves and the first-order derivative of the pulse spacing variation. Table 4.1 gives the results of the error analysis for the optical system of pulse train generation. Supposed that the uncertainty of each parameter were given bt $\Delta L_m = \pm 5$ µm, $\Delta L_s = \pm 5$ µm, $\delta\theta_i = \pm 1°$ and $\delta g = \pm 10$ l/mm. Using the coefficients listed in table 4.1, the uncertainty of pulse spacing for pulse trains with T_m of 150 fs, 200 fs and 250 fs was calculated to be 8 fs, 11 fs, and 14 fs, respectively.

In a real MP-LWFA experiment, the uncertainty of T_m is not a serious issue because n_0 can be adjusted to satisfy the resonance condition of wakefield generation once a pulse train is generated by the optical system. However, the non-uniformity of T_m is a problem because ψ_3 cannot be compensated by the plasma density. Thus, an

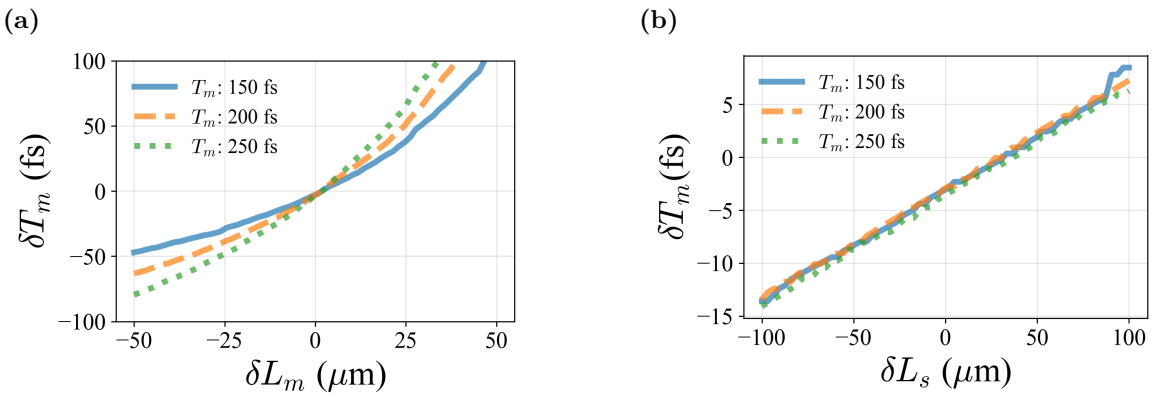


Figure 4.10: (a) δT_m versus δL_m. (b) δT_m versus δL_s.

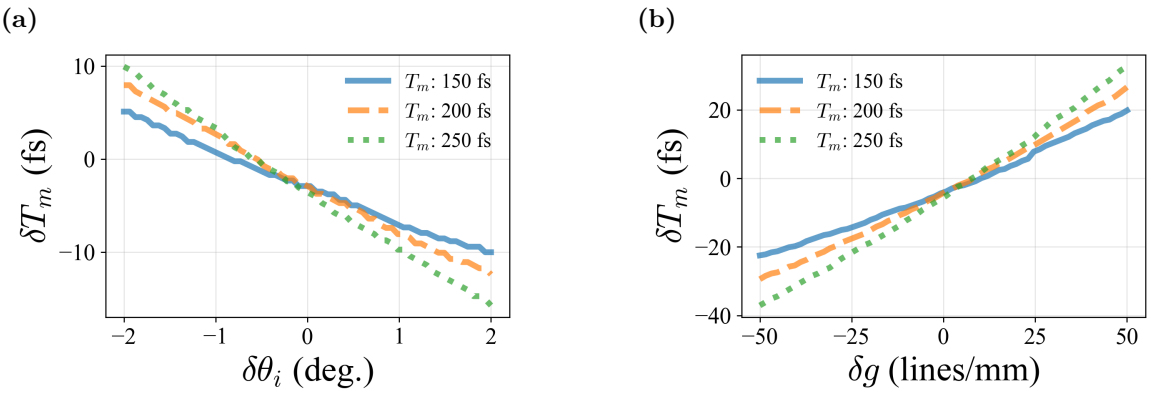


Figure 4.11: (a) δT_m versus $\delta\theta_i$. (b) δT_m versus δf.

uncertainty of T_m does not affect the operation of the experiment, but non-uniformity of T_m should be avoided.

4.3 Phase retrieval of multi-pulse trains

4.3.1 Selection of FROG algorithms

To choose the most appropriate phase retrieval algorithm for the pulse train measurement, this section compares the performance of phase retrieval algorithms reviewed in Section 3.4 in terms of the convergence rate of the FROG error and the pulse retrieval results. To simplify this analysis, four uniform pulse trains with the same T_m = 200 fs were studied for N_p = 1, 5, 10 and 15, and TBPs of 1, 5, 10, 16, respectively. It should be noted that the selection of T_m and N_p for all the simulations done in the following topics emulated possible experimental parameters of T_m and N_p that could be adopted in proof-of-principle MP-LWFA experiments.

T_m	$\frac{\partial T_m}{\partial L_m}$	$\frac{\partial T_m}{\partial L_s}$	$\frac{\partial T_m}{\partial \theta_i}$	$\frac{\partial T_m}{\partial g}$
150 fs	1.3 (fs/μm)	0.01 (fs/μm)	0.4 (fs/deg.)	0.9 (fs·mm/line)
200 fs	1.7 (fs/μm)	0.01 (fs/μm)	0.6 (fs/deg.)	1.2 (fs·mm/line)
250 fs	2.1 (fs/μm)	0.01 (fs/μm)	0.7 (fs/deg.)	2.5 (fs·mm/line)

Table 4.1: Error sources of pulse trains with N_p = 10 and T_m = 150, 200, and 250 fs.

The pulse trains were assumed to have no background noise so that the influence of the noise could be removed. No spectral constraints were applied in the ePIE algorithm to ensure a fair comparison between the algorithms. This was because the GP and PCGP algorithms did not include the input pulse spectrum as a constraint in the simulation. All the algorithms were given 50 iterations for the phase retrieval process. The GP and PCGP algorithm used in this simulation were written from scratch by the author, following the procedures described in [175, 177]. The ePIE algorithm was re-written based on the work published by Spangenberg et al. and Sidorenko at al. [184, 185]. All the computer programs were run on Python with no specific optimisation for any algorithm.

Figure 4.12 shows the convergence rates for each algorithm. The ePIE algorithm outperformed the other two algorithms when the complexity of a pulse train increased. In Figure 4.12a, all three algorithms performed similarly when $N_p = 1$. In Figure 4.12b, the PCGP algorithm produced a slightly lower G_{FROG} than the ePIE algorithm when N_p were from 5 to 10, approximately. In Figures 4.12d, the ePIE algorithm showed stagnation in the phase retrieval process when $N_p = 15$. This implies that the ePIE algorithm could not handle the retrieval of pulse trains with $N_p > 15$ for the 512-by-512 grid size in this simulation. According to this simulation result, the author concluded that the ePIE algorithm could deal with the phase retrieval of complex pulse trains. However, it provided similar performance to the other two algorithms when the complexity of pulse trains had a TBP < 10.

Examining G_{FROG} is a way to evaluate the convergence of the retrieval process. However, a lower G_{FROG} does not mean that the retrieved pulses are correct. Although Figure 4.12 shows the performance of different algorithms for the pulse retrieval of pulse trains, it is also important to look at the accuracy of retrieved temporal intensity profiles.

Figures 4.13, 4.14 and 4.15 show the pulse retrieval results corresponding to Figures 4.12b, 4.12c and 4.12d, respectively. Only the ePIE algorithm provided almost correct retrieval results of pulse trains with different values of TBPs. However, the retrieved pulses shown in Figure 4.15 had lower intensity contrast than the input pulse even though the intensity profile was otherwise close the correct solution.

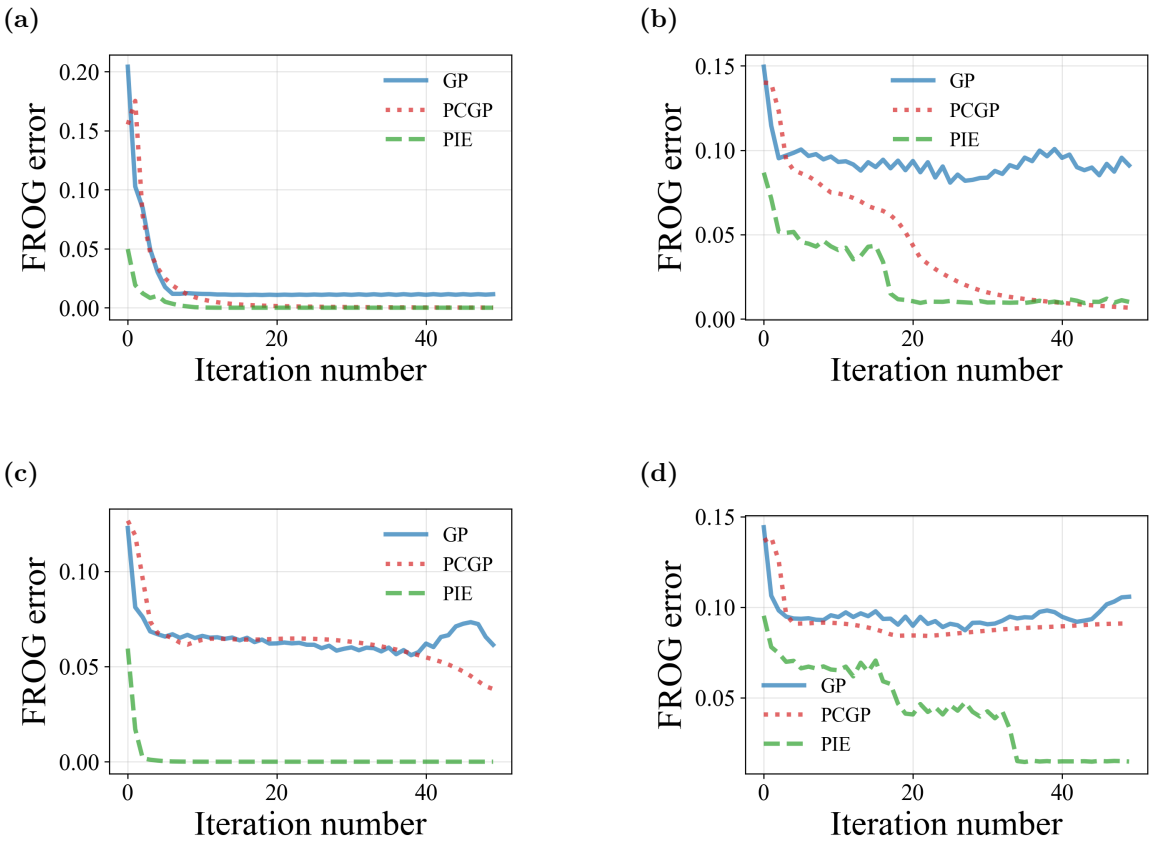


Figure 4.12: Comparison of the convergence rate of FROG algorithms for different pulse trains with $T_m = 200$ fs. (a) $N_p = 1$. (b) $N_p = 5$. (c) $N_p = 10$. (d) $N_p = 15$.

Based on this evaluation of the convergence rate and retrieved pulses by the GP, PCGP and ePIE algorithms, it can be concluded that the GP algorithm was not suitable for the pulse train measurement. Second, the PCGP algorithm seemed able to retrieve a pulse train with $N_p = 5$. Finally, the ePIE algorithm was the only one that could successfully retrieve all the pulses in the simulation among all algorithms. Accordingly, the ePIE algorithm was chosen as the phase retrieval algorithm for the measurement of pulse trains in the MP-LWFA. However, ePIE algorithm may struggle to provide reliable results with a $N_p > 15$ or a TBP > 16 for a grid size of 512×512. If choosing larger grid sizes, the pulse train could be retrieved, but the trade-off would be longer retrieval time and more stringent requirement on the resolution of imaging systems to resolve finer FROG trace structures, which might not be ideal for use of online analysis in a real MP-LWFA experiment.

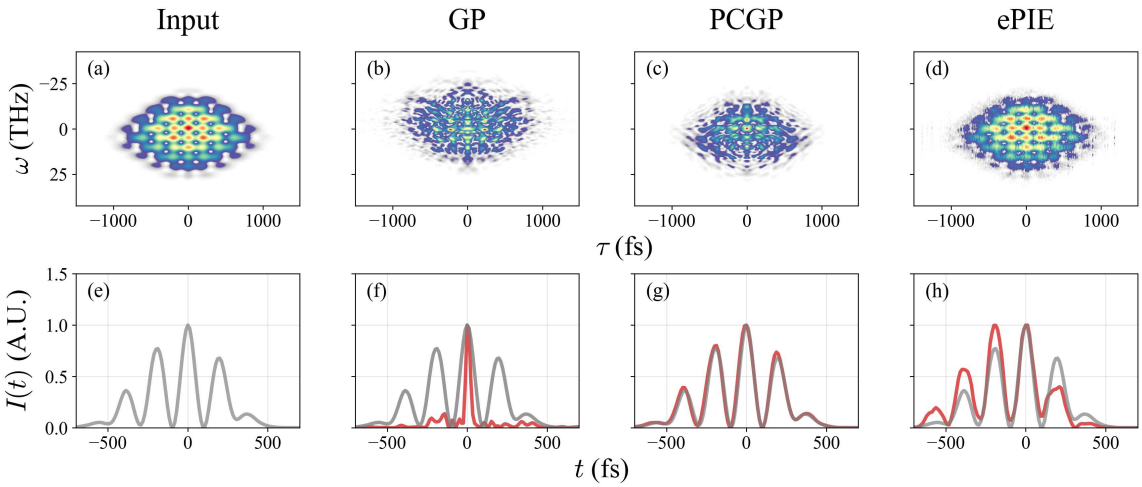


Figure 4.13: Retrieval results for $N_p = 5$ and $T_m = 200$ fs. The grey and red curves show the input pulse train and retrieved pulse train.

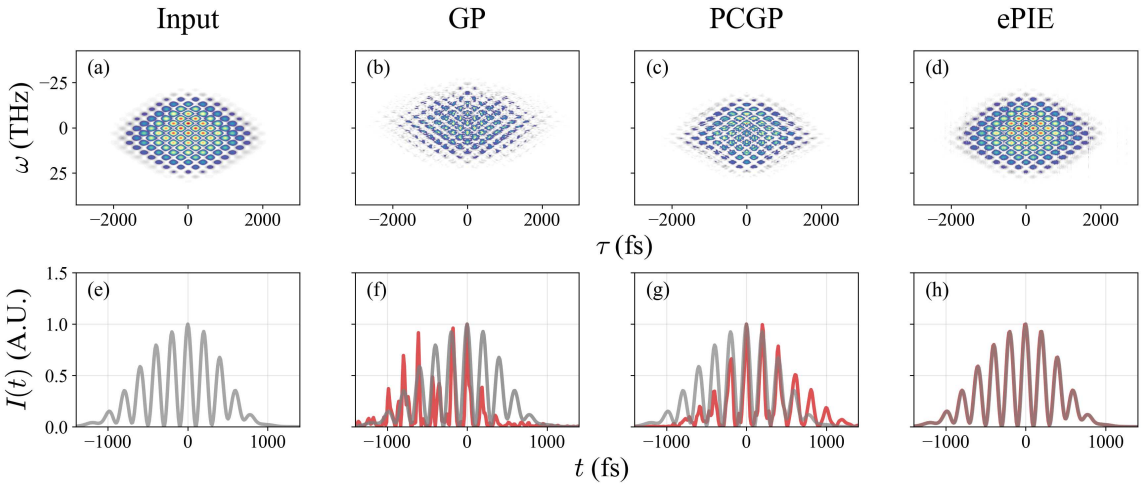


Figure 4.14: Retrieval results for $N_p = 10$. The definitions of coloured curves follows ones in Figure 4.13.

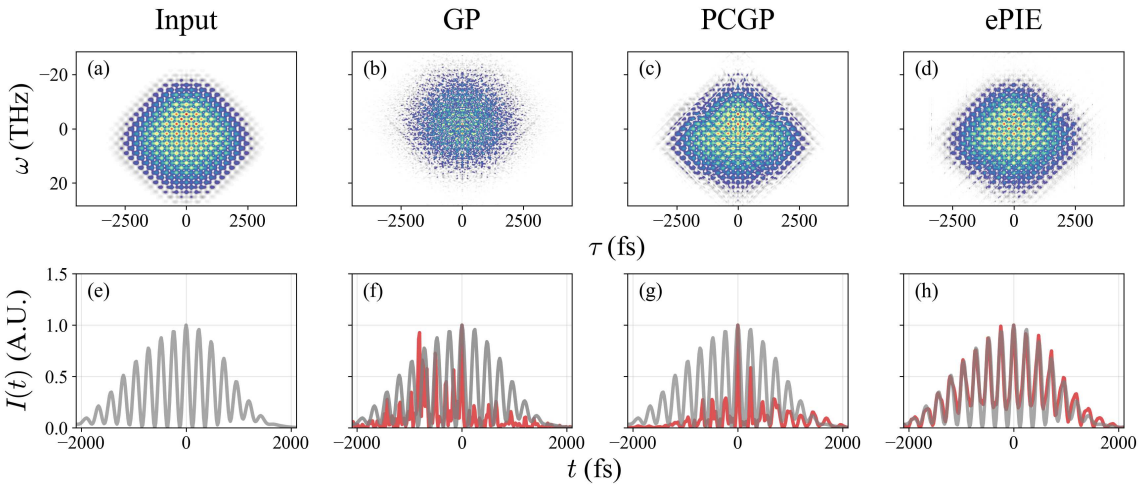


Figure 4.15: Retrieval results for $N_p = 15$. The definitions of coloured curves follows ones in Figure 4.13.

However, it should be noted that this simulation did not consider the uncertainty of the retrieval results, but rather focused on a general understanding of the convergence rate. The uncertainty means the standard error of nth retrieval results. Practically, this was because these algorithms were written from scratch and hence they were not seriously optimised. In addition, they were not the original versions of code used by the developers. Taking into account the time limitations to chose an appropriate phase retrieval algorithm for the pulse train measurement, the author eventually chose the ePIE algorithm

4.3.2 Influence of bandpass filters

As discussed in Sections 3.5.1 and 3.5.2, using a bandpass filter in a FROG device can remove the time ambiguity of SHG FROG traces and reveal spectral phase information from the mean conditional delay, $\langle\tau\rangle_\omega$, in the blind FROG trace. This section aims to present the effect of such a bandpass filter on the blind FROG traces formed by different types of pulse trains.

The parameters of pulse trains assumed in this simulation work were the same as those defined in Section 4.3.1. A bandpass filter with $\Delta\lambda = 10$ nm and $\lambda_0 = 800$ nm was adopted. Figure 4.16 shows the temporal intensity of input probe and gate pulses. Since the bandpass filter removed a large range of spectral frequency components, the gate pulses had simpler temporal structures than the probe pulses.

Figure 4.17 shows the FROG traces with and without the effect of the bandpass filter. In (a), (b), and (c) of Figure 4.17, the SHG FROG traces were symmetric. In contrast, the FROG traces shown in (d), (e), and (f) of Figure 4.17 are asymmetric and tilted. This means that the higher frequency components arrive later than the lower frequency components for the asymmetric FROG traces. This is consistent with the sign of the second-order spectral phase introduced by the grating-pair compressor in this simulation.

Table 4.2 shows a comparison of the input GDD and the GDD calculated by examining $\langle\tau\rangle_\omega$ in Equation (3.81) for the three traces shown in the lower row of Figure 4.17. The GDD calculated by finding $\langle\tau\rangle_\omega$ had an error of approximately 4% compared to the input GDD. In addition, the calculated GDD from $\langle\tau\rangle_\omega$ was smaller than the input GDD

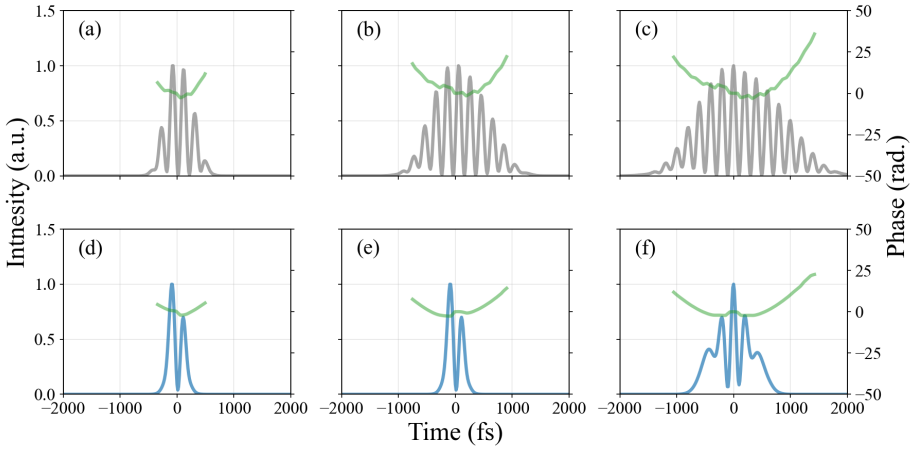


Figure 4.16: Probe and gate pulses forming the SHG FROG traces with the insertion of a bandpass filter whose $\Delta\lambda = 10$ nm. Pulses in the upper-row graphs are the probe pulses shown by the grey curves. Pulses in the lower-row graphs are the gate pulses shown by the blue curves. The graphs in each column represent a pair of probe and gate pulses with $N_p = 5, 10, 15$, respectively. The green curves represent the temporal phase of each pulse train.

Based on the results in Table 4.2, information about $\langle\tau\rangle_\omega$ accompanied by τ from a Michelson interferometer could be used to reconstruct the pulse trains without running a phase retrieval algorithm. This strategy could provide a quick understanding of the temporal intensity of pulse trains in a real experiment. However, it was found that this strategy was only useful when there was no ψ_3 introduced in the input spectrum. Instead, therefore, using the direct phase information calculated from $\langle\tau\rangle_\omega$ could only be used as an initial guess of the spectral phase applied at the beginning

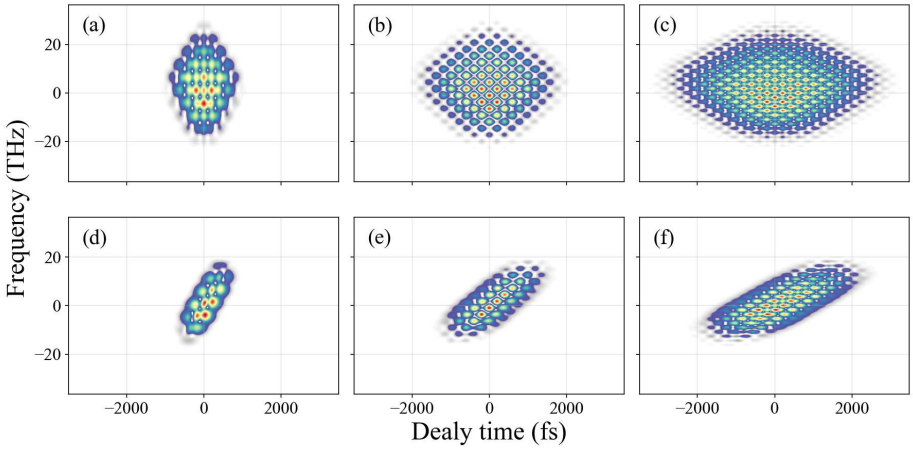


Figure 4.17: SHG FROG traces with and without the insertion of a bandpass filter. Graphs in the upper row are FROG traces without the insertion of a bandpass filter. Graphs in the lower row are FROG traces with insertion of a bandpass filter. (a) and (d) are traces formed by 5 pulses. (b) and (e) trace formed by 10 pulses. (c) and (f) trace formed by 15 pulses.

Number of pulses	5	10	15
Input GDD	5,798fs^2	11,605 fs^2	17,410fs^2
Calculated GDD	5,632 fs^2	11,138 fs^2	16,806 fs^2
Difference of GDD	166 fs^2	467 fs^2	694 fs^2

Table 4.2: Comparison of calculated GDD obtained from $\langle\tau\rangle_\omega$ and the input GDD for different numbers of pulses in pulse trains.

of the phase retrieval process.

Filters with various spectral widths were simulated to find an optimal bandwidth of bandpass filter in a FROG device. Figure 4.18a compares the calculated GDD from $\langle\tau\rangle_\omega$ with the input value for different filter widths. The calculated GDD began to deviate from the actual input GDD for $\Delta\lambda > 10$ nm, but gave similar results to the input value for $\Delta\lambda < 10$ nm.

Figure 4.18b shows the calculated ψ_2 from $\langle\tau\rangle_\omega$ varying with T_m ranging from 150 fs to 250 fs using a filter with $\Delta\lambda = 8$ nm. The results suggest that the calculated ψ_2 was not accurate for cases in which $T_m < 190$ fs and $N_p < 5$.

In conclusion, these simulations suggested that a bandpass filter in an SHG-FROG device could break the symmetry of the pulse train FROG traces and reveal direct

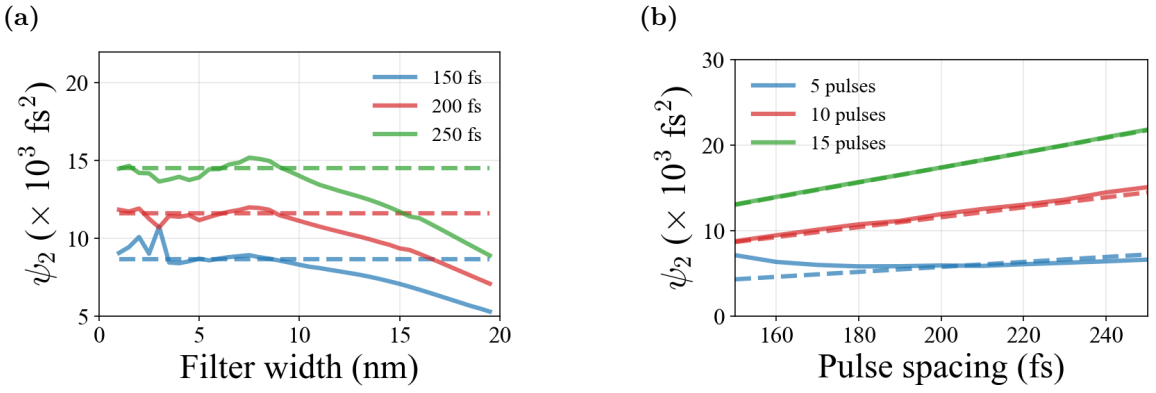


Figure 4.18: GDD versus spectral bandwidth of a filter and pulse spacing. Solid lines represent the calculated GDD. Dashed lines are the input GDD. (a) Calculated GDD from the mean conditional delay versus the spectral width of a bandpass filter. The blue, red, and green colours represent data for the pulse spacing of 150 fs, 200 fs and 250 fs. (b) Calculated GDD from the mean conditional delay versus the pulse spacing of pulse trains. Solid lines represent the calculated GDD. Dashed lines are the input GDD. The blue, red, and green colours represent data for N_p of 5, 10, and 25.

spectral phase by calculating $\langle\tau\rangle_\omega$ of the trace. Additionally, filters with $\Delta\lambda < 10$ nm could provide an accurate spectral phase directly calculated from $\langle\tau\rangle_\omega$ up to an accuracy of 4% for a wide range of pulse train parameters.

4.3.3 Influence of noise

Random fluctuation in optical and electronic signals is an unavoidable problem in real-world pulse measurement and regarded as noise of detection. Different types of noise are involved in the process of conversion between the photons of optical pulses and readout values of photodetectors. These types of noise sources include photon noise, photo-electron noise, amplifier noise, and readout noise [200–202].

The probability density functions of these noise sources can be generally categorised into Poisson and Gaussian distributions [203]. Random photon registration received by a photodiode results in a Poisson noise distribution and the dark current induced by the thermal effect in long integration time produces a Gaussian noise distribution. This section presents a examination of the influence of noise on the phase retrieval of pulse trains.

Two types of errors were adopted to evaluate the accuracy of the retrieved results: the RMS intensity error, σ_I, and the RMS intensity-weighted temporal phase error σ_ϕ, given in [204]. As indicated the Parseval's Theorem and discussed by R. Trebino in [204], σ_I of the temporal intensity of a retrieved pulse is equivalent to σ_I of its spectrum. Therefore, σ_I and σ_ϕ were used to evaluate the accuracy of retrieved pulses and traces with respect to their input data.

The definition of σ_I is given by

$$\sigma_I = \left\{ \frac{1}{N} \sum_{n=1}^{N} \left[I_{\mathrm{in}}(t_n) - I_{\mathrm{r}}(t_n) \right]^2 \right\}^{\frac{1}{2}}, \tag{4.4}$$

where I_{in} is the actual input intensity; I_{r} is the retrieved intensity; N is the number of data points; the subscript n means the nth data point; and the unit is in percentage.

The definition of σ_ϕ is given by

$$\sigma_\phi = \left\{ \frac{\sum_{n=1}^{N} {I_{\mathrm{in}}}^2(t_n) \left[\phi_{\mathrm{in}}(t_n) - \phi_{\mathrm{r}}(t_n) \right]^2}{\sum_{n=1}^{N} {I_{\mathrm{in}}}^2(t_n)} \right\}^{\frac{1}{2}}, \tag{4.5}$$

where ϕ_{in} is the actual input intensity; ϕ_{r} is the retrieved intensity; and the unit is in radian. For the RMS intensity-weighted spectral phase error, the symbol, ϕ, is replaced with ψ.

Two noise levels were given for each type of noise in order to understand the qualitative effect of the Poisson and Gaussian noise on the phase retrieval result of pulse trains. Based on [201, 205], the SNR is defined as

$$\text{SNR} = 10\log_{10}\frac{N_{\text{PE}}^2}{\sigma_{\text{noise}}^2}, \tag{4.6}$$

where the mean of photoelectrons is N_{PE}; and the variance of photoelectrons is ${\sigma_{\text{noise}}}^2 = N_{\text{PE}}$.

SNRs of 20 dB and 40 dB were used to determine Poisson noise in the simulation. The input FROG trace was generated with the defined Poisson noise levels using a Python Poisson noise generator [206]. The same SNRs were also used for Gaussian noise to ensure a fair comparison of the phase retrieval results. Since the Gaussian noise in this simulation was assumed to be additive, the noise was generated by a Python Gaussian noise generator [207] and directly added to the input FROG trace.

To simplify this analysis, these two noise sources were directly applied to simulated FROG traces so that the final effects of noise on the retrieved data could be analysed. The simulation conditions were the same as those in Section 4.3.2, including T_m, N_p and $\Delta\omega$. The statistics of the phase retrieval process was obtained by retrieving the same trace five times with each of 30 iterations and different noise. The ePIE algorithm was used to retrieve the input multi-pulse trains and FROG traces. The spectrum of the gate pulse was used as a spectral constraint.

Figure 4.19 shows the retrieval results of FROG traces for the Poisson noise with SNRs of 20 dB and 40 dB. The retrieved FROG traces from the ePIE algorithm produced a higher contrast and cleaner intensity distribution than the input FROG traces for both noise levels, which indicates that the ePIE algorithm could suppress the Poisson noise in FROG traces.

The average retrieved intensity profiles of the pulses and spectra with 20- and 40-dB Poisson noise are shown in Figure 4.20. The values of σ_I were 59% and 20%, and

the values of σ_ψ, were 9 and 3 radians for SNR of 20 and 40 dB, respectively. The Poisson noise affected the retrieved intensity distribution of pulses as well as the spectra. However, it is clear that the pulse spacing of the retrieved pulses did not vary with the SNR of noise in these two cases.

Figure 4.21 shows the retrieval results of FROG traces for Gaussian noise with SNRs of 20 dB and 40 dB, respectively. The simulation results suggest that the ePIE algorithm could retrieve a general profile of the input FROG trace and suppress some background noise for 20-dB SNR. The algorithm had no difficulty in retrieving the FROG trace when the SNR of the Gaussian noise increases to 40 dB.

The average retrieved intensity of the pulses and spectra with 20- and 40-dB Gaussian noise are shown in Figure 4.22. The values of σ_I were 31% and 14%, and the values of σ_ψ were 38 and 9 radians for SNR of 20 and 40 dB, respectively. For the influence of Gaussian noise on the retrieved pulses shown in Figure 4.22a, the T_m of the retrieved pulse train was similar to that of the input pulse. According to the above discussion,

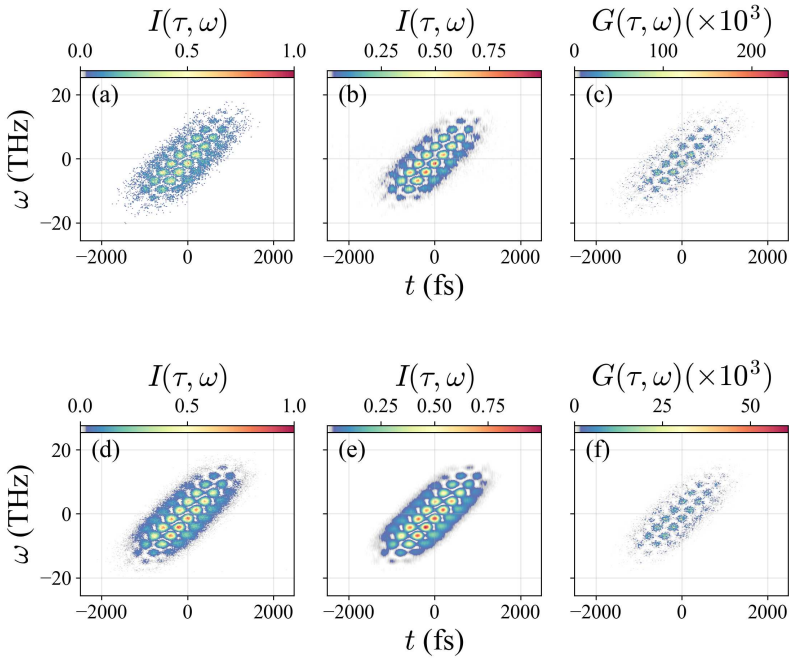


Figure 4.19: Retrieval results with 20-dB Poisson noise in (a), (b), and (c); and 40-dB Poisson noise in (d), (e), and (f). Input FROG traces are shown in (a) and (d). Retrieved FROG traces are shown in (b) and (e). FROG trace errors are shown in (c) and (f). The input pulse train had $N_p = 10$ and $T_m = 200$ fs. The bandwidth of filter $\Delta = 8$ nm.

the Gaussian background noise had a more severe effect on the phase retrieval results compared to the case of Poisson noise.

Figure 4.23a and 4.23b show the values of G_{FROG} and σ_I varying with SNR of Poisson noise which ranged from 10 dB to 90 dB. The SNR of the Poisson noise should be larger than 40 dB for σ_I to be below 10 %. Additionally, σ_I of the retrieved pulse trains with $T_m = 250$ fs did not change with the increasing SNR. This shows that the ePIE algorithm could not retrieve the pulse with such a complexity using a 256-by-256 grid size for the input FROG trace. Figure 4.23c and 4.23d show G_{FROG} and σ_I varying with SNR of Gaussian noise ranging from 10 dB to 100 dB. The results were similar to the case shown in Figures 4.23a and 4.23b

In conclusion, the Poisson and Gaussian noise affected the phase retrieval results in several ways. First, the temporal intensity of retrieved pulse trains was affected more

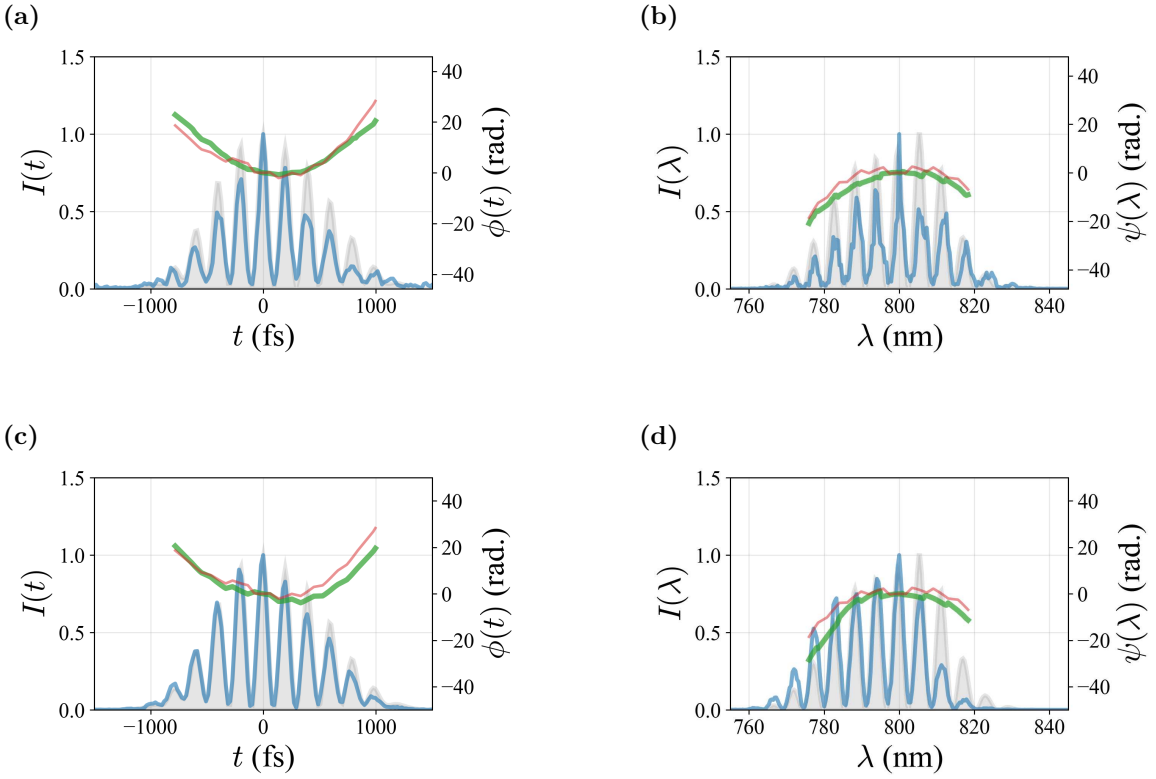


Figure 4.20: Retrieval results of temporal and spectral intensity with 20-dB Poisson noise in (a) and (b); and 40-dB Poisson noise in (c) and (d). The grey-shaded area and the solid blue curves represent the input and retrieved intensity, respectively. The green and red curves represent the input and retrieved phases, respectively. Input parameters were the same as in Figure 4.19.

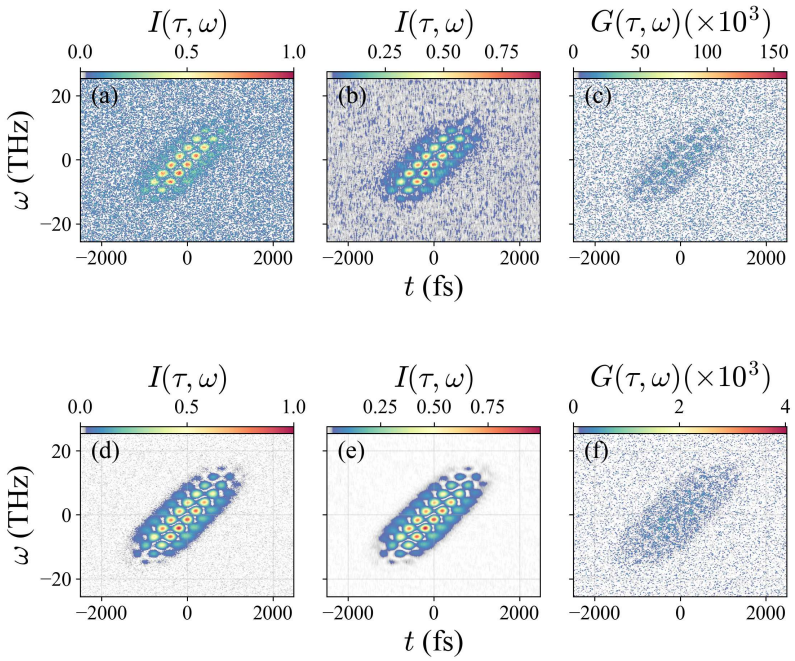


Figure 4.21: Retrieval results with 20-dB Gaussian noise in (a), (b), and (c); and 40-dB Gaussian noise in (d), (e), and (f). Input FROG traces are shown in (a) and (d). Retrieved FROG traces are shown in (b) and (e). FROG trace errors are shown in (c) and (f). Input parameters were the same as Figure 4.19.

by Gaussian noise than Poisson noise in terms of the temporal intensity. Below a 20-dB SNR in the Gaussian noise, the ePIE algorithm could not retrieve correct pulses trains. Second, the T_m of pulse trains was not significantly affected by the Poisson noise. In contrast, Gaussian noise had a more severe effect on the retrieved pulses at low SNRs. Finally, the simulation results show that pulse trains of interest to this work could be retrieved with an intensity error better than 10% for both Poisson and Gaussian noise, provided the SNR exceeds 40 dB.

This implies that using a dynamic range above 40 dB is essential for the pulse train measurement. For an imaging sensor (Sony IMX 249) with a well-capacity of 33,000 e^-, bit-depth of 12, dark current noise of 4.57 e^-/s, and exposure time of 1 µs, the dynamic range is approximately 43 dB based on the discussion in [201], which is sufficient for the pulse train measurement.

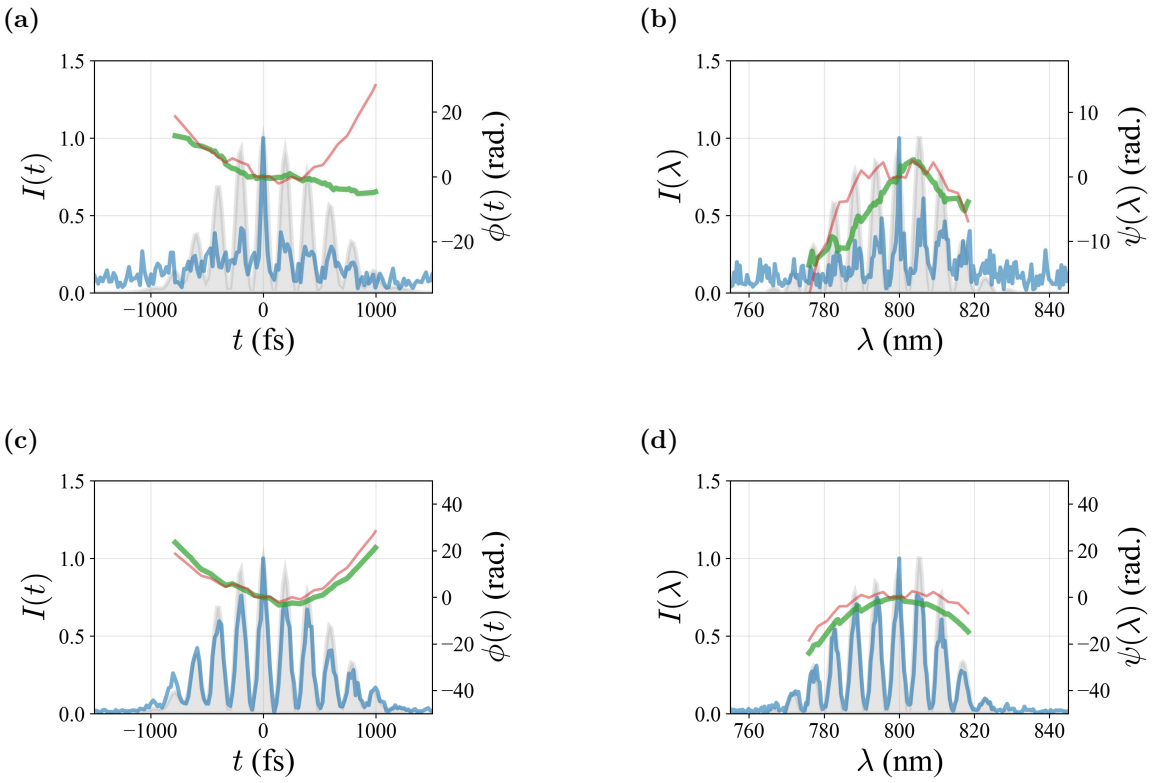


Figure 4.22: Retrieval results of temporal and spectral intensity with 20-dB Gaussian noise in (a) and (b); and 40-dB Gaussian noise in (c) and (d). The grey-shaded area and the solid blue curves represent the input and retrieved intensity, respectively. The green and red curves represent the input and retrieved phases, respectively. Input parameters were the same as Figure 4.19.

4.3.4 Retrieval of nonuniform pulse trains

Since the technique of pulse train generation uses a grating-pair compressor, the third-order spectral phase or third-order dispersion (TOD) introduced to pulse trains is unavoidable in a real MP-LWFA experiment. A large TOD resulted in the non-uniformity of pulse spacing in pulse trains. Because one of the purposes using a FROG device to measure pulse trains was to detect the non-uniformity of the pulse spacing, we investigated whether the ePIE algorithm was able to diagnose the non-uniformity of pulse spacing in pulse trains retrieved from the blind FROG traces in this section.

To see how the TOD affected the FROG trace, Figure 4.24 shows the blind FROG traces generated by pulse trains with $N_p = 10$, $T_m = 200$ fs, and three different values of TOD ranging from -35×10^3 to 35×10^3 fs^3. The TOD caused the tilted blind FROG traces to curve to the left or right, depending on its sign. Therefore, a blind

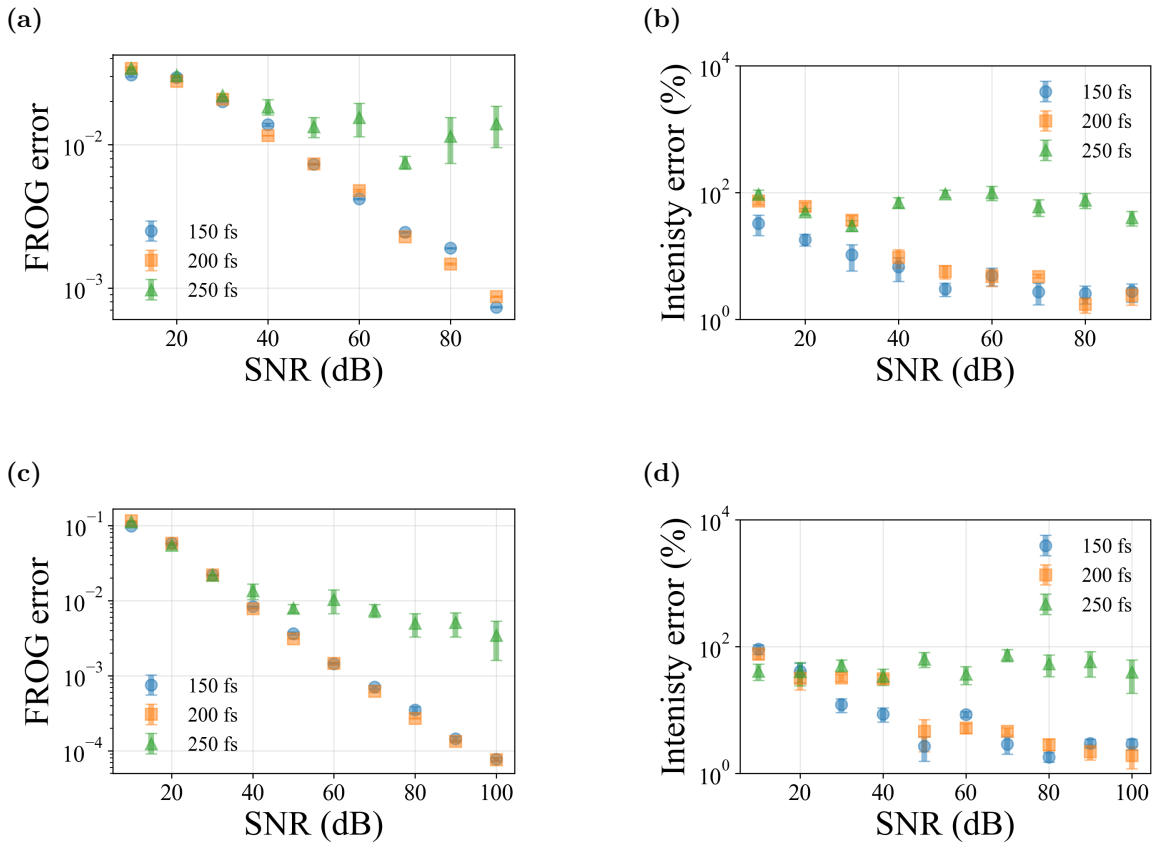


Figure 4.23: FROG error, G_{FROG}, and RMS intensity error, σ_I, versus SNR for the Poisson (a, b) and Gaussian noise (c, d) ranging from 10 to 90 dB. The error bars are the standard error. The blue dots, red squares and green triangles show the data for pulse spacing at 150 fs, 200 fs, and 250 fs, respectively.

FROG trace of pulse train provides intuitive time-frequency information about the relative values and signs of TOD.

The method used to calculate s_1 employed the Python interpolation routine, Cubic-Spline, to interpolate the retrieved and input pules. The T_m between each pulse in a retrieved pulse train was fit by a fourth-order polynomial curve fitting function. The form of this polynomial curve fitting function, $f(t)$, is given as

$$f(t) = s_0 + s_1 t + \frac{1}{2}s_2 t^2 + \frac{1}{3!}s_3 t^3 + \frac{1}{4!}s_4 t^4, \tag{4.7}$$

where the peak of each pulse is at time t.

Figure 4.25 shows the variation of s_1 for TOD in a range from -60×10^3 to 60×10^3 fs^3 for the same parameters of pule train shown in Figure 4.24. The simulation results show that s_1 could be detected with an average accuracy of approximately 6%. The

ePIE algorithm could diagnose nonuniform pulse spacing in a wide range of TOD which is sufficient for use of pulse train measurement in a real MP-LWFA experiment.

To understand the effect of background noise on the accuracy of the retrieved s_1, one simulation considered a range of Gaussian noise from 10 dB to 90 dB for three pulse trains with T_m = 150, 200, and 250 fs. The RMS errors of retrieved s_1 for values of TOD, -60×10^3, 0 and 60×10^3 fs^3, were calculated to represent the influence of noise on the accuracy of retrieved s_1.

Figure 4.25b shows that the lower the background noise, the better the RMS error. However, the RMS error did not effectively decrease when the SNR increased

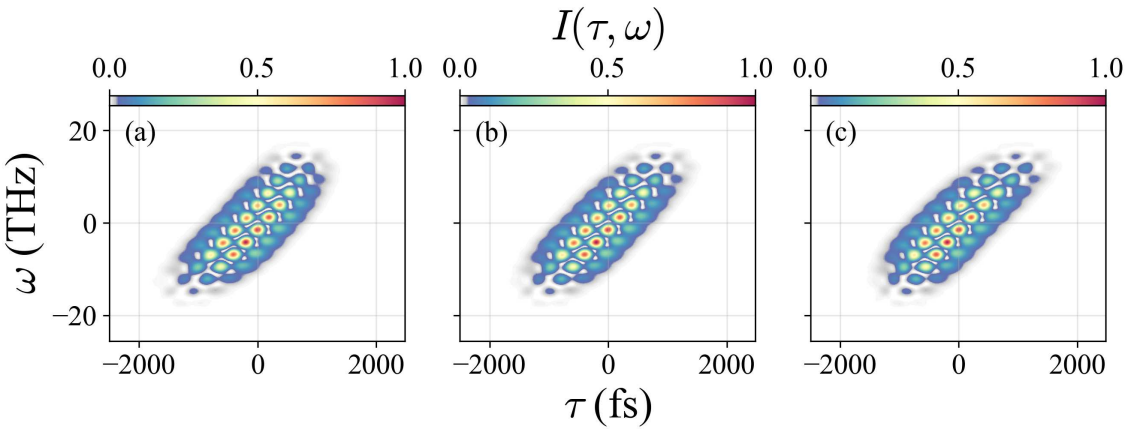


Figure 4.24: FROG traces influenced by GDD = 11,570 fs^2 and TOD. (a) TOD = -35×10^3 fs^3. (b) TOD = 0 fs^3 (c) TOD = 35×10^3 fs^3

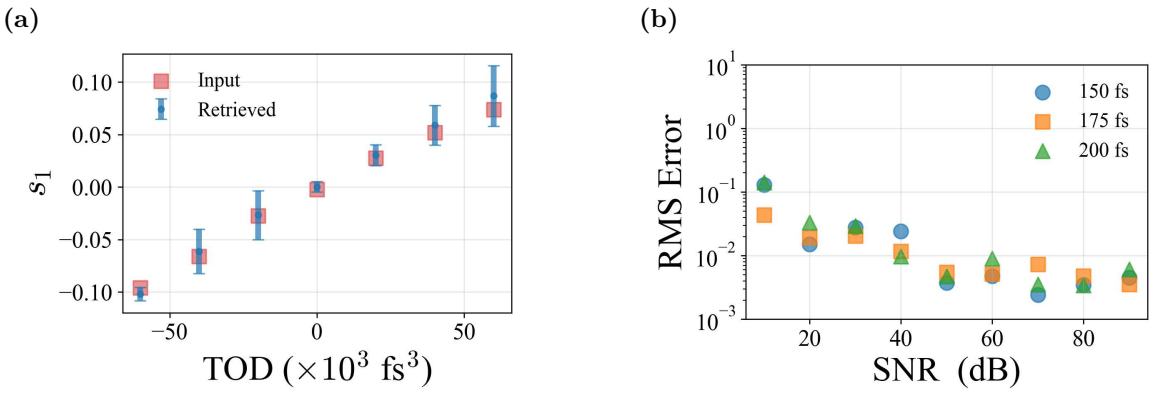


Figure 4.25: (a) s_1 versus TOD for pulse trains with T_m = 200 and N_p = 10. The red squares and blue dots represent the input and retrieved data. The error bar represents one standard error. (b) RMS error versus SNR of Gaussian noise for pulse trains with T_m = 150, 200, and 250 fs. The blue circles, orange squares and green triangles represent results for T_m = 150, 200, and 250 fs.

to above 50 dB. This implies that a Gaussian background noise with an SNR as low as 50 dB was generally sufficient for the ePIE algorithm to retrieve the non-uniform pulse spacing in pulse trains.

Based on the simulation results discussed in this section, it can be concluded that the ePIE algorithm could measure the nonuniform pulse spacing of pulse trains accurately. The ePIE algorithm could diagnose s_1 in pulse trains with $T_m = 200$ fs and TOD ranging from -60×10^3 to 60×10^3 fs^3. The accuracy of the retrieved s_1 with no influence of noise was approximately 6%. However, the Gaussian background noise could affect the accuracy of the retrieved s_1. It was found that an SNR of 50 dB would be required to allow the ePIE algorithm to retrieve accurate values of s_1. SNRs larger than 50 dB did not provide an effective reduction of the RMS error for the retrieved s_1.

4.4 Optical systems

4.4.1 Phase-matching angles and temporal window sizes

Pulse trains have unique features, such as fine structures on the fs-scale and $\Delta\tau_{\mathrm{rms}}$ of entire pulse trains on the ps-scale. The fine structures need to be fully characterised so that the pulse spacing between each pulse in a pulse train can be accurately measured. The entire ps-long pulse train also needs to be covered by a time delay range of a few ps that is supported by the nonlinear crystal. This section is aimed at providing information to assist in the selection of the correct crystal for the design of a single-shot SHG FROG device for the pulse train measurement.

The phase-matching conditions discussed in Section 3.3.4 can be achieved by sending input pulses into nonlinear crystals at certain phase-matching angles. The first question is what the crystal cut-angle, θ_{cut}, should be for the phase-matched SHG signal. The second question is how the phase-matching angle, θ_{p}, affects the available size of the temporal window for the single-shot FROG.

Four commonly-used nonlinear crystals were investigated in this simulation work: beta barium borate (BBO), potassium dideuterium phosphate (KDP), lithium iodate ($LiIO_3$) and lithium triborate (LBO). Their optical properties can be found in [208, 209]. It was assumed that the centre wavelength of the input pulse, λ_0, was at 800

nm and hence the wavelength of the SHG pulse was centred at 400 nm. The refractive indices n_o and n_e for each crystal were those given in [208, 209]. The polarisation of the input pulses that crossed at θ_{in} was set to be vertical to the plane of incidence. Using Equation (3.51), θ_p was obtained.

Figures 4.26a and 4.26b show the results of the simulated θ_p for the four nonlinear crystals with respect to θ_{cut}. All four crystals had crystal cut angles that could support the generation of an SHG signal of the input beams. BBO had a widest θ_p for a wide range of θ_{cut} from 30° to 90°.

Using Equation (3.54), the available size of the time delay window, Δt_d, supported by the crystals was calculated. It was assumed that the effective aperture of each crystal was 1 cm. Figure 4.29 shows Δt_d given by θ_{cut}. All of the crystals had θ_{cut} that could support a range of time delays at least 10 ps. Among these crystals, BBO had the widest available temporal window, which was above 20 ps when θ_{cut} was larger than 80 degrees.

In conclusion, there are at least four types of nonlinear optical crystals that could be adopted in a single-shot SHG FROG device. θ_p was calculated with respect to different values of θ_{cut}. Among the crystals examined in this section, BBO could provide the widest available temporal time delay window. Hence, BBO was an appropriate nonlinear crystal for use in a single-shot FROG device for the pulse train measurement.

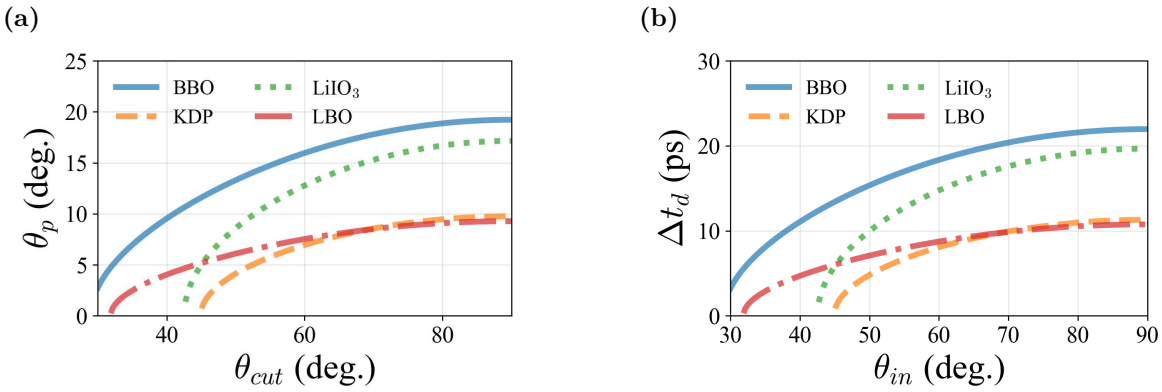


Figure 4.26: (a) θ_p versus θ_{cut}. The blue, green, orange and red curves represent θ_p of BBO, KDP, $LiIO_3$ and LBO, respectively. (b) Δt_d versus θ_{cut}. The coloured curves are defined in (a).

4.4.2 Phase-matching bandwidths and spectral window sizes

According to the Fourier transform theorem, the formation of fine structures ($\sim$ fs) in a pulse train requires a pulse with a wide spectrum ($\sim$ 30 nm). Therefore, it is also important to understand the available spectral window size that can be supported by the nonlinear crystals discussed in Section 4.4.1.

Equations (3.46) and (3.49) were used to estimate the available spectral window size, $\Delta\Lambda$. In this simulation work, θ_{in} ranged from 0° to 20°, and λ_{in} ranged from 700 to 900 nm. To compare the phase-matching bandwidth, $\Delta\Lambda$, nonlinear crystals with θ_{cut} of 60°, and a thickness, L_c, of 100 µm were used.

Figure 4.27 shows $\eta_{\text{SHG}}(\lambda, \theta_p)$ for the nonlinear crystals, BBO, $LiIO_3$, KDP, and LBO. The four efficiency curves had different efficiency distribution and bending curvatures. The red dashed lines locate θ_p for each crystal in $\Delta k = 0$. $\eta_{\text{SHG}}(\lambda, \theta_p)$ plotted along these lines was used to examine $\Delta\Lambda$.

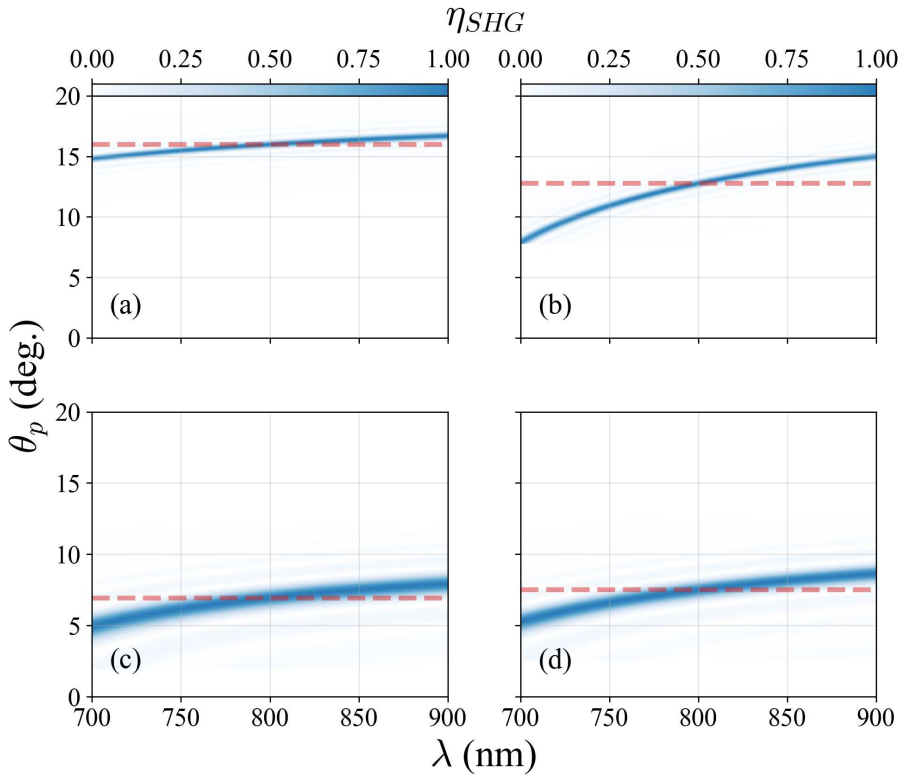


Figure 4.27: $\eta_{\text{SHG}}(\lambda, \theta_p)$ of four nonlinear crystals. The red dashed lines show θ_{in} for $\Delta k = 0$ at $\lambda_0 = 800$ nm. (a) BBO (b) $LiIO_3$ (c) KDP (d) LBO.

Figure 4.28 shows η_{SHG} versus λ in θ_p. For $\theta_p = 60°$ and $L_c = 100$ μm, $LiIO_3$ and KDP provided the narrowest and widest $\Delta\Lambda$, respectively. Figure 4.29a defines $\Delta\Lambda$, which should be equal to or greater than $\Delta\lambda$ of the input spectrum. The red curve shows a spectrum obtained by multiplying the grey spectrum by the blue-dashed efficiency curve. This curve gives an example of the spectral intensity being slightly clipped. This example indicates that $\Delta\Lambda$ should be large enough so that the SHG efficiency does not vary significantly across the bandwidth of the input pulse. Hence, this study suggested that a FROG device should choose a nonlinear crystal having $\Delta\Lambda \geq 1.5\Delta\lambda$ for the pulse train measurement.

Figure 4.29b shows the variation of $\Delta\Lambda$ with L_c ranging from 50 to 400 μm. As predicted by Equation (3.46), $\Delta\Lambda$ decreased exponentially as the thickness of the four crystals increased. Based on $\Delta\lambda$ of the input spectrum, located by the solid red line, the L_c of the crystals should be less than 100 μm for BBO, KDP and LBO. In contrast to $LiIO_3$, this crystal had to be thinner than 50 μm for its $\Delta\Lambda$ wide enough for the pulse train measurement.

Another important factor that affects the measurement of pulse trains is the uncertainty of θ_{p}. Due to the imperfect alignment of the two crossing input beams in a single-shot SHG FROG device, θ_{p} might not be exactly equal to the value predicted by the theory.

Figure 4.30a shows η_{SHG} in which θ_{p} was changed by $\pm 1°$, indicating η_{SHG} dropped to zero quickly when θ_{p} was not achieved. To quantify this effect, the power of the SHG spectrum multiplied by the phase-matching curves at different angles was calculated.

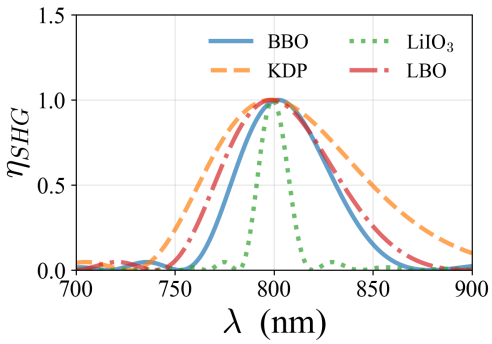


Figure 4.28: η_{SHG} versus λ at θ_{p} in $\theta_{\mathrm{cut}} = 60°$ and $L_s = 100$μm.

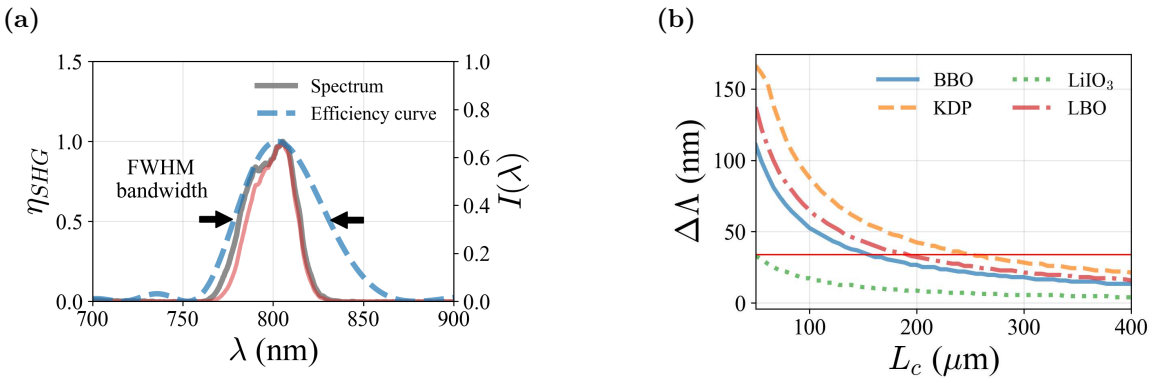


Figure 4.29: (a) Illustration of insufficiently wide $\Delta\Lambda$. The dashed blue curve shows $\eta_{\mathrm{SHG}}(\lambda)$. The solid grey line shows the spectrum of the input pulse. The solid red line shows the spectral intensity of the grey curve multiplied by the blue-dashed curve. (b) $\Delta\Lambda$ versus L_c. The solid red line shows $\Delta\lambda$ of the Gemini spectrum.

Figure 4.30b shows the normalised power of the SHG spectrum varying with θ_{p}. Different nonlinear crystals showed different tolerances for $\Delta k \neq 0$ caused by the variation of θ_{p}. To maintain the power of the SHG spectrum above 90% of its value when $\Delta k = 0$, the normalised power should be higher than the level marked by the black dashed line in Figure 4.30b. Therefore, the deviation of θ_{p} had to be smaller than $\pm 0.1°$ so that the output of the SH spectrum was not seriously distorted or weakened.

In conclusion, $\eta_{\mathrm{SHG}}(\lambda, \theta_p)$ gives a better understanding of the influence of L_c and the deviation of θ_{p}. A proper L_c that can be supported by the four crystals was found to be

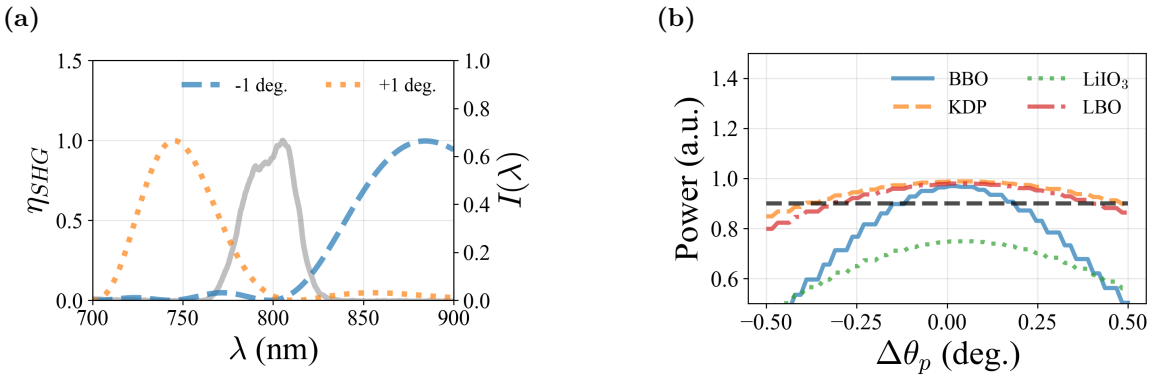


Figure 4.30: (a) Phase-matching curves at which the phase-matching angles are shifted by 1° (dotted orange curve) and −1° (dashed blue curve). The grey curve is the input spectrum. (b) Normalised power of the SHG spectrum versus deviation of phase-matching angle. The dashed black line indicates a power of 0.9. The thickness of the crystals and cut angle were 50 μm and 60° in this simulation.

100 μm. Among the four crystals, KDP could provide the widest $\Delta\Lambda$. Furthermore, the tolerance of deviation in θ_{p} was found to be below $\pm 0.1^{\circ}$ for all four crystals. Based on the discussion in Section 4.4.1, the author considered the balance between Δt_d and $\Delta\Lambda$ of these crystals and finally chose a commercially available BBO nonlinear crystal with $D = 10$ mm, $\theta_{\mathrm{cut}} = 44.3^{\circ}$, and $L_c = 100$ μm to support the pulse train measurement.

4.4.3 Temporal and spectral resolution of FROG traces

This section discusses the required temporal and spectral resolution and grid sizes of FROG traces for the pulse train measurement.

Based on the discussion in the book by Trebino [210], the ratio of the intensity at the edge of the FROG trace grid to its maximum intensity should be equal to or less than 10^{-4}. This criterion also implies that the intensity of the convolution and correlation contained in the FROG trace should be equal to or less than 10^{-4} at the edge of the data grid. Empirically, the width of the temporal window, T_{trace}, and the width of the spectral window, F_{trace}, in a FROG trace are related to $\Delta\tau_{\mathrm{rms}}$ and $\Delta\nu_{\mathrm{rms}}$. The relationship is given by

$$T_{\mathrm{trace}} = dtN_{\mathrm{grid}} \approx 5\Delta\tau_{\mathrm{rms}} \tag{4.8}$$

and

$$F_{\mathrm{trace}} = df M_{\mathrm{grid}} \approx 5\Delta\nu_{\mathrm{rms}}, \tag{4.9}$$

where N_{grid} and M_{grid} are the numbers of data points; dt and df are the sample intervals in the time domain and the frequency domain, respectively.

Suppose that the numbers of data points sampled from the temporal domain and spectral domain are identical, which implies $N_{\mathrm{grid}} = M_{\mathrm{grid}}$. Based on the Fourier transform theorem [211], Equation (4.8) can be written as

$$T_{\mathrm{trace}} = dtN_{\mathrm{grid}} = \frac{N_{\mathrm{grid}}}{F_{\mathrm{trace}}} \approx 5\Delta\tau_{\mathrm{rms}}. \tag{4.10}$$

Thus,

$$\begin{aligned} N_{\mathrm{grid}} &\approx 25\Delta\nu_{\mathrm{rms}}\Delta\tau_{\mathrm{rms}} \\ &= 25\mathrm{TBP}. \end{aligned} \tag{4.11}$$

Equation (4.11) gives the number of data points that should be used in both the temporal and spectral domains of a pulse train FROG trace. Following the above discussion, the spectral resolution, δf, required for the pulse train measurement is given by

$$\delta f = \frac{1}{T_{\text{trace}}} \leq \frac{1}{5\Delta\tau_{\text{rms}}}. \tag{4.12}$$

At the same time, the temporal resolution, δt, is given by

$$\delta t = \frac{1}{F_{\text{trace}}} \leq \frac{1}{5\Delta\nu_{\text{rms}}}. \tag{4.13}$$

According to Equations (4.12) and (4.13), δt is generally fixed by $\Delta\nu_{\text{rms}}$ of the input pulse spectrum. In contrast, δf varies with $\Delta\tau_{\text{rms}}$ of a pulse train. Figure 4.31a shows the variation of the required δf with the TBP of pulse trains. For pulse trains that could be used in the MP-LWFA experiments, a TBP of approximately 10 would be of interest. This corresponds to δf of 0.5 nm at 800 nm. Figure 4.31b shows the grid size required to measure complete FROG traces. For pulse trains with a TBP of approximately 10, a grid size of 256×256 was found to be ideal for the phase retrieval algorithm to retrieve pulse trains in the MP-LWFA.

In conclusion, the author chose $T_{\text{trace}} = 5\Delta\tau_{\text{rms}}$ and $F_{\text{trace}} = 5\Delta\nu_{\text{rms}}$ as the criteria for the complete measurement of pulse train FROG traces. These criteria result in a required δf of 0.5 nm at $\lambda_0 = 800$ nm and $N_{\text{grid}} = 256$ for the measurement of pulse trains with TBP $\sim$ 10.

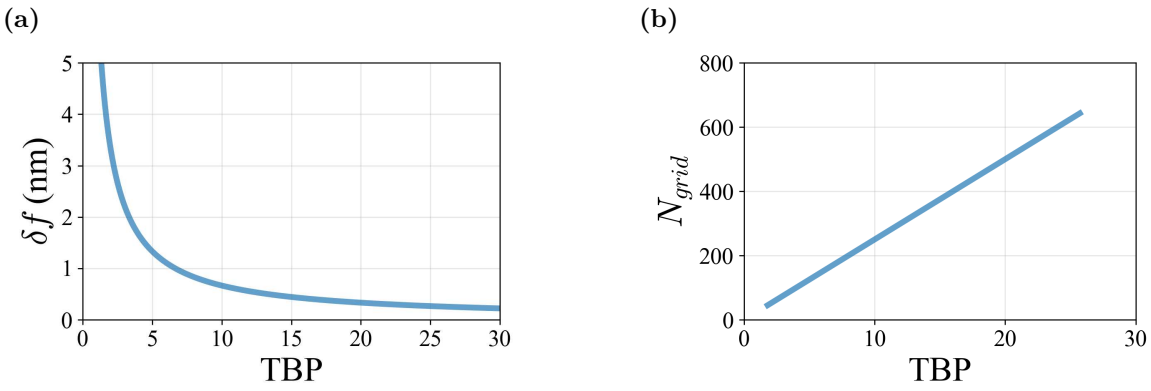


Figure 4.31: Variation of δf and N_{grid} for the pulse train measurement. (a) δf versus TBP. (b) N_{grid} versus TBP.

4.4.4 Design of imaging spectrometers in FROG

This section examines a range of optical components in an imaging spectrometer that could be used to measure complete FROG traces with sufficient temporal and spectral resolution given in Section 4.4.3 for the pulse train measurement.

The BBO crystal selected in Section 4.4.2 was used to in the design work of the imaging spectrometer. The actual range of available time delay provided by this crystal was calculated to be 10 ps considering 90 % of its full aperture. Figure 4.32 shows the variation of TBP with respect to N_p ranging from 5 to 30 for pulse trains with a constant Δt_{rms}. The TBP of pulse trains only slightly changed with a wide range of N_p. This result suggested that a given value of TBP could be used to represent a wide range of pulse trains with different combinations of N_p and T_m.

The selected BBO crystal could support $\Delta\tau_{\mathrm{rms}} = 2$ ps if the criterion of Equation (4.8) was applied. Therefore, the crystal could be used to measure pulse trains with a TBP up to 22. According to the discussion in Section 4.4.3, δf of 0.13/0.25 nm at λ_0 400/800 nm was needed to support a 10-ps time delay window. The required F_{trace} was 62/124 nm at λ_0 of 400/800 nm. Using Equation (4.11), the required N_{grid} was 512. Table 4.3 summarises the temporal and spectral properties of the BBO crystal.

An optical setup was adopted for the design of the imaging spectrometer, as shown in Figure 4.33. An SHG correlation signal contains temporal information along the z-axis and spectral information along the y-axis. The correlation signal was imaged at the entrance of the slit with a width of w_{s}. The collimation lens, $L1$, was used to collect the divergent correlation signal and illuminate the signal on a reflective grating,

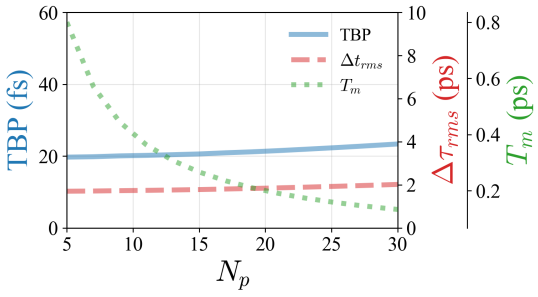


Figure 4.32: TBP versus N_p in pulse trains with a constant Δt_{rms}. The red, blue, and green curves show Δt_{rms}, TBP, and T_m.

Crystal name	BBO
Cut angle	44.3°
Aperture size	10 mm
Thickness	100 µm
Phase-matching bandwidth	50 nm
Delay time range	10 ps
Spectral window size	124 nm at λ_0 = 800 nm
Temporal resolution	19 fs
Spectral resolution	0.25 nm at λ_0 = 800 nm
Grid size	512 × 512
TBP limit	22

Table 4.3: Crystal specification of BBO for the measurement of pulse trains.

G. A focusing lens imaged the correlation signal, which was dispersed in the x-y plane by the grating, onto the sensor, C.

The grating equation used in this design of imaging spectrometer is given by [212]

$$\sin\theta_{\mathrm{d}} = \sin\theta_{\mathrm{i}} + m\frac{\lambda}{\lambda_g}, \tag{4.14}$$

where d is the diffraction angle; θ_{i} is the angle of incidence; m is the diffraction order, λ is the wavelength; and λ_g is the grating period.

Supposing that diffraction of m = -1 was used and the beam geometry followed the

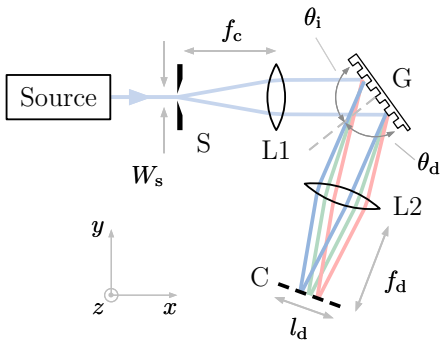


Figure 4.33: Schematic of a grating spectrometer: L—lens; G—grating; S—slit; W_{s}—slit width; C—sensor; l_{d}—width of sensor; f_{c}—focal length of L1; f_{d}—focal length of L2; θ_{i}—angle of incidence; and θ_{d}—diffraction angle.

Littrow configuration (θ_{i} = -θ_{d}), Equation (4.14) becomes

$$\sin\theta_{\mathrm{d}} = -\frac{\lambda}{2\lambda_g}. \tag{4.15}$$

The linear dispersion D_{g} of a grating is given by [213]

$$D_{\mathrm{g}} = \frac{d\lambda}{dl_{\mathrm{d}}} = m\frac{\cos\theta_d}{gf_{\mathrm{d}}}, \tag{4.16}$$

where the groove density is $g = 1/\lambda_g$.

The two lenses shown in Figure 4.33 were able to focus a range of wavelengths, $\Delta\lambda$, on the sensor. Using Equation (4.16) suggested in [214], the focal length, f_{d}, had a relationship with the grating given by

$$f_{\mathrm{d}} = \frac{l_{\mathrm{d}}\cos\theta_{\mathrm{d}}}{g\Delta\lambda}, \tag{4.17}$$

where l_{d} is the sensor size.

Figures 4.34a and 4.34b show θ_{d} and f_{d} varying with g, respectively. Using Equations (4.15) and (4.17) allowed f_{d} to be determined a given range of wavelengths, $\Delta\lambda_d$, imaged on the sensor, where $\Delta\lambda_d$ was the required spectral bandwidth to form a complete FROG trace.

To determine δf given by an imaging spectrometer in this design, the diffraction limit, r, based on the Rayleigh criterion was used, which is given by

$$r = 0.61\frac{\lambda_0}{\mathrm{NA}}, \tag{4.18}$$

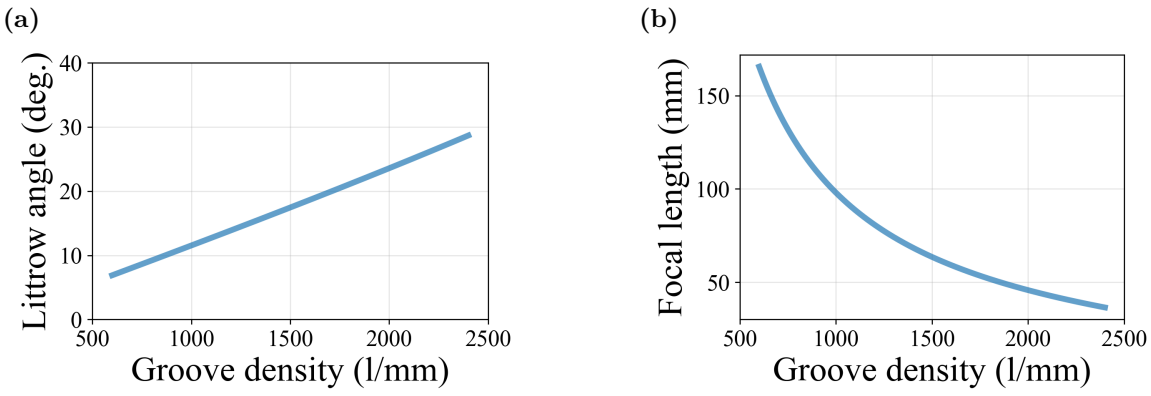


Figure 4.34: (a) Littrow angle versus groove density for m = −1. (b) Focal length versus groove density for m = −1, $\Delta\lambda$ = 100nm and l_{d} = 10 mm.

where NA $= \sin\theta_{\mathrm{NA}}$; and λ_0 is the centre wavelength of illumination.

Therefore, the ideal spectral resolution, $d\lambda$, provided by the imaging spectrometer is given by

$$d\lambda = D_{\mathrm{g}} r = 0.61 m \frac{\lambda_0 \cos\theta_d}{\sin\theta_{\mathrm{NA}} g f_{\mathrm{d}}}. \tag{4.19}$$

Assuming that the imaging system used in the imaging spectrometer has a 1X magnification, the Littrow configuration is adopted, and l_{d} is 7.1 mm, the spectral range is found to be 62 nm at $\lambda_0 = 400$ nm. Table 4.4 summarises the specification of the imaging spectrometer for diffraction gratings with different groove densities.

In conclusion, the BBO crystal used in Section 4.4.2 could support the measurement of pulse trains with TBP up to 22, a time delay range of 10 ps, and a spectral window of 62 nm. To achieve correct pulse train measurement, the required δt and δf were 19 fs and 0.13 nm, respectively. Based on this information, gratings with g of 1200 and 1800 l/mm were the best choices for use in a single-shot SHG FROG device for the pulse train measurement.

Groove density (l/mm)	600	1200	1800	2400
Diffraction order	-1	-1	-1	-1
Litrrow angle (deg.)	6.9	13.9	21.1	28.7
Focal length l_{d} (mm)	226	110	71	50
Spatial resolution l_{d} (μm)	8	4	3	2
Dispersion (nm/mm)	7.3	7.3	7.3	7.3
Spectral resolution (nm) at $\lambda_0 = 400$ nm	0.06	0.03	0.02	0.01
Spectral range (nm) at $\lambda_0 = 400$ nm	62	62	62	62
Temporal resolution (fs)	8.67	4.23	2.7	1.9
Temporal range (ps)	8	8	8	8

Table 4.4: Specification of imaging spectrometer for diffraction gratings with different groove densities.

4.5 Conclusions

In conclusion, the author has presented and discussed different simulations to support the implementation of a pulse train measurement device.

Section 4.2 demonstrated the reliability of the pulse train model and provided appropriate strategies to adjust the T_m and N_p of pulse trains in a real experiment. In addition, the author showed that the implementation of the pulse train generation technique in a real experiment would produce non-uniform pulse spacing in pulse trains, caused by ψ_3. It was found that potential non-uniform pulse spacing for a pulse train with $T_m = 200$ fs and $N_p = 10$ from the optical system would reduce the peak amplitude of the plasma wakefield by approximately 36%. Finally, the systematic errors in the optical system were studied. They would produce an uncertainty of up to 14 fs in a pulse train with $T_m = 250$ fs. This uncertainty could be compensated for by adjusting n_0 in a real experiment.

Section 4.3 presented an investigation of appropriate phase retrieval algorithms showing that the ePIE algorithm was suitable for the pulse trains measurement. A proper bandwidth of the bandpass filter smaller than 10 nm was found to be appropriate for removing the time direction ambiguity and revealing direct spectral phase information. Third, the simulation results showed that an SNR higher than 40 dB was sufficient for measuring pulse trains. This result suggested using a 12-bit camera, which has a capacity to provide a dynamic range of 43-dB, to measure FROG traces. Finally, the ePIE algorithm could be used to diagnose non-uniform pulse spacing with an accuracy of approximately 6% for pulse trains with $T_m = 200$ fs and $N_p = 10$.

Section 4.4 presented the study of the phase-matching angle and bandwidth supported by the nonlinear crystals. Based on the simulation results, the author selected a BBO crystal with $\theta_{\text{cut}} = 44.3°$, $L_c = 100$ μm and $D = 10$ mm for measuring pulse trains with TBP up to 22. Additionally, the author chose gratings with $g = 1200$ or 1800 l/mm in the imaging spectrometer of an FROG device to support the pulse train measurement with a sufficient spectral resolution.

Every careful measurement in science is always given with the probable error, which is a technical term, conveying a precise meaning. It means: that amount of error which is just as likely to be greater than the actual error as to be less.

— Bertrand Russell, British mathematician, 1872 -1970 [215]

5 Implementation of multi-pulse train characterisation

Contents

5.1 Introduction 103
5.2 Development of a single-shot FROG device 103
5.2.1 Design of the single-shot FROG device 103
5.2.2 Specification of the single-shot FROG device 106
5.3 Measurement of multi-pulse trains in OPAL 112
5.3.1 Experimental setup 112
5.3.2 Data analysis procedure 113
5.3.3 Pulse measurement results 118
5.3.4 Diagnosis of nonuniform pulse spacing 124
5.4 Measurement of multi-pulse trains in Gemini TA3 125
5.4.1 Introduction 125
5.4.2 Experimental setup 127
5.4.3 Procedure of pulse retrieval and data analysis 132
5.4.4 Pulse measurement results 134
5.5 Conclusions 138

5.1 Introduction

This chapter aims to present the experimental demonstration of a single-shot FROG device developed for the pulse train measurement in MP-LWFA. The author demonstrates (i) the specification of the single-shot FROG device, (ii) the ability of the device to measure pulse trains and diagnose nonuniform pulse spacing in the Oxford Plasma Accelerator Laboratory (OPAL), and (iii) the measurement of pulse trains used for a novel electron injection concept in Gemini TA3.

This chapter is organised as follows. Section 5.2 presents the design and experimental setup of the single-shot FROG device developed in OPAL. The procedure for obtaining a FROG device specification of is discussed. Section 5.3 describes an experiment conducted in OPAL for experimental demonstration of pulse train measurement. Section 5.4 discusses an experiment conducted in Gemini TA3 to demonstrate a novel electron injection mechanism using pulse trains.

5.2 Development of a single-shot FROG device

5.2.1 Design of the single-shot FROG device

According to the study discussed in Sections 4.3 and 4.4, a single-shot FROG device for measuring pulse trains has several important optical components: nonlinear optical crystal, a bandpass filter, an imaging system, two line-array spectrometers, and an imaging spectrometer.

The functions of these components are summarised as follows. The nonlinear crystal generates the SHG correlation signal of the input multi-pulse trains. The bandpass filter spectrally filters one of the crossing beams to break the symmetry of SHG FROG traces. The imaging system images the SHG correlation signal onto the entrance slit of the imaging spectrometer. The SHG correlation signal is spectrally resolved by the imaging spectrometer. Finally, a scientific camera records the blind FROG traces in the imaging spectrometer.

Figure 5.1 shows an optical layout of an 800-nm FROG device with a single-shot beam geometry used for the pulse train measurement. The input pulse enters this device

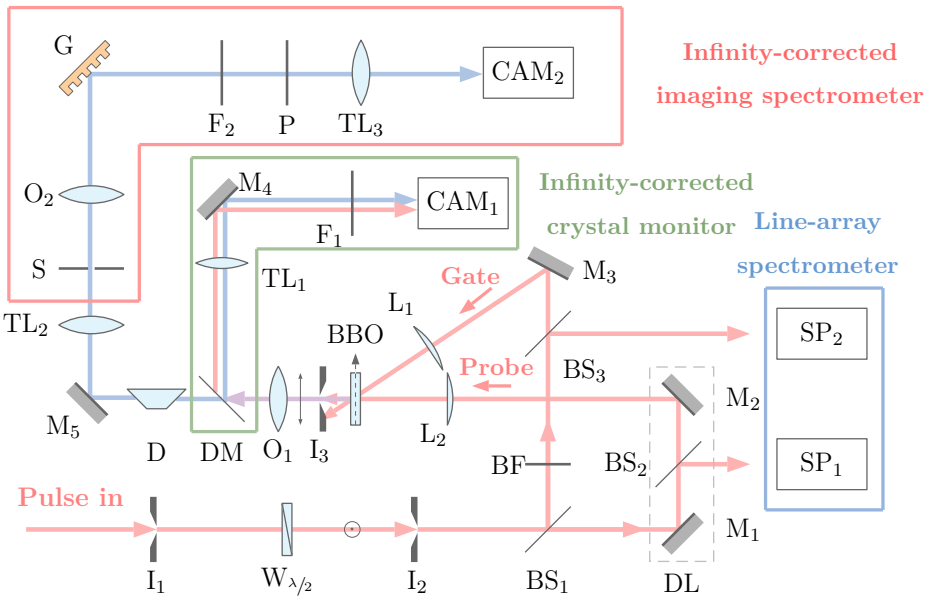


Figure 5.1: Optical layout of a single-shot FROG device. I—iris; $W_{\lambda/2}$—waveplate; L—lens; BS_n—beam splitter; DL—delay stage; M_n—mirror; SP_n—spectrometer; BF—bandpass filter; L_n—lens; P—beam block; O_n—microscope objective; DM—dichroic mirror; D—dove prism; TL_n—tube lens; S—slit; G—grating; F—low pass filter; P—polariser; and CAM_n—camera.

at the entrance at the bottom left corner. The input pulse passes through two irises, I_1 and I_2, used for the beam alignment. Between these two irises, a 0.5-inch half waveplate, $W_{\lambda/2}$, with $\lambda_0 = 800$ nm rotates the polarisation of the input beam if needed. Several 1-inch silver mirrors M_{1-5} guide the input beam through the entire beam path.

A 2-inch ultrafast beamsplitter (20RQ00UB.4, Newport), BS_1 , splits the input pulse into two pulse replicas. One pulse passes through the bandpass filter (FBH780-10, Thorlabs), BF, with a $\Delta\lambda$ of 10 nm centred at $\lambda_0 = 780$ nm. The BF is used to spectrally filter the crossing beam for the generation of blind FROG traces. The other pulse enters the delay stage DL which is used to adjust τ between the two pulse replicas.

Two line-array spectrometers (USB2000, Ocean Optics), SP_1 and SP_2, record the spectra of the two input pulse replicas. Two plate beamsplitters, BS_2 and BS_3, extract a small amount of energy from the two input beams and send it to the SP_1 and SP_2.

The two crossing beams separated by BS_1 are focused on a BBO crystal with plano-convex cylindrical lenses (f = 75 mm, AR-coated, LJ1703RM-B, Thorlabs), L_1 and L_2. The nonlinear crystal is a type-I BBO crystal made by Eksma Optics. It had a crystal cut angle θ_{cut} =44.3°, The thickness L = 100 µm, and the aperture D = 10 mm. An

s-polarised non-collinear beam geometry with an external crossing angle, $\theta = 37.84°$ at $\lambda_0 = 790$ nm, can satisfy the phase matching conditions.

A theoretical delay time window supported by the crystal was calculated as 12.67 ps at $\lambda_0 = 790$ nm across the entire crystal aperture. This time window size could support pulses with Δt_{rms} of 2 ps. The spectral resolution required to resolve such long pulses was estimated at about 0.17 nm at $\lambda_0 = 400$ nm.

An infinite-corrected optical system images the crystal at the entrance slit of the imaging spectrometer to achieve a high spectral resolution. The imaging system consists of microscope objective (Mag. = 2, TL2X-SAP, Thorlabs), O_1, tube lens (f = 200 mm, TTL200-A, Thorlabs), TL_1, and tube lens (f = 100 mm, TTL100-A, Thorlabs), TL_2. A Dove prism, D (D = 5 mm, PS990M, Thorlabs) rotates the image of the crystal to simplify the beam alignment. The detector (Mako 503-B, Allied Vision), CAM_1, monitors the image of the BBO crystal to assist in aligning the two crossing beams focused on the crystal.

An imaging spectrometer consists of microscope objective (Mag. = 2, EO M Plan Apo, Edmund Optics), O_2, tube lens (TTL100-A, f=100mm, Thorlabs), TL_3, and 2-inch reflective grating (1200 l/mm, $\theta_{\text{blaze}} = 400$ nm, No. 41-043, Edmund Optics), G, to resolve the spectral information of the SFG correlation signal. In this imaging spectrometer, a 1-inch short-pass filter ($\lambda_{\text{cut}} = 475$ nm, OD = 4, No. 84-705, Edmund Optics) can filter out unwanted high-frequency components. A 1-inch wire grid linear polariser (WP25M-VIS, Thorlabs) filters out the random polarisation of scattered blue light from the BBO crystal. The detector (Manta 507-B, Allied Vision), CAM_2, records blind FROG traces. Although this design has a single shot beam geometry, no trigger system was present for data acquisition in this device because of the experimental time limitation.

Following the above description, Figure 5.2 shows the experimental setup of the single-shot FROG device for the pulse train measurements in OPAL.

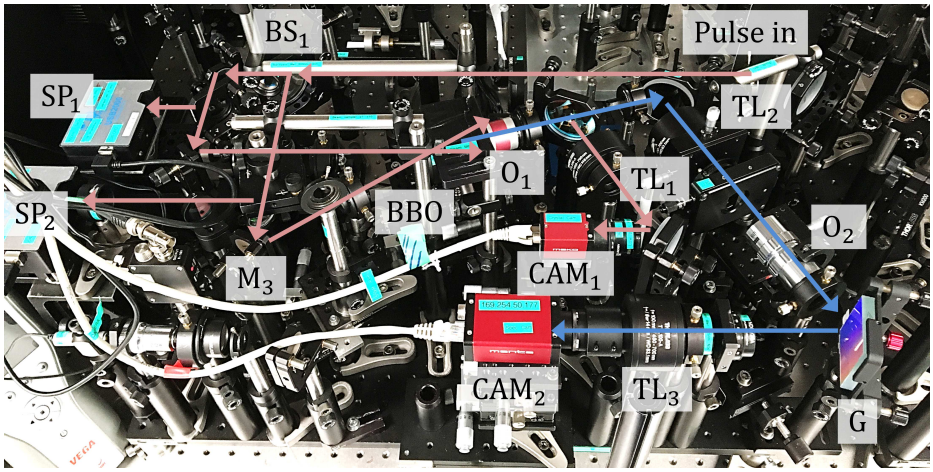


Figure 5.2: Experimental setup of the 800-nm FROG device. The definitions of labels follow those given in the caption to Figure 5.1. The red and blue arrows represent the input beam and SHG beam, respectively. The scale of this pulse measurement setp is 30×60 cm^2 (width-by-length). Because of the space constraint, only a few optical components are labelled in this picture.

5.2.2 Specification of the single-shot FROG device

Spatial resolution

To test the spatial resolution of the imaging system, R_s, in the FROG device shown in Figure 5.2, a resolution target (1951 USAF, Thorlabs) was used in an optical testing experiment. The resolution target was placed at the location of the BBO crystal and imaged on the sensor in CAM_2. The light source was a blue laser diode ($\lambda_0 = 405$ nm, CPS405, Thorlabs). Figure 5.3a displays the image of the resolution target. Because this image was the first-order diffraction of the resolution target dispersed along the vertical axis, the edges of patterns were blurred at the top and bottom parts. Groups 5 and 6 patterns were selected as the region of interest (ROI). Figure 5.3b shows the lineouts of these patterns along the horizontal axis. While the lineouts of Group 5 elements showed clear sharp peaks, those of Group 6 were not resolved except for Element 1.

To evaluate the actual resolution of the imaging system, the contrast of the image is defined by

$$\text{contrast} = \frac{I_{\max} - I_{\min}}{I_{\max} + I_{\min}} \times 100\%, \tag{5.1}$$

where $I_{\max}$ is the local maximum intensity, and $I_{\min}$ is the local minimum intensity.

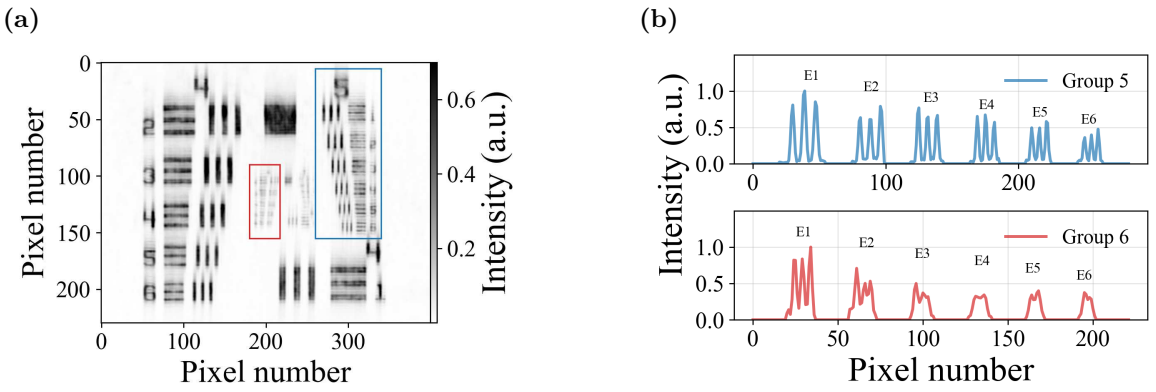


Figure 5.3: Resolution testing result (a) Image of the USAF target. The blue rectangles show the regions of interest (ROI). (b) Lineouts of the elements in Groups 5 and 6 of the USAF targets shown in (a). The lineouts show the average values of data.

The definition in Equation (5.1) is visualised in Figure 5.4a. The spatial resolution, R_s, is defined by the distance between the two local peaks for a given lineout of an element. Figure5.4b shows the measured contrast and resolution of different elements in Groups 5 and 6 using the specification of the resolution target provided by the supplier [216]. In this thesis, R_s of the smallest element with a contrast greater than 50% was regarded as the actual resolution of the FROG device. Therefore, the R_s of the single-shot FROG device was (15.6 ± 0.1) μm at λ_0 = 405 nm, and the spatial calibration, dl/dp, was calculated to be 3.2 μm/pixel.

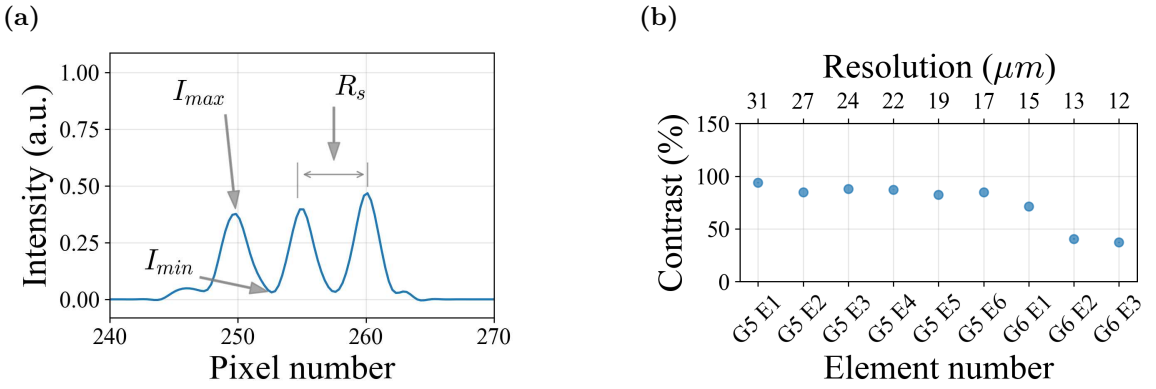


Figure 5.4: (a) Definition of the spatial resolution R_s (b) Optical contrast versus the group element in the resolution target. G: group. E: element. The data points show average values of data points.

Spectral resolution

To examine the spectral resolution of the FROG device, R_λ, a spectral calibration lamp (6035 mercury-argon lamp) [217] was placed in front of the entrance of a mechanically adjustable slit (10AOS10-1, Standa) which controlled the width of the illumination. Following the procedures described in the book by Neumann [218], the image of the spectral lines in the ultraviolet (UV) light range was as shown in Figure 5.5a. Referring to the spectral calibration spectrum of the mercury-argon lamp provided by Oriel Instrument [217], the two spectra lines at $\lambda_0 = 406.66$ and 435.84 nm were identified. The spectral range, $\Delta\lambda_s$, supported by the CMOS camera was 59 nm, assuming that the variation in the wavelength with respect to the pixel number was linear. This corresponded to a spectral calibration, $d\lambda/dp$, of 0.024 nm/pixel.

The FWHM spectral bandwidth was regarded as the actual R_λ, following the conventional definition given in [218]. The spectral line width at $\lambda_0 = 406.66$ nm is shown in Figure 5.5b. The calculated line width was 4.1 pixels, corresponding to a spectral resolution of (0.096 ± 0.005) nm at $\lambda_0 = 406.66$ nm. Since the smallest available slit width was approximately 15 µm, R_λ could not be further examined or reduced. Therefore, the actual R_λ of the FROG device was considered (0.10 ± 0.01) nm at $\lambda_0 = 407$ nm.

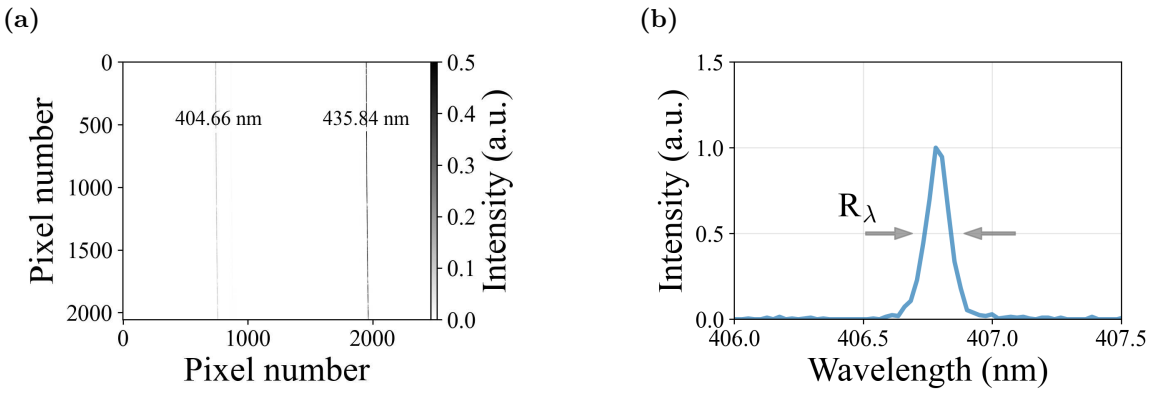


Figure 5.5: Spectral lines and FWHM spectral bandwidth(a)Image of the spectral lines at $\lambda = 406.66$ and 435.84 nm. (b) FWHM spectral bandwidth at $\lambda = 406.66$ nm. The lineout shows an average value of the spectral peak.

Temporal calibration

To calculate the temporal resolution, R_t, and the temporal range, ΔT_s, a series of SHG-SSA at different time delays, τ_{d}, was measured. Laser pulses with $\Delta t_{\mathrm{rms}} = 50$ fs and $\lambda_0 = 790$ nm were generated from a Ti:sa laser amplifier (Spitfire Pro, Spectra Physics). The laser pulses were sent to the FROG device to generate the SHG-SSA signal in the BBO crystal. The signal was imaged on the CMOS sensor in a camera (Manta-507B, Allied Vision). Figure 5.6a the recorded SSA signal at different time delays.

Since the relative positions of the delay stage were related to τ_{d} of the SSA signal represented by those coloured curves in Figure 5.6a, the temporal calibration, $d\tau_{\mathrm{d}}/dp$,for this FROG device was calculated from

$$\tau_{\mathrm{d}} = 2\frac{\Delta L_{\mathrm{d}}}{c}, \tag{5.2}$$

where τ_{d} is the time delay; ΔL_{d} is the displacement of the delay stage; and c is the speed of light.

A Python curve-fitting routine using the 3$^{\mathrm{rd}}$-polynomial function was applied to find the best fit of the raw data points represented by the peaks of the SSA signal at each τ_{d}. The temporal calibration curve is shown in Figure 5.6b, and the R^2 of the curve fit was 0.9999. According to the calculation, the corresponding $d\tau_{\mathrm{d}}/dp$ for the image was 8 fs/pixel, and ΔT_s supported by the BBO crystal was 9 ps. Therefore, the smallest R_t was (36 $\pm$ 3.2) fs using the smallest R_s available for this FROG device.

Spectral calibration

During the experiment, the imaging system in the FROG device needed optimisation to have the optimal SNR, R_t and R_λ. Using the calibration lamp was not a proper way to implement the spectral calibration of FROG traces because only two or three spectral lines were present at around 400 nm. Therefore, Trebino [219] suggested using the auto-convolution signal of input pulses ($\Delta\lambda \sim 30$ nm) to assist in calculating $d\lambda/dp$.

Another experiment was conducted to measure a series of auto-convolution signals for the spectral calibration of the FROG device. First, a FROG trace of two collinearly propagating pulses was measured, as shown in Figure 5.7a. The time delay, τ_n, between

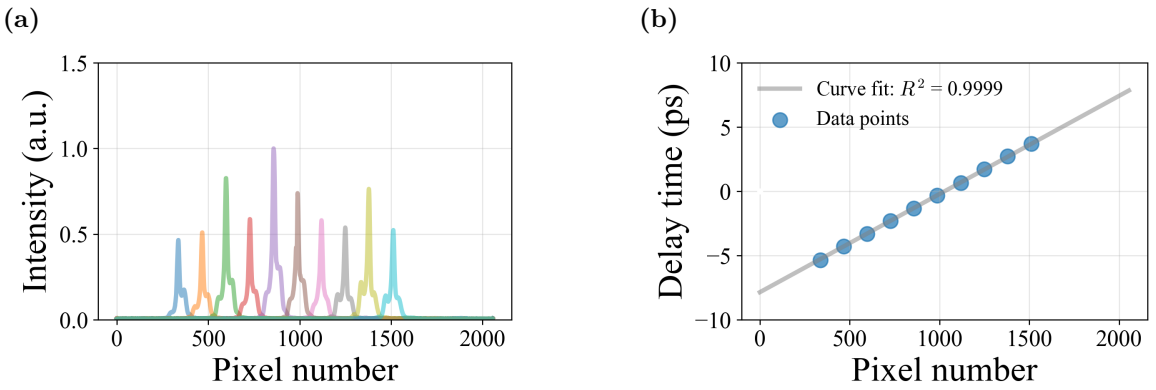


Figure 5.6: (a) SSA signal versus pixel number. The coloured curves show the SSA signal at different time delays. (b) The positions of the peaks in (a) versus τ_d calculated from Equation (5.6b). The blue dots and grey line represent the data points and the best fit of the data points, respectively. The error bars are not shown since their scales are smaller than the size of data points.

the two pulses was obtained by calculating the correlation signal along the horizontal axis, where n represents the nth signal. Next, the auto-convolution signal for each τ_n, was obtained and shown in Figure 5.7b by summing up the FROG trace along the horizontal axis in the ROI shown by the red rectangle.

Third, the modulation period within a range of $\Delta\lambda$ was calculated using prior knowledge of τ_n and λ_0 according to Equation (5.3) [219]. To obtain the spectral calibration, $d\lambda/dp$, from Equation (5.3), the modulation period, Δp, was calculated by taking the Fourier transform of the auto-convolution signal and finding the reciprocal

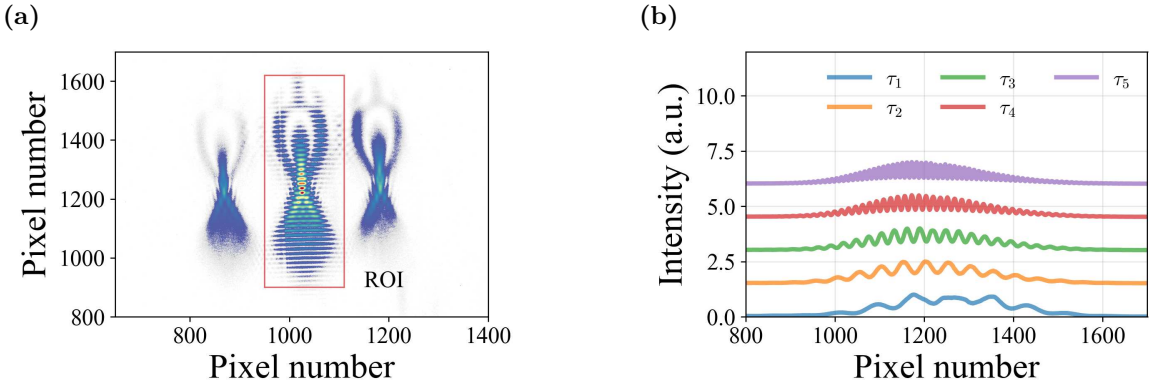


Figure 5.7: FROG trace and auto-convolution signal for the spectral calibration: (a) FROG trace of two collinearly propagating pulses separated by a time delay τ; and (b) Auto-convolution signal at different time delays between two input pulses. Coloured curves show the auto-convolution signal at different time delays τ_n between the two input pulses.

of the frequency as shown in Figure 5.8a.

$$\begin{aligned}\frac{d\lambda}{dp} &= \frac{\Delta\lambda}{\Delta p} \\ &= \frac{{\lambda_0}^2}{4c\Delta t\Delta p},\end{aligned} \tag{5.3}$$

where λ_0 is the centre wavelength of the input pulse, Δt is the time delay between two pulses and Δp is the period of modulation in pixel.

The spectral calibration curve is shown in Figure 5.8b. The R^2 was 1.0000. Using Equation (5.3), the spectral calibration was 0.028 nm/pixel. According to this result, the spectral window supported by the FROG device was (70 ± 1) nm by taking into account the total number of pixels on the frequency axis.

Specification

Based on the experimental results, the specification of the single-shot FROG device for the pulse train measurements is summarised in Table 5.1.

The FROG device developed in OPAL had the following resolution values: R_s = 15.6 µm, R_t = 36 fs, and R_λ = 0.1 nm. The available ΔT_s and $\Delta\lambda_s$ were 9 ps and 70 nm, respectively. Therefore, the device could support pulse train measurement with $\Delta\tau_{\text{rms}}$ = 1.9 ps and TBP up to 20.

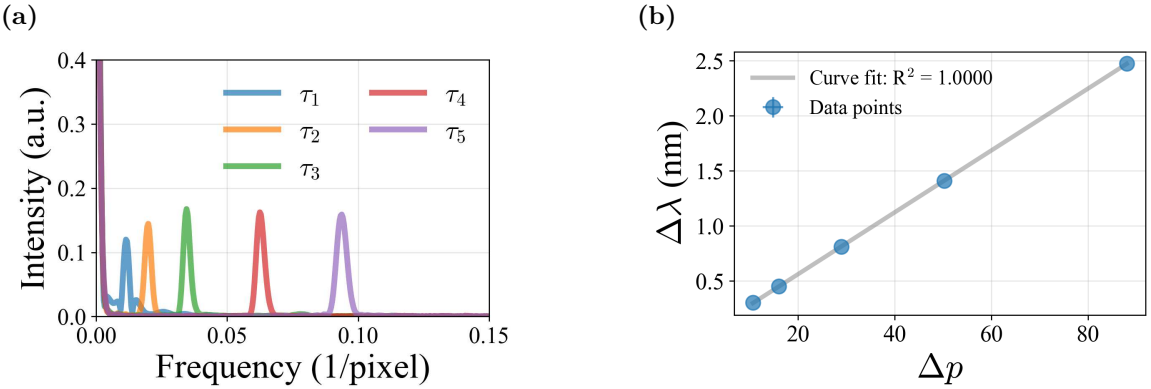


Figure 5.8: (a) Spatial frequency of the auto-convolution signal. Each coloured curve represents the average spectrum of the auto-convolution signal at τ_n. (b) Wavelength separation, $\Delta\lambda$, versus modulation period, Δp. The blue dots and grey line are defined in Figure 5.6b. The error bars are not shown since their scales are smaller than the size of data points.

λ_0	R_s	R_λ	$\Delta\lambda_s$	R_t	ΔT_s	Δt_{rms}	TBP
800 nm	15.6 µm	0.1 nm	70 nm	36 fs	9 ps	1.8 ps	20

Table 5.1: Specification of the 800-nm single-shot SHG FROG.

5.3 Measurement of multi-pulse trains in OPAL

5.3.1 Experimental setup

Figure 5.9 shows a simple layout of the pulse train measurement. Laser pulses with $\Delta\lambda = 55$ nm and $\lambda_0 = 800$ nm were produced in a laser oscillator (Mai Tai, Spectra Physics) and further compressed by an internally prism-pair compressor. These seed pulses with a pulse duration of 30 fs and a repetition rate of 84 MHz were sent to a regenerative amplifier (Spitfire Pro, Spectra Physics) for pulse amplification.

In the laser amplifier, the seed pulses first passed through a Faraday rotator used to prevent the seed pulses with undesired polarisation from being reflected to the oscillator. The seed pulses then entered a two-pass grating stretcher used to stretch the pulses to approximately 100 ps long for the further amplification process. The stretched seed pulses were guided into a Ti-Sapphire laser cavity. In the laser cavity, two Pockels cells were used to control the polarisation of the intra-cavity pulses and the round-trip times of pulses in the laser cavity. The Ti-sapphire laser crystal was pumped by a Nd:YLF pump laser (Evolution-X, Spectra Physics) with an output power of 11 W and a centre wavelength at 527 nm. The amplified pulses with a repetition rate of 1 kHz were guided into a four-pass grating compressor and compressed to pulses with a pulse duration of 50 fs and pulse energy of 3 mJ at the best performance.

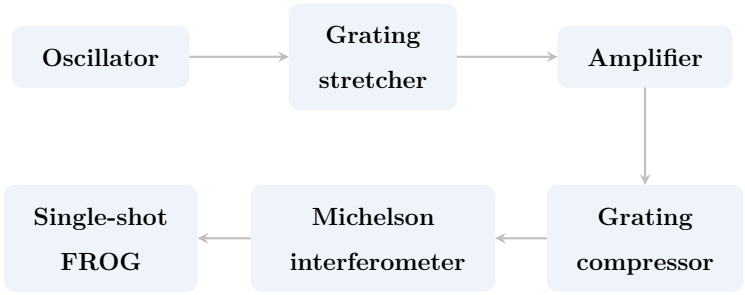


Figure 5.9: Schematic of multi-pulse train measurement.

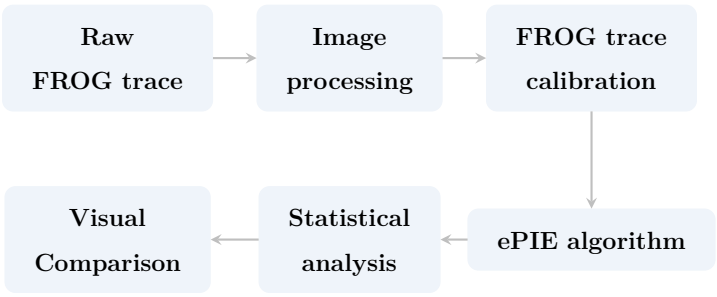


Figure 5.10: Schematic of data analysis procedure for pulse train measurement.

The compressed pulses passed through a Michelson interferometer used to split an input pulse into two pulse replicas by an ultra-fast beamsplitter (20RQ00UB.4, Newport). By moving one of the Michelson arms, the time delay between the two pulse replicas could be adjusted. This Michelson interferometer and the grating compressor inside the regenerative amplifier were used to control τ and ψ_2 of the pulses and produce different pulse trains. The output pulse from the Michelson interferometer was then guided into the single-shot FROG device for pulse characterisation.

5.3.2 Data analysis procedure

All measured FROG traces were retrieved using the ePIE algorithm discussed in Section 3.4.3. The algorithm operated on a Windows 10 laptop (Intel Core i7-8565U CPU @ 1.80GHz, 1992 Mhz, four Cores).

The procedures for analysing FROG trace data are shown in Figure 5.10. First, experimentally measured FROG data traces were stored on a local hard drive. Second, the image processing was completed using the Python programming language. Third, the spectral and temporal axes were calibrated using the correlation and convolution signal contained in the calibration FROG traces as discussed in Section 5.2.2. Fourth, the calibrated FROG traces were input into the PIE algorithm obtain the retrieved FROG traces and amplitudes of the probe and gate pulses. The spectra were obtained by taking the Fourier transform of the retrieved pulse amplitude, followed by statistics calculates of the retrieved results. Finally, the retrieval results were visualised in figures for comparison.

Image processing

The image processing procedure included the edge background subtraction and the application of a median filter to the measured FROG traces. The following context describes the noise removal procedure for the measured FROG traces.

First, the histogram of background noise in the corner of a FROG image was calculated. Figures 5.11a and 5.11b show the histogram of background noise in the corner of a raw FROG trace and an image of a raw FROG trace, respectively. Second, a median filter with a 3×3 kernel size provided by the Python package, Numpy, was applied to the image. The histogram shows that the background noise above 50 counts was removed, as illustrated in Figure 5.11c showing the filtered FROG trace. The last step was subtracting the mean of background noise from the filtered FROG trace. The histogram and final processed FROG trace are shown in Figures 5.11e and 5.11f. It should be noted that the author carefully adjusted the SNR so that each measured FROG trace had lowest possible background noise level in the experiment. Therefore, the example FROG trace shown in Figures 5.11b, 5.11d, and 5.11f did not reveal very noticeable influence of background noise.

FROG trace calibration

Using the calibration procedures discussed in Section 5.2.2, $d\tau_d/dp$ and $d\lambda/dp$ of FROG traces were calculated as (7.66 ± 0.02) and (0.02669 ± 0.0003) nm/pixel, respectively. Figures 5.12a and 5.12b show the temporal and spectral calibration curves, respectively. According to the calibration data, ΔT_s supported by the crystal was approximately 10 ps, and $\Delta\lambda_s$ was approximately 66 nm.

Dispersion calibration in FROG device

In the single-shot FROG device shown in Figure 5.1, several optical components contributed extra dispersion that was not inherent in the input pulse. Their contributions to the dispersion had to be removed. For the following calculation, the centre wavelength of the input pulse was assumed to be at 790 nm. For cylindrical lenses (ACY254-075-B, Thorlabs), two materials were used to form an achromatic doublet:

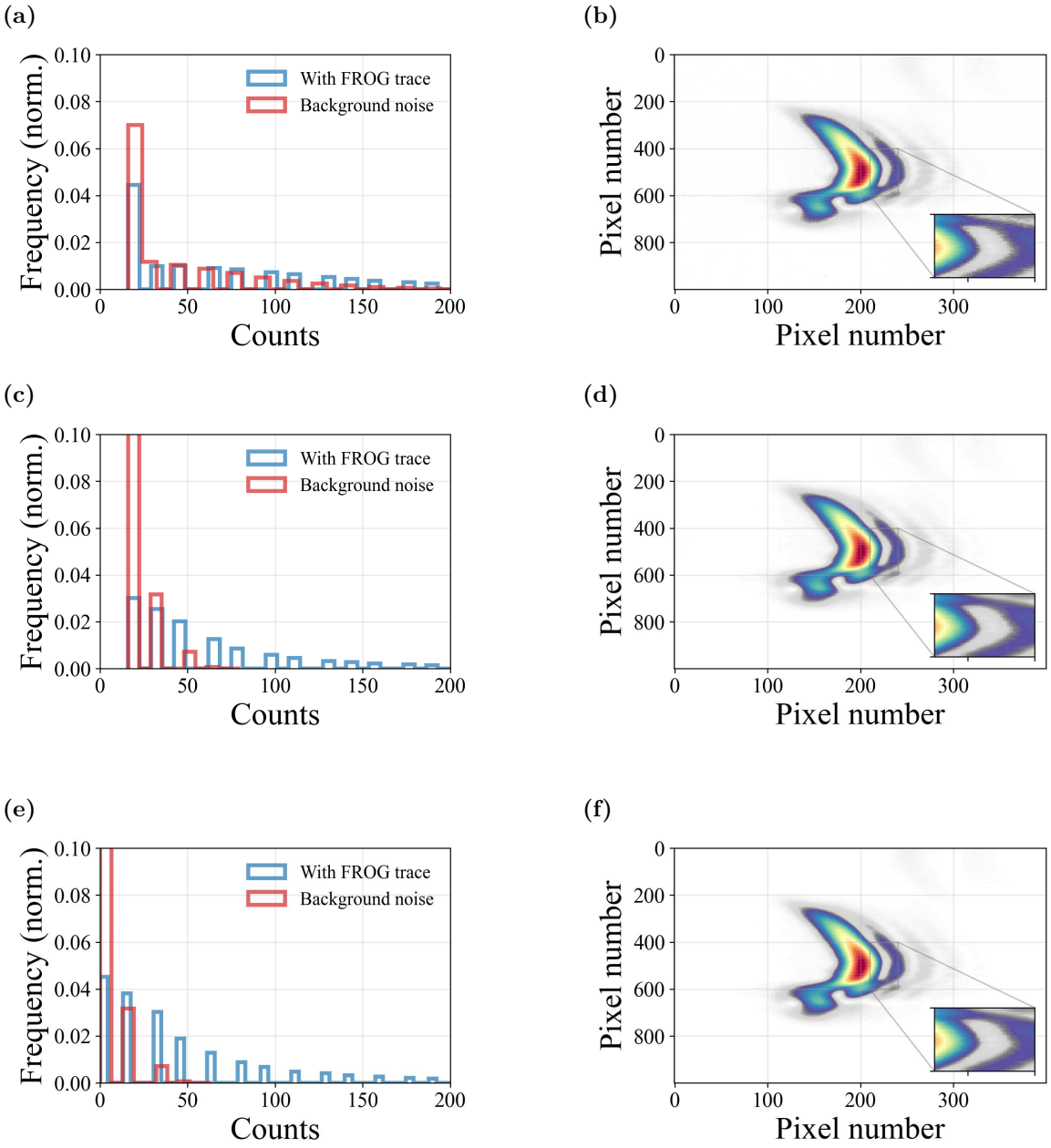


Figure 5.11: Histogram of background noise and corresponding FROG trace images: (a) and (b) raw data; (c) and (e) after applying a median filter; (e) and (f) after applying the background subtraction; The definition of the blue and red bars are the frequency of counts for the trace data and the frequency of counts for the background noise, respectively

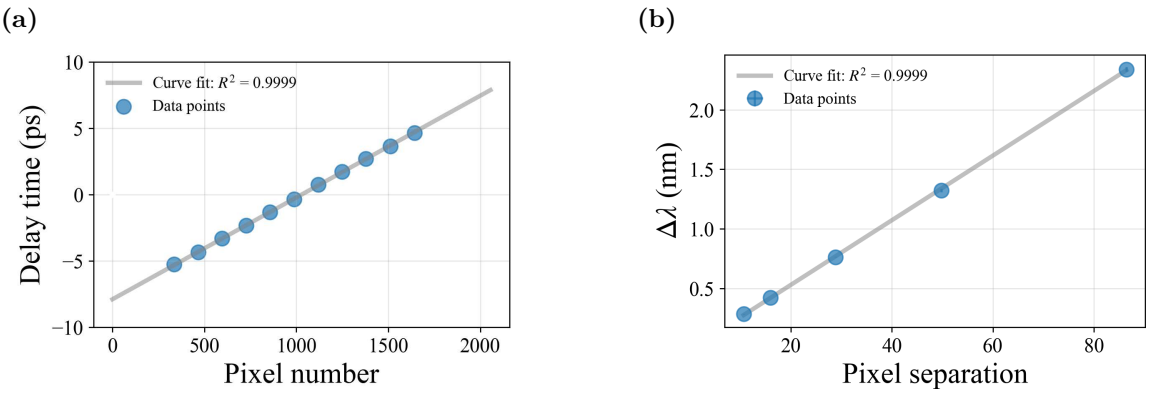


Figure 5.12: (a) Temporal calibration of the FROG device. (b) Spectral calibration of the FROG device. The error bars are not shown in (a) and (b) since their scales are smaller than the size of data points.

BK7 and SF11. The group velocity dispersion (GVD) for each material was 45 and 188 fs^2/mm, respectively. According to the lens design [220], the thicknesses of BK7 and SF11 were 4 and 6 mm, respectively, which corresponded to a GDD of approximately 180 fs^2 and 1,128 fs^2 for the BK7 and SF11, respectively. Thus, the total dispersion contributed by the cylindrical lenses was 1,408 fs^2. Another optical component in the FROG device was a half-waveplate (WPH10M-808, Thorlabs) with a thickness of 1.81 mm [221]. The GVD of this quartz waveplate was 36 fs^2/mm. The total GDD was approximately 65 fs^2. In addition, two beam samplers contributed a GDD of 74 fs^2. Therefore, the total GDD inherent in the FROG device was approximately 1,473 fs^2.

Table 5.2 summarises the dispersion contributed by the materials discussed above.

Calculation of spectral phase

The phase calculation procedure is listed as follows:

Material	GVD (fs^2/mm)	Thickness (mm)	GDD (fs^2)
BK7	45	4	180
SF11	188	6	1,128
Quartz	36	1.81	65
Fused silica	37	2	74

Table 5.2: Dispersion of materials in the 800-nm single-shot SHG FROG device.

1. Recovered the centroids of the temporal amplitudes from the probe pulses, and the gate pulses were centred on the temporal axis;
2. Obtained the spectral amplitude of these two pulses by taking the Fourier transform of the temporal amplitude of the probe and gate pulses;
3. Calculated the spectral phase of the probe and gate spectrum by the Python routine, angle. Then, unwrap the calculated spectral phases in radians using a Python routine, unwrap;
4. Used a fourth-order polynomial curve fitting routine in Python, curve fit to obtain the coefficients of n^{th}-order spectral phase. Since the retrieved phase has no meaning in the region where the intensity of the spectra and the pulse is close to zero, the curve fitting routine only found the best fit of the retrieved phase in the region where the intensity of the spectra was greater than 1% of the peak value;
5. Subtracted the extra dispersion contributed by the optical components discussed in the previous paragraph to obtain the actual spectral phase in an input pulse from the retrieved spectrum. The actual phase, ψ_a, had the form given by

$$\psi_a(\omega) = \sum_{n=1}^{4} \frac{1}{n!}\left(\frac{\partial^n \psi_r}{\partial {\psi_r}^n} - \frac{\partial^n \psi_e}{\partial {\psi_e}^n}\right)(\omega - \omega_0)^n, \tag{5.4}$$

where ψ_r is the retrieved phase; and ψ_e is the phase contributed by the optical components in the FROG device.

Statistical analysis

For statistical analysis, each measured FROG trace was retrieved ten times. To obtain each input pulse, this study used five individual FROG traces. It should be noted that a larger number of retrieval results only decreases the standard error and lower the pulse contrast of average intensity profiles of pulses. This would not help the analysis of temporal structures of pulses. Therefore, 50 retrieval results were analysed for each input pulse. The mean and standard error of each pulse property are reported below. The pulse properties included $\Delta\tau_{\mathrm{rms}}$, TBP, and ψ_2. In addition, the pulse spacing, T_m, and the first-order non-uniformity, s_1, for each retrieved pulse train are reported below.

5.3.3 Pulse measurement results

Short pulse

The retrieval result of the FROG traces formed by single short pulses is shown in Figure 5.13a, b, and c. The measured FROG trace shows a curvature, indicating a large amount of third-order spectral phase in the input pulse. The FROG error was $(4.2 \pm 0.1) \times 10^{-3}$. Figures 5.13d and e show the retrieved intensity of the probe and gate pulses, demonstrating obvious modulation of intensity at the tails of the pulses. These results are consistent with the time frequency distribution of the input FROG trace. $\Delta\tau_{\text{rms}}$ and TBP of the probe pulse was (343 ± 1) fs and 3.6, respectively. The retrieved spectra of the gate and probe pulses are shown in Figures 5.13f and g. The σ_I of the gate and probe pulses were (2.21 ± 0.24)% and (17.74 ± 0.20)%, respectively. The retrieved ψ_2 of the probe pulse was (-3,501 ± 460) fs^2. The average run time of the retrieval process was (1.3 ± 0.6) s.

Long pulse

Blind FROG traces of the short pulses passing through a block of 105-mm glass (SF10) were measured by the FROG device. Figure 5.14a, b, and c show the measured, retrieved, and error of the FROG trace. The measured FROG trace exhibited a diagonal line, indicating that the input pulse had a large ψ_2. The FROG error was (3.7 ± 0.1)$\times 10^{-3}$. Since the SF-10 glass contributed a positive chirp to the single short pulse at λ_0 = 790 nm, the higher frequencies should arrive later than the lower frequencies. Using the arrival times of different frequencies, the image orientation of the FROG traces was calibrated so that the time-frequency variation was consistent with the prediction of frequency chirp for the SF-10 glass. All the measured FROG traces were calibrated through this process.

The retrieved intensity of the probe and gate pulses is shown in Figures 5.14d and e. $\Delta\tau_{\text{rms}}$ of the probe pulse was (1,208 ± 74) fs. The TBP of the probe pulse was (14 ± 1). The retrieved spectra of the gate and probe pulses are shown in Figures 5.14f and g. σ_I of the gate pulse and probe pulses were 5% and 22%, respectively. The retrieved ψ_2 of the probe pulse was (13,030 ± 1,243) fs^2. Taking into account the spectral phase of the

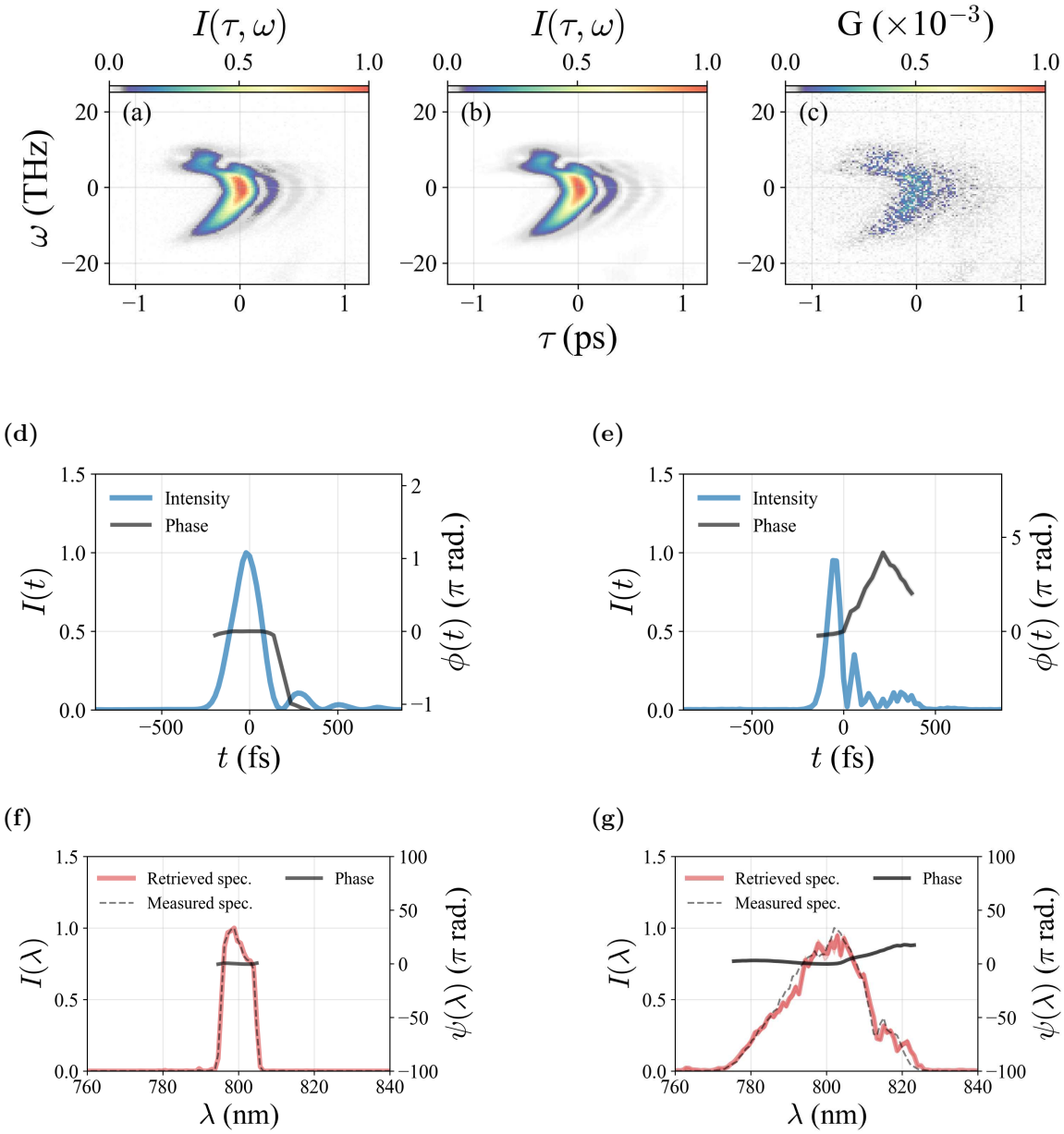


Figure 5.13: Retrieval result of a 343-fs short pulse. (a) Measured FROG trace; (b) Retrieved FROG trace; (c) Error of the retrieved FROG trace compared to the measured FROG trace; (d) Retrieved probe pulse; (e) Retrieved gate pulse; (f) Retrieved probe spectrum; and (g) Retrieved gate spectrum. The blue, red, and black curves show the retrieved pulse, spectrum, and phase on average. The dashed black curve shows the input spectrum on average. The blue-, red- and gray-shaded areas show the one standard error. If the shaded areas are not shown in the graphs, the scale of corresponding one standard error is smaller than the width of data lines.

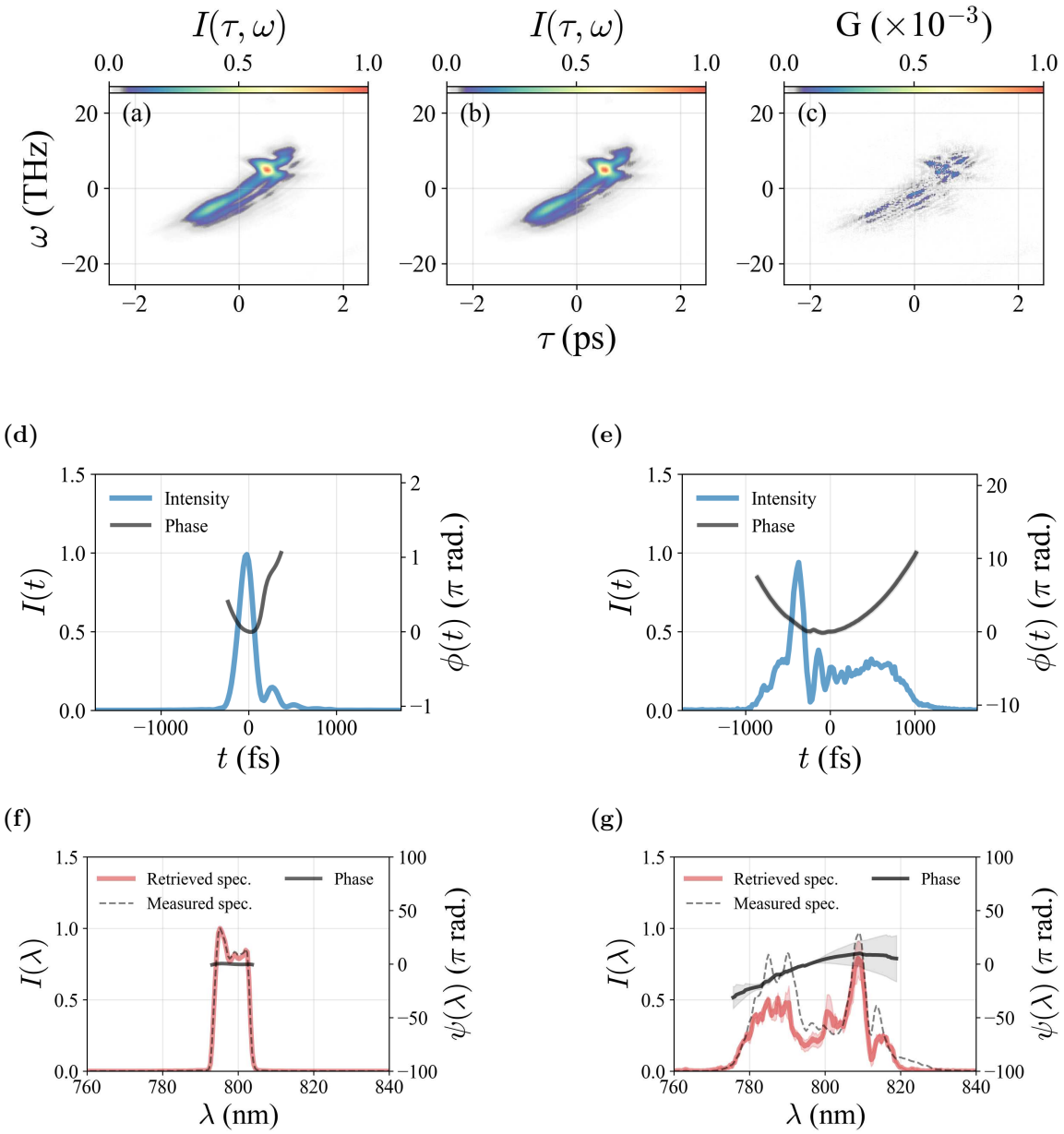


Figure 5.14: Retrieval results of a short pulse passing through a block of 105-mm SF-10 glass. (a) Measured FROG trace; (b) Retrieved FROG trace; (c) Error of the retrieved FROG trace compared to the measured FROG trace; (d) Retrieved probe pulse; (e) Retrieved gate pulse; (f) Retrieved probe spectrum; and (g) Retrieved gate spectrum. The coloured curves are defined in Figure 5.13.

input pulse, the actual spectral phase contributed by the glass was 16,531 fs^2 = 13,030 fs^2 + 3,501 fs^2. The theoretical ψ_2 of the SF-10 glass at λ_0 = 790 nm was 16,757. The retrieved ψ_2 was therefore consistent with the theoretical value and had an experimental error of 1.3%. The averaged run time of the retrieval process was (4.4 ± 1.1) s.

Multi-pulse trains

The pulse trains measured in OPAL were produced by the grating compressor and a Michelson interferometer. To test whether the FROG device and the PIE phase retrieval algorithm could retrieve multi-pulse trains with non-uniform pulse spacing, two types of multi-pulse trains were successfully measured and retrieved.

Because of time limitations, the FROG traces of the input pulse without passing through the Michelson interferometer were not measured. Therefore, the ψ_2 of the input pulses before the Michelson interferometer was unknown. This situation implies the author could not verify the multi-pulse train model discussed in Section 3.2.1. Hence, this section mainly focuses on reporting the pulse properties that could be directly retrieved from the FROG traces of multi-pulse trains.

Figure 5.15b shows the retrieved FROG trace of the first pulse train. The input multi-pulse train shown in Figure 5.15a had a positive chirp, since the time frequency distribution in its FROG trace had a variation similar to the FROG trace shown in Figure 5.14. The FROG error was (0.0109 ± 0.0005).

Figures 5.15d and e show the retrieved gate and probe pulse trains. The $\Delta\tau_{\mathrm{rms}}$ and TBP of the probe pulse was (1,439 ± 18) fs and (14.1 ± 0.1), respectively. The retrieved gate and probe pulse spectra are shown in Figures 5.15f and g. σ_I of the gate and probe pulse were 15% and 10%, respectively. The average run time of the retrieval process was (4.7 ± 1.5) s.

After moving the grating in the pulse compressor from one end to the other, the author took another data set for a pulse train with an opposite chirp. The retrieved FROG trace of the second pulse train is shown in Figure 5.16b. The input FROG trace shows a different time-frequency distribution whose variation was opposite to the FROG trace shown in Figure 5.15, indicating that the input pulse train had a negative

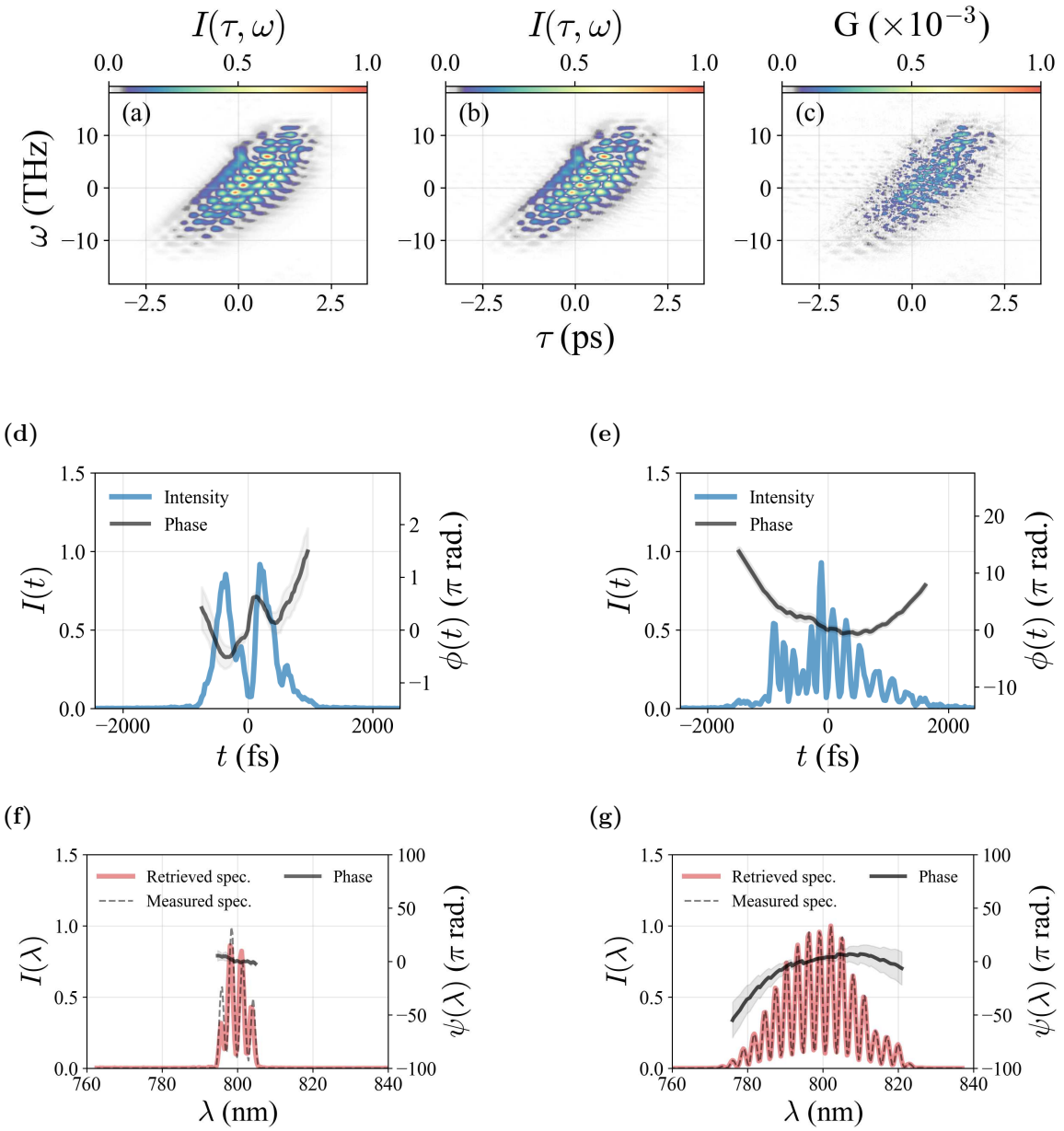


Figure 5.15: Retrieval results of a pulse train with a positive chirp, $\Delta\tau_{\mathrm{rms}} = 1.4$ ps and TBP = 14.1. (a) Measured FROG trace; (b) Retrieved FROG trace; (c) Error of the retrieved FROG trace compared to the measured FROG trace; (d) Retrieved probe pulse; (e) Retrieved gate pulse; (f) Retrieved probe spectrum; and (g) Retrieved gate spectrum. The coloured curves are defined in Figure 5.13.

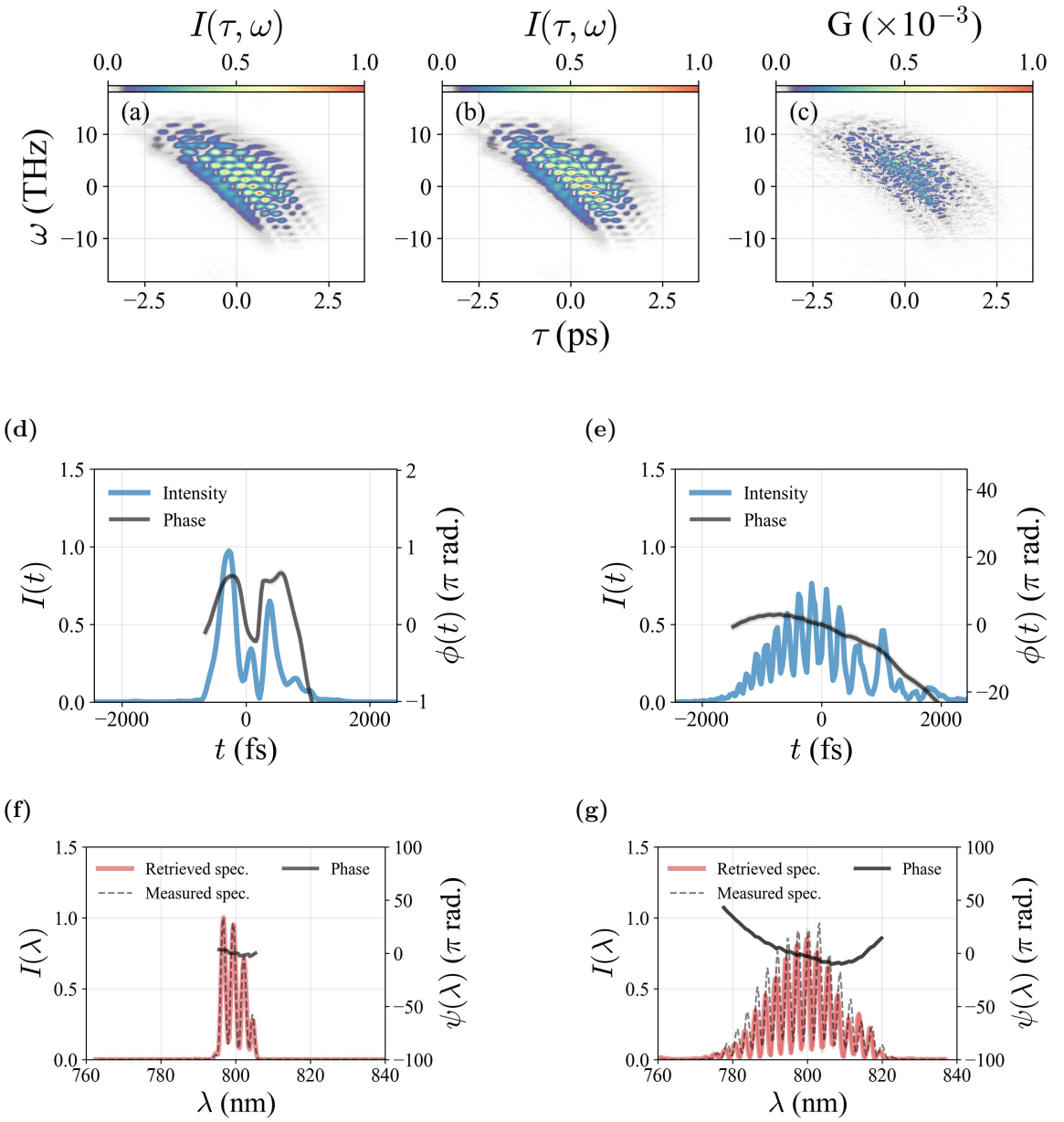


Figure 5.16: Retrieval results of pulse train with a negative chirp, $\Delta\tau_{\mathrm{rms}} = 1.6$ ps and TBP = 16.1. (a) Measured FROG trace; (b) Retrieved FROG trace; (c) Error of the retrieved FROG trace compared to the measured FROG trace; (d) Retrieved probe pulse; (e) Retrieved gate pulse; (f) Retrieved probe spectrum; and (g) Retrieved gate spectrum. The coloured curves are defined in Figure 5.13.

chirp because the higher frequency components arrive earlier than the lower frequency components in time. The FROG error was (0.0137 ± 0.01).

The gate pulse and the probe pulse trains retrieved from the FROG trace in Figure 5.16b are shown in Figures 5.16d and e. The $\Delta\tau_{\mathrm{rms}}$ and TBP of the probe pulse was (1,646 ± 4) fs and (16.1 ± 1.4), respectively. The retrieved spectra of the gate pulse and the probe pulse are shown in Figures 5.16f and g, and the σ_I of the gate and probe pulses were 16% and 12%, respectively. The average run time of the retrieval process was (8.68 ± 4.10) s.

5.3.4 Diagnosis of nonuniform pulse spacing

Figure 5.17 shows the retrieved pulse trains and calculated T_m as two examples. In Figure 5.17a, the average T_m was (198 ± 10) fs, s_1 was (0.05 ± 0.01), and N_p was 10 within the region where the intensity was $1/e^2$ of the peak. This corresponded to a average increment of (10 ± 2) fs in T_m from one pulse to the next in the pulse train. Comparing to the retrieved pulse train shown in Figure 5.17b, the average T_m was (232 ± 7) fs, N_p was 10.80 and s_1 was (0.12 ± 0.03), showing an average increase in local T_m by (27 ± 7) fs from the head to the tail of the pulse train.

According to the experimental results shown in this section, the FROG device developed by the author could measure different types of pulses with an average TBP

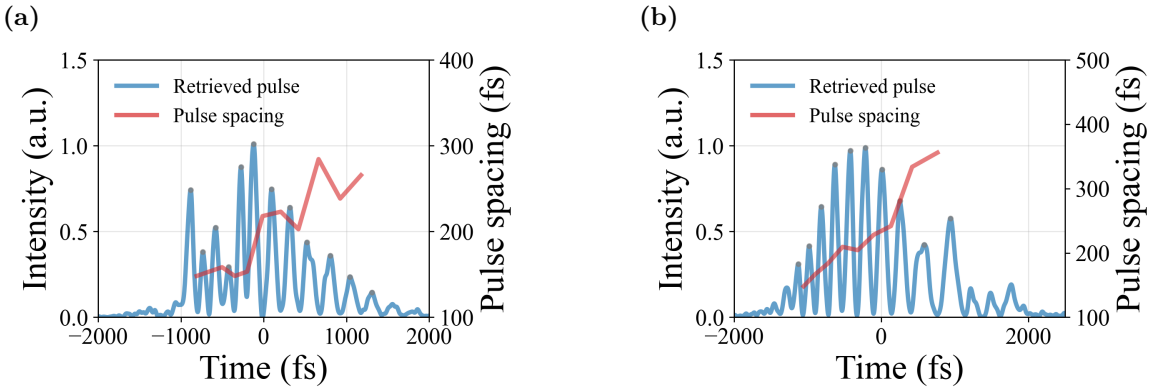


Figure 5.17: Retrieved pulse trains with average T_m of (a) 198 fs. (b) 232 fs, respectively. The blue curves show the retrieved intensity of pulse trains from FROG traces shown in Figures 5.15b and 5.16b, respectively. The red curves show the local pulse spacing between each intensity peak.

of up to 16. Two pulse trains with average T_m = 198 and 232 fs were successfully measured and characterised. Nonuniform pulse spacings with averaged s_1 = 0.05 and 0.12 were detected by the FROG device using the ePIE algorithm, which corresponding to increments of pulse spacing of 10 and 27 fs from one pulse to the next, respectively.

It can be observed that the two retrieved pulse trains had different signs of chirp according to the time-frequency distribution in their FROG traces, but the signs of s_1 were the same. According to the retried pulses shown in Figure 5.17, the temporal intensity variation of the two pulse trains were different. One explanation for this issue is that the compressor setting in the experiment had a large TOD even though ΔL_s in the compressor was moved to opposite directions with respect to the position producing full pulse compression. This demonstrates the importance of characterising the time direction of pulse trains with the FROG technique in MP-LWFA.

Based on the author's successful experimental demonstration, this FROG device was later adopted in an MP-LWFA experiment for the pulse train characterisation. The experimental result is discussed in the next section.

5.4 Measurement of multi-pulse trains in Gemini TA3

5.4.1 Introduction

Background

Resonant down-ramp injection (RDI) of electrons in MP-LWFA is a new approach to injecting, trapping and accelerating electrons with intense laser pulse trains and plasma channels, which was proposed by Simon Hooker et al.[222] in 2022. The author participated in a proof-of-principle experiment aimed to demonstrate the RDI-in-MP-LWFA at RAL in 2023.

The down-ramp injection of electrons in plasma wakefields has been studied over the past 20 years [223–226]. In this controlled injection scheme, a plasma wakefield is excited by an intense ultra-short laser pulse ($\sim$ 30 fs) propagating in a plasma. This plasma has a down-ramp distribution of n_e, along the propagation direction of the laser pulse. After the wakefield leaves the down-ramp, it sees an increase in $\lambda_p = (\pi c^2 m_e / e^2 n_e)^{1/2}$. The

wakefront of the wakefield falls further behind the laser pulse even though $v_g \approx c(1 - {\omega_p}^2/2\omega)^{1/2}$ increases after leaving the plasma down ramp. The increase of λ_p implies that v_p decreases on the plasma down-ramp because $v_p = c(1+{k_p}^{-1}\zeta dk_p/dz)$, where $\zeta = z-ct$ [224]. According to the physical picture of the electron injection discussed in Section 2.2.1, the decrease in v_p can reduce the threshold for trapping electrons. Therefore, the injection of electrons can be restricted in the region of the plasma down-ramp.

The uniqueness of RDI in MP-LWFA involves the resonance between the interaction of the plasma wakefields and the pulse trains. The RDI in MP-LWFA uses a multi-pulse train ($\sim$ 1 ps) instead of an ultra-short laser pulse ($\sim$ 30 fs). This pulse train can resonantly excite the plasma wakefield when $\lambda_p \approx T_s$, where T_s is the pulse spacing. Hence, the pulse train can only excite plasma wakefields in a small region of the down-ramp, where n_e satisfies the resonance condition. Once the condition is satisfied, the excited plasma wakefield results in a faster forward velocity of electrons, which is considered the initial velocity of the electrons, v_z. Since v_p is also reduced by the plasma down-ramp, electron trapping can occur in a localised region when $v_z > v_p$ and $\lambda_p \approx T_s$ are both satisfied. Based on this mechanism, the electron injection only happens in a small resonance region ($\sim$ a few μm) and the generated electron bunches have a smaller energy spread and lower emittance.

Because a pulse train consists of many pulses ($N_p \sim 10$), the electron injection can happen in every wakefield cycle once $v_z > v_p$ and $\lambda_p \approx T_s$ are both satisfied. The RDI in MP-LWFA leads to a situation in which electron bunches are injected into different plasma wakefield buckets. Provisional PIC simulations showed that these electron bunches had different energy peaks. After this bunch train was accelerated while the plasma wakefield was propagating in the region of uniform plasma density, these bunches were accelerated to the same energy peak.

Objectives

The main objectives of the 2023 Gemini experiment were (i) to demonstrate electron injection in a MP-LWFA using the RDI; and (ii) to observe multi-coloured bunch trains

accelerated by the pulse trains. The author's role in this experiment was to implement the measurement of pulse trains using the single-shot FROG device developed in OPAL.

Two research groups collaborated on this research project: the research group at Ludwig Maximilian University of Munich (LMU) in Germany, led by Professor Stefan Karsch, and the Oxford team, led by Professor Simon Hooker and Professor Roman Walczak. Several tasks were required to achieve the objectives: (i) the generation and diagnostics of pulse trains; (ii) the formation and characterisation of plasma down-ramp; and (iii) Diagnostics of longitudinal electron bunches and electron energy.

5.4.2 Experimental setup

Overview

Several techniques required in this experiment were proposed by Hooker et al. and developed by the author's colleagues and collaborators. These techniques included pulse train generation, plasma channel formation, electron bunch diagnostics, and other diagnostic techniques. The pulse train generation technique was accomplished by the temporal interference of chirped pulses [100]. Plasma channel formation for an electron injector and pulse guiding were achieved by generating hydrodynamic optical-field-ionised (HOFI) plasma channels developed by the Oxford team [227–229]. The electron bunch diagnostic technique was based on the principle of coherent transition radiation (CTR) [230]. The CTR apparatus was provided by the LMU group [231, 232]. The electron spectrometer was designed and built by the author, using conventional magnetic dipoles and the edge focusing effect for electron energy diagnostics [233–237]. The measurement of pulse trains used the FROG discussed in Section 3.3. The author designed and built the FROG device.

Figure 5.18 the experimental layout. The south beam provided 30-fs pulses with an energy of approximately 8 J and $\lambda_0 = 800$nm after the final pulse compression. This main beam generated pulse trains with T_p =10 and T_m = 170 fs in the experiment. According to the pulse train model and pulse train generation technique discussed in Section 3.2, the required ψ_2 and τ between the two pulses were approximately 9,992 fs^2 and 369 fs, respectively. Based on these numbers, the required Michelson spacing

ΔL_m in the Michelson interferometer was set to 55 μm. The required grating pair spacing ΔL_s of the south beam compressor was set to 1.62 mm. The resonant λ_p and n_e required to excite plasma wakefield for the pulse train were approximately 53 μm and 4.3×10^{17} cm^{-3}, respectively.

To have enough peak intensity to study the RDI in MP-LWFA, an f/20 parabola was used to focus the south beam on a gas target. The gas species was hydrogen supplied by a gas nozzle. According to the simulation conducted by the author's colleagues, the laser pulse was focused at 3 mm above the gas nozzle. The laser focus quality was monitored by the forward diagnostic setup provided by RAL.

The generated electron bunches were expected to pass through a tape drive made of 10-μm thick steel. The normal to the plane of the steel tape was inclined at 4° relative to the propagation axis of the laser pulse. In addition, the 25-μm thick Kapton tape was used for dumping the laser pulses focused by the f/20 parabola. The forward CTR was expected to be produced at the backside of the steel tape. A reflective Al-coated pellicle separated the electron bunches and the CTR. An off-axis gold-coated parabola was arranged to collect the CTR signal, allowing the analysis of CTR spectra of multi-coloured bunch trains. A CTR spectrum range (0.4 μm – 7.1 μm) was beam-split and guided into three spectrometers for data analysis and bunch retrieval.

The electron bunches generated at the IP were expected to pass through the electron spectrometer (ESPEC) consisting of two magnetic dipoles (NdFeB, provided by RAL) and three Lanex screens (15 cm × 30 cm, Lanex Regular, Carestream), which was expected to measure electron energy ranging from 10 MeV to 1.7 GeV. Three CMOS scientific cameras (Neo sCMOS, Andor Technology) were used to capture fluorescence light (λ_0 =527 nm) emitted from the back surfaces of the Lanex screens.

The north beam was used to provide laser energy for the transverse HOFI injector and the guiding of pulse trains. A small amount of energy (5 mJ) was extracted from the North beam to generate SHG light for the probe pulses. The injector was focused by a lens and transversely passed through the IP after its wavefront was flattened by a deformable mirror. The injector pulses and the probe pulses were arranged to propagate with the injector through the IP in a collinear beam geometry. The probe pulses were

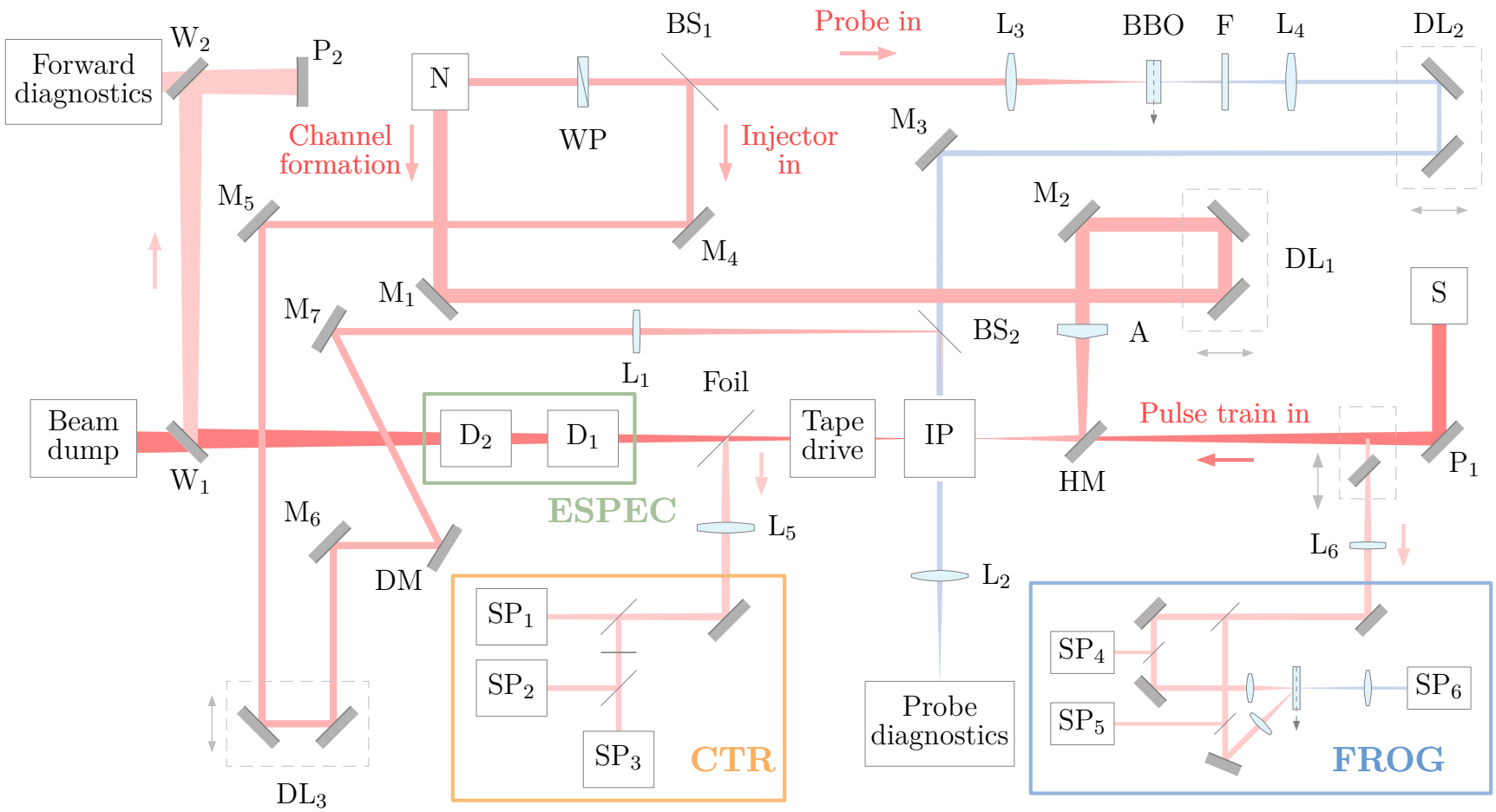


Figure 5.18: Experimental layout of the 2023 experiment to demonstrate the RDI in a MP-LWFA in Gemini TA3 at RAL. N—the north beam; S—the south beam; IP—interaction point; P_n—parabola; HM—holy mirror; D_n—dipole magnet, W_n—wedge; M_n—mirror; L_n—lens; WP—quarter waveplate; BS_n—beamsplitter; F—filter; DL_n—delay stage; DM—deformable mirror; and A—axicon lens.

separated after the IP for diagnostics of channel formation. The other energy was used to form HOFI channels to guide pulse trains by a transmissive axicon.

Experimental setup of pulse train measurement

A pick-off mirror was installed between the beam path of the f/20 parabola and the IP for the measurement of multi-pulse trains. The pulses from the south beam in the medium power mode, providing pulse energy of 5 mJ at a repetition rate of 5 Hz, were extracted by the pick-off mirror and guided through a 2-inch concave lens (LC1611-B, Thorlabs). The pulse then passed through a 5-mm fused silica window to the outside of the chamber and was reflected by two silver mirrors to the FROG device. Figure 5.19 shows this beam path.

In the setup of the FROG device, the pulse trains were guided through a Michelson interferometer used to calibrate the FROG images. After finishing the temporal and spectral calibrations, the Michelson interferometer was bypassed. The input multi-pulse trains passed through a half-waveplate for the adjustment of the input polarisation. The pulse trains were beam-split into two replicas. A pulse replica passing through a bandpass filter was spectrally filtered and viewed as the gate pulse. The other pulse replica viewed as the probe pulse was guided through a time-delay stage for the adjustment of time-delay between the two pulse replicas. The probe and gate pulse crossed at a BBO crystal for the generation of the SHG correlation signal. The scattered fundamental light was imaged on camera, CAM_1, to monitor beam alignment at the crystal. The SHG correlation signal was imaged and dispersed by an imaging spectrometer and the FROG traces were recorded by camera, CAM_2. It should be mentioned that the single-shot FROG device used in this experiment did not have a function of accepting laser trigger signals.

Experimental conditions of pulse train measurement

In the experiment, our research group found that the pulse trains produced using the medium power mode of the Gemini laser system were too weak to provide a high SNR for high-quality data. Therefore, the bandpass filter originally installed in the FROG device

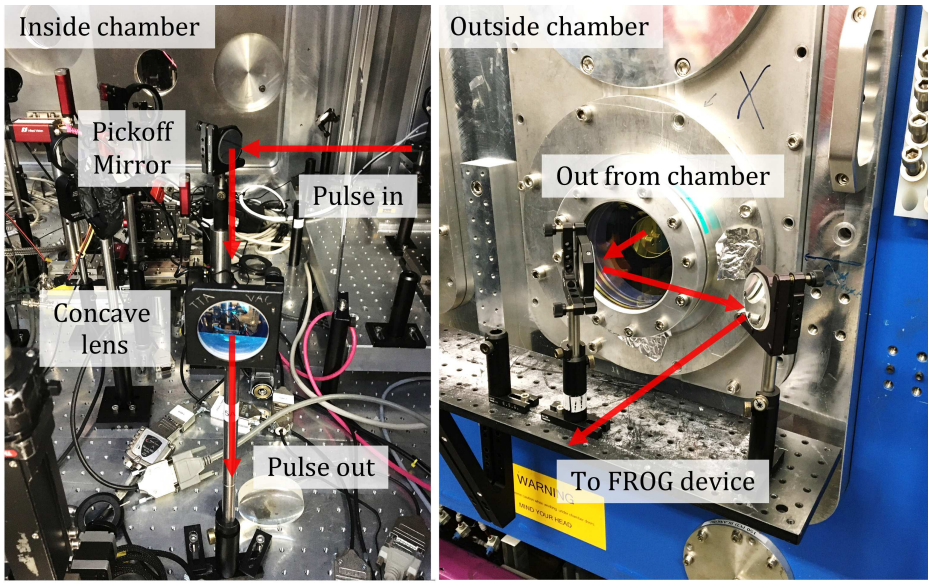


Figure 5.19: Beam path of the pulse train measurement in the 2023 RDI-in-MP-LWFA experiment.

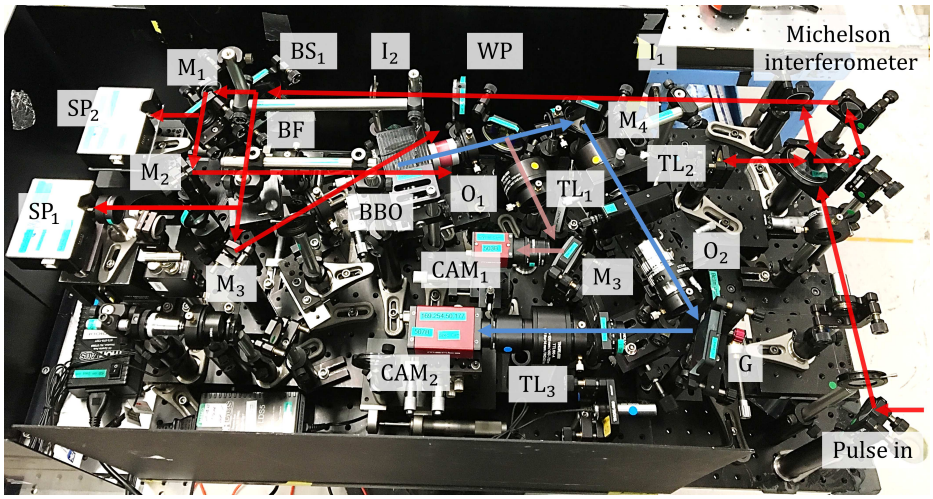


Figure 5.20: Experimental setup of the single-shot FROG device used in the 2023 RDI in MP-LWFA experiment. I_n—iris; WP—half waveplate; M_n—mirror; BS_n—beamsplitter; BBO—nonlinear crystal; O_n—microscope objective; TL_n—tube lens; CAM_n—camera; and G—grating.

was removed to enhance the SNR. This implies that all the FROG traces of pulse trains were SHG FROG traces, not the blind FROG traces that were planned to be measured.

In addition, the repetition rate of the laser was only 5 Hz in the medium power mode, which caused some difficulty in beam alignment for the FROG beam line during the experiment. This situation led to an unoptimised beam collimation of the input laser pulse in the FROG device. As a consequence, the author could not optimise the measured FROG traces within the limited experimental time available.

Furthermore, the laser system was not as stable as expected. The beam profile of the laser pulses from the medium-power mode had a very low quality after the pulses passed through the concave lens in the FROG beam path. The distribution of laser energy was uneven, and the laser beam profile contained many hot spots. Although a wavefront sensor (HASO4 Broadband, Imagine Optic) and a deformable mirror (ILAO STAR, Imagine Optic) were used to assist in wavefront optimisation, the beam quality could not be improved.

Because of these issues, complete time-frequency information was missing from the measured FROG traces which had serious distortion in the intensity distribution. Hence, complete pulse trains with stable intensity and spectral phases were difficult to retrieve from these measured FROG traces.

5.4.3 Procedure of pulse retrieval and data analysis

To overcome the above-mentioned problems, the author developed a pulse method to retrieve pulse trains. This method combined the ePIE and SSA algorithms to retrieve pulse trains for distorted and incomplete FROG traces. The SSA algorithm was discussed in Section 3.3.1. The procedure for retrieving pulse trains are shown in Figure 5.21.

The first step was to use the ePIE algorithm to retrieve a general temporal profile of a pulse train. Since the time-frequency information in the input FROG trace was incomplete, a pulse train retrieved by the ePIE algorithm might not provide an appropriate solution to the input FROG trace. However, if the FROG trace was retrieved many times (> 50), a few retrieved pulse trains from a single FROG trace could produce a close solution to the input FROG trace. This was because a FROG trace contained redundant time-frequency information and the ePIE algorithm could use this fact to retrieve pulses

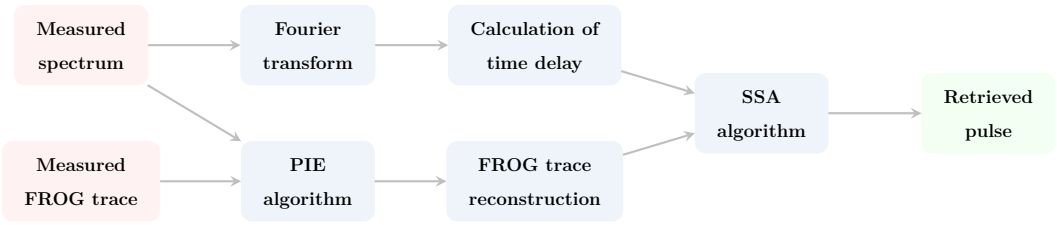


Figure 5.21: Procedure of pulse train reconstruction for the 2023 Gemini experiment.

from incomplete FROG traces, as discussed in Spangenberg et al. and Kane et al. [184, 189, 190]. With this unique feature, pulses retrieved from a distorted and incomplete FROG trace might contain actual information about the intensity of an input pulse train.

To select pulse trains with a close-to-correct intensity profile, each retrieved pulse train was Fourier transformed into the frequency domain first. T_m was found in the frequency domain by finding the frequency, f_s, which was the location of the first sideband, and calculating $T_m = 1/f_s$. The criterion for selecting an optimal pulse train was selecting data with a ratio, r_1, of the peak intensity of the sideband to the peak of the zero frequency greater than 0.25.

An optimal retrieved pulse train was found by retrieving the same input FROG trace multiple times and choosing output pulse trains which satisfy the condition, $r_1 \geq 0.25$. This pulse train was used to reconstruct an optimal FROG trace with complete time-frequency information. After obtaining a complete FROG trace, the autocorrelation of this FROG trace was calculated. This correlation signal served as an input in the SSA.

The value of τ between the two pulse replicas produced in the Michelson interferometer was calculated by finding the modulation period of the pulse train spectrum. The period can be found by Fourier transforming the spectrum and finding the location of the first sideband in the time axis. The τ was used as a constraint in the SSA algorithm to improve the convergence of the phase retrieval. Using the SSA algorithm designed for retrieving pulse trains, ψ_2 of the optimal pulse train was retrieved. An actual pulse train forming the incomplete input FROG trace was retrieved using the spectral phase retrieved by the SSA algorithm.

To collect enough data for the statistical analysis for each pulse spacing of pulse trains, five input FROG traces were individually retrieved ten times. As a result, the data analysis 10 optimal pulse trains from 50 retrieved pulse trains. These optimal pulse trains were used to reconstruct the FROG traces. The input autocorrelation signal was calculated from the reconstructed FROG traces and sent to the SSA algorithm as input. The retrieved pulse trains by the SSA algorithm were analysed in the end.

The temporal and spectral calibrations followed the methods discussed in Section 5.2.2. For all FROG traces measured by the single-shot FROG device, the $d\tau/dp$ and

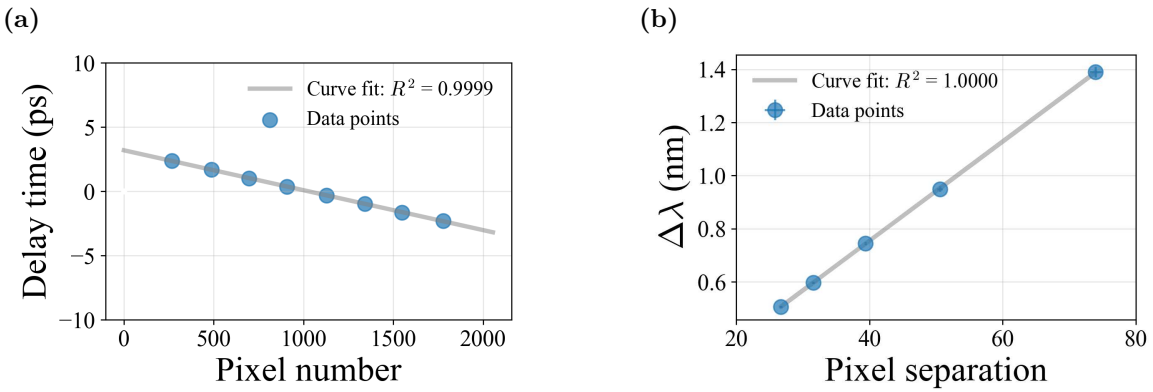


Figure 5.22: Calibration of FROG images for the 2023 RDI experiment. (a) Temporal calibration. (b) Spectral calibration. The error bars are not shown in (a) and (b) since their scales are smaller than the size of data points.

$d\lambda/dp$ were (3.11 ± 0.01) fs/pixel and (0.0188 ± 0.001) nm/pixel, respectively. The corresponding ΔT_s and $\Delta\Lambda$ provided by the FROG device were approximately 5 ps and 47 nm, respectively. Figures 5.22a and 5.22b show the temporal and spectral calibration curves.

5.4.4 Pulse measurement results

Measurement of pulse trains with a 153-fs pulse spacing

Figure 5.23a shows a measured FROG trace for a pulse train with a T_m of (153 ± 3) fs. This measured FROG trace did not have a complete intensity profile. Using the FROG trace reconstruction method, a complete intensity profile of the FROG trace shown in Figure 5.23a was reconstructed. Comparing the measured and reconstructed FROG trace, the reconstructed FROG trace contained more complete time-frequency information in the lower right part of the FROG trace. As a result, this reconstructed FROG trace was used to generate an autocorrelation signal.

Using the measured spectrum of the pulse train as shown in Figure 5.23c, the value of τ between the two chirped pulses was calculated by finding the modulation period of the spectrum as shown in Figure 5.23d. The calculated period was (457 ± 1) fs, which was introduced by the Michelson interferometer. Using this figure as a constraint in the SSA algorithm yielded actual pulse train. Figure 5.23e shows the retrieved autocorrelation signal. The retrieved GDD produced by the final compressor was (-9,319 $\pm$ 361) fs^2. The retrieved TOD was (21,870 $\pm$ 15,421) fs^3. The theoretical GDD predicted by the

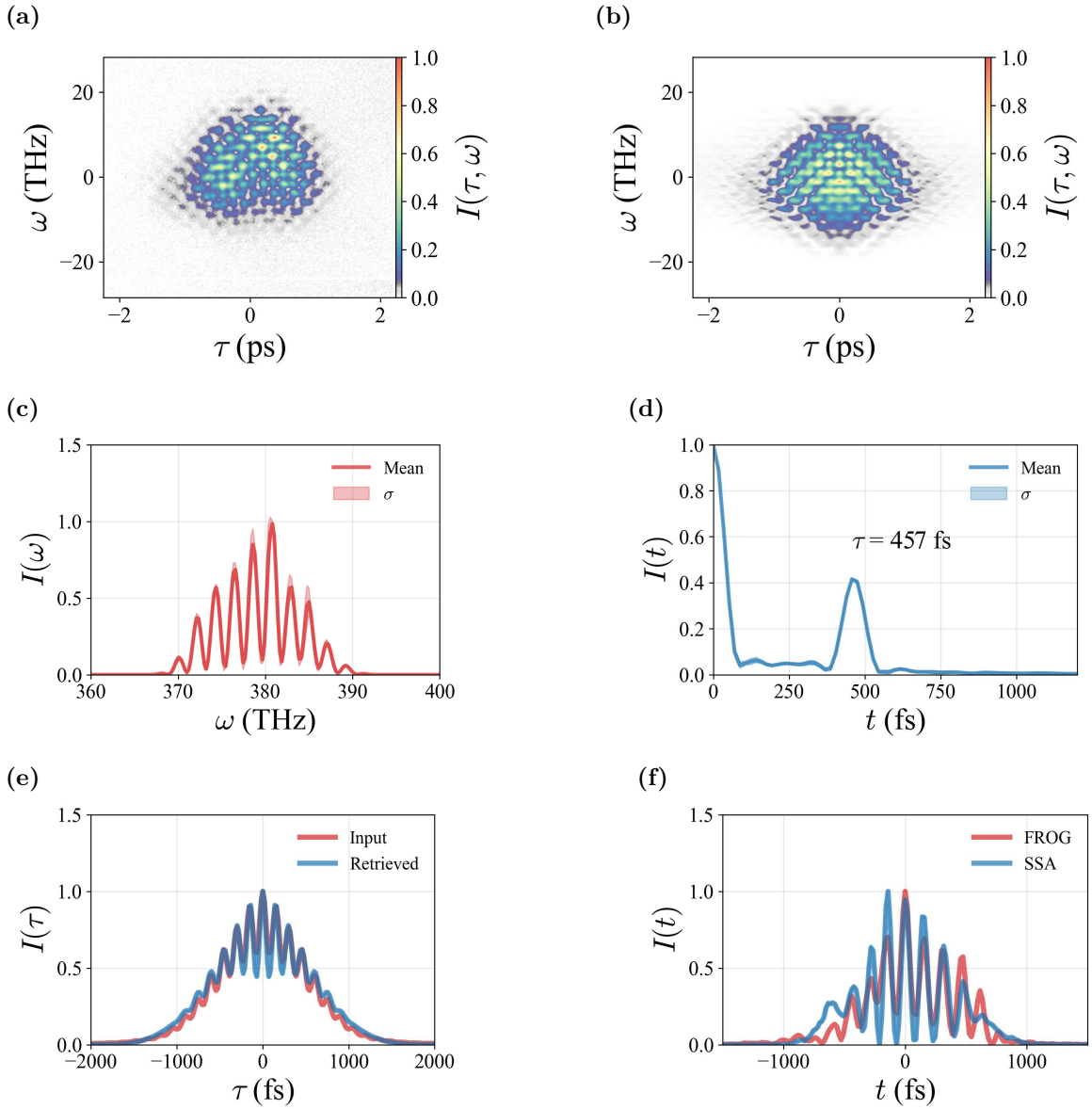


Figure 5.23: Retrieval results for a pulse train with a 153-fs pulse spacing. (a) Measured FROG trace; (b) Reconstructed FROG trace; (c) Spectrum of the pulse train on average. The red-shaded area shows the one standard error; (d) Fourier transform of the spectrum in (a). The signal peak is at $\tau = (457 \pm 1)$ fs; (e) Auto-correlation signal. The red and blue curves show the input and retrieved autocorrelation signals on average, respectively; (f) Retrieved pulse trains. The red and blue curves show the pulse trains on average retrieved by the ePIE and the SSA algorithms, respectively.

compressor model was 9,992 fs^2. Therefore, the retrieved GDD was consistent with the theoretical value and had an error of approximately 7%.

Using the retrieved phase and time delay, a pulse train was reconstructed using the pulse train model discussed in Section 3.2.2. Figure 5.23f shows the retrieved pulse train intensity, indicating that the pulse train from the PIE algorithm contained less energy at the wings of the pulse train compared to that from the SSA algorithm. T_m of the two pulse trains were the same as each other, which was (153 ± 3) fs and corresponded to a resonant plasma density at 5.2×10^{17} cm^{-3}.

Measurement of pulse trains with a 124-fs pulse spacing

After the author adjusted the displacement of the Michelson interferometer, ΔL_m, another pulse train was measured by the FROG device. Figure 5.24a shows a measured FROG trace for a pulse train with T_m of (124 ± 2) fs, which had a worse quality in terms of missing data and distorted intensity distribution. Using the same method shown in Figure 5.21, a complete intensity profile of the FROG trace was reconstructed, as shown in Figure 5.24b.

Using the measured spectrum of the pulse train as shown in Figure 5.24c, the value of τ between the two chirped pulses generated by the Michelson interferometer was calculated by finding the modulation period of the spectrum, as shown in Figure 5.24d, which gave a τ of (615 ± 1) fs. The actual pulse train was retrieved using this figure as a constraint in the SSA algorithm. Figure 5.24e shows the retrieved autocorrelation signal. The retrieved GDD produced by the final compressor was (-9,973 ± 361) fs^2. The TOD was (22,940 ± 12,847) fs^3. Therefore, the retrieved GDD was also consistent with the theoretical value and had an error of approximately 0.2%. The pulse train was reconstructed using the retrieved phase and τ from the SSA algorithm.

Figure 5.24f shows the retrieved intensity, indicating that the retrieved pulse train from the ePIE algorithm contained less energy at the wings of the pulse compared to that from the SSA algorithm although T_m were approximately equal. The retrieved τ was (124 ± 2) fs, corresponding to a resonant plasma density at 8.1×10^{17} cm^{-3}.

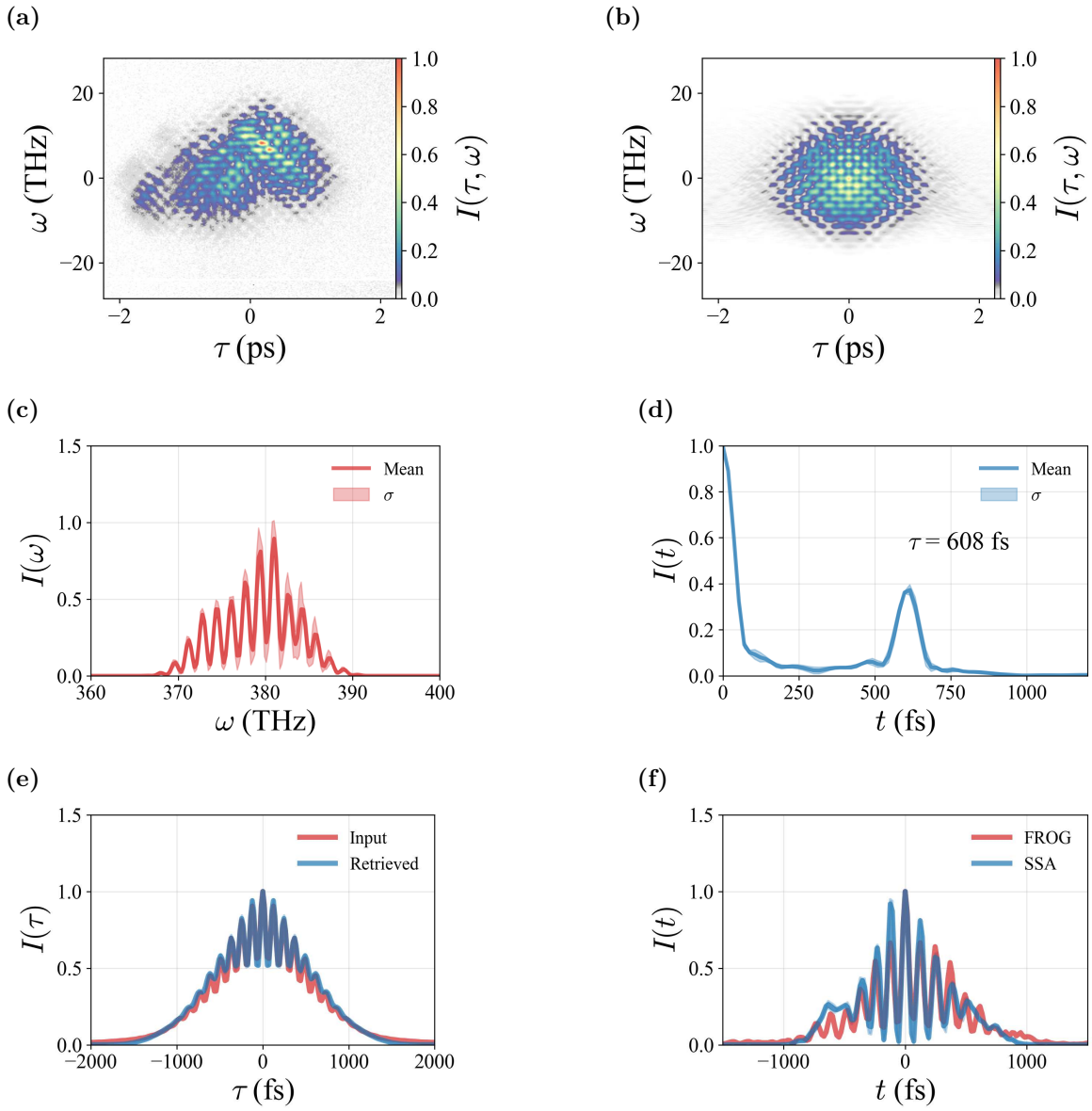


Figure 5.24: Retrieval results for a pulse train with a 124-fs pulse spacing. (a) Measured FROG trace; (b) Reconstructed FROG trace; (c) Spectrum of the pulse train; (d) Fourier transform of the spectrum in (a). The signal peak is at $\tau = (615 \pm 1)$ fs; (e) Auto-correlation signal. The red and blue curves show the input and retrieved autocorrelation signals on average, respectively; (f) Retrieved pulse trains. The red and blue curves show the pulse trains on average retrieved by the ePIE and the SSA algorithms, respectively.

According to the experimental results measured in Gemini TA3, the author provided a method combining the SSA and ePIE algorithms to reconstruct the pulse trains with average pulse spacings of 124 and 153 fs. The retrieved phase was consistent with theoretical values using the grating-pair compression model. However, the author can conclude that serious systematic errors occurred in the FROG traces during the pulse measurement. Even though the FROG traces were somehow reconstructed, the retrieved pulses from the ePIE and SSA algorithms did not match well at the wings of pulses, which indicates that the crossing beams at the nonlinear crystal might be seriously misaligned in addition to other problems mentioned earlier.

5.5 Conclusions

In conclusion, the author successfully developed a pulse measurement device capable of measuring pulse trains with single-shot beam geometry. This device measured pulse trains in OPAL and Gemini TA3 for proof-of-principle experiments.

Section 5.2 described the optical layout of the FROG device with a single-shot beam geometry and demonstrated the device developed in OPAL using optical components studied in Section 4.4.

Section 5.3 presented a series of experiments conducted to evaluate the optical properties of the FROG device. Based on the experimental results, the device had the following properties: $R_s = (15.6 \pm 0.1)$ μm, $R_\lambda = (0.10 \pm 0.01)$ nm, and $R_t = (36 \pm 3.2)$ fs. This lead to $\Delta T_s \approx 9$ ps and $\Delta\Lambda \approx 70$ nm. As a result, the device could measure pulse trains with a maximum TBP of 20.

Section 5.4 described two experiments conducted to demonstrate that the FROG device was able to measure complex pulse trains. One successful experiment in OPAL showed that the FROG device could measure pulse trains with a TBP of up to 15. Two retrieved pulse trains showed average $T_m = 198$ and 232 fs, with $s_1 = 0.07$ and 0.12, respectively. The increments of pulse spacing from one pulse to the next were 10 and 27 fs, respectively. However, the FROG device did not successfully measure pulse trains in Gemini TA3 because of experimental constraints related to the low quality and instability of the available laser pulses. The author adopted a strategy to reconstruct

pulse trains with average T_m = 124 and 153 fs using ePIE and SSA algorithms. The retrieved spectral phases were consistent with the theoretically predicted spectral phases.

However, the nonuniform pulse spacing of the two pulse trains measured in Gemini TA3 could not be diagnosed since the algorithm relied on the reconstructed SSA signal from FROG traces to retrieve that spectral phase. As the author mentioned in Section 3.3.1, the SSA algorithm was not sensitive to the third-order spectral phase. In addition to this problem, the time direction of the two pulse trains could not be identified because the measured FROG traces and SSA signal were symmetrical and hence no time information was contained in the measured signal.

An Experiment, like every other event which takes place, is a natural phenomenon; but in a Scientific Experiment the circumstances are so arranged that the relations between a particular set of phenomena may be studied to the best advantage.

— James C. Maxwell, Scottish scientist, 1831 - 1879 [238]

6

Pulse characterisation of plasma-modulated pulse trains

Contents

6.1 Introduction 141
6.2 Theory 141
6.2.1 Plasma-modulated laser pulses 141
6.2.2 Generation of P-MoPA pulse trains 144
6.2.3 Representation of P-MoPA pulse trains 145
6.2.4 Frequency-resolved optical gating (revisited) 147
6.2.5 Self-referenced spectral interferometry 148
6.2.6 Cross-referenced spectral interferometry 150
6.3 Simulation 152
6.3.1 Simulation conditions 152
6.3.2 Characterisation of reference pulses 155
6.3.3 Characterisation of plasma-modulated laser pulses 158
6.4 Experiment 162
6.4.1 Design considerations of the pulse measurement device 162
6.4.2 Optical layout of the pulse measurement device 163
6.5 Conclusions 165

6.1 Introduction

Following the discussion in Section 2.3, the P-MoPA concept developed by the Oxford group has paved the way for the use of new laser technologies, such as thin-disk lasers with a high wall-plug efficiency and a high repetition rate, to excite plasma wakefields. However, the thin-disk laser with desired properties can only deliver ps-long pulses which is not suitable in the conventional LWFA. Current progress in the P-MoPA concept involves making use of a ytterbium:yttrium–aluminium–garnet (Yb:YAG) laser system ($E = 112$ mJ, $\Delta\tau = 1.3$ ps) [239] to demonstrate the conversion of ps-long drive pulses to P-MoPA pulse trains in a proof-of-principle experiment

One of the most important tasks in this experiment is to diagnose the formation of P-MoPA pulse trains in preparation for the electron acceleration stage. Based on the author's research and demonstration of the single-shot FROG device, the aim of this chapter was to present an investigation of spectral interferometry (SI) for the complete characterisation of P-MoPA pulse trains. The author wanted to understand whether the cross-referenced SI could quantify the properties of P-MoPA pulse trains, such as the temporal and spectral phases.

This chapter is organised as follows. Section 6.2 presents the principle of pulse train generation in P-MoPA. Section 6.3 provides simple simulations to demonstrate that the complete characterisation of pulse trains in P-MoPA. Section 6.4 describes a provisional optical design of the pulse measurement device is discussed, and demonstrates a prototype of experimental setup that would be applicable for the future P-MoPA experiment.

6.2 Theory

6.2.1 Plasma-modulated laser pulses

A laser pulse can be temporally modulated by a sinusoidal plasma density variation. In a plasma modulator, as shown in Figure 6.1, a short seed pulse ($\Delta\tau \sim$ fs) is used to excite a linear plasma wakefield in a long plasma channel ($L_p \sim$ cm). A long drive pulse ($\Delta\tau \sim$ ps) collinearly following the seed pulse can be modulated by the plasma wakefield in the plasma channel. The fundamental frequency of the drive pulse ω_0

has spectral sidebands at $\omega_0 \pm m\omega_p$ induced by plasma modulation, where m is the mth mode number. The detailed physical model of the plasma modulator has been discussed by Jakobsson et al. [119]. In this section, the aim is to summarise the theoretical background of the pulse conversion process.

In the 1D linear theory of the modulator, the plasma-modulated drive pulse is given by

$$\begin{aligned} b(\zeta,\tau) &\approx |b_0(\zeta)| \exp\left[-i\frac{1}{2}\frac{\omega_{p0}^2}{\omega_0}\frac{\delta n}{n_0}\frac{z}{v_g}\cos\left(\frac{\omega_{p0}}{v_g}\zeta + \Delta\phi\right)\right] \\ &\approx |b_0(\zeta)| \sum_{m=-\infty}^{\infty} i^m J_m(-\beta)\exp\left[im\left(\omega_{p0}\tau' + \Delta\phi'\right)\right], \end{aligned} \tag{6.1}$$

where the local coordinate $\zeta = z - v_g t$ in which z is the axis of propagation in space; t is time; $\tau' = t$; and the group velocity of the radiation pulse is $v_g \approx v_p$. Considering the time of interest, $\tau' \approx z/v_g$; the envelope of the normalised vector potential $b_0 = b(\zeta, 0)$; ω_{p0} is the plasma angular frequency; and ω_0 is the centre angular frequency of the modulated pulse.

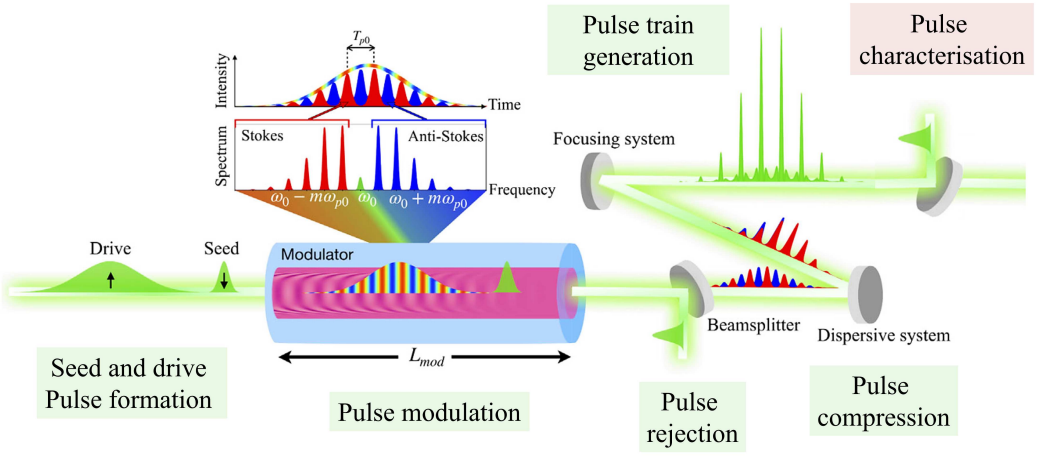


Figure 6.1: Schematic of the pulse train generation process in the P-MoPA, adopted from [119]. A long and high-energy drive pulse collinearly propagates behind a short and high-intensity seed pulse. The drive pulse and seed pulse enter a plasma channel with a modulator length of L_{mod}. The intense seed pulse excites a low-amplitude plasma wakefield which temporally modulates the drive pulse inside the plasma channel. Due to the periodic modulation of the temporal phase, the spectrum of the drive pulse develops the Stoke and anti-Stoke sidebands located at $\omega_0 \pm m\omega_{p0}$. After the drive pulse and seed pulse leave the plasma channel, the seed pulse is removed by a beam splitter. The drive pulse then passes through a dispersive optic which manipulates the relative spectral phase of each spectral sideband. The long drive pulse is therefore converted into a P-MoPA pulse train with a pulse spacing of T_{p0}. A small amount of energy from the P-MoPA pulse train is extracted for pulse characterisation (red box).

In Equation (6.1), δn and n_0 have a relationship defined by

$$n_e = n_0 + \delta n \cos\left[\frac{\omega_{p0}}{v_p}(\zeta + \Delta v\tau') + \Delta\phi\right], \tag{6.2}$$

where $\Delta v = v_g - v_p \approx 0$; and $\Delta v\tau \ll \lambda_p$.

Also in Equation (6.1), β is defined by

$$\beta = \frac{1}{2}\frac{\omega_{p0}^2}{\omega_0}\frac{\delta n}{n_0}\frac{z}{v_g}. \tag{6.3}$$

$\Delta\phi'$ in Equation (6.1) is defined by

$$\Delta\phi' = -\left(\Delta\phi + \omega_{p0}\frac{z}{v_g}\right), \tag{6.4}$$

with $\Delta\phi$ being the phase offset of a plasma wakefield.

The sum of the Bessel function term can be simplified as

$$\begin{aligned} b(\zeta,\tau) &\approx |b_0(\zeta)| \sum_{m=-\infty}^{\infty} i^m J_m(-\beta)\exp\left[im\left(\omega_{p0}\tau' + \Delta\phi'\right)\right] \\ &\approx -|b_0(\zeta)| \sum_{m=-\infty}^{\infty} J_m(\beta)\exp\left[-im\left(\varphi + \frac{\pi}{2}\right)\right], \end{aligned} \tag{6.5}$$

where $\varphi = \omega_{p0}\tau' - k_{p0}z - \Delta\phi$.

Equation (6.5) implies that the spectrum of a plasma-modulated laser pulse develops the mth spectral sidebands located at $\omega_0 \pm m\omega_{p0}$ with a relative spectral phase of $|m|\pi/2$. The field strength of the mth sidebands is controlled by the coefficient $J_m(\beta)$. Figure 6.2a shows an example of a sinusoidal plasma wakefield ($n_0 = 2.5 \times 10^{17}$ cm^{-3}, $\delta n = 0.02n_0$) excited by a seed pulse ($\tau_0 = 40$ fs, $\lambda_0 = 1030$ nm, $b_0 = 0.19$). The trailing drive pulse ($\tau_0 = 1$ ps, $\lambda_0 = 1030$ nm, $b_0 = 0.13$) is temporally modulated by the sinusoidal wakefield. The time delay, τ_d, between the two pulses is 1.7 ps.

Figure 6.2b shows the spectral intensity, $S(\lambda)$, of the drive pulse and its spectral phase $\psi(\lambda)$ after passing through a 120-mm plasma channel. The relative spectral phase $\Delta\psi$ is $|m|\pi/2$ as predicted by the theory.

6.2.2 Generation of P-MoPA pulse trains

To convert the plasma-modulated laser pulse to a P-MoPA pulse train, a pulse compressor could remove the relative spectral phase in a "V-shape" ideally. However, considering a realistic situation, the theory suggests using a dispersive optical system, such as a grating pair compressor or chirped mirrors, producing "quadratic" dispersion (GDD) to remove the "V-shaped" spectral phase by minimising χ^2 as defined by

$$\chi^2 = \sum_{-N}^{N} |J_m(\beta)| \left[\frac{1}{2}\psi^{(2)}(m\omega_{p0})^2 - (-\psi_m)\right]^2, \tag{6.6}$$

where $\psi^{(2)} = \partial\psi^2(\omega)/\partial\omega^2$; and ψ_m is the spectral phase of the mth sideband.

For $\beta \backsimeq 3.83$, the optimal compression $\psi^{(2)}_{\text{opt}}$ that can minimise χ^2 is given by

$$\psi^{(2)}_{\text{opt}} = \pm\frac{\sum_{m=1}^{N}|J_m(\beta)|m^3}{\sum_{m=1}^{N}|J_m(\beta)|m^4}\frac{\pi}{\omega_{p0}^2}, \tag{6.7}$$

where the sign of Equation (6.7) implies that either a positive or negative second-order spectral phase introduced by the optical system can provide the effect of compression on the plasma-modulated pulses.

Figure 6.3a shows a compressed drive pulse after applying a spectral phase, $\psi^{(2)} \backsimeq -1480$ fs^2. It can be seen that the ps-long drive pulse with a smooth intensity profile (shown in Figure 6.2a) is converted into a pulse train. However, there is non-zero intensity between each pulse. This was caused by the imperfect removal of the relative

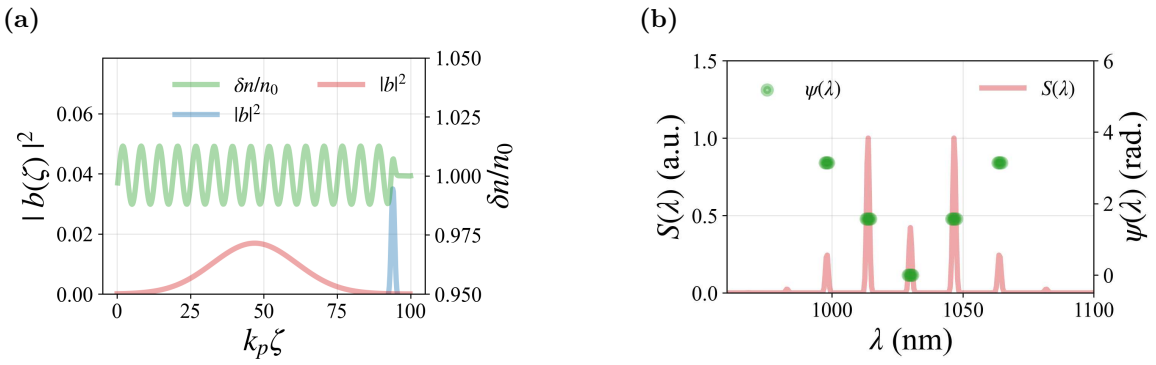


Figure 6.2: (a) Example of a plasma wakefield excited by a seed pulse followed by a drive pulse in a 1D plasma fluid model. The blue and red curves show the seed and drive pulses, respectively. The green curve shows the variation in plasma density. (b) Spectral intensity of the plasma-modulated drive pulse. The red curve and green dots show the spectral intensity and phase, respectively.

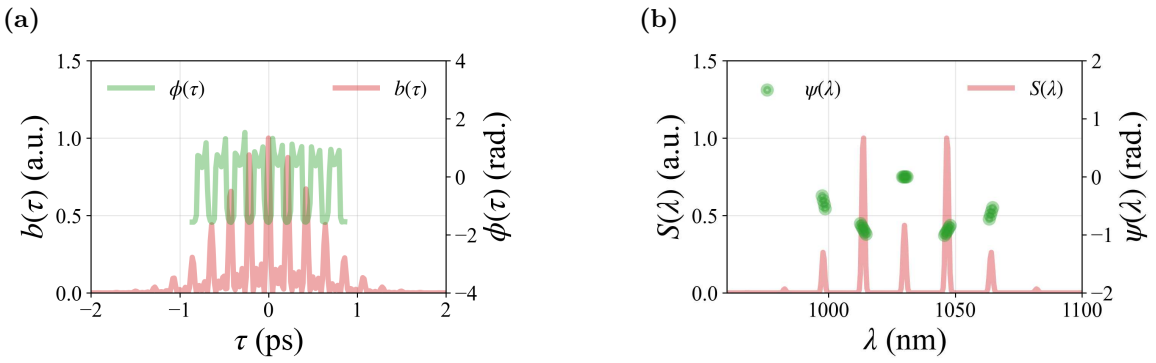


Figure 6.3: Examples of compressed drive pulse in the P-MoPA. The optimal GDD introduced to the pulse was $\psi^{(2)} \approx -1480$ fs^2: (a) Temporal intensity of the compressed drive pulse. The red and the green curves represent the temporal intensity, and the temporal phase of the pulse train, respectively; and (b) Spectral intensity of the compressed drive pulse. The red curve and green dots represent the spectral intensity and phase, respectively.

spectral phase by a quadratic phase $\psi^{(2)}$. The pulse spacing between each pulse in the P-MoPA pulse train is approximately 222 fs, which is equal to a plasma period at 222 fs given by $n_0 = 2.5 \times 10^{17}$ cm^{-3}. Figure 6.3b shows the spectrum of the compressed drive pulse. The spectral sidebands do not change in their relative intensity for a given linear system. However, the spectral phase of these spectral sidebands is manipulated by the applied $\psi^{(2)}$ such that the relative phase between each spectral sideband is smaller than $\pi/2$.

The generation of pulse trains in a P-MoPA involves:

(i) the formation of collinearly propagating seed pulses and drive pulses;

(ii) the excitation of linear plasma wakefields by the seed pulses in plasma channels;

(iii) the spectral modulation of drive pulses by the wakefield in the plasma channels;

(iv) the rejection of the seed pulses;

(v) the compression of modulated pulses by a dispersive optic; and

(vi) characterisation of the pulses.

6.2.3 Representation of P-MoPA pulse trains

Figures 6.4a and 6.4b show the structures of a P-MoPA pulse train in the temporal and spectral domains, respectively. The characteristics are summarised as follows. The

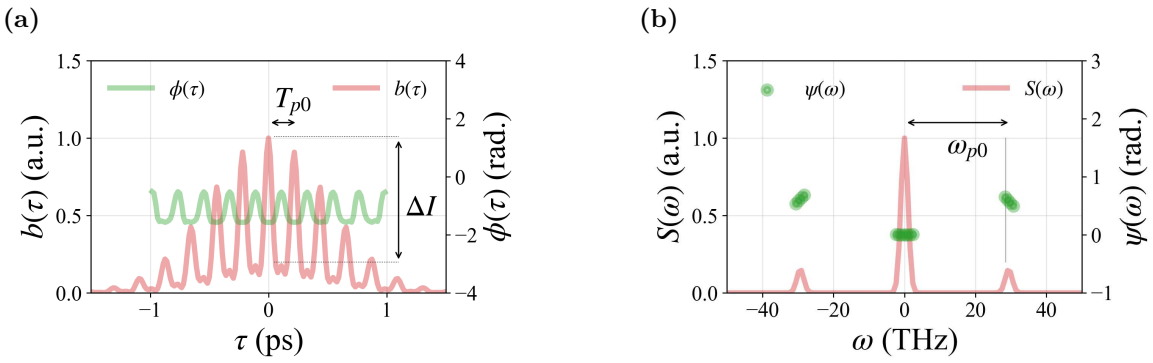


Figure 6.4: Examples of P-MoPA pulse train structures. The red curves show the temporal and spectral intensity. The green dots show the temporal and spectral phase. (a) The temporal structure. T_{P0} is the pulse spacing. (b) The spectral structure. ω_{p0} is the spectral separation of the sidebands.

P-MoPA pulse train shows:

(i) a train of short pulses separated by a plasma period T_{p0} underneath an approximately Gaussian temporal envelope of $\Delta\tau \sim 1$ ps;

(ii) non-zero intensity distribution between each low-energy pulses;

(iii) continuous and periodic temporal phase before and after pulse compression;

(iv) a fundamental laser frequency with narrow spectral sidebands well-separated by the plasma frequency, ω_{p0};

(v) a zero intensity distribution between each spectral peak;

(vi) a discontinuous global spectral phase before and after the pulse compression;

(vii) spectral sidebands with a relative phase difference of $\pi/2$ before pulse compression; and

(viii) a frequency-independent local phase across each sideband before compression and frequency-dependent local phase across each sideband after compression.

To optimise P-MoPA pulse trains for plasma wakefield excitation and verify the theoretical model, it is necessary to completely characterise the temporal and spectral structures of P-MoPA pulse trains. This includes determining the pulse spacing, T_{p0}, pulse contrast, ΔI, temporal phase, $\phi(\tau)$, and spectral phase, $\psi(\omega)$. To accomplish this task, the spectral phase of the spectrum has to be measured correctly. Because the

measured spectra provide direct information about the plasma frequency, ω_{p0}, and hence the pulse spacing from the location of the sidebands, the only thing that needs to be completely characterised is the discontinuous spectral phase of the sidebands. Therefore, the most important measurement involves the characterisation of the discontinuous local phase jumps in the spectral sidebands.

6.2.4 Frequency-resolved optical gating (revisited)

As discussed in Section 3.3.2, the FROG technique measures the time-frequency distribution of pulses and uses phase retrieval algorithm to retrieve the spectral and temporal amplitudes of a test pulse. However, it is not able to distinguish the signal field, E_{sig}, with the mathematical forms

$$\begin{aligned} &E_{\text{sig}}(x,y)\exp(j\phi_0), \\ &E_{\text{sig}}(x-x_0,y-y_0), \text{and} \\ &E^*_{\text{sig}}(-x,-y), \end{aligned} \tag{6.8}$$

where x and y represent the time delay and frequency, respectively; and ϕ_0, x_0, and y_0 are constants.

This implies that the FROG algorithms cannot retrieve the zeroth or first-order spectral phases, ψ_0 and ψ_1, respectively because the measured FROG traces are the magnitude-squared quantity containing no absolute phase or time references [240, 241]. Recall that the temporal representation of P-MoPA pulse trains in Equation (6.5) contain a discontinuous ψ_0, which is only dependent on the mode of the spectral sidebands. This zeroth-order spectral phase will appear in E_{sig}

This limit imposes a problem on the diagnostics of P-MoPA pulse trains, which requires the complete measurement of the discontinuous spectral phase contained in the spectra of P-MoPA pulse trains. Hence, all the FROG techniques that use iterative Fourier-transform algorithms cannot be solely used to accomplish the task of pulse measurement in P-MoPA.

6.2.5 Self-referenced spectral interferometry

Spectral phase interferometry for direct electric field reconstruction (SPIDER) is a type of self-referenced SI technique developed by Iaconis et al. [242]. An optical setup of the SPIDER technique is shown in Figure 6.5. The technique uses a pulse pair and the ancillary pulse to produce a sum-frequency generation (SFG) pulse pair. The SFG pulse interferes with its frequency-sheared replica to form a SPIDER interferogram, $I_{\mathrm{sp}}(\omega)$, recorded by the spectrometer.

The measured interferogram, $I_{\mathrm{sp}}(\omega)$, can be written as

$$\begin{aligned} I_{\mathrm{sp}}(\omega) &= |E(\omega) + E(\omega - \Omega)\exp(i\omega\tau)|^2 \\ &= I(\omega) + I(\omega - \Omega) + 2\sqrt{I(\omega)I(\omega - \Omega)}\cos(i\phi_{\mathrm{sp}}), \end{aligned} \tag{6.9}$$

where the amplitude of the test pulse $E(\omega) = |A(\omega)|\exp[i\phi(\omega)]$; $A(\omega)$ is the envelope function, $\phi(\omega)$ is the phase to be measured; Ω is a constant frequency shear; and the spectral phase $\phi_{\mathrm{sp}} = \phi(\omega) - \phi(\omega - \Omega) + \omega\tau$.

Using the calibrated interferogram, $I_{\mathrm{cal}}(\omega)$, which is the spectrum of the pulse pair centred at ω_0, τ can be calculated by taking the inverse Fourier-transform of $I_{\mathrm{cal}}(\omega)$ and finding the position of the ac sideband. After removing the linear phase $\omega\tau$, the

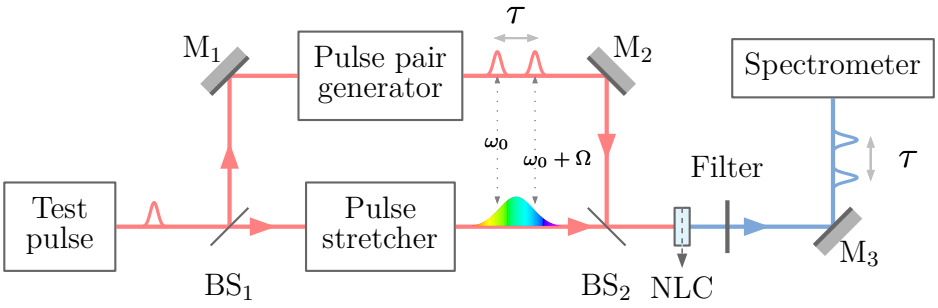


Figure 6.5: Schematic of a SPIDER setup. BS_n—beam splitter; M_n—mirror; and NLC—nonlinear crystal; The test pulse from the source is split into two pulses by BS_1. One pulse and its replica are generated and separated by a time delay, τ. The pulse stretcher generates a highly chirped test pulse (ancillary pulse). The pulse pair and the ancillary pulse are beam-combined by BS_2 and focused into the NLC to generate the SFG signal. The fundamental frequency components are filtered out by a low-pass filter. The SFG signal or the SPIDER interferogram is measured by the spectrometer.

spectral phase difference, $\Delta\phi_{\mathrm{sp}}$, is given as

$$\begin{aligned}\Delta\phi_{\mathrm{sp}} &= \Omega\frac{\phi(\omega)-\phi(\omega-\Omega)}{\Omega}\\ &\simeq \Omega\frac{\partial\phi(\omega)}{\partial\omega}.\end{aligned} \tag{6.10}$$

For a case in which the linear chirp introduced by the pulse stretcher cannot be accurately measured, $\Omega = |\omega_1 - \omega_2|$, where ω_1 and ω_2 are the centre frequencies of the SFG pulse spectra with and without spectral shear. For a case in which the linear chirp is known, for example, using a block of glass with a known length as a pulse stretcher, Ω can be related to the known GDD or $\psi^{(2)}$. Hence, $\Omega = \tau/\psi^{(2)}$. After finding Ω, $\phi(\omega)$ can be obtained by $\int d\omega\Delta\phi_{\mathrm{sp}}/\Omega$.

The Fourier-transform SI (FTSI) algorithm used in the SPIDER technique is illustrated in Figure 6.6.

Based on equation (6.10), it can be understood that the SPIDER technique and its advanced version — the spatially encoded arrangement for SPIDER (SEA-SPIDER)

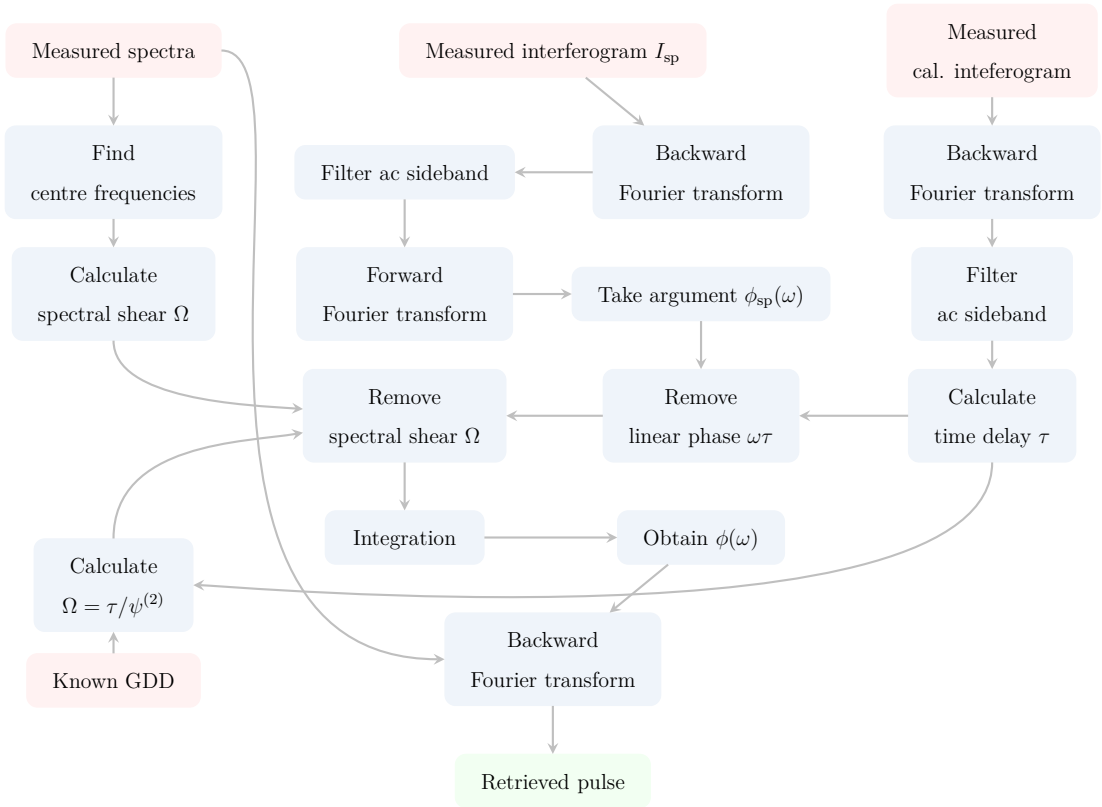


Figure 6.6: Schematic of an FTSI algorithm used in SPIDER. The pink boxes indicate the input data. The light-blue boxes emphasize the numerical procedures used in pulse reconstruction. The green box is the final step in obtaining the retrieved pulse.

— measure the scaled derivative of $\phi(\omega)$ in the test pulse [243]. This means that the SPIDER technique cannot measure the zeroth-order or first-order spectral phases. For a pulse with a discontinuous spectral content, such as plasma-modulated pulses or P-MoPA pulse trains, the relative spectral phase of each sideband cannot be measured correctly because there is no reference phase in the region between each sideband.

It is worth mentioning another type of self-referenced SI commonly known as the Wizzler technique in the ultra-fast optical measurement community [244]. The Wizzler technique utilises a third-order nonlinear optical effect known as — crossed-polarized wave (XPW) generation — to flatten the spectral phase of the input pulse to be measured [245, 246]. The phase ϕ_{XPW} is treated as a reference phase and used in an FTSI algorithm for the retrieval of the input pulse [247]. Because this technique relies on phase flattening and an FTSI algorithm similar to the FTSI algorithm used in SPIDER, the Wizzler technique is not able to measure pulses with complicated structures and phases. This includes the relative local phase in discontinuous spectra.

6.2.6 Cross-referenced spectral interferometry

In P-MoPA pulse trains, the relative phase is contained in well-separated multiple-frequency components. To verify the P-MoPA theory, it is important to characterise this type of phase. Keusters et al. [248] provided a detailed theoretical study on the relative phase ambiguities in different types of pulses with well-separated multiple-frequency components and gave solutions for tackling the task of pulse characterisation. One of the solutions relied on the cross-referenced SI, which requires a well-characterised pulse with a broad spectral bandwidth to serve as the reference pulse.

The idea of using cross-referenced SI to characterise extremely complex pulses (TBP ~ 400) has been demonstrated by Bowlan et al. [249]. The technique developed in their experiment is called spatial encoded arrangement for temporal analysis by dispersing a pair of light E-fields (SEA-TADPOLE). An optical layout of SEA-TADPOLE is shown in Figure 6.7. The reference pulse and test pulses are collimated by the lens and spectrally resolved by the grating along the x-z plane. The collimated pulses are imaged at the

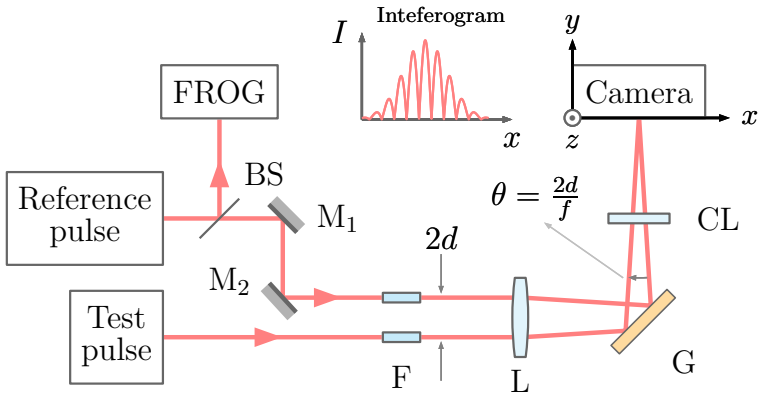


Figure 6.7: Schematic of a SEA-TADPOLE setup. BS—beam splitter; M_n—mirror; F—fibre; L—spherical lens; CL—cylindrical lens; G —grating; and f—focal length. The reference pulse is previously characterised by the FROG device. The reference pulse and the test pulse that passes through the optical fibres are separated by $2d$ and used for beam alignment. The lens L with a focal length of f collimates the input light from the exit of the fibres. The cylindrical lens images the collimated and spectrally resolved reference pulse and test pulse crossing by an angle $\theta_{cs} = 2d/f$ at the camera.

camera and cross with a crossing angle, θ_{cs}. The interferogram—the SEA-TADPOLE trace—is thus measured by a 2-D camera.

The SEA-TADPOLE trace, $S(x, \tilde{\omega})$, can be written as

$$\begin{aligned} S(\tilde{\omega}, x) &= |A_t(\tilde{\omega}, x) + A_r(\tilde{\omega}, x)|^2 \\ &= |A_t(\tilde{\omega}, x)|^2 + |A_r(\tilde{\omega}, x)|^2 + A_t(\tilde{\omega}, x)A_r^*(\tilde{\omega}, x) \\ &\times \exp\left[2ik\sin(\theta_{cs}x) + i\Delta\psi(\tilde{\omega})\right] + \text{c.c.} \end{aligned} \tag{6.11}$$

where $\Delta\psi(\tilde{\omega}) = \psi_r(\tilde{\omega}) - \psi_t(\tilde{\omega})$; $\psi_r(\tilde{\omega})$; ψ_t is the spectral phase of the reference pulse and test pulses, respectively; A_r and A_t are the spectral amplitude of the reference pulse and the test pulse, respectively; $\tilde{\omega} = \omega - \omega_0$; $k = 2\pi/\lambda_0$; x is the position; and $\theta_{cs} = 2d/f$.

Figure 6.8 shows the FTSI algorithm used in the SEA-TADPOLE technique. The SEA-TADPOLE algorithm is a direct phase retrieval algorithm, which implies very fast and straightforward pulse reconstruction. Compared to the iterative phase retrieval algorithms, FROG techniques usually suffer from beam misalignment and image distortion. The phase retrieval results from the FROG techniques are usually not stable if the FROG traces have unremovable systematic errors.

There are several advantages of using the SEA-TADPOLE method. First, the algorithm is a direct phase retrieval algorithm, which implies high stability and accuracy of phase reconstruction. Second, it is very sensitive to the input signal, which means

that it is suitable for the measurement of long pulses in a single shot. Third, it supports the measurement of spatio-temporal coupling. For these reasons, it is worth considering this technique for the characterisation of P-MoPA pulse trains.

6.3 Simulation

6.3.1 Simulation conditions

To understand whether a P-MoPA pulse train generated in the P-MoPA can be characterised, a simulation work was conducted. Here, P-MoPA refers to a low-energy P-MoPA pulse train that will be demonstrated in in the first proof-of-principle experiment. To simplify the analysis, several experimental conditions, such as non-uniformity of the laser beam profile, mismatch of the laser spot size in the plasma channels and the pulse-guiding quality, were not taken into account.

To emulate the available seed and drive pulses in the proof-of-principle P-MoPA experiment, it was assumed that the drive pulse was generated from a diode-pumped

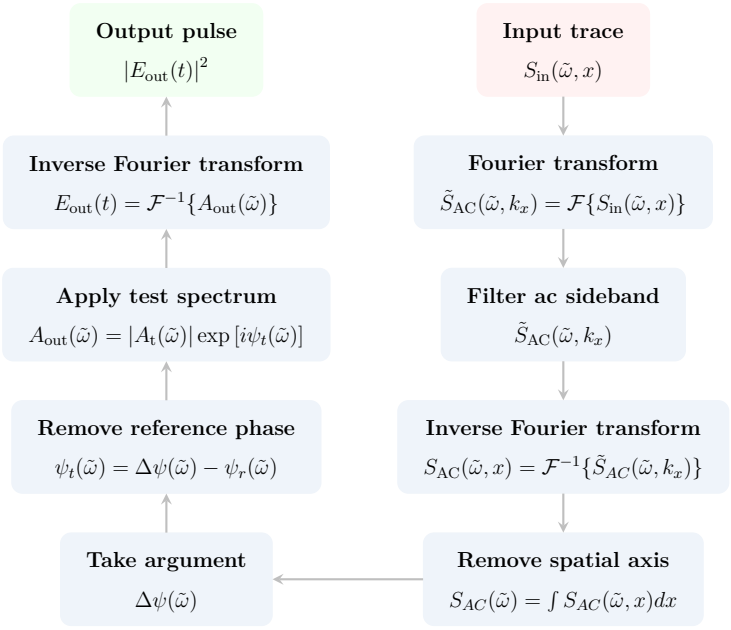


Figure 6.8: Schematic of an FTSI algorithm in SEA-TADPOLE. First, the input SEA-TADPOLE trace $S_{\mathrm{in}}(\tilde{\omega}, x)$ is Fourier transformed into the k-domain. Second, one of the ac sidebands $\tilde{S}_{\mathrm{AC}}(\tilde{\omega}, k_x)$ is selected and inverse Fourier-transformed back to the x-domain as $S_{\mathrm{AC}}(\tilde{\omega}, x)$. Third, the spatial axis is removed by integrating $S_{\mathrm{AC}}(\tilde{\omega}, x)$ along the x-axis. Fourth, the spectral phase $\Delta\psi(\tilde{\omega})$ is extracted from $S_{\mathrm{AC}}(\tilde{\omega})$. The spectral phase of the test pulse $\psi_t(\tilde{\omega})$ can be obtained by subtracting $\psi_r(\tilde{\omega})$ from $\Delta\psi(\tilde{\omega})$. Finally, the test pulse can be retrieved by taking the inverse Fourier-transform of the test spectrum multiplied by $\exp[i\psi_t(\tilde{\omega})]$.

Yb:YAG thin-disk laser system [250]. The drive pulse had a pulse duration of 1.3 ps and an FWHM spectral bandwidth of 1.3 nm centre at 1030 nm. The seed pulse was assumed to be generated by the self-phase modulated drive pulse in a Herriott cell [239]. The compressed seed pulse had a pulse duration of 37 fs and an FWHM spectral bandwidth of 70 nm centred at 1030 nm.

Figure 6.9a shows the input spectra of the drive and seed pulses adopted from Kaumanns' thesis [251]. The seed pulse was assumed to be generated by the self-phase modulation of the drive pulse in a Herriot-type cell. The seed and drive pulses are shown in Figure 6.9b. The spectral and temporal phases of the drive pulse were assumed to be flat and so are not shown in the Figures 6.9a and 6.9b. The spectral phase and spectrum of the seed pulse showed periodic oscillation, which is a typical feature resulting from the effect of the self-phase-modulated drive pulse [252]. The seed pulse and drive pulse both had Gaussian temporal intensity profiles.

Following the simulation conditions established by Jakobsson et al. [119], and taking into account the most realistic experimental conditions, the 1-D P-MoPA theory was adopted. It was assumed that the drive pulse experienced a low-amplitude periodic plasma density modulation in a plasma channel with $L_d = 50$ mm. After the plasma-modulation stage, the modulated drive pulse passed through a prism-pair compressor with an adjustable length of L_{pc} ranging from 0 mm to 80 mm. The prism pair is made of glass, BK7, with a GVD of 25 fs^2/mm at 1030 nm. To simplify the analysis,

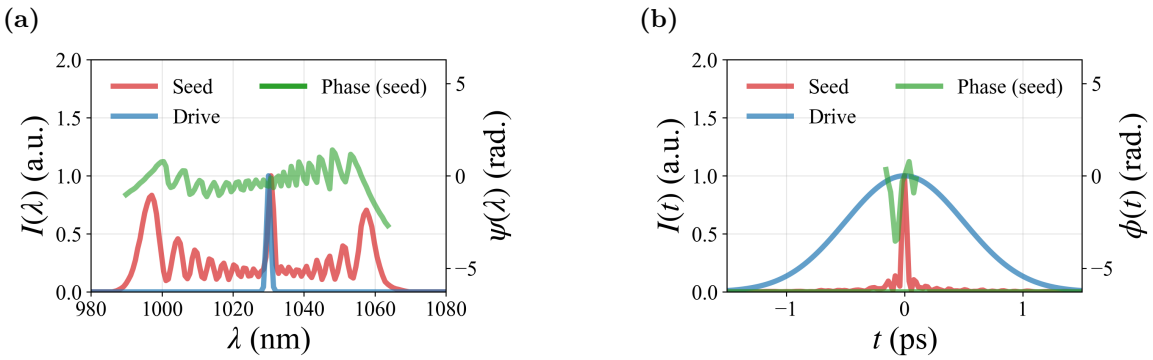


Figure 6.9: (a) Input spectra of the drive (blue) and seed (red) pulses. The spectral phase of the seed pulse is indicated by the green curve. (b) Temporal intensity of the seed (red) and drive (blue) spectra. The temporal phase of the seed pulse is indicated by the green curve.

it was assumed that $L_{\mathrm{pc}} = 60$ mm, which corresponded to a total GDD of 1,500 fs^2. It should be mentioned that this prism-pair compressor was designed by the author's colleague, Sebastian Kalos.

Figures 6.10a and 6.10b show input spectra and pulse envelopes of the plasma-modulated pulse and P-MoPA pulse train under the simulation conditions. The spectra of both pulses had the same spectral sidebands at 1030 nm ± 16 nm. The spectral phase of both pulses were discontinuous. The phase of the P-MoPA pulse train had slopes of different signs for different sidebands. The spectral phase of the P-MoPA pulse train was closer to zero than the phase of the plasma-modulated drive pulse, which resulted from the introduction of the spectral phase of the prism pair compressor. The temporal profiles of the plasma-modulated pulse was Gaussian. In contrast, the P-MoPA pulse train had distinct peaks separated by 222 fs.

To simplify the analysis, it was assumed that the timing jitter between the seed and drive pulses was zero and thus the time delay separation between the seed and drive pulses was 1.7 ps following the condition given in Jakobsson et al. [119]. However, it should be noted that the drive pulse would experience the plasma wakefield excited by the seed pulse at different phase in the co-moving frame if the timing jitter was nonzero. This would resulted in a source of nonzero phase-offset, $\Delta\phi$, as shown in Equation (6.1).

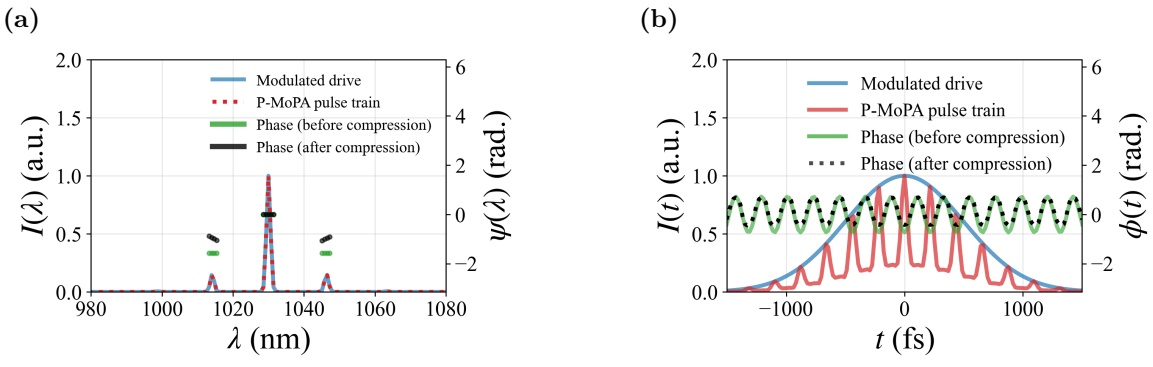


Figure 6.10: (a) Spectra of the plasma-modulated drive pulse (blue line) before pulse compression and the P-MoPA pulse train (red dotted line) after pulse compression. The spectral phases of the plasma-modulated drive pulse and the P-MoPA pulse train are shown by the green and the black curves, respectively. (b) Temporal intensity of the plasma-modulated drive pulse (blue line) and the P-MoPA pulse train (red line). The temporal phases of the plasma-modulated drive pulse and the P-MoPA pulse train are shown by the green and black dotted curves, respectively.

Considering the plasma density instability that would happen in a real experiment, the simulation assumed that the mean n_0 on axis in the plasma channel was $2.5 \times 10^{17}\text{cm}^{-3}$ accompanied by a 5% of standard deviation (SD) about the mean according to the observation in the past experiments related to plasma channels done by the author's colleagues. This effect influenced β and $\Delta\phi'$, causing a shot-by-shot instability of the plasma density modulation.

To estimate the noise from the detectors in the simulation, a CMOS imaging sensor was assumed to measure the pulses of interest. In the two systems, the shot noise, dark current noise, quantisation noise and noise floor were all included in the noise model [201]. The camera was assumed to be a Sony IMX 249 silicon imaging sensor with a bit depth of 12 and a well capacity of 33,000 e^-/pixel [253]. Accordingly, the signal-to-noise ratio of the detectors was approximately 43 dB. The headroom was assumed to be 30% of the maximum well capacity in order to emulate a realistic experimental condition for data acquisition.

6.3.2 Characterisation of reference pulses

As mentioned in Section 6.2.6, a reference pulse with a broad and continuous spectrum is required for the complete spectral phase retrieval of a test pulse with multiple and discontinuous spectral content. In this section the aim is to understand whether the spectral phase of a reference pulse used in the P-MoPA can be correctly characterised, and what types of FROG techniques can be adopted for this measurement.

In the P-MoPA, the four pulses directly available for the task of pulse characterisation—the seed pulse, drive pulse, plasma-modulated drive pulse and P-MoPA pulse train—are shown in figures 6.9 and 6.10, respectively. Among these four pulses, only the seed pulse has continuous spectral components whose bandwidth is wider than the spectrum of the plasma-modulated drive pulse and the P-MoPA pulse train. Therefore, the seed pulse can serve as the reference pulse in the SEA-TADPOLE technique.

Based on the pulse measurement techniques available in OPAL, blind FROG and cross-correlation FROG techniques were considered for the characterisation of the seed pulse. The seed pulse can form four types of FROG traces using the other available

pulses. For instance, these pulses include the spectrally filtered test pulse, the drive pulse, the plasma-modulated drive pulse and the P-MoPA pulse train. A spectrally filtered seed pulse can be generated from the original seed pulse passing through a bandpass filter whose FWHM bandwidth is 10 nm, centred at 1030 nm. These pulses are called gate pulses in this section.

Figure 6.11 shows the FROG traces formed by the seed pulse and the four gate pulses individually. Among these four traces, Figure 6.11a shows minimal fine structures in the FROG trace. The time-frequency distribution of this FROG trace implies a minimal amount of the second-order spectral phase. Comparing Figures 6.11b and 6.11c, the FROG trace of the latter showed more complex fine structures than Figure 6.11b even though these two FROG traces had similar convolution and cross-correlation intensity profiles.

Comparing Figures 6.11c and 6.11d, it can be seen that there are subtle differences

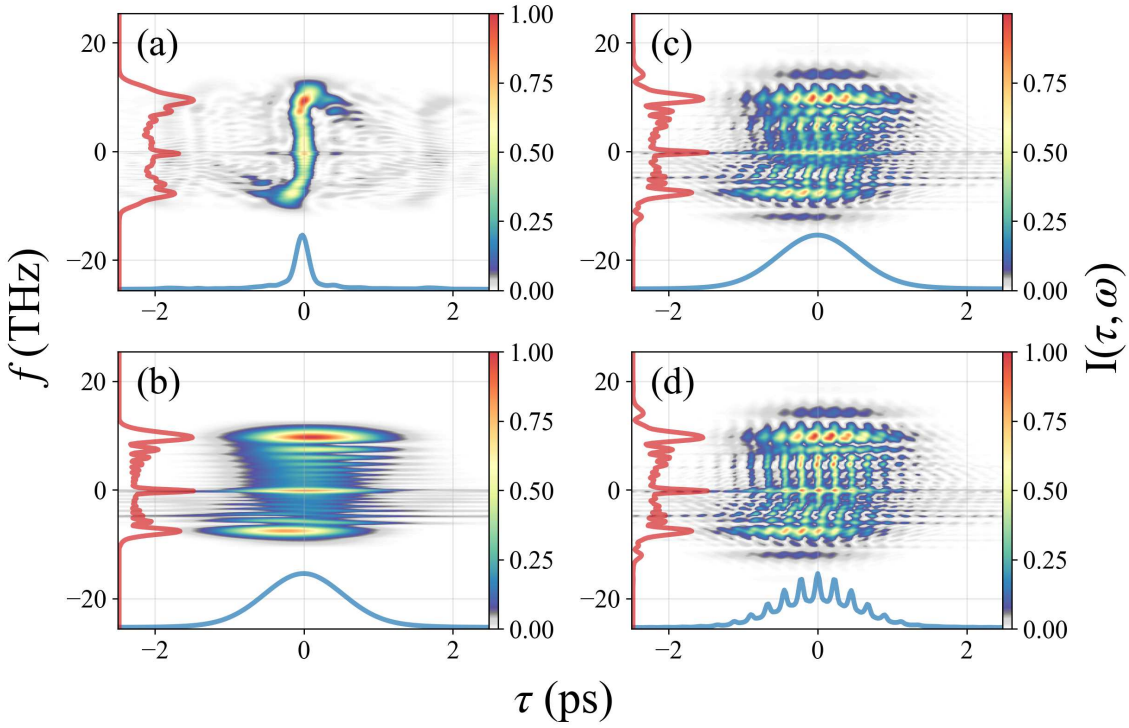


Figure 6.11: Blind and cross-correlation FROG traces in the P-MoPA. The red and blue curves show the normalised convolution and cross-correlation intensity from the FROG traces, respectively.(a) Blind FROG trace formed by the seed pulse and its spectrally filtered counterpart. (b) Cross-correlation FROG trace formed by the seed pulse and drive pulse. (c) Cross-correlation FROG trace formed by the seed pulse and the plasma-modulated drive pulse. (d) Cross-correlation FROG trace formed by the seed pulse and P-MoPA pulse train.

in the two FROG traces. In the middle area in Figure 6.11c, the time-frequency distribution is blurred and has lower contrast than the same area in Figure 6.11d. The difference can be simply revealed by their cross-correlation intensity profiles, although the two FROG traces have similar convolution intensity profiles. The cross-correlation intensity in Figure 6.11d develops periodic intensity peaks, which do not appear in the cross-correlation intensity in Figure 6.11c.

Using the ePIE algorithm discussed in Section 3.4.3, the spectral phase of the seed pulse were retrieved from the four FROG traces, as shown in Figure 6.12. Qualitatively, the spectral phase of the seed pulse retrieved from the FROG trace shown in Figure 6.11b did not match the input spectral phase of the seed pulse. In contrast, the spectral phases was correctly retrieved by the ePIE algorithm from the FROG traces shown in Figures 6.11a, 6.11c and 6.11d.

Table 6.1 summarises the phase retrieval results for the seed pulse using the ePIE algorithm. Cases (a) - (d) shown in the top column are the phase-retrieval results that correspond to the FROG traces shown in Figure 6.11a, 6.11b, 6.11c and 6.11d. Comparing the RMS intensity-weighted spectral phase error of the retrieved seed pulse σ_ψ, Case (b) yielded an approximately six times higher σ_ψ than the other three cases. In Case (a), its RMS spectral intensity error σ_ω was much higher than σ_ω in Cases (c) and (d) although the σ_ψ in Case (a) is slightly higher than the σ_ψ in Cases (c) and (d).

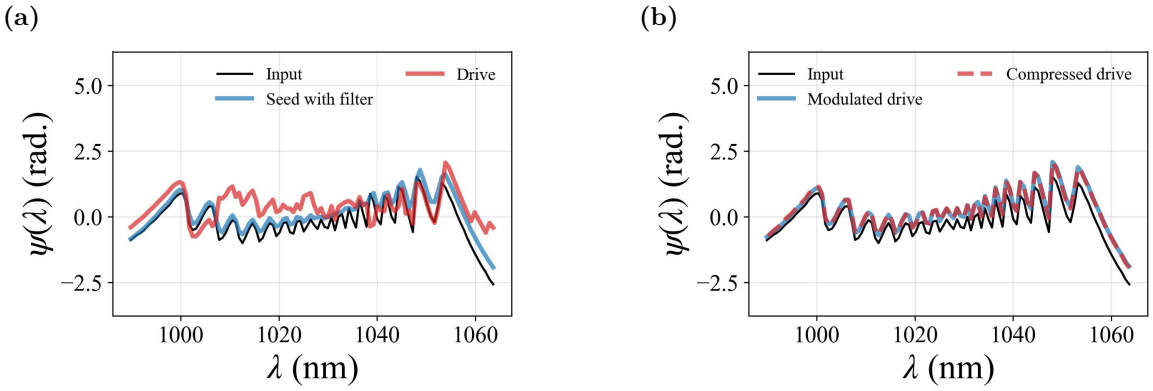


Figure 6.12: Retrieved spectral phase of the seed pulse. The black curve shows the input spectral phase. (a) Retrieved spectral phase from the FROG traces shown in Figures 6.11a (blue curve) and 6.11b (red curve). (b) Spectral phase retrieved from the FROG traces shown in Figures 6.11c (blue curve) and 6.11d (red curve).

	(a)	(b)	(c)	(d)
σ_t	1.66 ± 1.02	9.45 ± 2.90	1.75 ± 1.14	1.59 ± 0.79
σ_ω	2.48 ± 0.08	7.87 ± 0.07	0.01 ± 0.01	0.01 ± 0.01
σ_ϕ	0.08 ± 0.01	4.88 ± 0.01	0.05 ± 0.13	0.04 ± 0.01
σ_ψ	0.27 ± 0.09	1.30 ± 0.52	0.21 ± 0.04	0.21 ± 0.04

Table 6.1: Phase retrieval results for characterising the seed pulse. The terms σ_t, σ_ω, σ_ϕ and σ_ψ represent the RMS temporal intensity error, RMS spectral intensity error, RMS intensity-weighted temporal phase error and RMS intensity-weighted spectral phase error, respectively. Cases (a) - (d) represents the cases using the FROG traces shown in figures 6.11a - 6.11d, respectively.

In conclusion, it was found not suitable to use the seed pulse retrieved from the cross-correlation FROG traces shown in Figures 6.11a and 6.11b as the reference pulse because the PIE algorithm could not retrieve the seed pulse more accurately from the FROG traces that the Case (c) and (d). To have a more accurate reference pulse, the technique generating the FROG traces shown in Figure 6.11c and 6.11d are recommended because the retrieval results showed a retrieved spectral phase and a spectral intensity with much higher accuracy.

6.3.3 Characterisation of plasma-modulated laser pulses

In Section 6.3.2, it was shown that the reference (seed) pulse could be correctly characterised by the cross-correlation FROG technique. In this section, the aim is to demonstrate that the plasma-modulated drive pulse can be characterised by the SEA-TADPOLE technique, as shown in Figure 6.7, in a simulation.

To simplify the analysis, it was assumed that the spot size of the two crossing beam in a SEA-TADPOLE device, D_s, was 1 mm, the separation of fibres, was $2d = 1$ mm in the x-axis, and the focal length of the collimation lens was $f = 150$ mm. The spatial beam profile was assumed to be uniform and there was no spatial-temporal coupling in the reference pulse and the signal pulse. The reference (seed pulse) and test pulses (plasma-modulated drive pulse) were assumed to have the same energy. The initial conditions used to produce the input pulses were discussed in Section 6.3.1. The reference pulse was assumed to be the well-characterised seed pulse provided by the FROG technique. The

test pulses were the plasma-modulated drive pulse before and after pulse compression. The time delay, τ_s, between the reference and test pulse was assumed to be zero. The input pulses and spectra of the test pulses were shown in Figure 6.10.

The simulated SEA-TADPOLE traces of the test pulse before and after pulse compression, using Equation (6.11), are shown in Figures 6.13a and 6.13b, respectively. It is clear that the crossing beam angle resulted in interference fringes in the x-axis. Comparing the two SEA-TADPOLE traces, there was little observable difference. This is because only the spectral phase of the pulses were changed by the compressor. Taking a closer look at the regions in the red rectangles as shown in Figure 6.13c and 6.13d, the interference fringes of the sidebands shifted slightly along the vertical axis. However, the interference fringes of the fundamental frequency did not change with respect to both axes. This indicates that the values of the discontinuous spectral phase were converted to the relative positions of interference fringes along the x-axis.

Following the FTSI algorithm discussed in Section 6.2.6, the Fourier transform of the SEA-TADPOLE traces in the x-axis were computed and are shown in Figure 6.14. The ac signal showed a spectral intensity distribution similar to the spectrum of the test pulse. Comparing the two SEA-TADPOLE traces in the k_x domain, there was no directly observable difference. After filtering out the region outside the blue rectangle in Figure 6.13 and integrating the trace along the k_x-axis, the spectral phase of the test pulses, ψ, could be extracted by the tan2 Python routine.

The retrieved spectral phases of the plasma-modulated drive pulses, ψ, before and after pulse compression are shown in Figures 6.15a and 6.15b, respectively. The Fourier-transformed interference patterns showed no observable difference, indicating that the modulus of the patterns were equal. However, The spectral phases of the two test pulses before and after pulse compression were retrieved with ϵ_ω values of 0.11 and 0.08 radians, respectively. The spectra, $I(\lambda)$, of the two test pulses could be easily measured by dedicated infrared IR spectrometers.

Using the measured spectra from the IR spectrometer and the retrieved spectral phases from the SEA-TADPOLE device, the temporal structures of the test pulses before and after pulse compression can be obtained by taking the inverse Fourier-transform of

the spectra and multiplying this by the exponential terms of the retrieved spectral phases. The reconstructed temporal intensity, $I(t)$, of the test pulses before and after pulse compression are shown in Figures 6.16a and 6.16b, respectively. The temporal

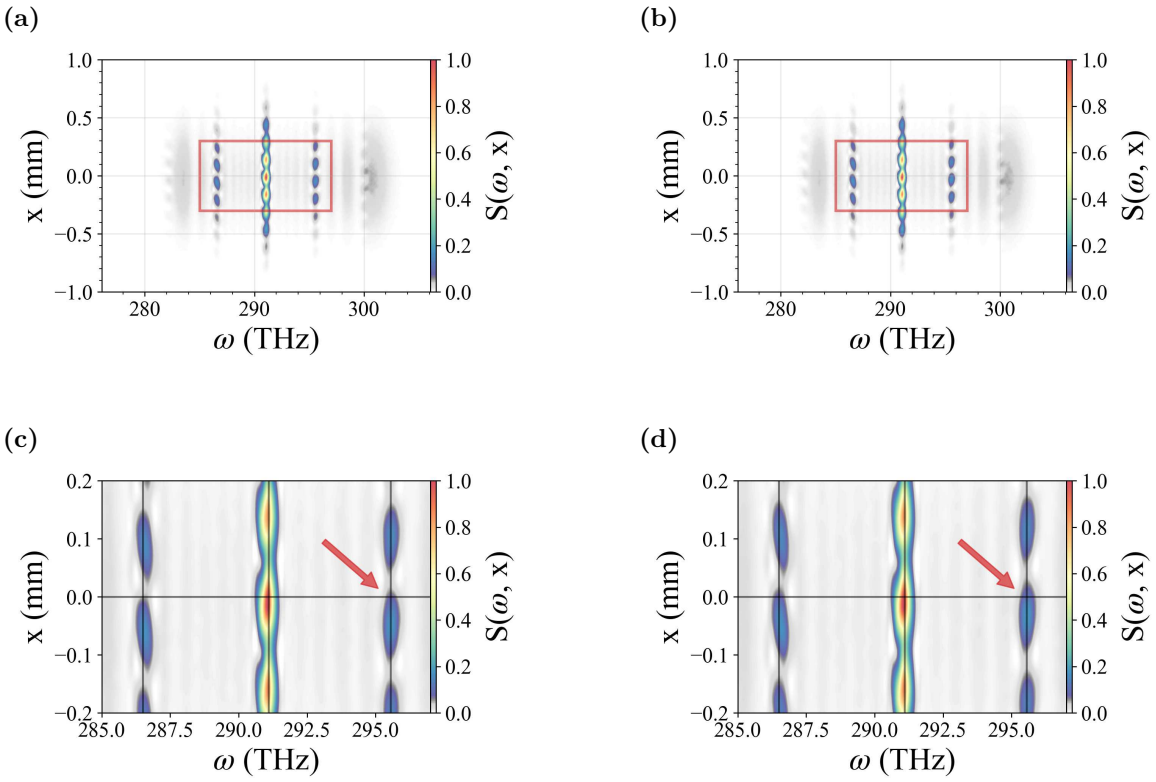


Figure 6.13: SEA-TADPOLE traces of the plasma-modulated drive pulse: (a) before pulse compression; (b) after pulse compression; (c) zoomed-in version of (a); and (d) zoomed-in version of (b). The red rectangles highlight the subtle difference between the two SEA-TADPOLE traces. The black lines are references lines for graph comparison.

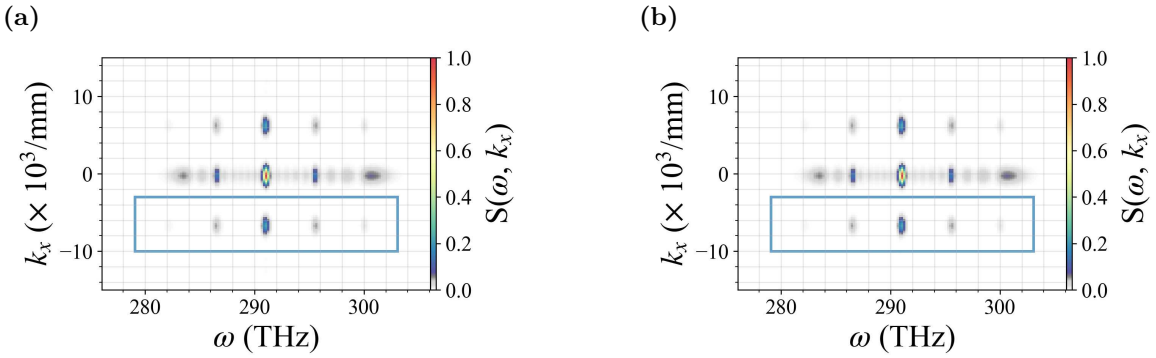


Figure 6.14: Fourier-transformed SEA-TADPOLE traces of the plasma-modulated drive pulse: (a) before; and (b) after pulse compression. The blue rectangles highlight the region selected for the FTSI algorithm in the SEA-TADPOLE technique.

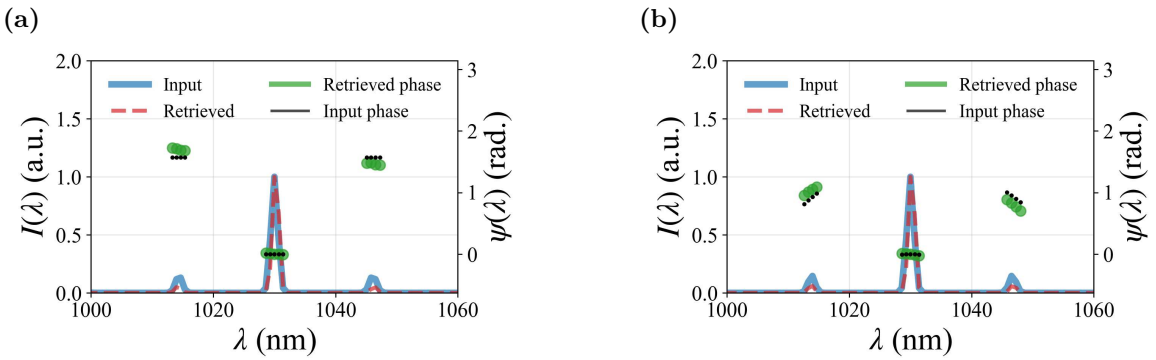


Figure 6.15: Retrieved spectra of the plasma-modulated drive pulse: (a) before; and (b) after pulse compression.

phases of the test pulses retrieved before and after pulse compression were 0.06 and 0.02 radians, respectively. As can be seen from Figure 6.16a, the temporal intensity, $I(t)$, and phase, ϕ, were retrieved correctly.

In conclusion, simulation results for the phase retrieval process of the test pulses were achieved. Under the defined initial conditions, the plasma-modulated drive pulse before and after pulse compression could be correctly retrieved by the SEA-TADPOLE technique, with the RMS intensity-weighted phase error being below 0.11 radians in the simulation. The simulation demonstrates that the P-MoPA pulse trains can be characterised by the SEA-TADPOLE technique with very high accuracy.

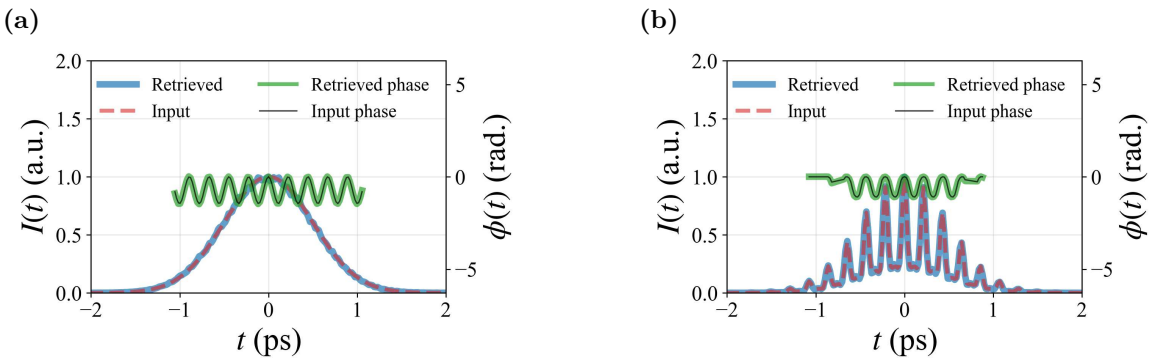


Figure 6.16: Retrieved plasma-modulated drive pulses: (a) before; and (b) after pulse compression.

6.4 Experiment

6.4.1 Design considerations of the pulse measurement device

To provide an accurate pulse measurement instrument for the complete characterisation of P-MoPA pulse trains, including the plasma-modulated pulses before pulse compression, it was necessary to correctly select several optical components, including the nonlinear crystal and spectrometer in the cross-correlation FROG and the fibre and optical grating in the SEA-TADPOLE. In the following, the pulse measurement device with cross-correlation FROG and SEA-TADPOLE devices is referred to as the P-MoPA pulse train measurement device.

With the desire to characterise three pulses (seed, plasma modulated drive, and P-MoPA pulse train) in the P-MoPA pulse measurement device, ideally, the FROG device would do this in a single-shot. This would require a temporal window of 4 ps and a delay time window of 8 ps, and because the spectral content of the seed pulse occupies a spectral window of 80 nm at $\lambda_0 = 1030$ nm, a spectral window of 100 nm would be needed.

Based on these requirements, a nonlinear crystal made of BBO ($\theta_{\text{cut}} = 44.3°$) was chosen. Using Equation (3.50), the phase-matching angle, θ_p, was calculated as approximately 21°. Using equation (3.46), the thickness of the crystal was estimated to be 50 μm. Hence, this nonlinear crystal would support a time delay window of 10 ps and a phase-matching bandwidth of approximately 100 nm.

To support enough spectral resolution to cover the temporal window of 4 ps, the imaging system used in the FROG setup, as discussed in Section 5.2.1 was adopted. This can support a spatial resolution of 15.6 μm with a 1:1 magnification. Based on the analysis presented in Section 4.4.4, the imaging spectrometer in the FROG device would need a grating with a groove density of 1200 l/mm, which could provide a 50-nm spectral window at $\lambda_0 = 515$ nm using a CMOS sensor (pixel size – 5.86 μm, sensor size – 11×7 mm^2, IMX249, Sony). Hence, the temporal window available to represent each measured pulse would be approximately 9 ps.

The same CMOS sensor (IMX249, Sony) was adopted in the SEA-TADPOLE device. This could provide the maximum available window in the spatial frequency domain of approximately 171×10^3 mm^{-1}. Using Equation 6.11, a maximum separation between the two fibres, d, was determined to be approximately 13 mm. Using Equation 4.17, a grating with a groove density of 600 l/mm was calculated as being able to provide an approximately 114-nm spectral range for measuring the seed pulse spectrum. Assuming that the imaging spectrometer could provide a spatial resolution of 15.6 μm at $\lambda_0 =$ 1030 nm, then the spectral resolution of 0.25 nm would be available. Therefore, the maximum temporal window that could be supported by the SEA-TADPOLE device would be approximately 14 ps.

6.4.2 Optical layout of the pulse measurement device

Based on the discussion in Section 6.4.1, an optical layout of the P-MoPA pulse measurement device is shown in Figure 6.17. There are generally three parts in the P-MoPA pulse measurement device — the beam combiner, cross-correlation FROG and SEA-TADPOLE.

The beam combiner highlighted by the light green area is used to combine the seed, plasma-modulated drive pulse, and P-MoPA pulse train in the same beam path. These three pulses are referred to as the test pulses in the following. The reference pulse propagates in the beam path which is indicated by the red lines. The reference pulse and test pulses are separately focused by two cylindrical mirrors, CM_1 and CM_2. The focused pulses cross at the nonlinear BBO crystal in order to generate the SHG auto-correlation and cross-correlation signal. The SHG auto-correlation is generated by the reference pulse and its replica for calibration of the FROG trace image.

In the cross-correlation FROG device (highlighted by the pink area in Figure 6.17), the cross-correlation signals formed by the reference and test pulses are spectrally resolved by the imaging spectrometer using an infinity-corrected microscope imaging system and a grating with a groove density of 1200 l/mm. The dove prism is used to rotate the image of the cross-correlation signal in order to obtain a simpler beam geometry in the imaging spectrometer. The polariser is used to remove the scattered

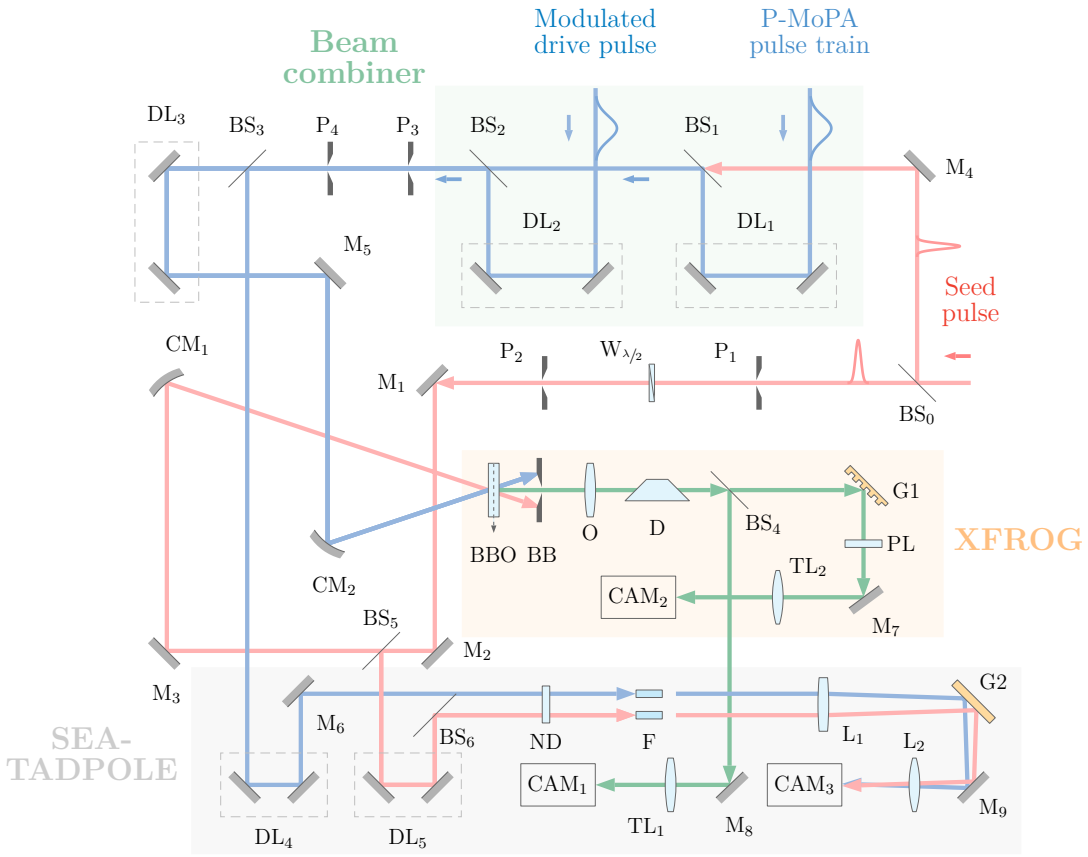


Figure 6.17: Schematic of the pulse measurement device. BS_n—beam splitter; M_n—mirror; F—fibre, L_n—lens; TL_n—tube lens; O—microscope objective; G_n—grating; P_n—pinhole; CM_n —cylindrical mirror; $W_{\lambda/2}$—half-waveplate; DL_n—delay stage; ND—neutral density filter; PL—polariser; CAM_n—camera; and BB—beam block. Green-, orange-, and gray-shaded areas represent beam paths of the beam combiner, XFROG, and SEA-TADPOLE.

SFG signal that has undesired polarisation. The FROG traces are measured by the camera (ace acA1920-40gm, Basler).

In the SEA-TADPOLE device (grey-highlighted area in figure 6.18), two delay stages are used to adjust the delay time between the seed and test pulse. The neutral density filter is used to reduce the input energy of the pulses. Two fibres are placed before the collimation lens, L_1, which allow the input pulses to cross at the camera, CAM_2. The grating with a groove density of 600 l/mm and a lens, L_2, are used to spectrally resolve the input pulses and form the SEA-TADPOLE trace.

The experimental setup of the P-MoPA pulse measurement device is shown in Figure 6.18. Due to limitations in the research budget and experimental time, the entire setup only included the cross-correlation FROG device portion. Because the

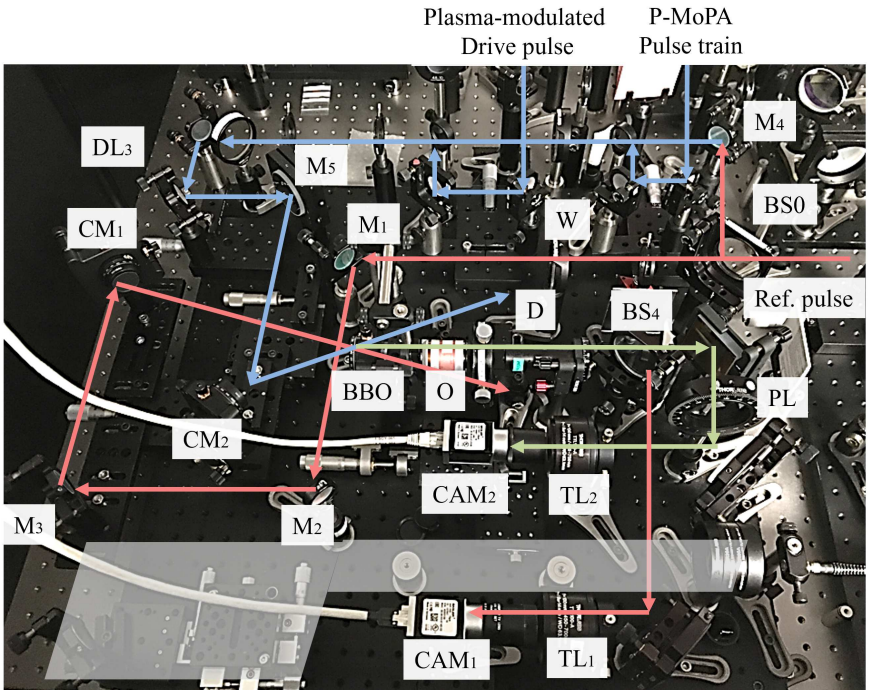


Figure 6.18: Experimental setup of the 1030-nm cross-correlation FROG device following the design layout shown in Figure 6.17. The grey-shaded area is the region prepared for the development of the SEA-TADPOLE device. The scale of this pulse measurement setup is 60×60 cm^2 (width-by-length). Due to space limitations, not every optical component is labelled in this picture.

pulse energy available in OPAL was not enough to demonstrate the measurement of ps pulses similar to those of the P-MoPA pulse trains, it was not possible to test the FROG device experimentally.

6.5 Conclusions

The novel concept of pulse train generation in plasma-modulator plamsa accelerators (P-MoPA) was investigated. A single ps-duration laser pulse form a Yb:YAG laser from a Yb:YAG laser system can be converted into a P-MoPA pulse train via plasma-modulation and pulse compression. In future experimental tests of the P-MoPA concept, it will be essential to characterise these pulse trains for the verification of the P-MoPA theory and the optimisation of the generated pulse trains for the acceleration stage of the P-MoPA.

Based on the investigation of past research on pulse measurement, the spatial encoded arrangement for temporal analysis by dispersing a pair of light E-fields (SEA-

TADPOLE) technique was chosen as the most suitable technique for the complete characterisation of pulses with relative phases in multiple spectral components.

The pulse measurement of P-MoPA pulse trains was achieved using the SEA-TADPOLE technique in a numerical simulation. It was shown that the seed pulse could serve as the reference pulse, and its spectral phase could be characterised with an accuracy as low as 0.21 radians by the cross-correlation FROG technique. Using the FTSI algorithm, the relative phase in the spectral sidebands of the plasma-modulated drive pulses before and after pulse compression could be correctly measured with a high accuracy as low as 0.02 radians.

Based on the simulation results, a provisional pulse measurement device, using the cross-correlation FROG and the SEA-TADPOLE, was proposed and designed. A prototype of the pulse measurement device was partly built in order to demonstrate a proof-of-principle experiment for the measurement of pulses with a temporal structure similar to that of the P-MoPA pulse trains. However, due to time limitations and research budget, the author is not able to complete the entire demonstration of P-MoPA pulse measurement in OPAL and the low-energy P-MoPA experiment in Munich. Hence, only a cross-correlation FROG device was presented in Section 6.4.1.

However, several topics remain undiscussed due to the limitations of research time and available experimental resources. First, the uncertainty analysis of the pulse measurement was not presented. Second, the influence of the time separation of the drive and seed pulses on the modulation of the temporal phase would need attention since it could affect the analysis of the retrieved spectral phase. Third, the optical design of the SEA-TADPOLE is incomplete in that the detailed specification of some optical components remains to be determined. The selection of appropriate optical components, such as the fibres, collimation lens and imaging lens, should be studied in detail. Last, the influence of the non-uniform spatial beam profiles of the drive and seed pulse has not been studied. The problem of the non-uniform beam profiles may be critical for the accuracy of the pulse measurement results.

A dedicated optical beamline is required for the future development of the P-MoPA pulse train measurement. The quality of the beam is affected by the management of the

beam collimation and pulse energy, which is a critical issue in pulse measurement. A clean and short pulse reference pulse pulse is desired to simplify the entire measurement of the P-MoPA pulse train. The seed pulse used in the P-MoPA has an imperfect temporal profile and too much energy in the wings of the seed pulse. Another way to generate a clean reference pulse with a simple spectral phase would be preferable.

According to the author's research in pulse characterisation techniques for temporally-structured pulses, the most appropriate strategy to characterise pulse trains with complex temporal and spectral structures is to:

(i) identify the features of pulses to be measured;

(ii) prepare a simple and short pulse with wide enough spectral bandwidth as a reference pulse;

(iii) use the frequency-resolved optical gating technique (FROG) to characterise the reference pulse first;

(iv) adopt cross-referenced spectral interferometry such as SEA-TADPOLE to characterise the input pulse trains with well-characterised reference pulse; and

(v) use measured spectrum of the input pulse and reconstructed spectral phase from SEA-TADPOLE to retrieve the input pulse.

The reasons for adopting this strategy are that:

(i) the phase retrieval algorithms used in the FROG techniques could not provide stable and consistent retrieval results for the characterisation of complex pulse trains;

(ii) retrieval time of iterative Fourier transform phase retrieval algorithms was long (several seconds) for large grid sizes of FROG traces ($N_{\text{grid}} > 256 \times 256$);

(iii) the phase retrieval algorithm easily encountered stagnation in the retrieval process and hence increased the time to producing reliable retrieval results;

(iv) long pulse trains had lower intensity than short pulses and hence reduced the efficiency of second harmonic generation (SHG) in FROG and caused low contrast of FROG traces recorded by sensors; and

(v) single-shot SHG FROG beam geometries require uniform beam profiles of input pulse trains for the generation of FROG traces. This increased the difficulty of pulse train measurement in LWFA experiments because the available laser pulses from high-power Ti:sa lasers did not have uniform beam profiles before and after interaction with plasma.

The advantages of adopting the strategy are that:

(i) the Fourier transform spectral interferometry algorithm is a direct phase retrieval algorithm which is not involved in any iterative process of solving the spectral phase of an input pulse train;

(ii) the sensitivity of SEA-TADPOLE is very high since it does not rely on the nonlinear optical effect to generate harmonic correlation signal;

(iii) cross-referenced spectral interferometry can measure any type of spectral phase, including discontinuous and relative spectral phase; and

(iv) SEA-TADPOLE can support the measurement of multiple well-separated pulses in the time domain with just a reference pulse and the overall spectrum of the input pulses if the spectral resolution can support the required size of the temporal window.

However, there are several challenges before successfully implementing the strategy, as shown below:

(i) preparation of simple reference pulses with minimal high-order spectral phase and a spectral bandwidth equal to or wider than the test pulse to be measured;

(ii) use of high-quality imaging spectrometer with low aberration and low spectral resolution;

(iii) an extra optical system that can support the beam geometry of two pulses crossing at the sensor; and

(iv) higher cost of building an entire pulse measurement instrument, including one FROG device and one SEA-TADPOLE device.

Science is the systematic classification of experience.

— George H. Lewes, English philosopher
1817–1878 [254]

7 Conclusions

Contents

7.1 Author's contributions 169
7.2 Summary 170
7.3 Limitations 172
7.4 Outlook 174

7.1 Author's contributions

Multi-pulse laser-plasma wakefield accelerators (MP-LWFA) and plasma-modulated plasma accelerators (P-MoPA) are two types of LWFA based on advanced acceleration concepts. Both rely on structured laser pulse trains to excite plasma wakefields resonantly for GeV-scale electron acceleration. The author's contributions in these two research fields are (i) investigating appropriate pulse measurement techniques for the characterisation of laser pulse trains; (ii) conducting physical simulations to assist in the analysis and design of two pulse measurement devices; and (iii) demonstrating a pulse measurement device capable of characterising complex multi-pulse trains.

The pulse measurement instrument built by the author uses the single-shot second-harmonic-generation frequency-resolved optical gating (SHG-FROG) technique with a bandpass-filter and the extended ptychographic iterative engine (ePIE) algorithm.

The pulse measurement device and the algorithm successfully measured and retrieved complex pulse train structures at the Oxford Plasma Accelerator Laboratory (OPAL) in Oxford. To the best of the author's knowledge, the measurement of these pulse trains had not been demonstrated by any other research group using the same technique. Therefore, the author's research can be a good reference in not only the LWFA community but the field of ultrashort pulse measurement community.

This chapter summarises the author's research, limitations and proposes potential future research directions.

7.2 Summary

Chapter 1 emphasised the problem of the low wall-plug efficiencies and repetition rates of Ti:Sa laser systems commonly used in the mainstream LWFA. These problems motivate adopting the MP-LWFA concept for the development of future plasma-based particle accelerators capable of using new laser technology, such as thin-disk lasers and fibre lasers. To assist in the development of MP-LWFA and P-MoPA, reliable pulse measurement instruments are required for pulse characterisation and optimisation.

Chapter 2 briefly discussed the physical principles of LWFA and its limitations. The advantages of MP-LWFA over other types of LWFA are (i) the adjustable pulse spacing and pulse duration between each sub-pulse in a pulse trains for the efficient use of laser energy, (ii) the ability of shifting the energy storage problem in laser media to the plasma, and (iii) the suitability of using picosecond (ps)-long laser pulses to excite plasma wakefield instead of using femosecond (fs)-long pulses.

Chapter 3 presented background knowledge about ultra-short pulse measurement techniques. The author adopted the SHG-FROG technique to conduct pulse measurement because of the simplicity of its beam geometry and its high sensitivity to the input pulses.

Chapter 4 presented the results of simulations aimed at assisting in the design of a pulse measurement instrument.

First, a physical model of generating pulse trains based on the temporal interference of chirped pulses was constructed to serve as a tool for the analysis of the uncertainty

of pulse spacing in pulse trains. The analysis gave an uncertainty of pulse spacing of 11 fs when the input pulse spacing was defined to be 200 fs.

Second, the ePIE algorithm was adopted to implement the phase retrieval process because it had better convergence rates and ability to retrieve complex pulse trains than other phase retrieval algorithms.

Third, a bandpass filter was adopted in the design of a FROG device for the pulse train measurement because it was capable of removing time-direction ambiguity and revealing direct time information in FROG traces. An appropriate FWHM bandwidth of the bandpass filter for pulse measurement of pulse trains was found to be 8 nm at a centre wavelength of 800 nm.

Fourth, a study of the influence of noise on the phase retrieval results suggested that a camera with a signal-to-noise ratio (SNR) of at least 40 dB was required for the pulse measurement device to overcome the camera noise. Under this noise level, the PIE algorithm could provide an RMS intensity error of 0.3% at a pulse spacing of 200 fs.

Fifth, a BBO nonlinear crystal with a θ_{cut} of 44.3°, diameter of 10 mm, and thickness of 100 μm was investigated. This crystal could support a delay time window of 10 ps at a crossing beam angle of 38° and had an angle tolerance of ±0.1°. Additionally, the numerical calculation suggested that a grating with a groove density of 1,200 or 1,800 l/mm was suitable for the construction of an imaging spectrometer.

Chapter 5 describes the procedures of demonstrating a pulse measurement instrument for characterising pulse trains. The results are summarised as follows:

First, the author built a pulse measurement device with a spectral range of 70 nm at a centre wavelength of 400 nm, a temporal range of 9 ps, a minimum spectral resolution of 0.1 nm, and a minimum temporal resolution of 0.6 fs. The imaging spectrometer built into the device used a compact infinity-corrected optical system and a grating with a groove density of 1,200 l/mm.

Second, analysis of the experimental data collected in OPAL at Oxford showed two types of pulse trains, which were successfully measured by the pulse measurement device and retrieved by the ePIE algorithm. The first and second retrieved pulse trains had averaged $\Delta\tau_{\text{rms}}$ of approximately 1.4 ps and 1.6 ps, with TBPs of (14.1 ± 0.1)

and (16.1 ± 1.4) respectively. The averaged T_m were (198 ± 10) fs and (232 ± 7) fs, with non-uniformity of pulse spacing at (10 ± 2) fs and (27 ± 7) fs, respectively. The RMS intensity errors were 15% and 16%, respectively. Both pulse train had approximately the same N_p of 11.

Third, the FROG device, successfully demonstrated in the OPAL, was used to measure the pulse train in a proof-of-principle experiment of the resonance down-ramp injection in an MP-LWFA, conducted at Rutherford Appleton Laboratory (RAL), UK. Unfortunately, the pulse trains were not successfully measured by the FROG device due to experimental constraints. With the SSA phase retrieval algorithm devised by Professor Simon Hooker and the ePIE algorithm, two pulse trains were reconstructed, with pulse spacings of (153 ± 3) fs and (124 ± 2) fs.

Chapter 6 discussed pulse measurement techniques based on spectral interferometry (SI) and described an appropriate pulse measurement technique using cross-referenced SI for the pulse characterisation of P-MoPA pulse trains. The technique adopted for the pulse measurement is the spatial encoded arrangement for temporal analysis by dispersing a pair of light E-fields (SEA-TADPOLE). Preliminary simulation work showed that P-MoPA pulse trains with well-separated multiple spectral components and relative local phase could be successfully retrieved with RMS intensity-weighted spectral phase errors of 0.06 radians and 0.02 radians before and after pulse compression, respectively. In addition to the simulation work, the author built a cross-correlation FROG device in preparation for the construction of a SEA-TADPOLE device.

7.3 Limitations

The research described in Chapter 4, 5, and 6 has important limitations.

In Chapter 4, the physical model used in the uncertainty analysis does not incorporate a detailed design of the entire pulse compressor used in a real experiment, which is involved in optical imaging systems and grating misalignment in a three-dimensional (3-D) space. This would potentially increase the uncertainty of pulse spacings in pulse trains generated in real experiments.

Additionally, the physical simulation conducted in the investigation of the phase retrieval performance of FROG traces did not take into account the influence of imperfect imaging systems used in the FROG device capable of measuring ps-long and complex pulse trains. Aberrations in imaging systems can distort the simulated FROG traces and thus cause larger systematic errors in the phase retrieval results.

Finally, the SHG efficiency was not taken into account when analysing the effect of the bandpass filter on the FROG traces in Section 4.4. This limitation caused a problem in which the use of a bandpass filter reduced the peak power of the spectrally filtered input pulses and thus lowered the SHG efficiency and increased the SNR. This issue resulted in a serious problem during the experiment conducted at RAL, which was one of the reasons leading to unsuccessful pulse measurement.

In Chapter 5, an experimental setup that could produce well-defined reference pulse trains was not successfully implemented due to time constraints and the failure of data collection. The generation of such a pulse train would be beneficial because it could provide a reference for the calibration of the FROG device in the experiment. Although two types of pulse trains were successfully measured and retrieved in the OPAL, the lack of simulated pulse trains based on a known compressor model led to the results that might be unconvincing.

Additionally, the ePIE algorithm did not provide stable pulse retrieval results. This means that the retrieved multi-pulse trains did not always have consistent temporal intensity profiles. According to the author's experience, the algorithm would stagnate, and the FROG errors could not be reduced to target values when retrieving the measure FROG traces. The author adopted a strategy of rerunning the algorithm and giving a new initial guess to resolve the problem of stagnation. However, the algorithm did not always produce satisfying retrieval results based on this strategy.

Furthermore, the pulse measurement device based on a single-shot beam geometry suffers from measuring pulses with non-uniform spatial, temporal, and spectral contents across the entire beam profiles. It should be emphasised that the phase retrieval theory and algorithm assume that the measured FROG trace is formed by an input pulse with uniform spatial intensity, spectral contents and temporal structure across the entire time

delay range. However, the practical situation in the experiment was opposite to this requirement, which lead to difficulty in the pulse characterisation. Hence, the FROG device used at RAL needed specially designed and built collimation beam lines. Since the FROG device required a uniform beam profile across the entire aperture of the nonlinear crystal, the collimated high-power laser pulses at RAL provided a low-quality beam profile, which was not suitable for the FROG technique used in the MP-LWFA.

In Chapter 6, several issues were not addressed. These include a detailed analysis of the optical design used in the SEA-TADPOLE device for measuring P-MoPA pulse trains, image aberrations of SEA-TADPOLE interferogram and an uncertainty analysis of pulse retrieval results based on the SEA-TADPOLE technique. Most importantly, the spatio-temporal coupling of real P-MoPA pulse trains was not taken into account in the simulation, which might have a significant effect on the pulse retrieval results and stability. Due to time limitations and experimental resources, the SEA-TADPOLE device could not be demonstrated experimentally.

7.4 Outlook

The first challenge is the stagnation of the ePIE algorithm when solving complex pulse trains. To stabilise the phase retrieval process of the ePIE algorithm and generate more consistent retrieval results, a strategy of using a preliminary search for an optimal initial guess could be adopted. Aboushelbaya et al. [255] developed a memetic algorithm and adopted Kane's principle component general projections algorithms [176, 177] to overcome the problem of stagnation. Their algorithm implemented an initialisation of searching for a series of possible solutions that could provide the best retrieval result in the first step. The algorithm then proceeded with the steps, including selection, crossover, mutation and local improvement, so that the final solution could be found and the FROG error was significantly reduced compared to the cases without the memetic algorithm. Compared to the author's approach, which reran the algorithm with a new initial guess of the input electric field, the memetic algorithm has the potential to provide stable retrieval process and results in a tradeoff of longer retrieval time.

It should be noted that the problem of stagnation in iterative Fourier transform phase retrieval algorithms was first mentioned and studied by Fienup et al. [256] in 1986 in the optical imaging community. Other approaches have been researched to overcome the problem of stagnation in the phase retrieval algorithms for optical pulse measurement. These methods include the deep learning reconstruction [257], the spectral initialisation and multi-grid algorithm [258], and the line-search algorithm with low-pass filtering [259]. All these methods could also be adopted to reduce the influence of stagnation of the ePIE algorithm on the pulse retrieval process for the characterisation of pulse trains in MP-LWFA and P-MoPA.

The greatest challenge in pulse measurement in the MP-LWFA and P-MoPA is the spatio-temporal coupling of laser pulses, such as pulse front tilt, pulse front curvature, spatial chirp, and spatial beam breakup. Structured laser pulse trains generated by these schemes for proof-of-principle experiments would have nonuniform temporal and spectral contents across the entire beam profile caused by the unstable guiding of laser pulse in plasma channels or low quality of input laser drivers. These results in a difficulty in using the conventional single-shot FROG technique to characterise complete the spatio-temporal coupling of pulses generated from complicated pulse-shaping processes. Therefore, an investigation of measurement techniques capable of determining the full 3D profile of the pulses used in MP-LWFAs and P-MoPAs would be an interesting direction for future work.

The simplest option to overcome the spatio-temporal couplings would be to spatially filter out the entire beam profile and allow a small portion of the laser energy at the beam centre to leave the spatial filter for the pulse characterisation. This solution has the lowest cost and requires a relatively simple experimental setup, which would only be suitable for proof-of-principle experiments. Presumably, a pinhole can be designed to scan the entire laser beam profile so that the pulse structure at different location across a laser pulse can be measured by a conventional FROG device. However, this method does not allow complete characterisation of the structured pulses in a single shot, which might be a hurdle to the development of P-MoPA in the future.

The second option would be to adopt a technique known as spatially and temporally resolved intensity and phase evaluation device: full information from a single hologram (STRIPED FISH) [260]. STRIPED FISH, or simply FISH, is a multi-spectral holographic technique capable of reconstructing the spatio-temporal information of test pulses with well-characterised reference pulses. Because this technique can measure pulses in a single-shot beam geometry, it has been implemented to characterise pulses with a duration of 2 ps and a centre wavelength of 1052 nm at the Jupiter Laser Facility in the US [261]. However, the measured pulses had relatively simple temporal profiles and spectral contents. For the measurement of P-MoPA pulse trains, the FISH technique would be worth investigating in future work.

The third option would be to develop a new type of spatio-temporal pulse measurement technique with a single-shot geometry. Hence, I propose an idea that uses a direct-space-time (DST) pulse shaper, invented by Weiner et al. [262], and the conventional single-shot cross-correlation FROG technique to measure spatio-temporal couplings of pulses. The DST shaper is used to generate a series of reference pulses and sample the local beam profile in a nonlinear crystal. Following the same principle as used in the cross-correlation FROG technique, a series of FROG traces can be generated in the nonlinear crystal with the reference pulses and test pulse crossing at different locations in the nonlinear crystal. These FROG traces can then be retrieved by any phase retrieval algorithm used in FROG. The retrieved information of local test pulses can be combined to reflect the entire spatio-temporal couplings of the test pulse. Although the idea was proposed during the author's doctoral research, it has not been extensively studied or implemented, which leaves some uncertainty about its feasibility. More investigation is required to understand whether this idea can be implemented for pulse characterisation in the MP-LWFA or P-MoPA.

To fully characterise structured laser pulse trains, especially P-MoPA pulse trains, well-characterised reference pulses is critical. Using the seed pulse in P-MoPA as a reference pulse might have some drawbacks. In particular, the seed pulse has complex spectral contents with modulated spectral phase and the temporal structure has

a low pulse contrast and a nonuniform beam profile, which will pose challenges in the pulse characterisation.

For the measurement of spatio-temporal coupling of P-MoPA pulse trains, well-characterised reference pulses should have a uniform beam profile, simple temporal structures, and continuous spectral contents. To satisfy these conditions, a passive spatio-temporal filter is essential. A conventional spatial filter is relatively simple to implement using a pinhole and focusing imaging optics. However, the implementation of temporal filtering is not as straightforward as the spatial filter.

One option to implement a passive temporal filter would be to use cross-polarised wave (XPW) generation, which has been used to enhance the pulse contrast in Petawatt laser systems and few-cycle laser pulses [263, 264]. An alternative option would be to use the drive pulse to create another simple and short pulse with cascaded nonlinearity in bulk nonlinear crystals [265, 266]. When the orientation of a second-order nonlinear crystal is controlled with respect to the polarisation orientation of the input drive pulse, a spectral broadening effect can be induced. The output pulse with a broader spectrum can then be compressed with proper dispersion management using chirp mirrors. These two techniques can also be integrated to form a self-consistent referenced pulse generator for the pulse measurement using SEA-TADPOLE in P-MoPA.

Appendices

The nature of light is a subject of no material importance to the concerns of life or to the practice of the arts, but it is in many other respects extremely interesting.

— Thomas Young, English physicist, 1773–1829, [267]

A

Supplemental material for the pulse train generation

Contents

A.1 Michelson interferometer 179
A.2 Grating-pair compressor 181

A.1 Michelson interferometer

The Michelson interferometer is a type of interferometers consisting of an optical beam splitter and two mirrors, as shown in Figure A.1. The input pulse entering this optical device is split into two replicas after passing through the beam splitter. The two pulse replicas are then reflected back to the beam splitter by the two mirrors. One of the two mirrors can be moved by a distance, ΔL_m, along the propagation direction of the incoming beam. The two input pulse replicas are split again by the beam splitter. At one side of the beam splitter, the two pulse replicas are re-combined and collinearly propagate to form the output signal.

Assume that the input pulse has a form of

$$u(t, \mathbf{r}) = a(t, \mathbf{r}) \exp\left[j(\omega t - \mathbf{k} \cdot \mathbf{r})\right], \tag{A.1}$$

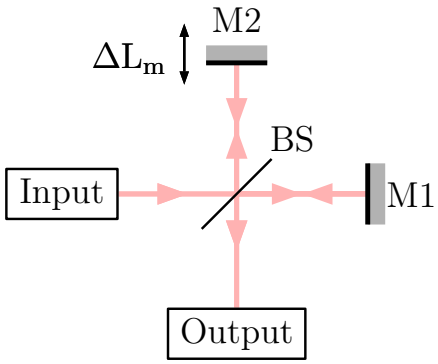


Figure A.1: Schematic of a Michelson interferometer. BS—beam splitter; and M—mirror;

where ω is the angular frequency; $\mathbf{k}$ is the propagation vector; and $\mathbf{r} = (x, y, z)$ is the position.

Assuming that the input pulse propagates in the x-z plane, Equation (A.1) becomes

$$u(t, \mathbf{r}) = a(t, \mathbf{r}) \exp(j\omega t) \exp\left[-j(kz\cos\theta + kx\sin\theta)\right]. \tag{A.2}$$

The output electric field, $u_o(t, \mathbf{r})$, is given by

$$u_o(t, \mathbf{r}) = \frac{1}{2}\left[u_1(t, \mathbf{r}) + u_2(t, \mathbf{r})\right]. \tag{A.3}$$

Thus, the intensity of the output pulse, $I_o(t, \mathbf{r})$, can be written as

$$\begin{aligned} I_o(t, \mathbf{r}) &= \left|\frac{1}{2}\left[u_1(t, \mathbf{r}) + u_2(t, \mathbf{r})\right]\right|^2 \\ &= \frac{1}{4}\left(|u_1|^2 + |u_2|^2 + u_1^* u_2 + u_1 u_2^*\right). \end{aligned} \tag{A.4}$$

Assume that

$$u(t, \mathbf{r}) = |u(t, \mathbf{r})| \exp\left[j\psi(t, \mathbf{r})\right] \exp\left[j(\omega t - kz\cos\theta + kx\sin\theta)\right], \tag{A.5}$$

where $\psi(t, \mathbf{r})$ is the spectral phase introduced by the beam splitter.

The third and fourth terms in Equation (A.4) are equal to

$$u_1^* u_2 + u_1 u_2^* = 2|u_1||u_2|\cos\left[\Delta\phi(t, \mathbf{r})\right], \tag{A.6}$$

where the phase term, $\phi(t, \mathbf{r})$, is given by

$$\Delta\phi(t, \mathbf{r}) = \phi_2(t, \mathbf{r}) - \phi_1(t, \mathbf{r}). \tag{A.7}$$

Assume that the output pulse replicas propagate collinearly and the beam splitter is thin enough. This implies that $\omega = ck$, $\theta \approx 0$ and $\psi(t, \mathbf{r}) \approx 0$. Therefore, the phase of the output pulse can be written as

$$\begin{aligned} \Delta\phi(t, \mathbf{r}) &= k(z_1 - z_2) \\ &= \omega \frac{2\Delta L_m}{c}, \end{aligned} \tag{A.8}$$

where ΔL_m is the displacement of the mirror.

According to Equation (A.8), the time delay between the two pulse replicas, τ, introduced by the Michelson interferometer is given by

$$\tau = \frac{2\Delta L_m}{c}. \tag{A.9}$$

A.2 Grating-pair compressor

The complex electric field of a pulse, $u(t, \mathbf{r})$, can be represented by a superposition of plane waves [268]. These plane waves have different angular frequencies and propagate at different angles in space. Assume that the plane waves travel along the x-z plane and the centre angular frequency is ω_0, $u(t, \mathbf{r})$ can be written as

$$u(t, \mathbf{r}) = \frac{1}{2\pi} \int_{-\infty}^{\infty} a(\tilde{\omega}, \mathbf{r}) \exp\left[j(\tilde{\omega}t - \beta \cdot \mathbf{r})\right] d\tilde{\omega}, \tag{A.10}$$

whare $\tilde{\omega} = \omega - \omega_0$; and $\beta(\omega)$ is defined by

$$\beta(\omega) = n(\omega)\frac{\omega}{c}\left[\cos\theta(\omega)\hat{z} + \sin\theta(\omega)\hat{x}\right]. \tag{A.11}$$

The electric field, $u(0, 0)$, is given as

$$u(t, \mathbf{r}) = \frac{1}{2\pi} \int_{-\infty}^{\infty} a(\tilde{\omega}, \mathbf{r}) \exp\left(j\tilde{\omega}t\right) d\tilde{\omega}. \tag{A.12}$$

The electric field, $u(L_z, L_z)$, is given by

$$u(t, \mathbf{r}) = \frac{1}{2\pi} \int_{-\infty}^{\infty} a(\tilde{\omega}, \mathbf{r}) \exp\left[j\tilde{\omega}t - n\frac{\omega}{c}\left(L_z\cos\theta + L_x\sin\theta\right)\right] d\tilde{\omega}, \tag{A.13}$$

where $n = n(\omega)$ is the refractive index; $\omega = \omega(\omega)$ is the angular frequency; and $\theta = \theta(\omega)$ is the propagation angle.

If $u(t, \mathbf{r})$ propagates by a distance, L_s, along the z-axis, the frequency-dependent phase difference, $\psi(\omega)$, between the origin $(0, 0)$ and point $(0, L_s)$ can be written as

$$\psi(\omega) = -\frac{\omega}{c} P \tag{A.14}$$

$$= -\frac{\omega}{c} n(\omega) L_s \cos\theta(\omega), \tag{A.15}$$

where $P = n(\omega) L_s \cos\theta(\omega)$.

Since

$$\lambda = \frac{2\pi c}{\omega}, \tag{A.16}$$

the second- and third-order derivatives of λ with respect to ω are given by

$$\frac{d\lambda}{d\omega} = -\frac{\lambda^2}{2\pi c}, \tag{A.17}$$

and

$$\frac{d^2\lambda}{d\omega^2} = -\frac{\lambda^4}{4\pi^2 c^2}. \tag{A.18}$$

Thus, the second-order spectral phase, ψ_2, defined in Equation (3.6) is given by

$$\frac{d^2\psi}{d\omega^2} = \frac{d^2\psi}{d\lambda^2}\frac{d\lambda^2}{d\omega^2} \tag{A.19}$$

$$= -\frac{\lambda^3}{2\pi c^2}\frac{d^2 P}{d\lambda^2}, \tag{A.20}$$

where

$$\frac{d^2 P}{d\lambda^2} = L_s \left[\frac{d^2 n}{d\lambda^2}\cos\theta - 2\frac{dn}{d\lambda}\sin\theta \left(\frac{d\theta}{d\lambda}\right) - \right. \tag{A.21}$$

$$\left. n\cos\theta \left(\frac{d\theta}{d\lambda}\right)^2 - n\sin\theta \frac{d^2\theta}{d\lambda^2} \right]. \tag{A.22}$$

If taking $\omega = \omega_0$ and $\theta = 0$ as the reference angular frequency and propagation direction,

$$\frac{d^2 P}{d\lambda^2} = L_s \left[\left.\frac{d^2 n}{d\lambda^2}\right|_{\omega=\omega_0} - n(\omega_0) \left.\left(\frac{d\theta}{d\lambda}\right)^2\right|_{\theta=0} \right]. \tag{A.23}$$

Figure A.2 shows a schematic of grating pair compressor. The grating equation is given by

$$\sin\theta_{\mathrm{d}} = \sin\theta_{\mathrm{i}} + m\frac{\lambda}{\lambda_g}, \tag{A.24}$$

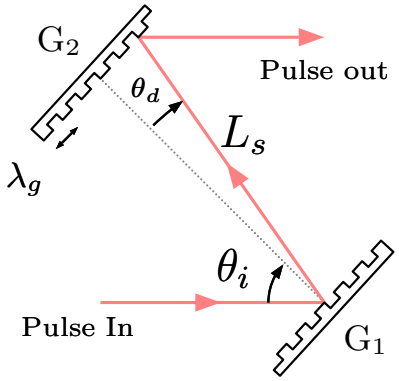


Figure A.2: Schematic of a grating-pair compressor. G_n: grating.

where θ_d is the diffraction angle; m is the order of diffraction; λ is the wavelength; and λ_g is the grating period.

Differentiating equation (A.24) with respect to λ results in

$$\frac{d\theta}{d\lambda} = \frac{m}{\lambda_g \cos\theta_d}. \tag{A.25}$$

Since a grating-pair compressor commonly operates in air or vacuum, the first term in equation (A.23) can be neglected. Hence, the second-order spectral phase, ψ_2, introduced to an input pulse by the compressor is given by [268]

$$\begin{aligned}\psi_2 &= \frac{d^2\psi}{d\omega^2} \\ &= -\frac{\lambda^3}{2\pi c^2} L_s \left(\frac{d\theta}{d\lambda}\right)^2 \\ &= \frac{m^2\lambda^3 L_s}{2\pi c^2 {\lambda_g}^2 \cos^2\theta_d}.\end{aligned} \tag{A.26}$$

The third-order spectral phase, ψ_3, introduced by the compressor is given by [268]

$$\begin{aligned}\psi_3 &= \frac{d^3\psi}{d\omega^3} \\ &= \frac{\lambda^4}{4\pi^2 c^3}\left(3\frac{\partial^2 P}{\partial\lambda^2} + \lambda\frac{\partial^3 P}{\partial\lambda^3}\right) \\ &= -\frac{3m^2\lambda^4 L}{4\pi^2 c^3 {\lambda_g}^2 \cos^2\theta_d}\left(1 + \frac{m\lambda\tan\theta_d}{\cos\theta_d}\right).\end{aligned} \tag{A.27}$$

Programming is a skill best acquired by practice and example rather than from books.

— Alan W. Turing, English mathematician, 1912–1954, [269]

B

Computer codes for the pulse train characterisation

Contents

B.1 Generation of multi-pulse trains 184
B.2 Generation of P-MoPA pulse trains 191
B.3 The ePIE algorithm 198
B.4 The SSA algorithm 206

B.1 Generation of multi-pulse trains

```
# The following code uses the Python programming language.
import numpy as np
import matplotlib.pyplot as plt
from scipy.fftpack import fft, ifft, fftshift, ifftshift
from scipy.signal import find_peaks

class pulse_train():

  def __init__(self, wl, Tp, n_e, Np, pc, T_window, N_point):

    self.c = 2.99792458e8  # the speed of light [m/s]
    self.ne = n_e # plasma density [#/cm^3]
    self.me = 9.109e-31 # the mass of electron [kg]
    self.e = 1.602e-19 # the charge of electron [C]
    self.q = -self.e # charge [C]
    self.ep0 = 8.854e-12 # the permittivity of free space [C^2/(N m^2)
   ]
```

```
17      self.plasma_f =np.sqrt(self.ne*(self.q**2)*1e6/(self.me*self.ep0))
        # the plasma frequency [rad]
18      self.lamp = 2*np.pi*self.c/self.plasma_f # the plasma wavelength
19      self.pulse_sp = self.lamp/self.c*1e15 # the pulse spacing of a
      uniform pulse train [fs]
20      self.wl0 = wl*1e-9  # centre laser wavelength[m]
21      self.f0 = self.c/self.wl0  # central frequency, [Hz]
22      self.w0 = 2*np.pi*self.f0  # central angular frequency, [rad]
23      if Tp == []:
24        self.Tp = self.pulse_sp
25      else:
26        self.Tp = Tp  # pulse spacing [fs]
27
28      self.Np = Np  # number of pulses
29      self.TW = 2*self.Np*self.Tp/1000 # temporal window size
30      self.pc = pc  # the number of points to resolve one cycle
31      self.T0 = 1/self.f0  # the period of one cycle [s]
32      self.rs = self.T0/self.pc*1e12  # resolution to distinguish a cyle
        [ps]
33      self.N = int(self.TW/self.rs) # the number of data points
34      self.F = self.N/self.TW  # the spectral window size [THz]
35      self.T_window = T_window
36      self.N_point = N_point
37
38      self.workflow()
39
40    def workflow(self):
41
42      self.A, self.B, self.C = self.get_pulse_train('TA3_spectrum.txt')
43      self.get_variable()
44
45    def get_variable(self):
46
47      self.t = self.A[0]
48      self.ef = self.A[1]
49      self.I = self.A[2]
50      self.t_phase = self.A[3]
51      self.t_ms = self.A[4]
52
53      self.f = self.B[0]
54      self.spec = self.B[1]
55      self.S = self.B[2]
56      self.f_phase = self.B[3]
57      self.f_ms = self.B[4]
58
59      self.Pt = self.C[0]
60      self.PI = self.C[1]
61      self.SPt = self.C[2]
62      self.SP = self.C[3]
63
64    def get_p_density(self, Tp): # get the plasma density
65
66      ne = (2*np.pi/(Tp*1e-15))**2*(self.me*self.ep0)/(self.q**2*1e6)*1e
        -18
67      return ne # in [10^17 cm^-3]
68
69    def get_sp(self, ne): # get the resonance pulse spacing
```

```
70
71      t = 2*np.pi/np.sqrt(self.ne*(self.q**2)*1e6/(self.me*self.ep0))
72      return t # in [10^17 cm^-3]
73
74    def spectrum_processing(self, wl, I): # process the input spectrum
75      # wl: wavelength [nm]
76      # I: power spectrum [A.U.]
77
78      wlp = wl.copy()  # spectrum from a file, unit: m
79      Ip = I.copy()  # normalised spectral intensity
80      Np = len(wlp)  # get the length of array
81      f1 = self.c/(wlp*1e-9)*1e-12  # frequency [THz]
82      f_0 = self.f0*1e-12  # central frequency [THz]
83
84      for n in np.arange(0, Np, 1):  # remove noise
85        if wlp[n] <= 750 or wlp[n] >= 850:
86          Ip[n] = 0
87          Ip[Ip<0]=0
88      # A process changing the window size in the frequency domain. This
        process can control the resolution in time domain.
89      # Because the direction of frequency array is opposite to
      wavelength array, it must be reversed to place the minimum value at
        the beginning of a frequency array.
90
91      f1p = np.flip(f1, 0)
92      Ipp = np.flip(Ip, 0)
93      f2 = np.linspace(min(f1p), max(f1p), self.N)
94      Ip2 = np.interp(f2, f1p, Ipp)
95      f3 = np.linspace(f_0 - self.F/2, f_0 + self.F/2, self.N)
96      Ip3 = np.interp(f3, f2, Ip2)
97
98      return f3*1e12, Ip3
99
100   def uniform_pulse(self, W, thr): # Calculate the required time delay
        and GDD to form a uniform pulse train
101
102     # W: one sigma bandwidth of a transform limited gaussian pulse.
103     # thr: threshold defining the number of pulses within a region
104
105     if thr == 'Exp_2':
106       threshold = np.exp(2)
107
108     elif thr == 'FWHM':
109       threshold = 2
110
111     elif thr == 'Exp_1':
112       threshold = np.exp(1)
113
114     W = W*1e-15  # one sigma bandwidth [fs]
115
116     psi2 = np.sqrt((2*W**2*(self.Np*self.Tp)**2 - 16*np.log(threshold)
      )/(4*W**4*np.log(threshold))) # GDD in [fs^2] (can be either
      negative or positive.)
117
118     psi1 = (8*np.pi + 2*np.pi*psi2**2*W**4)/(psi2*W**4*self.Tp)  #
      delay time in fs
119     GD = -psi1
```

```
    GDD = -psi2

    return GD, GDD

  def michelson(self, fp, Ip, GD, GDD, TOD, FOD, mode): # Simulate the
    Michelson interferometer
    # fp: spectrum in frequency
    # Ip: power spectrum
    # GD and GDD: the 1st and 2nd spectral phase from "uniform_pulse"

    phi1 = -GD
    phi2 = -GDD/2
    phi3 = -TOD/6
    phi4 = -FOD/24

    f = fp.copy()  # frequency
    I = Ip.copy()  # power spectrum

    # prepare for b. and f. Fourier transform
    F = (max(f) - min(f))*1e-15
    df = (f[1] - f[0])*1e-15
    w = (2*np.pi*(f - self.f0)*1e-15)
    T = 1/df
    dT = T/self.N
    t = np.linspace(-T/2, T/2, self.N)

    E1 = np.sqrt(I/2)*np.exp(1j*((phi1/2)*w + phi2*w**2 + phi3*w**3 +
    phi4*w**4))
    E2 = np.sqrt(I/2)*np.exp(1j*((-phi1/2)*w + phi2*w**2 + phi3*w**3 +
    phi4*w**4))

    # Please, refer to Eq. 3.12 in the book, Ultrafast optics by
    Weiner

    if mode == 'DFT':  # Don't use this. It's just for double check
    the results
      e1 = 0
      e2 = 0

      for n in np.arange(0, self.N, 1):

        e1 = e1 + E1[n]*np.exp(1j*w[n]*t)
        e2 = e2 + E2[n]*np.exp(1j*w[n]*t)

    elif mode == 'FFT':  # Use this when you only want to look at the
    intensity of a pulse train
      e1 = 1/(2*np.pi)*ifftshift(ifft(fftshift(E1))*self.N)
      e2 = 1/(2*np.pi)*ifftshift(ifft(fftshift(E2))*self.N)

    ef = (e1+e2)*np.exp(1j*self.w0*t*1e-15)  # amplitude

    I = abs(ef)**2/max(abs(ef)**2)  # normalised intensity [A.U.]

    t = t*1e-15  # back to [s]

    return t, ef, I

```

```
171   def find_peaks(self, t, I, thr): # Calculate the pulse spacing in a
       pulse train
172
173     # t: time
174     # I: pulse
175     # thr: threshold defining a region for the peak finding routine to
       find peaks
176
177     if thr == 'Exp_2':
178       threshold = 1/np.exp(2)
179
180     elif thr == 'FWHM':
181       threshold = 1/2
182
183     elif thr == 'Exp_1':
184       threshold = 1/np.exp(1)
185
186     else:
187       threshold = thr
188
189     dt = t[1] - t[0]
190     peaks, _ = find_peaks(I/max(I), height=threshold)
191     PI = I[peaks]
192     Pt = t[peaks]
193
194     SP = np.array([])
195     SPt = np.array([])
196
197     for n1 in np.arange(0, len(PI)-1, 1):
198       SP = np.append(SP, abs(Pt[n1+1] - Pt[n1]))
199       SPt = np.append(SPt, (Pt[n1+1] + Pt[n1])/2)
200
201     # Pt: peak position, PI: peak, SPt: spacing position, SP: spacing
202
203     return Pt, PI, SPt, SP
204
205   def bandwidth_spectral(self, wl, I, tr): # Calculate the spectral
       bandwidth
206     # wl: wavelength [nm]
207     # I: power spectrum [A.U.]
208     # tr: threshold of finding defined bandwidth, FWHM or 1/e^2
209     # n: ratio of the new window size to the original one
210
211     Ip = I.copy()
212     wlp = wl.copy()
213     Ip = Ip/max(Ip)
214     N = len(wlp)
215     Nmax = np.argmax(Ip)
216     idx1 = np.argmin(abs(Ip[0:Nmax] - tr))  # index for 1st minima
217     idx2 = np.argmin(abs(Ip[Nmax:N-1] - tr)) + Nmax
218     # index for 2nd minimum
219
220     wl2 = wlp[idx2]
221     wl1 = wlp[idx1]
222     WL = abs(wl2 - wl1)*1e-9  # bandwidth in wavelength [m]
223     F = self.c/(self.wl0 - WL/2) - self.c/(self.wl0 + WL/2)  #
       bandwidth in frequency [Hz]
```

```
224
225     return F, WL, idx1, idx2
226
227   def duration_time(self, fo, Io, tr): # Calculate the pulse duration
228     # fo: frequency [Hz]
229     # Io: power spectrum [A.U.]
230     # tr: threshold of finding defined pulse duration, FWHM or 1/e^2
231
232     f = fo.copy()
233     I = Io.copy()
234
235     # Prepare for the inverse Fourier transform
236     df = f[1] - f[0]
237     f = f - self.f0
238     T = 1/df
239     dt = T/self.N
240     tp = np.arange(-T/2, T/2, dt)
241
242     # inverse Fourier transform
243     pulse = abs(1/(2*np.pi)*fftshift(ifft(np.sqrt(I)*self.N)))**2
244     pulse = pulse/max(pulse)  # normalise with peak
245
246     idx1 = np.argmin(abs(pulse[0:int(self.N/2)] - tr))  # index for
    the 1st minimum
247     idx2 = np.argmin(abs(pulse[int(self.N/2):self.N-1] - tr)) + int(
    self.N/2) # index for the 2nd minimum
248
249     t1 = tp[idx1]
250     t2 = tp[idx2]
251     dt = abs(t2 - t1)
252
253     return tp, pulse, dt, idx1, idx2
254
255   def bandwidth_convertor(self, dt_fwhm, dF_fwhm): # Convert the FWHM
     bandwidth to rms bandwidth
256     # dt_fwhm: FWHM pulse duration
257     # dF_fwhm: FWHM bandwidth
258
259     tp = dt_fwhm/np.sqrt(2*np.log(2))  # rms pulse duration [s]
260     W = 2*np.pi*dF_fwhm/np.sqrt(2*np.log(2))  # rms bandwidth [Hz]
261
262     return tp, W
263
264   def spectrum(self, t, e, bw):
265     # t: time [fs]
266     # e: E-field [A.U.]
267     # bw: bandwidth [Hz]
268
269     F = 50*bw
270     df = F/self.N
271     T = 1/df
272     dt = 1/F
273     tp = np.arange(-T/2, T/2, dt)
274     f = np.arange(-F/2, F/2, df)
275     ep = np.interp(tp, t, e)
276     spec = abs(fftshift(fft(ifftshift(ep))/self.N/np.pi))**2
277     spec = spec/max(spec)  # normalised with the peak value
```

```
278
279     return f, spec
280
281   def load_file(self, name): # Load the power spectrum of laser pulse
282
283     inputfile = name
284     with open(inputfile, 'r') as f:
285
286       Data = np.loadtxt(f, delimiter=None)
287
288     wlp = Data[:, 0]  # wavelength, [nm]
289     Ip = Data[:, 1]  # spectral intensity, [counts]
290     Ip = Ip/max(Ip)  # normalised with the peak
291     Ip = Ip - Ip[-1]
292
293     return wlp, Ip
294
295   def get_pulse_train(self, name):
296     # This function is to generate a pulse train without tedious step
      by step procedures. Users should prepare a power spectrum of laser
      pulse for the function, self.load_file.
297
298     wl, I = self.load_file(name)
299     fo, Io = self.spectrum_processing(wl, I)
300     td, pulse, dt_fwhm, idx_t_a, idx_b = self.duration_time(fo, Io,
      0.5)
301     dF_fwhm, Wl_fwhm, idx_f_a, idx_f_b = self.bandwidth_spectral(wl, I
      , 0.5)
302
303     tp, W = self.bandwidth_convertor(dt_fwhm, dF_fwhm)
304     tau, GDD = self.uniform_pulse(W, 'Exp_2')
305     t, ef, I = self.michelson(fo, Io, tau, GDD, 0, 0, 'FFT')
306
307     dt = self.T_window/self.N_point
308     t2 = np.arange(-self.T_window/2,self.T_window/2,dt)
309     df = 1/self.T_window
310     F = self.N_point*df
311     f2 = np.arange(-F/2,F/2,df)
312     ef2 = np.interp(t2, t*1e15, ef)
313
314     I2 = abs(ef2)**2/max(abs(ef2)**2)
315     spec = fftshift(fft(fftshift(ef2)))
316     spec = spec/max(abs(spec))
317     S = abs(spec)**2/max(abs(spec)**2)
318     Pt, PI, SPt, SP = self.find_peaks(t2, I2, 'Exp_2')
319     t_phase = np.unwrap(np.angle(ef2))
320     f_phase = np.unwrap(np.angle(spec))
321     t_ms = I2 > 1/np.exp(2)
322     f_ms = S > 1/np.exp(2)
323
324     # t: time [t]
325     # I: pulse train [[A.U.]]
326     # tau & GDD: the first and second order spectral phase [fs, fs^2]
327     # ef: amplitude of E-field [A.U.]
328     # fs: frequency [Hz]
329     # spec: signal of spectrum [A.U.]
330     # dF_fwhm: FWHM bandwidth [Hz]
```

```
    # Pt: peak location [T]
    # PI: peak signal [U.A.]
    # Spt: spacing location [t]
    # SP: spacing [t]

    return [t2, ef2, I2, t_phase, t_ms], [f2, spec, S, f_phase, f_ms
    ,], [Pt, PI, SPt, SP]

if __name__ == "__main__":

  ############ Initial conditions ###############
  wl0 = 800 # central wavelength [nm]
  Np = 4 # number of pulses
  ne = 3e17 # plasma density [#/cm^2]
  Tp = 200 # pulse spacing in [fs]
  Rc = 1 # Points to resolve one E-field cycle
  T = Tp*Np*2.5 # pulse duration [fs]
  N = 128 # the number of data points
  ##############################################

  train_1 = pulse_train(wl0, Tp, ne, Np, Rc, T, N) # Initialise the
   pulse train object

  # Plot results
  fig, ax = plt.subplots(figsize = (5.5,3.5))
  ax.plot(train_1.t, train_1.I, '-', c= 'tab:blue', lw = 4, alpha =
   0.6, label = 'Pulse')

  ax.set_xlabel(r'$t$ (ps)')
  ax.set_ylabel(r'$I(t)$ (a.u.)')
  ax.grid(alpha = 0.3)

  fig, ax = plt.subplots(figsize = (5.5,3.5))
  ax.plot(train_1.f, train_1.S, '-', c= 'tab:red', lw = 4, alpha =
   0.6, label = 'Spectrum')

  ax.set_xlabel(r'$f$ (ps)')
  ax.set_ylabel(r'$I(f)$ (a.u.)')
  ax.grid(alpha = 0.3)
```

B.2 Generation of P-MoPA pulse trains

```
# The following code uses the Python programming language.
import numpy as np
import matplotlib.pyplot as plt
from scipy.fftpack import fft, ifft, fftshift, ifftshift
from scipy.misc import derivative
from scipy.optimize import curve_fit
import warnings

class PMOPA_parameters():

  def __init__(self):

    self.h = 6.62607015*1e-34 # Plank's constant
```

```
14      self.c = 2.99792458e8  # the speed of light
15      self.e = 1.602e-19 # the charge of electron [C]
16      self.me = 9.109e-31 # the mass of electron [kg]
17      self.q = -self.e # charge [C]
18      self.ep0 = 8.854e-12 # the permittivity of free space [C^2/(N m^2)
        ]
19
20    self.workflow()
21
22      def workflow(self):
23      self.pulse_properties()
24      self.plasma_properties()
25      self.prism_properties()
26
27    def pulse_properties(self):
28
29      self.wl0 = 1030e-9  # centre wavelength [m]
30      self.f0 = self.c/self.wl0 # centre frequency [m]
31      self.tau_p_long = 1e-12 # long pulse duration [s]
32      self.tau_p_short = 37e-15 # pulse duration
33      self.T = 5e-12 # time window [s] # 8e-12 40e-12
34      self.Np = 256 # number of points [#] # 512 1024
35      self.E_p = 5e-5 # driver energy (moduated pulse)[J]
36      self.energy_ratio = 1 # E_seed/E_drive
37      self.phase_mode = 'original'# 'original' or 'flat'
38      self.flatten_phase_fc = 1 # factor to flatten the phase. 0: off,
        1: on
39      self.SNR_spec = 80#20 #[dB] random noise (white noise) in spectrum
40      self.SNR_energy = 5 # in percentage rms
41      self.timing_jitter = 0e-15 # timing between the seed and drive
        pulse
42      self.timing_jitter_mode = 0 # 0: no, 1: yes
43      self.N_timing = 0
44
45    def plasma_properties(self):
46
47      self.ne = 2.5e17 # plasma density [#/cm^3]
48      self.plasma_w0 = np.sqrt(self.ne*(self.q**2)*1e6/(self.me*self.ep0
        ))
49      # plasma frequency [rad]
50      self.d_ne = self.ne*0.02 # plasma perturbation [#/cm^3]
51      self.lamp = 2*np.pi*self.c/self.plasma_w0 # plasma wavelength
52      self.Lp = 0.05 # length of plasma channels [m] # 0.05
53      self.SP_pulse = 1/(self.plasma_w0/(2*np.pi))*1e15
54      self.SNR_plasma = 0 #[%] random noise (white noise) of plasma
        density
55
56    def prism_properties(self):
57
58      self.Lg = 80e-3 # length of glass [m]
59      self.name_g = 'BK7' # type of glass
60
61  class PMOPA_propagation():
62
63    def __init__(self, parameters):
64
65      self.par = parameters
```

```
66      self.workflow()
67
68    def workflow(self):
69
70      self.variable_ini()
71      self.get_time_domain()
72      self.get_frequency_domain()
73      self.get_noise()
74      self.through_prism()
75      self.get_pulse()
76      self.add_noise()
77      self.normalisation()
78      self.get_plasma_channels()
79      self.through_prism()
80      self.train_generation()
81      self.get_energy()
82
83    def variable_ini(self):
84
85      self.wl0 = self.par.wl0 # the centre wavelength [m]
86      self.f0 = self.par.c/self.wl0 # the centre frequency [Hz]
87      self.w0 = self.f0*2*np.pi # the centre angular freuqency [rad.]
88      self.k0 = 2*np.pi/self.wl0 # the propagation constant [1/m]
89      self.tau_p_long = self.par.tau_p_long # pulse duration [s]
90      self.tau_p_short = self.par.tau_p_short # pulse duration [s]
91      self.T = self.par.T # time window [s]
92      self.Np = self.par.Np # number of points [#]
93      self.E_p = self.par.E_p # driver energy (moduated pulse)[J]
94      self.Ep = self.par.h*self.f0 # photon energy
95
96    def get_time_domain(self): # Initialise the time domain
97
98      self.dt = self.T/self.Np
99      self.t = np.arange(-self.T/2, self.T/2, self.dt)
100     self.tau = self.t
101
102   def get_frequency_domain(self): # Initialise the frequency domain
103
104     self.F = 1/self.dt
105     self.df = self.F/self.Np
106     self.f = np.arange(-self.F/2, self.F/2, self.df)
107     self.w = self.f*2*np.pi
108     self.wl = self.par.c/(self.f + self.f0)
109     self.k = self.par.c/self.wl
110
111   def get_pulse(self): # Create input pulses
112
113     self.driver_I_long = np.exp(-2*(self.t)**2/(self.tau_p_long)**2)
114     self.driver_E_long = np.exp(-(self.t)**2/(self.tau_p_long)**2)
115     self.seed_I_short = np.exp(-2*(self.t)**2/(self.tau_p_short)**2)
116     self.seed_E_short = np.exp(-(self.t)**2/(self.tau_p_short)**2)
117     self.spectrum_E_long = fftshift(fft(fftshift(np.sqrt(self.
      driver_I_long))))*self.dt
118     self.spectrum_I_long = np.abs(self.spectrum_E_long)**2
119     self.spectrum_E_long = np.sqrt(self.spectrum_I_long)
120     self.spectrum_E_short = fftshift(fft(fftshift(np.sqrt(self.
      seed_I_short))))*self.dt
```

```
121     self.spectrum_I_short = np.abs(self.spectrum_E_short)**2
122     self.spectrum_E_short = np.sqrt(self.spectrum_I_short)
123     self.spec_phase_seed = np.exp(1j*np.zeros((self.par.Np)))
124     self.driver_I_long = np.exp(-2*(self.t)**2/(self.tau_p_long)**2)
125     self.driver_E_long = np.exp(-(self.t)**2/(self.tau_p_long)**2)
126
127   def get_noise(self):
128
129     self.spectral_noise = np.random.random((self.par.Np))
130     self.plasma_noise = np.random.normal(0, self.par.SNR_plasma/100,
      1)
131     self.spectrometer_noise = np.random.random((self.par.Np))
132     self.energy_noise =  np.random.normal(0, self.par.SNR_energy/100,
      1)
133
134   def add_noise(self): # Add background noise to pulses
135
136     filter_1 = self.super_gaussian_filter(self.spectrum_E_long, int(
      self.par.Np/2), 15, 5)
137     self.spectrum_E_long = self.spectrum_E_long/max(self.
      spectrum_E_long)
138     self.spectrum_E_long = self.spectrum_E_long*filter_1
139     self.spectrum_I_long = np.abs(self.spectrum_E_long)**2
140
141     filter_2 = self.super_gaussian_filter(self.spectrum_I_short, int(
      self.par.Np/2+50), 415, 7)
142     self.spectrum_E_short = self.spectrum_E_short/max(self.
      spectrum_E_short)
143     self.spectrum_E_short = self.spectrum_E_short + 10**(-self.par.
      SNR_spec/20)*self.spectral_noise
144     self.spectrum_E_short = self.spectrum_E_short*filter_2
145     self.spectrum_I_short = np.abs(self.spectrum_E_short)**2
146
147     self.driver_E_long = fftshift(ifft(ifftshift(self.spectrum_E_long)
      ))*self.df
148     self.driver_I_long = abs(self.driver_E_long)**2
149     self.seed_E_short = fftshift(ifft(ifftshift(self.spectrum_E_short)
      ))*self.df
150     self.seed_I_short = abs(self.seed_E_short)**2
151
152   def normalisation(self): # Normalise pulse energy
153
154     self.phase_E_short = np.unwrap(np.angle(self.seed_E_short, deg =
      False))
155     A_long = self.E_p/np.sum(self.driver_I_long)/self.dt
156     self.driver_I_long = self.driver_I_long*A_long*(1 + self.
      energy_noise)
157     self.driver_E_long = self.driver_E_long*np.sqrt(A_long)
158
159     A_short = self.E_p/np.sum(self.seed_I_short)/self.dt
160     self.seed_I_short = self.seed_I_short*A_short*(1 + self.
      energy_noise)
161     self.seed_E_short = self.seed_E_short*np.sqrt(self.par.
      energy_ratio*A_short)
162
163     self.spectrum_E_long = fftshift(fft(fftshift(np.sqrt(self.
      driver_I_long))))*self.dt
```

```
164     self.spectrum_I_long = np.abs(self.spectrum_E_long)**2
165
166     self.spectrum_E_short = fftshift(fft(fftshift(self.seed_E_short)))
    *self.dt
167     self.spectrum_I_short = np.abs(self.spectrum_E_short)**2
168
169   def get_energy(self): # Calculate pulse energy
170
171     self.pulse_energy_seed = np.sum(self.seed_I_short)*self.dt
172     self.pulse_energy_long = np.sum(self.driver_I_long)*self.dt
173     self.spectrum_energy_long = np.sum(self.spectrum_I_long)*self.df
174     self.pulse_mod_energy = np.sum(abs(self.drive_mod)**2)*self.dt
175     self.spectrum_mod_energy = np.sum(abs(self.spec_mod)**2)*self.df
176     self.drive_shaped_energy = np.sum(abs(self.drive_shaped)**2)*self.
    dt
177     self.spec_shaped_energy = np.sum(abs(self.spec_shaped)**2)*self.df
178
179     print('=== Pulse ===')
180     print('Pulse energy: %.2f mJ'%(self.pulse_mod_energy*1e3))
181     print('Seed energy %.2f mJ'%(self.pulse_energy_seed*1e3))
182     print('Mod. pulse energy: %.2f mJ'%(self.pulse_energy_long*1e3))
183     print('Shaped pulse energy: %.2f mJ'%(self.drive_shaped_energy*1e3
    ))
184     print('=== Spectrum ===')
185     print('Spectrum energy: %.2f mJ'%(self.spectrum_energy_long*1e3))
186     print('Mod. spectrum energy: %.2f mJ'%(self.spectrum_mod_energy*1
    e3))
187     print('Shaped spectrum energy: %.2f mJ'%(self.spec_shaped_energy*1
    e3))
188
189   def get_plasma_channels(self): # Simulate the phase introduced by
     the plasma wakefield in a plasma channel
190
191     self.ne = self.par.ne*(1+self.plasma_noise)
192     self.wp0 = np.sqrt(self.ne*(self.par.q**2)*1e6/(self.par.me*self.
    par.ep0))
193     self.vg = self.par.c
194     self.delta_t = np.random.normal(0, self.par.timing_jitter, 1)
195     self.beta = 0.5*self.wp0**2/self.w0/(self.ne)/self.vg*self.par.Lp*
    self.par.d_ne
196
197     if self.par.timing_jitter_mode == 0 :
198       self.angle = -self.beta*np.cos(self.wp0*self.t)
199     elif self.par.timing_jitter_mode == 1 :
200       self.angle = -self.beta*np.cos(self.wp0*(self.t - self.delta_t))
201
202     self.phase = np.exp(1j*self.angle)
203     self.drive_mod = self.driver_E_long*self.phase
204     self.phase_drive_mod = (np.angle(self.drive_mod, deg = False))
205
206   def through_prism(self): # Calculate spectral dispersion introduced
     by the prism pair compressor
207
208     wl = self.wl*1e6 # wavelength converted to [micron]
209     wl0 = self.par.wl0*1e6 # centre wavelength converted to [micron]
210     s = 0  # initiate a variable
211     s0 = 0
```

```
    if self.par.name_g == 'BK7':
    # SCHOTT Zemax catalog
      A = [1.03961212, 0.231792344, 1.01046945]
      B = [0.00600069867, 0.0200179144, 103.560653]
      B = np.sqrt(B)

    wl_range = [0.3,2.5]

    for m in np.arange(0, len(A), 1):

      s = s + A[m]*wl**2/(wl**2 - B[m]**2)
      s0 = s0 + A[m]*wl0**2/(wl0**2 - B[m]**2)

    s = s + 1
    s0 = s0 + 1
    n = np.sqrt(s)
    self.n0 = np.sqrt(s0)

    func = lambda x: np.sqrt(1 + A[0]*x**2/(x**2 - B[0]**2) + A[1]*x**2/(x**2 - B[1]**2) + A[2]*x**2/(x**2 - B[2]**2))

    dwl = abs(wl[1] - wl[0])
    with warnings.catch_warnings():
    warnings.simplefilter("ignore")
    dn1 = derivative(func,wl0,dx=dwl/2,n=1)*1e6
    dn2 = derivative(func,wl0,dx=dwl/2,n=2)*1e12
    dn3 = derivative(func,wl0,dx=dwl/2,n=3,order=5)*1e18

    ng = (self.n0 - wl0*1e-6*dn1)
    GV = self.par.c/ng
    GD = self.par.Lg/GV
    GDD = wl0**3/(2*np.pi*self.par.c**2)*dn2*1e-18
    TOD = -wl0**4/(4*np.pi**2*self.par.c**3)*(3*dn2 + wl0*1e-6*dn3)*1e-24
    beta = n/self.par.c
    para, opt = curve_fit(self.func, self.w, beta*self.par.Lg*(self.w + self.w0))
    self.phase_glass = np.exp(1j*(self.par.Lg*beta - GD)*(self.w + self.w0))
    phase = 1/2*para[2]*self.w**2 + 1/6*para[3]*self.w**3
    self.phase_glass_2nd = np.exp(1j*(phase))
    self.angle_glass = np.unwrap(np.angle(self.phase_glass_2nd, deg = False))

  def func(self, x, a0, a1, a2, a3):
    return a0 + a1*x + 1/2*a2*x**2 + 1/6*a3*x**3

  def train_generation(self): # procedure to generate a P-MoPA pulse train

    self.spec_mod = fftshift(fft(fftshift(self.drive_mod)))*self.dt # get the modulated spectrum
    self.phase_spec_mod = np.unwrap(np.angle(self.spec_mod, deg = False)) # get the spectral phase of modulated spectrum
    self.spec_mask = abs(self.spec_mod)**2/max(abs(self.spec_mod)**2) > 0.1
    self.spec_shaped = (self.spec_mod*self.phase_glass_2nd) # compress
```

```
     the modulated spectrum
260     self.phase_spec_shaped = (np.angle(self.spec_shaped, deg = False))
     # get the spectral phase of the compressed pulse
261     # self.phase_spec_shaped = self.phase_spec_mod +  self.angle_glass
262     self.drive_shaped = self.max_shift(fftshift(ifft(ifftshift(self.
    spec_shaped)))*self.df*self.par.Np) # get the compressed pulse
263
264     self.phase_drive_shaped = (np.angle(self.drive_shaped, deg = False
    )) # get the temporal phase of the compressed pulse
265     self.phase_short = np.unwrap(np.angle(self.seed_E_short, deg =
    False))
266     self.phase_long = np.unwrap(np.angle(self.driver_E_long, deg =
    False))
267
268   def max_shift(self, Eo):
269
270     E = Eo.copy()
271     id2 = np.argmax(abs(E)**2/max(abs(E)**2)) # find the max point
272     Ex = np.roll(E, int(len(E)/2) - id2, axis = 0) # shift to the max
    point
273
274     return Ex
275
276   def super_gaussian_filter(self, signal, dx, S, rk):
277
278     Nx = len(signal)
279     x = np.arange(0,Nx,1)
280     peak = np.argmax(signal)
281     f = np.exp(-((x - int(dx))**2/S**2)**rk)
282
283     return f
284
285 if __name__ == '__main__':
286
287   par = PMOPA_parameters() # Initialise pulse parameters
288   train = PMOPA_propagation(par) # Initialise the pulse train object
289
290   # Plot results
291   mk1 = abs(train.drive_shaped)**2/max(abs(train.drive_shaped)**2)
     >0.05
292   mk2 = abs(train.spec_shaped)**2/max(abs(train.spec_shaped)**2) >
     0.01
293   fig, ax = plt.subplots(figsize = (5.5,3.5))
294   ax.plot(train.t*1e12, abs(train.drive_shaped)**2/max(abs(train.
     drive_shaped)**2), lw = 4, c = 'tab:red', alpha = 0.4, label = r'$b
     (\tau)$')
295   ax2 = ax.twinx()
296   ax2.plot(train.t[mk1]*1e12, train.phase_drive_shaped[mk1], lw = 4, c
      = 'tab:green', alpha = 0.4, label = r'$\phi(\tau)$')
297   ax.grid(alpha = 0.3)
298   ax.set_ylim(0,1.5)
299   ax2.set_ylim(-4,4)
300   ax.set_xlim(-2,2)
301   ax.set_xlabel(r'$\tau$ (ps)')
302   ax.set_ylabel(r'$b(\tau)$ (a.u.)')
303   ax2.set_ylabel(r'$\phi(\tau)$ (rad.)')
304   ax.legend(frameon = False)
```

```
  ax2.legend(frameon = False, loc = 2)

  fig, ax = plt.subplots(figsize = (5.5,3.5))
  ax.plot(train.wl*1e9, abs(train.spec_shaped)**2/max(abs(train.
    spec_shaped)**2), '-', lw = 4, c = 'tab:red', alpha = 0.4, label =
    r'$S(\lambda)$')
  ax2 = ax.twinx()
  ax2.scatter(train.wl[mk2]*1e9, train.phase_spec_shaped[mk2], lw = 4,
     c = 'tab:green', alpha = 0.4, label = r'$\psi(\lambda)$')
  ax.grid(alpha = 0.3)
  ax.set_xlim(1030 - 30,1030 + 30)
  ax.set_ylim(0, 1.5)
  ax2.set_ylim(-2, 2)
  ax.set_xlabel(r'$\lambda$ (nm)')
  ax.set_ylabel(r'$S(\lambda)$ (a.u.)')
  ax2.set_ylabel(r'$\psi(\lambda)$ (rad.)')
  ax.legend(frameon = False)
  ax2.legend(frameon = False, loc = 2)
```

B.3 The ePIE algorithm

```
# The following code uses the Python programming language.
import numpy as np
from timeit import default_timer as timer
from scipy.fftpack import fft, ifft, fftshift
import matplotlib.pylab as plt
import os

class parameters():

  def __init__(self):

    self.c = 2.99792458e8
    self.wl0 = 791e-9
    self.f0 = self.c/self.wl0
    self.workflow()

  def workflow(self):

    self.folder_setup()
    self.process_FROG_trace()
    self.set_retrieval()

  def folder_setup(self):

    # Users should define their own file directories and file names.
    self.dirctory = # This is the main directory storing the input
    data.
    self.path_trace =  # This is for the input FROG trace.

    self.path_spec =  # This is for the two input spectra.

  def process_FROG_trace(self):

    self.Nf_trace = 1 # number of file loaded
```

```
34      self.Ns_trace = 200 # region of interest for noise reconstruction
35      self.Nf_spec = self.Nf_trace # number of file loaded
36      self.Ns_spec = 200 # region of interest for noise reconstruction
37      ##### trace coupling ####
38      self.T_size = 6000e-15 # temporal window size [s]
39      self.Np_t = 256 # how many points to resolve a pulse
40      self.Np_f = self.Np_t # how many points to resolve a spectrum
41
42    def set_retrieval(self):
43
44      #### retrieval parameters ####
45      self.Nr_trace = 1 # number of traces loaded
46      self.Nr_run = 2 # number of runs to retrieve a pulse
47      self.N_success = 10 # number of success
48      self.filter_width = 1/3
49      self.error_function = 'least' # 'least', 'rms'
50      self.target_error = 0.012 # target error that the algorithm
      reaches
51      #####  algorithm parameters #####
52      self.alphap = 0.7 # 0.06 ptychographic search length
53      self.etap = 0.5 # initial momentum
54      self.random_momentum = 0.1 # random momentum
55      self.Error_momentum_factor = 3 # how large of the error to
      activate
56      self.N_momentum = 10 # wait for how many runs to activate momentum
57      self.Error_to_clean = 1 # when to consider re-run
58      self.N_clean = 50 # number of iteration to impose re-run
59      self.spec_locking_outer_probe = 1  # lock the unfiltered pulse in
      the outer loop
60      self.spec_locking_outer_object = 0 # lock the filtered pulse in
      the outer loop
61      self.spec_locking_inner_probe = 1 # lock the unfiltered pulse in
      the inner loop
62      self.spec_locking_inner_object = 0  # lock the filtered pulse in
      the inner loop
63      self.remove_1st_phase = 0 # 0: no, 1:yes
64      self.N_inner_lock = 1 # lock the filtered pulse in the inner loop
65      ##### masking ####
66      self.Nms = 1 # delay time step to adopt in the algorithm
67      self.Ts = self.Np_t # delay time window to adopt in the algorithm
68      self.Tc = self.Np_t/2
69
70  class retrieval():
71
72    def __init__(self, parameters):
73
74      self.par = parameters
75      self.engin = algorithm(self.par, self)
76      self.workflow()
77
78    def workflow(self):
79
80      self.load_data()
81      self.get_FOFM()
82      self.clean_signal()
83      self.get_results()
84
```

```
85  def load_data(self):
86
87    self.trace = []
88    self.f = []
89    self.t = []
90    self.spec_1 = []
91    self.spec_2 = []
92    # create file path
93    path_trace = self.par.dirctory + self.par.path_trace
94    path_spec = self.par.dirctory + self.par.path_spec
95
96    # load spectral data. Users should change the file paths of input
      spectra and centre frequency.
97    file_spec_1 = os.path.join(path_spec,'spectrum_0.csv')
98    file_spec_2 = os.path.join(path_spec, 'spectrum_1.csv')
99    spec_1 = np.genfromtxt(file_spec_1, delimiter = ',')
100   spec_2 = np.genfromtxt(file_spec_2, delimiter = ',')
101
102   # load trace data
103   for n1 in range(self.par.Nf_trace):
104     trace = np.genfromtxt(file_trace, delimiter = ',')
105     # Here, file_trace is the file name of the input FROG trace
106     self.f.append(np.genfromtxt(file_frequency, delimiter = ','))
107     self.t.append(np.genfromtxt(file_time, delimiter = ','))
108     # Here, users should load the calibration files for the time and
      frequency of the input FROG trace.
109     self.trace.append(trace)
110     self.spec_1.append(spec_1[n1,:])
111     self.spec_2.append(spec_2[n1,:])
112
113 def clean_signal(self): # Remove background noise
114
115   self.trace_in = []
116   self.spec_1_in = []
117   self.spec_2_in = []
118   spec_1_temp = 0
119   spec_2_temp = 0
120
121   for n in range(self.par.Nr_trace):
122
123     self.trace_in.append(np.sqrt(self.trace[n]))
124     spec_1_temp = self.spec_1[n]
125     spec_2_temp = self.spec_2[n]
126     spec_1_temp = np.sqrt(spec_1_temp)
127     spec_2_temp = np.sqrt(spec_2_temp)
128     self.spec_1_in.append(spec_1_temp)
129     self.spec_2_in.append(spec_2_temp)
130     self.spec_1_avg = np.mean(np.array(self.spec_1), axis = 0)
131     self.spec_2_avg = np.mean(np.array(self.spec_2), axis = 0)
132
133 def get_results(self):
134
135   self.Results = []
136   self.Tot_time = []
137   self.Tot_error = []
138   self.Error_success = []
139   self.FOFM_phase = self.phase(0)
```

```
    #Initial phase must have this form to reach stable end results

    for n1 in range(self.par.Nr_trace):
      phase_ini = self.phase(n1)
      self.engin.initialisation(n1)
      P = (ifft(fftshift(self.spec_1_in[n1]*phase_ini)))
      O = (ifft(fftshift(self.spec_2_in[n1]*phase_ini)))
      for n2 in np.arange(0, self.par.Nr_run,1):
        print('===== Run %d Start ====='%(n2+1))
        start = timer()
        results = self.engin.ePIE_engin(n1,
                        P,
                        O,
                        self.trace_in[n1],
                        self.spec_1_in[n1],
                        self.spec_2_in[n1],
                        self.par.target_erro)
        end = timer()
        self.Tot_time.append(end - start)
        self.Tot_error.append(results[6])
        self.Results.append(results)

      P = results[0]
      O = results[1]


  def phase(self, n): # Setup initial phase

    w = self.f[n]*1e-12*np.pi*2

    # can be any input value for different orders of spectral phase

    GDD = np.random.normal(1000,1000)

    TOD = np.random.normal(1000,1000)

    FOD = np.random.normal(1000,1000)

    psi = 1/2*GDD*w**2 + 1/6*TOD*w**3 + 1/24*FOD*w**4

    phase_out = np.exp(-1j*psi)

    return phase_out

class algorithm():

  def __init__(self, parameters, retrieval):

    self.par = parameters
    self.retrieval = retrieval

  def initialisation(self, n):

    ##### initialise parameters #####
    self.Error = []  # initialise error array
    self.Nit = [] # initialise iteration array
    self.Time = [] # initialise timing array
```

```
197     self.current_error = 10 # real-time FROG error
198     f = fftshift(self.retrieval.f[n])*1e-12
199     self.tau = self.retrieval.t[n]*1e12 # time array
200     self.w = 2*np.pi*f # angular frequency
201     self.Nf = len(self.w)
202     self.Nt = len(self.tau)
203     self.Ir = np.zeros((self.Nf, self.Nt)) # Trace
204     self.nit = 0 # counter for outer iteration
205     self.t0 = 0 # set initial time zero
206     self.Error_success_inner = []
207 
208     #####  initialise momentum #####
209     self.cp = 1 # cycle counter for the momentum
210     self.vp = 0 # initial velocity
211     self.vo = 0 # initial velocity
212     self.Objp = 0 # initial guess of pro for the velocity map
213     self.Objo = 0 # initial guess of obj for the velocity map
214 
215     #####  masking #####
216     self.dT = self.par.Ts
217     self.T_array = np.arange(int(self.Nt/2 - self.dT/2),
218     int(self.Nt/2 + self.dT/2),
219     self.par.Nms)
220 
221     self.phase_mask = np.zeros((self.Nf)) # suffled delay time array
222     dF = self.Nf
223     self.phase_mask[int(self.Nf/2 - dF/2):int(self.Nf/2 + dF/2)] = 1
224     self.phase_mask = fftshift(self.phase_mask) # phase mask
225     self.NtNf = len(self.T_array)*self.Nf
226 
227   def re_initialisation(self):
228 
229     ##### Initialise arrays #####
230     self.Ir = np.zeros((self.par.Np_f, self.par.Np_t)) # Trace
231     self.Error_success_inner = [] # initialse array of successful run
232     self.Error = []  # initialise error array
233     self.Nit = [] # initialise iteration array
234     self.Time = [] # initialise timing array
235     self.nit = 0 # counter for outer iteration
236     self.t0 = 0 # set initial time zero
237     self.current_error = 10 # real-time FROG error
238 
239     #####  Initialise momentum #####
240     self.cp = 1 # cycle counter for the momentum
241     self.vp = 0 # initial velocity
242     self.vo = 0 # initial velocity
243     self.Objp = 0 # initial guess of pro for the velocity map
244     self.Objo = 0 # initial guess of obj for the velocity map
245 
246   def ePIE_engin(self, Nr, P, O, trace_in, spec_1, spec_2, t_error):
247     # The author wants to emphasise that this algorithm is a modified
      version of the original work done by Sidorenko et al. [185].
      Readers should refer to the original research work to obtain
      detailed explanation of each retrieval steps.
248 
249     self.re_initialisation()
250     start = timer()
```

```
251     N_success = 0
252
253     while N_success <= self.par.N_success:
254
255       if self.current_error > 1.25*t_error:
256         Nms = self.par.Nms*3
257       elif self.current_error > 1*t_error:
258         Nms = self.par.Nms*2
259       elif self.current_error <= t_error:
260         Nms = self.par.Nms
261       if N_success == self.par.N_success-1:
262         Nms = 1
263       if self.current_error > self.par.target_error*self.par.
    Error_momentum_factor :
264         self.cp = self.cp + 1
265         if self.nit > 10 and self.cp%self.par.N_momentum == 0:
266         P, O = self.momentum(P, O)
267         print('\nJump!')
268
269        #### locking the spectrum at the beginning ####
270       if self.par.spec_locking_outer_probe == 1:
271         if self.nit > 0:
272           phase_spec_p = np.exp(1j*np.angle(fft(P), deg= False))
273           P = ifft(fftshift(spec_1)*phase_spec_p)
274
275       if self.par.spec_locking_outer_object == 1:
276         if self.nit > 0:
277           phase_spec_o = np.exp(1j*np.angle(fft(O), deg= False))
278           O = ifft(fftshift(spec_2)*phase_spec_o)
279
280       self.T_array = np.arange(int(self.par.Tc - self.dT/2),
281       int(self.par.Tc + self.dT/2),
282       Nms)
283       self.NtNf = len(self.T_array)*self.Nf
284       np.random.shuffle(self.T_array)
285       cc = 0
286       for nx in self.T_array: # create a new FROG trace
287
288         phi1 = self.tau[nx]
289
290         # self.centering(P)
291         # self.centering(O)
292         Ps = ifft(fft(P)*np.exp(1j*self.w*phi1))
293         psi = O*Ps # first SHG FROG constraint
294         psi_n = fft(psi)/self.Nf # go into frequency domain
295         phase_p = np.exp(1j*np.angle(psi_n, deg= False))#*self.
    phase_mask
296         # calculate the phase
297         # Vol. 28, No. 4 / April 2011 / J. Opt. Soc. Am. A 6
298
299         psi_n = ifft(fftshift(trace_in[:,nx])*phase_p)*self.Nf
300         # add the new phase from the new FROG trace
301         # back to time domain
302         if self.current_error >= 1.2*t_error:
303           alpha = self.par.alphap*(1 - 0.2*np.random.random((1))) #
    create stochastic search length
304         else:
```

```
305           alpha = self.par.alphap
306
307         # gradient descent udate function
308         Update1 = abs(Ps)*np.conj(Ps)/(max(abs(Ps))*abs(Ps)**2)
309         Update2 = abs(O)*np.conj(O)/(max(abs(O))*abs(O)**2)
310         ### ptychographic update function for trace ###
311         Corr1 = alpha*Update1*(psi_n - psi)
312         O = O +  Corr1
313         Corr2 = alpha*Update2*(psi_n - psi)
314         Ps = Ps + Corr2
315         P = ifft(fft(Ps)*np.exp(-1j*self.w*phi1))
316         if self.par.spec_locking_inner_object == 1:
317           if self.current_error <= 2*self.par.target_error:
318             if cc%self.par.N_inner_lock==0:
319               phase_spec_o = np.exp(1j*np.angle(fft(O), deg= False))
320               O_psi = ifft(fftshift(spec_2)*phase_spec_o)
321               Update4 = abs(P)/max(abs(P))*np.conj(P)/(abs(P)**2)
322               Corr4 = alpha*Update4*(O_psi - O)
323               P = P +  Corr4
324               O = O_psi
325               cc = 0
326         if self.par.spec_locking_inner_probe == 1:
327           if self.current_error <= 2*self.par.target_error:
328             if cc%self.par.N_inner_lock==0:
329               phase_spec_p = np.exp(1j*np.angle(fft(P), deg= False))
330               P_psi = ifft(fftshift(spec_1)*phase_spec_p)
331               Update3 = abs(O)/max(abs(O))*np.conj(O)/(abs(O)**2)
332               Corr3 = alpha*Update3*(P_psi - P)
333               O = O +  Corr3
334               P = P_psi
335               cc = 0
336         cc = cc + 1
337         self.Ir[:,nx] = abs(fftshift(fft(O*Ps)/self.Nf))**2
338
339          ######## monitoring the FROG trace error ###########
340       if self.par.error_function == 'least':
341         self.current_error = np.sqrt(sum(sum((self.Ir[:,self.T_array]
    - trace_in[:,self.T_array]**2)**2) )/self.NtNf)
342
343       elif self.par.error_function == 'rms':
344         self.current_error = sum(sum((self.Ir[:,self.T_array] -
    trace_in[:,self.T_array]**2)**2/self.Ir[:,self.T_array]))
345
346       if self.nit > 1:
347         if self.current_error >= self.par.target_error*self.par.
    Error_to_clean:
348           if self.nit%self.par.N_clean == 0:
349             print('\nRe-run')
350             P, O = self.re_run(Nr, spec_1, spec_2)
351       print('\r %dth iteration: error: %0.3e' % (self.nit,  self.
    current_error), end='')
352       if self.current_error <= self.par.target_error:
353         N_success = N_success + 1
354         self.retrieval.Error_success.append(self.current_error)
355
356       self.Error.append(self.current_error)
357       self.nit = self.nit + 1
```

```
358         self.Nit.append(self.nit)
359         end = timer()
360         self.Time.append(end - start)
361         # print('\r', end='', flush=True)
362 
363       self.Time = np.array(self.Time)
364       self.Nit = np.array(self.Nit)
365       self.Time = np.array(self.Time)
366       self.Error = np.array(self.Error)
367       w = fftshift(self.w)
368       self.centering(P)
369       self.centering(O)
370 
371       return [P, O, self.Ir, self.Nit, self.Time,
372       self.Error, self.current_error, w, self.retrieval.t[Nr]*1e12]
373 
374   def re_run(self, n, spec_1, spec_2):
375 
376       phase_p = self.retrieval.phase(n)
377       P = fftshift(ifft(fftshift(spec_1*phase_p)))
378       O = fftshift(ifft(fftshift(spec_2*phase_p)))
379 
380       return P, O
381 
382   def momentum(self, P, O):
383 
384       eta = self.par.etap - \
385       self.par.random_momentum*np.random.random((1))
386       self.vp = self.vp + (P - self.Objp)
387       P = P + eta*self.vp
388       self.Objp = P
389       self.vo = self.vo + (O - self.Objo)
390       O = O + eta*self.vo
391       self.Objo = O
392 
393       return P, O
394 
395   def centering(self, E):
396 
397       s = abs(E)
398       idx = np.argmax(s)
399       E = np.roll(E, int(self.par.Np_t/2) - idx)
400 
401 if __name__ == "__main__":
402 
403   P1 = parameters()
404   R1 = retrieval(P1) # Implement the phase retrieval process.
405 
406   # Plot results
407   fig, ax = plt.subplots()
408   ax.plot(R1.t[0]*1e12, abs(R1.Results[0][1])**2/max(abs(R1.Results
      [0][1])**2), lw = 4, alpha = 0.7)
409   ax.set_xlabel('Time (ps)')
410   ax.set_ylabel('Intensity (a.u.)')
411   ax.grid(alpha = 0.3)
```

B.4 The SSA algorithm

```
# The following code uses the Python programming language.
import numpy as np
from numpy import fft
import matplotlib.pyplot as plt
from scipy.optimize import curve_fit
import lib_shift as sf
from scipy.fftpack import fft, ifft, fftshift, ifftshift
from scipy.signal import find_peaks
import parameters as pa
# Users should load the class parameters in B.3
import lib_algorithm as la
# Users should load the class algorithm in B.3
import lib_retrieval as al
# Users should load the class retrieval in B.3

class SSA():

  def __init__(self, parameters, retrieval):

    self.par = parameters
    self.retrieval = retrieval
    self.Nr = len(self.retrieval.Results)
    self.diagnostics = ld.diagnostics(self.par, [], self)
    self.sf = sf.shift(self.par)
    self.w = self.retrieval.Results[0][7]
    self.f = self.w/(2*np.pi)
    self.f0 = self.par.f0
    self.t = self.retrieval.Results[0][8]
    self.Np = len(self.t)
    self.engin = la.algorithm(self.par, self)
    self.workflow()

  def workflow(self):

    self.get_trace()
    self.pulse_selection()
    self.fing_pulse_spacing()
    self.recreate_FROG_trace()
    self.recreate_SSA()
    self.get_spectrum()
    self.get_pulse_from_ssa()

  def get_trace(self):

    self.trace_o = []
    self.trace_r = []

    for n in range(self.par.Nr_trace):

      self.trace_o.append(self.retrieval.trace[n])

    for n in range(self.Nr):

      trace = self.retrieval.Results[n][2]
```

```
55        self.trace_r.append(trace)
56
57    def pulse_selection(self): # select the optimal pulses that can be
       used to reconstruct SSA signal
58
59      phase_p = self.phase_compensate()
60      self.probe = []
61      self.object = []
62      self.phase_o = []
63      self.phase_p = []
64      self.spacing = []
65      self.f_probe = []
66      self.pulse = []
67      self.trace = []
68      for n in range(self.Nr):
69        self.retrieval.Results[n][0] = fftshift(ifft(fft(fftshift(self.
       retrieval.Results[n][0]))*phase_p))
70        self.retrieval.Results[n][1] = fftshift(ifft(fft(fftshift(self.
       retrieval.Results[n][1]))*phase_p))
71
72      probe = self.sf.max_shift(self.retrieval.Results[n][0])
73      obj = self.sf.max_shift(self.retrieval.Results[n][1])
74
75      # probe = self.sf.centroid_shift(probe, 3)
76      # obj = self.sf.centroid_shift(obj, 3)
77
78      pht_p = np.unwrap(np.angle(probe, deg = False))
79      pht_p = pht_p - pht_p[int(len(pht_p)/2)]
80
81      pht_o = np.unwrap(np.angle(obj, deg = False))
82      pht_o = pht_o - pht_o[int(len(pht_p)/2)]
83
84      self.probe.append(abs(probe)**2/np.max(abs(probe)**2))
85      self.object.append(abs(obj)**2/np.max(abs(obj)**2))
86
87      self.phase_o.append(pht_o)
88      self.phase_p.append(pht_p)
89
90      f_probe = abs(fftshift(fft(fftshift(self.probe[n]))))
91      f_probe = f_probe/np.max(f_probe)
92
93      peaks1, _ = find_peaks(f_probe, height = 0.25, rel_height=0.5)
94      peaks2, _ = find_peaks(self.probe[n], height = 0.3, rel_height
       =0.5)
95
96      if len(peaks1) == 3:
97        spacing = 1/self.f[peaks1[0]]
98
99      if abs(spacing)*1e3 < 160 and abs(spacing)*1e3 > 140:
100     # if abs(spacing)*1e3 < 140 and abs(spacing)*1e3 > 120:
101       self.spacing.append(spacing*1e3)
102       self.f_probe.append(f_probe)
103       self.pulse.append(probe)
104       self.trace.append(self.trace_r[n])
105
106   def fing_pulse_spacing(self):
107
```

```
108     self.f_probe_avg = np.mean(np.array(self.f_probe), axis = 0)
109     self.pulse_avg = []
110     for n in range(len(self.pulse)):
111     pulse = abs(self.pulse[n])**2/max(abs(self.pulse[n])**2)
112     peaks_, _ = find_peaks(pulse, height = 0.2, rel_height=0.5)
113     self.pulse_avg.append(pulse)
114     self.pulse_avg = np.mean(np.array(self.pulse_avg), axis = 0)
115     self.pulse_std = np.std(np.array(self.pulse_avg), axis = 0)
116
117   def recreate_FROG_trace(self):
118
119     self.trace_re = []
120     self.trace_avg = 0
121
122     for n in range(len(self.pulse)):
123       self.trace[n] = self.centroid_shift_2D(self.trace[n])
124       trace, ssa = self.FROG_device(self.t, self.f, self.pulse[n],
    self.pulse[n])
125       trace = trace - np.mean(trace[0:50,0:50])
126       trace[trace<0] = 0
127       self.trace_re.append(trace)
128       trace = self.centroid_shift_2D(trace)
129       self.trace_avg = self.trace_avg + trace
130
131     self.trace_avg = self.trace_avg/len(self.pulse)
132
133   def recreate_SSA(self):
134
135     self.ssa_re = []
136     self.ssa_o = []
137     self.ssa_avg = np.sum(self.trace_avg, axis = 0)
138     self.ssa_avg = self.ssa_avg/np.max(self.ssa_avg)
139
140     for n in range(len(self.pulse)):
141
142       ssa = np.sum(self.trace_re[n], axis = 0)
143       ssa_in = np.sum(self.trace[n], axis = 0)
144       ssa_in = self.sf.max_shift(ssa_in/np.max(ssa_in))
145       ssa = self.sf.max_shift(ssa/np.max(ssa))
146       self.ssa_o.append(np.roll(ssa_in, 18))
147       self.ssa_re.append(ssa)
148
149     self.ssa_av = np.mean(self.ssa_re, axis = 0)
150     self.ssa_st = np.std(self.ssa_re, axis = 0)
151
152   def get_pulse_from_ssa(self): # implement the SSA algorithm
153
154     self.GDD = []
155     self.TOD = []
156     self.I_ssa = []
157     self.pulse_ssa = []
158     data = np.loadtxt('Spec_Gemini.txt',
159     dtype= 'float', delimiter = '\t', skiprows=14)
160     spec=data[:,1]
161     spec = spec - np.mean(spec)
162     spec[spec<0] = 0
163     cx = self.sf.get_1D_centroid(spec)
```

```
164     self.wl0 = data[cx,0]*1e-9
165     f = self.par.c/data[:,0]*1e-3
166     f_new = self.f + (self.par.c/self.wl0)*1e-12
167     spec_new = np.interp(f_new, np.flipud(f), np.flipud(spec))
168     spec_new[spec_new<0]=0
169     spec_new = spec_new/np.max(spec_new)
170 
171     T_Sp = []
172     Sp = []
173     Peak = []
174 
175     for n in range(len(self.retrieval.spec_1)):
176       t_spec = abs(fftshift(fft(fftshift(self.retrieval.spec_1[n]))))
177       Sp.append(self.retrieval.spec_1[n])
178       t_spec = t_spec/np.max(t_spec)
179       T_Sp.append(t_spec)
180       peaks_, _ = find_peaks(t_spec, height = 0.3)
181       Peak.append(peaks_[2])
182 
183     Sp_avg = np.mean(np.array(Sp), axis = 0)
184     Sp_std = np.std(np.array(Sp), axis = 0)
185     T_SP_avg = np.mean(np.array(T_Sp), axis = 0)
186     T_SP_std = np.std(np.array(T_Sp), axis = 0)
187     Peak = np.array(Peak)
188     tau = np.mean(self.t[Peak]*1e3)
189     tau_std = np.std(self.t[Peak]*1e3)
190 
191     phi = [tau, -11000, 20000]
192 
193     for n in range(len(self.ssa_o)):
194 
195       tau_in, Io2, pulse2, GD2, GDD2, TOD2 = self.fit_SSA(self.t, self
    .ssa_o[n], spec_new, phi)
196 
197       tau_in, I_ssa, pulse_ssa, GD, GDD, TOD = self.fit_SSA(self.t,
    self.ssa_re[n], spec_new, phi)
198 
199       self.I_ssa.append(I_ssa)
200       self.pulse_ssa.append(pulse_ssa)
201       self.GDD.append(GDD)
202       self.TOD.append(TOD)
203 
204     self.I_ssa_avg = np.mean(np.array(self.I_ssa),axis = 0)
205     self.pulse_ssa_avg = np.mean(np.array(self.pulse_ssa),axis = 0)
206     self.GDD_avg = np.mean(self.GDD)
207     self.TOD_avg = np.mean(self.TOD)
208 
209     self.I_ssa_std = np.std(np.array(self.I_ssa),axis = 0)
210     self.pulse_ssa_std = np.std(np.array(self.pulse_ssa),axis = 0)
211     self.GDD_std = np.std(self.GDD)
212     self.TOD_std = np.std(self.TOD)
213 
214     print('\n--------')
215     self.spacing_avg = np.mean(np.array(self.spacing))
216     self.spacing_std = np.std(np.array(self.spacing))
217     print('Pulse spacing: %.2f +- %.2f fs'%(self.spacing_avg, self.
    spacing_std))
```

```
218     print('--- SSA ---')
219     print('Retrived phi2: %.2f +- %.2f'%(self.GDD_avg,self.GDD_std))
220     print('Retrived phi3: %.2f +- %.2f'%(self.TOD_avg,self.TOD_std))
221 
222   def plot_results(self):
223 
224     fig, ax = plt.subplots(figsize = (5, 3.5))
225     p1 = ax.imshow(self.trace_avg, cmap = self.par.newcmap,
226     aspect = 'auto',
227     alpha = 0.9,
228     extent = [min(self.t),
229     max(self.t),
230     min(self.f),
231     max(self.f)])
232     ax.set_xlabel(r'$\tau$ (ps)')
233     ax.set_ylabel(r'$\omega$ (THz)')
234     cb = plt.colorbar(p1,
235     pad = 0.00,
236     aspect = 40)
237     cb.set_label(label = r'$I(\tau, \omega)$', labelpad = 12)
238     p1.set_clim(0,1)
239 
240     fig, ax = plt.subplots(figsize = (5, 3.5))
241     p1 = ax.imshow(np.roll(self.trace_o[0], -20, axis = 0),
242     cmap = self.par.newcmap,
243     aspect = 'auto',
244     alpha = 0.9,
245     extent = [min(self.t),
246     max(self.t),
247     min(self.f),
248     max(self.f)])
249     ax.set_xlabel(r'$\tau$ (ps)')
250     ax.set_ylabel(r'$\omega$ (THz)')
251     cb = plt.colorbar(p1,
252     pad = 0.00,
253     aspect = 40)
254     cb.set_label(label = r'$I(\tau, \omega)$', labelpad = 12)
255     p1.set_clim(0,1)
256 
257     fig, ax = plt.subplots(figsize = (5, 3.5))
258     ax.plot(self.t*1e3, self.ssa_avg, '-',
259     c = 'tab:red', lw = 4, alpha = 0.7, label = 'Input')
260     ax.plot(self.t*1e3, self.I_ssa_avg, '-',
261     c = 'tab:blue', lw = 4, alpha = 0.7, label = 'Retrieved')
262 
263     ax.fill_between(self.t*1e3, self.I_ssa_avg - self.I_ssa_std ,
264     self.I_ssa_avg + self.I_ssa_std,
265     color = 'tab:blue', lw = 2, alpha = 0.3)
266     ax.set_ylim(0, 1.5)
267     ax.set_xlim(-2000,2000)
268     ax.grid(alpha = 0.3)
269     ax.set_xlabel(r'$\tau$ (fs)')
270     ax.set_ylabel(r'$I(\tau)$')
271     ax.legend(frameon = False)
272 
273     fig, ax = plt.subplots(figsize = (5, 3.5))
274     ax.plot(self.t*1e3, self.pulse_avg, '-',
```

```
    c = 'tab:red', lw = 4, alpha = 0.7, label = 'FROG')
    ax.plot(self.t*1e3, self.pulse_ssa_avg, '-',
    c = 'tab:blue', lw = 4, alpha = 0.7, label = 'SSA')

    ax.fill_between(self.t*1e3, self.pulse_ssa_avg - self.
   pulse_ssa_std ,
    self.pulse_ssa_avg + self.pulse_ssa_std,
    color = 'tab:blue', lw = 2, alpha = 0.3)

    ax.set_ylim(0, 1.5)
    ax.set_xlim(-1500,1500)
    ax.grid(alpha = 0.3)
    ax.set_xlabel(r'$t$ (fs)')
    ax.set_ylabel(r'$I(t)$')
    ax.legend(frameon = False)

  def get_TBP(self, t, e, w, a):

    def func_rms(x, y):

      f = np.sum(x*abs(y)**2)/np.sum(abs(y)**2)

      return f

    t_rms = 2*np.sqrt(func_rms(t**2,e) - func_rms(t,e)**2)
    f_rms = 1/np.pi*np.sqrt(func_rms(w**2,a) - func_rms(w,a)**2)

    TBP = t_rms*f_rms

    return TBP, t_rms, f_rms

  def get_spectrum(self):

    self.spec_re = []
    self.TBP_probe = []
    self.rmst_probe = []

    for n in range(len(self.pulse)):

      sp = fftshift(fft(ifftshift(self.pulse[n])))
      tbp_p, t_rms_p, f_rms_p = self.get_TBP(self.t, self.pulse[n],
    self.w, sp)
      sp = self.sf.centroid_shift(sp, 1)
      self.TBP_probe.append(tbp_p)
      self.rmst_probe.append(t_rms_p)
      self.spec_re.append(abs(sp)**2/np.max(abs(sp)**2))
      phs_p = np.unwrap(np.angle(sp, deg = False))
      mask_p = abs(self.f) <  12
      pov_p, cov_p = curve_fit(self.phase_func,
      self.w[mask_p],
      phs_p[mask_p])
      phs_p_f = np.exp(-1j*self.phase_func(self.w, 0, pov_p[1],0,0,0))
      sp = sp*phs_p_f
      phs_p = np.unwrap(np.angle(sp, deg = False))
      phs_p = phs_p - phs_p[int(len(phs_p)/2)]

  def phase_compensate(self):
```

```
330
331     w = self.f*1e-3*np.pi*2
332     GDD = 0
333     psi = 1/2*GDD*w**2
334     phase_out = fftshift(np.exp(-1j*psi))
335
336     return phase_out
337
338   def FROG_device(self, t, f, pulse_1, pulse_2): # Generate a FROG
        trace and extract SSA signal
339
340     N = len(f)
341     trace = np.zeros((N, N))
342     cn = 0
343     w = 2*np.pi*f
344
345     for phi1 in t:
346       Px = ifft(fft(pulse_1)*np.exp(1j*phi1*w))
347       trace[:, cn] = abs(fftshift(fft(Px*pulse_2)))**2
348       cn = cn + 1
349     trace = trace/np.amax(trace)
350     ssa = np.sum(trace,axis = 0)
351     ssa = ssa/np.max(ssa)
352
353     return trace, ssa
354
355   def get_delay_time(self): # Initialise a matrix for creating ssa
        signal
356
357     N = len(self.t)
358     self.tau_matrix_p = np.zeros((N,N)) + 0j
359     self.tau_matrix_n = np.zeros((N,N)) + 0j
360     for n in range(len(self.t)):
361       self.tau_matrix_p[:,n] = np.exp(1j*self.t[n]/2*self.w)
362       self.tau_matrix_n[:,n] = np.exp(-1j*self.t[n]/2*self.w)
363
364   def get_SSA(self, spec_1, spec_2): # Create the SSA signal from a
        FROG trace
365
366     spec_matrix_s1 = (spec_1*np.ones((self.Np, self.Np))).T
367     spec_matrix_s2 = (spec_2*np.ones((self.Np, self.Np))).T
368     s1 = spec_matrix_s1*self.tau_matrix_p
369     s2 = spec_matrix_s2*self.tau_matrix_n
370     p1 = ifftshift(ifft(fftshift(s1), axis = 0))
371     p2 = ifftshift(ifft(fftshift(s2), axis = 0))
372     trace = abs(fftshift(fft(fftshift(p1*p2), axis = 0)))**2
373     ssa = np.sum(trace, axis = 0)
374     ssa = ssa/np.max(ssa)
375
376     return ssa
377
378   def centroid_shift_2D(self, trace):
379
380     cx = self.get_1D_centroid(trace)
381     Nx = len(trace[:,0])
382     trace_out = np.roll(trace, int(Nx/2 - cx), axis = 0)
383
```

```
384     return trace_out
385
386   def get_1D_centroid(self, trace):
387
388     E = np.sum(trace, axis = 1)
389     Nx = len(E)
390     X = np.arange(0, Nx, 1)
391     E[E==0] = 1e-16
392     cx = int(np.sum(X*E)/np.sum(E))
393     E[E==1e-16] = 0
394
395     return cx
396
397   def phase_func(self, w, phi0, phi1, phi2, phi3, phi4):
398
399     psi = phi0 + phi1*w + 1/2*phi2*w**2 + 1/6*phi3*w**3  + 1/24*phi4*w
      **4
400
401     return psi
402
403   def fit_SSA(self, tau_in, Issa, spec_in, phi):
404     # This is the SSA algorithm rewritten by the author to support the
       retrieval of pulse trains used in the 2023 Gemini resonance down-
      ramp injection.
405
406     # The author wants to emphasise that the original code of the SSA
      algorithm was devised by Professor Simon Hooker [134]. Readers
      should refer to the original work for explanation of each step in
      detail.
407
408     self.get_delay_time()
409
410     w = self.w*1e-3
411
412     def gauss(x, x0, y0, sigma):
413       f = x0*np.exp(-((x-y0)/sigma)**2)#+(a + b*x + c*x**2 + d*x**3)
414
415       return f
416
417     def compressor(w, spec, GDD, TOD):
418
419       phase_p = 1/2*GDD*w**2 + 1/6*TOD*w**3
420       E = np.sqrt(spec)*np.exp(-1j*phase_p)
421
422       return E
423
424     def michelson(w, E, delay):
425       E_train = E*np.exp(-1j*delay/2*w) + E*np.exp(1j*delay/2*w)
426       return E_train
427
428     def func(x, taug, phi2g, phi3g):
429
430       E = compressor(w, spec_in, phi2g, phi3g)
431       E_train =  michelson(w, E, taug)
432       Iox = self.get_SSA(E_train, E_train)
433       fx = np.interp(x, self.t, Iox)
434
```

```
435         return fx
436
437     phi1 = phi[0]+ 0.00*phi[0]*(1 - 2*np.random.random(1))
438     phi2 = phi[1] + 0.01*phi[1]*(1 - 2*np.random.random(1))
439     phi3 = phi[2] + 0.001*phi[2]*(1 - 2*np.random.random(1))
440
441     pi = [phi1[0], phi2[0], phi3[0]]
442     bd = ((phi1[0]*0.999, phi2[0]-2000, phi3[0] - 20000),
443     (phi1[0]*1.001, phi2[0]+2000, phi3[0] + 20000))
444
445     popt, pcov = curve_fit(func, tau_in, Issa, p0 = pi, bounds = bd,
        method = 'dogbox')
446
447     E = compressor(w, spec_in, popt[1], popt[2])
448     E_train = michelson(w, E, popt[0])
449
450     pulse = abs(ifftshift(ifft(fftshift(E_train))))**2
451     pulse = pulse/np.max(pulse)
452     Io = func(tau_in, *popt)
453
454     return tau_in, Io, pulse, popt[0], popt[1], popt[2]
455
456 if __name__ == "__main__":
457
458   P1 = pa.parameters() # The class parameter used in B.3 ePIE
       algorithm.
459   R1 = al.retrieval(P1) # The class retrieval used in B.3 ePIE
       algorithm.
460   S1 = SSA(P1, R1) # Implement the SSA algorithm.
461   S1.plot_results()
```

References

[1] Stephen Hawking and Leonard Mlodinow. "The Grand Design". In: Bantam Books, 2010. Chap. 1, p. 14 (cit. on p. 1).

[2] Alessandro Bettini. "Introduction to Elementary Particle Physics". In: Cambridge University Press, Feb. 2014, pp. 19–21. DOI: 10.1017/cbo9781107279483 (cit. on p. 1).

[3] M. G Bowler. "Femtophysics: A Short Course on Particle Physics". In: Pergamon Press, 1990, p. 3 (cit. on p. 1).

[4] Abbe. "The Relation of Aperture and Power in the Microscope (continued).*". In: *Journal of the Royal Microscopical Society* 2.4 (Aug. 1882), pp. 460–473. DOI: 10.1111/j.1365-2818.1882.tb04805.x (cit. on p. 1).

[5] Louis-Victor de Broglie. "On the Theory of Quanta". PhD thesis. University of Paris, 1892 (cit. on p. 1).

[6] Klaus Wille. "The Physics of Particle Accelerators: An Introduction". In: Oxford University Press, Oxford, Feb. 2001, pp. 4–22. DOI: 10.1093/oso/9780198505501.001.0001 (cit. on p. 2).

[7] Javier Resta-Lopez. "Long-term future particle accelerators". In: *arXiv* (2022). DOI: 10.48550/ARXIV.2206.08834 (cit. on p. 2).

[8] Robert W Hamm and Marianne E Hamm. *Industrial Accelerators and Their Applications*. WORLD SCIENTIFIC, Nov. 2011. DOI: 10.1142/7745 (cit. on p. 2).

[9] Soren Moller. "Accelerator Technology: Applications in Science, Medicine, and Industry". In: Springer International Publishing, 2020. Chap. 6. DOI: 10.1007/978-3-030-62308-1 (cit. on p. 2).

[10] Manjit Dosanjh. "From Particle Physics to Medical Applications". In: *From Particle Physics to Medical Applications*. IOP Publishing, 2017. DOI: 10.1088/978-0-7503-1444-2ch1 (cit. on p. 2).

[11] Klaus Wille. "The Physics of Particle Accelerators: An Introduction". In: Oxford University Press, Oxford, Feb. 2001, pp. 152–168. DOI: 10.1093/oso/9780198505501.001.0001 (cit. on p. 2).

[12] Frank Zimmermann. "Accelerator Physics for ILC and CLIC". In: *Proceedings in Science*. 2009 (cit. on pp. 2, 4).

[13] Klaus Wille. "The Physics of Particle Accelerators: An Introduction". In: Oxford University Press, Oxford, Feb. 2001, pp. 169–176. DOI: 10.1093/oso/9780198505501.001.0001 (cit. on p. 3).

[14] Canon Electron Tubes and Devices. *Pulsed Klystron Amplifier*. Tech. rep. 1385, Shimoishigami, Otawara-shi, Tochigi 324-8550, Japan: Canon Ltd. (cit. on p. 3).

[15] CERN. "CERN Yellow Reports: The Compact Linear Collider (CLIC) – Project Implementation Plan". en. In: *CERN, CH-1211 Geneva 23, Switzerland* (2019). DOI: 10.23731/CYRM-2018-004 (cit. on p. 3).

[16] A. Grudiev, S. Calatroni, and W. Wuensch. "New local field quantity describing the high gradient limit of accelerating structures". In: *Physical Review Special Topics - Accelerators and Beams* 12.10 (Oct. 2009), p. 102001. DOI: 10.1103/physrevstab.12.102001 (cit. on p. 3).

[17] M. Jacewicz et al. "Spectrometers for RF breakdown studies for CLIC". In: *Nuclear Instruments and Methods in Physics Research Section A: Accelerators, Spectrometers, Detectors and Associated Equipment* 828 (Aug. 2016), pp. 63–71. DOI: 10.1016/j.nima.2016.05.031 (cit. on p. 3).

[18] Dillon Merenich et al. "Breakdown insensitive acceleration regime in a metamaterial accelerating structure". In: *Physical Review Accelerators and Beams* 27.4 (Apr. 2024), p. 041301. DOI: 10.1103/physrevaccelbeams.27.041301 (cit. on p. 3).

[19] Philip Bambade et al. "The International Linear Collider: A Global Project". In: (2019). DOI: 10.48550/ARXIV.1903.01629 (cit. on p. 3).

[20] Barry C. Barish. *THE INTERNATIONAL LINEAR COLLIDER From Design to Reality*. Tech. rep. 1-1 Oho, Tsukuba, Ibaraki, 305-0801, Japan: High Energy Accelerator Research Organization, 2013 (cit. on p. 3).

[21] Mangles S.P.D. "An Overview of Recent Progress in LaserWakefield Acceleration Experiments". In: *CERN Yellow Reports* (2016). DOI: 10.5170/CERN-2016-001.289 (cit. on p. 4).

[22] T. Tajima and J. M. Dawson. "Laser Electron Accelerator". In: *Physical Review Letters* 43.4 (July 1979), pp. 267–270. DOI: 10.1103/physrevlett.43.267 (cit. on pp. 4, 14, 18).

[23] Wentao Wang et al. "Free-electron lasing at 27 nanometres based on a laser wakefield accelerator". In: *Nature* 595.7868 (July 2021), pp. 516–520. DOI: 10.1038/s41586-021-03678-x (cit. on p. 4).

[24] Marie Labat et al. "Seeded free-electron laser driven by a compact laser plasma accelerator". In: *Nature Photonics* 17.2 (Dec. 2022), pp. 150–156. DOI: 10.1038/s41566-022-01104-w (cit. on p. 4).

[25] C. B. Schroeder et al. "Physics considerations for laser-plasma linear colliders". In: *Physical Review Special Topics - Accelerators and Beams* 13.10 (Oct. 2010), p. 101301. DOI: 10.1103/physrevstab.13.101301 (cit. on pp. 4, 25).

[26] C.B. Schroeder et al. "Linear colliders based on laser-plasma accelerators". In: *Journal of Instrumentation* 18.06 (June 2023), T06001. DOI: 10.1088/1748-0221/18/06/t06001 (cit. on p. 4).

[27] S. M. Hooker. "Developments in laser-driven plasma accelerators". In: *Nature Photonics* 7.10 (Sept. 2013), pp. 775–782. DOI: 10.1038/nphoton.2013.234 (cit. on p. 4).

[28] S M Hooker et al. "Multi-pulse laser wakefield acceleration: a new route to efficient, high-repetition-rate plasma accelerators and high flux radiation sources". In: *Journal of Physics B: Atomic, Molecular and Optical Physics* 47.23 (Nov. 2014), p. 234003. DOI: 10.1088/0953-4075/47/23/234003 (cit. on pp. 4, 23, 26).

[29] J.N. Galayda. "The New LCLS-II Project : Status and Challenges". In: *Proceedings of LINAC2014*. 2014 (cit. on p. 4).

[30] A. J. Ross et al. "Resonant excitation of plasma waves in a plasma channel". In: *Physical Review Research* 6.2 (Apr. 2024), p. l022001. DOI: 10.1103/physrevresearch.6.l022001 (cit. on pp. 6, 23, 40, 69).

[31] A. Picksley et al. "All-Optical GeV Electron Bunch Generation in a Laser-Plasma Accelerator via Truncated Channel Injection". In: *Physical Review Letters* 131.24 (Dec. 2023), p. 245001. DOI: 10.1103/physrevlett.131.245001 (cit. on p. 6).

[32] Isaac Newton. "Mr. Isaac Newtons Answer to Some Considerations upon His Doctrine of Light and Colors; Which Doctrine Was Printed in Numb. 80. of These Tracts". In: *Philosophical Transactions* 7.88 (Nov. 1672), pp. 5084–5103. DOI: https://www.jstor.org/stable/100964 (cit. on p. 8).

[33] J. A. Bittencourt. "Fundamentals of Plasma Physics". In: Springer New York, NY, 2004. Chap. 1. DOI: https://doi.org/10.1007/978-1-4757-4030-1 (cit. on p. 9).

[34] Umran S. Inan. "Principles of Plasma Physics for Engineers and Scientists". In: Cambridge University Press, 2012. Chap. 1. DOI: https://doi.org/10.1017/CBO9780511761621 (cit. on p. 9).

[35] Umran S. Inan. "Principles of Plasma Physics for Engineers and Scientists". In: Cambridge University Press, 2012. Chap. 1, p. 15. DOI: https://doi.org/10.1017/CBO9780511761621 (cit. on p. 9).

[36] Paul Gibbon. "Short Pulse Laser Interactions with Matter: An Introduction". In: Imperial College Press, 2005. Chap. 4, p. 57. DOI: https://doi.org/10.1142/p116 (cit. on p. 9).

[37] Lewi Tonks and Irving Langmuir. "Oscillations in Ionized Gases". In: *Physical Review* 33.2 (Feb. 1929), pp. 195–210. DOI: 10.1103/physrev.33.195 (cit. on p. 10).

[38] J. A. Bittencourt. "Fundamentals of Plasma Physics". In: Springer New York, NY, 2004. Chap. 11. DOI: https://doi.org/10.1007/978-1-4757-4030-1 (cit. on p. 10).

[39] Paul Gibbon. "Short Pulse Laser Interactions with Matter: An Introduction". In: Imperial College Press, 2005. Chap. 2, p. 38. DOI: https://doi.org/10.1142/p116 (cit. on p. 10).

[40] Paul Gibbon. "Short Pulse Laser Interactions with Matter: An Introduction". In: Imperial College Press, 2005. Chap. 2, p. 39. DOI: https://doi.org/10.1142/p116 (cit. on p. 11).

[41] Paul Gibbon. "Short Pulse Laser Interactions with Matter: An Introduction". In: Imperial College Press, 2005. Chap. 4, p. 73. DOI: https://doi.org/10.1142/p116 (cit. on p. 11).

[42] David J. Griffiths. "Introduction To Electrodynamics 4th Edition". In: Pearson Education Inc., 2008. Chap. 9 (cit. on p. 11).

[43] J. A. Bittencourt. "Fundamentals of Plasma Physics". In: Springer New York, NY, 2004. Chap. 5. DOI: https://doi.org/10.1007/978-1-4757-4030-1 (cit. on p. 11).

[44] Bengt Eliasson C. S. Liu V. K. Tripathi. "High-Power Laser-Plasma Interaction". In: Cambridge University Press, 2019. Chap. 2. DOI: https://doi.org/10.1017/9781108635844 (cit. on p. 11).

[45] Paul Gibbon. "Short Pulse Laser Interactions with Matter: An Introduction". In: Imperial College Press, 2005. Chap. 4, p. 66. DOI: https://doi.org/10.1142/p116 (cit. on p. 12).

[46] Paul Gibbon. "Short Pulse Laser Interactions with Matter: An Introduction". In: Imperial College Press, 2005. Chap. 4, p. 67. DOI: https://doi.org/10.1142/p116 (cit. on p. 12).

[47] Mary L. Boas. "Mathematical Methods in the Physical Sciences, 3rd Edition". In: John Wiley and Sons, Inc, 2006. Chap. 4, pp. 461–464 (cit. on p. 12).

[48] L. M. Gorbunov and V. I. Kirsanov. "The excitation of plasma waves by an electromagnetic wave packet". In: *Zhurnal Eksperimental'noi i Teoreticheskoi Fiziki* 93 (Aug. 1987), pp. 509–518 (cit. on pp. 12, 13).

[49] Paul Gibbon. "Short Pulse Laser Interactions with Matter: An Introduction". In: Imperial College Press, 2005. Chap. 4, p. 69. DOI: https://doi.org/10.1142/p116 (cit. on p. 13).

[50] P. Sprangle, E. Esarey, and A. Ting. "Nonlinear interaction of intense laser pulses in plasmas". In: *Physical Review A* 41.8 (Apr. 1990), pp. 4463–4469. DOI: 10.1103/physreva.41.4463 (cit. on p. 14).

[51] P. Sprangle, E. Esarey, and A. Ting. "Nonlinear theory of intense laser-plasma interactions". In: *Physical Review Letters* 64.17 (Apr. 1990), pp. 2011–2014. DOI: 10.1103/physrevlett.64.2011 (cit. on pp. 14, 22).

[52] Paul Gibbon. "Short Pulse Laser Interactions with Matter: An Introduction". In: Imperial College Press, 2005. Chap. 4, p. 62. DOI: https://doi.org/10.1142/p116 (cit. on p. 14).

[53] John M. Dawson. "Nonlinear Electron Oscillations in a Cold Plasma". In: *Physical Review* 113.2 (Jan. 1959), pp. 383–387. DOI: 10.1103/physrev.113.383 (cit. on p. 14).

[54] A I Akhiezer and R V Polovin. "Theory of Wave Motion of An Electron Plasma". In: *Soviet Phys. JETP* 3 (Dec. 1956). DOI: https://www.osti.gov/biblio/4361348 (cit. on p. 14).

[55] J. M. Dawson et al. "Damping of Large-Amplitude Plasma Waves Propagating Perpendicular to the Magnetic Field". In: *Physical Review Letters* 50.19 (May 1983), pp. 1455–1458. DOI: 10.1103/physrevlett.50.1455 (cit. on p. 15).

[56] T. Katsouleas and J. M. Dawson. "Unlimited Electron Acceleration in Laser-Driven Plasma Waves". In: *Physical Review Letters* 51.5 (Aug. 1983), pp. 392–395. DOI: 10.1103/physrevlett.51.392 (cit. on p. 15).

[57] Eric Esarey and Mark Pilloff. "Trapping and acceleration in nonlinear plasma waves". In: *Physics of Plasmas* 2.5 (May 1995), pp. 1432–1436. DOI: 10.1063/1.871358 (cit. on pp. 15, 16, 19).

[58] Bengt Eliasson C. S. Liu V. K. Tripathi. "High-Power Laser-Plasma Interaction". In: Cambridge University Press, 2019. Chap. 6, pp. 107–109. DOI: https://doi.org/10.1017/9781108635844 (cit. on p. 15).

[59] A.J.W. REITSMA and D.A. JAROSZYNSKI. "Coupling of longitudinal and transverse motion of accelerated electrons in laser wakefield acceleration". In: *Laser and Particle Beams* 22.4 (Oct. 2004), pp. 407–413. DOI: 10.1017/s0263034604040054 (cit. on p. 17).

[60] M. N. Rosenbluth and C. S. Liu. "Excitation of Plasma Waves by Two Laser Beams". In: *Physical Review Letters* 29.11 (Sept. 1972), pp. 701–705. DOI: 10.1103/physrevlett.29.701 (cit. on p. 18).

[61] C. Joshi et al. "Ultrahigh gradient particle acceleration by intense laser-driven plasma density waves". In: *Nature* 311.5986 (Oct. 1984), pp. 525–529. DOI: 10.1038/311525a0 (cit. on p. 18).

[62] C. M. Tang, P. Sprangle, and R. N. Sudan. "Dynamics of space-charge waves in the laser beat wave accelerator". In: *The Physics of Fluids* 28.6 (June 1985), pp. 1974–1983. DOI: 10.1063/1.865375 (cit. on p. 18).

[63] C. Joshi et al. "Beatwave acceleration experiments at UCLA". In: *Proceedings of the 1989 IEEE Particle Accelerator Conference, . 'Accelerator Science and Technology.* IEEE, 1989. DOI: 10.1109/pac.1989.73234 (cit. on p. 18).

[64] C. E. Clayton et al. "Acceleration and scattering of injected electrons in plasma beat wave accelerator experiments*". In: *Physics of Plasmas* 1.5 (May 1994), pp. 1753–1760. DOI: 10.1063/1.870679 (cit. on p. 18).

[65] S. Ya. Tochitsky et al. "Enhanced Acceleration of Injected Electrons in a Laser-Beat-Wave-Induced Plasma Channel". In: *Physical Review Letters* 92.9 (Mar. 2004), p. 095004. DOI: 10.1103/physrevlett.92.095004 (cit. on p. 18).

[66] S. Ya. Tochitsky et al. "Experiments on laser driven beatwave acceleration in a ponderomotively formed plasma channel". In: *Physics of Plasmas* 11.5 (May 2004), pp. 2875–2881. DOI: 10.1063/1.1651100 (cit. on p. 18).

[67] M. Luo et al. "Control of autoresonant plasma beat-wave wakefield excitation". In: *Physical Review Research* 6.1 (Mar. 2024), p. 013338. DOI: 10.1103/physrevresearch.6.013338 (cit. on pp. 18, 26).

[68] J. Fajans and L. Frièdland. "Autoresonant (nonstationary) excitation of pendulums, Plutinos, plasmas, and other nonlinear oscillators". In: *American Journal of Physics* 69.10 (Oct. 2001), pp. 1096–1102. DOI: 10.1119/1.1389278 (cit. on p. 18).

[69] Vadim R. Munirov, Lazar Friedland, and Jonathan S. Wurtele. "Multiphase nonlinear electron plasma waves". In: *Physical Review E* 106.5 (Nov. 2022), p. 055201. DOI: 10.1103/physreve.106.055201 (cit. on p. 18).

[70] P. Maine et al. "Generation of ultrahigh peak power pulses by chirped pulse amplification". In: *IEEE Journal of Quantum Electronics* 24.2 (Feb. 1988), pp. 398–403. DOI: 10.1109/3.137 (cit. on pp. 19, 21).

[71] P. Sprangle et al. "Laser wakefield acceleration and relativistic optical guiding". In: *Applied Physics Letters* 53.22 (Nov. 1988), pp. 2146–2148. DOI: 10.1063/1.100300 (cit. on pp. 19, 24).

[72] W.P. Leemans et al. "Plasma guiding and wakefield generation for second-generation experiments". In: *IEEE Transactions on Plasma Science* 24.2 (Apr. 1996), pp. 331–342. DOI: 10.1109/27.509997 (cit. on pp. 19, 24).

[73] Guido Toci et al. "Conceptual Design of a Laser Driver for a Plasma Accelerator User Facility". In: *Instruments* 3.3 (Aug. 2019), p. 40. DOI: 10.3390/instruments3030040 (cit. on pp. 19, 26).

[74] J. R. Marques et al. "Temporal and Spatial Measurements of the Electron Density Perturbation Produced in the Wake of an Ultrashort Laser Pulse". In: *Physical Review Letters* 76.19 (May 1996), pp. 3566–3569. DOI: 10.1103/physrevlett.76.3566 (cit. on p. 20).

[75] C. W. Siders et al. "Laser Wakefield Excitation and Measurement by Femtosecond Longitudinal Interferometry". In: *Physical Review Letters* 76.19 (May 1996), pp. 3570–3573. DOI: 10.1103/physrevlett.76.3570 (cit. on p. 20).

[76] F. Amiranoff et al. "Observation of Laser Wakefield Acceleration of Electrons". In: *Physical Review Letters* 81.5 (Aug. 1998), pp. 995–998. DOI: 10.1103/physrevlett.81.995 (cit. on p. 20).

[77] S. P. D. Mangles et al. "Monoenergetic beams of relativistic electrons from intense laser–plasma interactions". In: *Nature* 431.7008 (Sept. 2004), pp. 535–538. DOI: 10.1038/nature02939 (cit. on p. 20).

[78] J. Faure et al. "A laser–plasma accelerator producing monoenergetic electron beams". In: *Nature* 431.7008 (Sept. 2004), pp. 541–544. DOI: 10.1038/nature02963 (cit. on p. 20).

[79] C. G. R. Geddes et al. "High-quality electron beams from a laser wakefield accelerator using plasma-channel guiding". In: *Nature* 431.7008 (Sept. 2004), pp. 538–541. DOI: 10.1038/nature02900 (cit. on pp. 20, 24).

[80] A. J. Gonsalves et al. "Petawatt Laser Guiding and Electron Beam Acceleration to 8 GeV in a Laser-Heated Capillary Discharge Waveguide". In: *Physical Review Letters* 122.8 (Feb. 2019), p. 084801. DOI: 10.1103/physrevlett.122.084801 (cit. on pp. 20, 24).

[81] N. A. Bobrova et al. "Laser-heater assisted plasma channel formation in capillary discharge waveguides". In: *Physics of Plasmas* 20.2 (Feb. 2013), p. 020703. DOI: 10.1063/1.4793447 (cit. on p. 21).

[82] Peter Moulton. "Ti-doped sapphire: tunable solid-state laser". In: *Optics News* 8.6 (Nov. 1982), p. 9. DOI: 10.1364/on.8.6.000009 (cit. on p. 21).

[83] P. F. Moulton. "Spectroscopic and laser characteristics of Ti:Al_2O_3". In: *Journal of the Optical Society of America B* 3.1 (Jan. 1986), p. 125. DOI: 10.1364/josab.3.000125 (cit. on p. 21).

[84] H. Haus. "Theory of mode locking with a slow saturable absorber". In: *IEEE Journal of Quantum Electronics* 11.9 (Sept. 1975), pp. 736–746. DOI: 10.1109/jqe.1975.1068922 (cit. on p. 21).

[85] C Joshi. "Plasma-based accelerators: then and now". In: *Plasma Physics and Controlled Fusion* 61.10 (Aug. 2019), p. 104001. DOI: 10.1088/1361-6587/ab396a (cit. on p. 21).

[86] T. Tajima, X. Q. Yan, and T. Ebisuzaki. "Wakefield acceleration". In: *Reviews of Modern Plasma Physics* 4.1 (May 2020). DOI: 10.1007/s41614-020-0043-z (cit. on p. 21).

[87] Hyung Taek Kim et al. "Laser wakefield electron acceleration with PW lasers and future applications". In: *Journal of the Korean Physical Society* 80.8 (Mar. 2022), pp. 670–683. DOI: 10.1007/s40042-022-00443-9 (cit. on p. 21).

[88] P. Sprangle et al. "Propagation and guiding of intense laser pulses in plasmas". In: *Physical Review Letters* 69.15 (Oct. 1992), pp. 2200–2203. DOI: 10.1103/physrevlett.69.2200 (cit. on pp. 21, 24).

[89] J. Krall et al. "Enhanced acceleration in a self-modulated-laser wake-field accelerator". In: *Physical Review E* 48.3 (Sept. 1993), pp. 2157–2161. DOI: 10.1103/physreve.48.2157 (cit. on p. 21).

[90] C. B. Darrow et al. "Strongly coupled stimulated Raman backscatter from subpicosecond laser-plasma interactions". In: *Physical Review Letters* 69.3 (July 1992), pp. 442–445. DOI: 10.1103/physrevlett.69.442 (cit. on p. 21).

[91] K. Nakajima et al. "Observation of Ultrahigh Gradient Electron Acceleration by a Self-Modulated Intense Short Laser Pulse". In: *Physical Review Letters* 74.22 (May 1995), pp. 4428–4431. DOI: 10.1103/physrevlett.74.4428 (cit. on p. 21).

[92] F. Albert et al. "Observation of Betatron X-Ray Radiation in a Self-Modulated Laser Wakefield Accelerator Driven with Picosecond Laser Pulses". In: *Physical Review Letters* 118.13 (Mar. 2017), p. 134801. DOI: 10.1103/physrevlett.118.134801 (cit. on p. 21).

[93] J. L. Shaw et al. "Role of Direct Laser Acceleration of Electrons in a Laser Wakefield Accelerator with Ionization Injection". In: *Physical Review Letters* 118.6 (Feb. 2017), p. 064801. DOI: 10.1103/physrevlett.118.064801 (cit. on pp. 21, 22).

[94] P. M. King et al. "Predominant contribution of direct laser acceleration to high-energy electron spectra in a low-density self-modulated laser wakefield accelerator". In: *Physical Review Accelerators and Beams* 24.1 (Jan. 2021), p. 011302. DOI: 10.1103/physrevaccelbeams.24.011302 (cit. on pp. 21, 22).

[95] Guy Bonnaud, Denis Teychenné, and Jean-Louis Bobin. "Wake-field effect induced by laser multiple pulses". In: *Physical Review E* 50.1 (July 1994), R36–R39. DOI: 10.1103/physreve.50.r36 (cit. on p. 22).

[96] S Dalla and M Lontano. "Resonant and quasi-resonant excitation of plasma waves by means of sequences of laser pulses". In: *Plasma Physics and Controlled Fusion* 36.12 (Dec. 1994), pp. 1987–2002. DOI: 10.1088/0741-3335/36/12/003 (cit. on p. 22).

[97] D. Umstadter, E. Esarey, and J. Kim. "Nonlinear Plasma Waves Resonantly Driven by Optimized Laser Pulse Trains". In: *Physical Review Letters* 72.8 (Feb. 1994), pp. 1224–1227. DOI: 10.1103/physrevlett.72.1224 (cit. on p. 22).

[98] D A Johnson et al. "Plasma wakefield generation by multiple short pulses". In: *Physica Scripta* T52 (Jan. 1994), pp. 77–81. DOI: 10.1088/0031-8949/1994/t52/013 (cit. on p. 22).

[99] D. Umstadter et al. "Resonantly laser-driven plasma waves for electron acceleration". In: *Physical Review E* 51.4 (Apr. 1995), pp. 3484–3497. DOI: 10.1103/physreve.51.3484 (cit. on p. 22).

[100] J. Cowley et al. "Excitation and Control of Plasma Wakefields by Multiple Laser Pulses". In: *Physical Review Letters* 119.4 (July 2017), p. 044802. DOI: 10.1103/physrevlett.119.044802 (cit. on pp. 23, 32, 39, 127).

[101] Christopher Arran. "Techniques for High Repetition Rate Laser Wakefield Acceleration". PhD thesis. University of Oxford, 2018 (cit. on pp. 23, 73).

[102] Jakob Jonnerby. "Multi-pulse laser wakefield acceleration". PhD thesis. University of Oxford, 2021 (cit. on p. 23).

[103] Bahaa E. A. Saleh and Malvin Carl Teich. "Fundamentals of Photonics". In: John Wiley and Sons, Inc., 1991. Chap. 3 (cit. on p. 24).

[104] T. C. Chiou et al. "Laser wake-field acceleration and optical guiding in a hollow plasma channel". In: *Physics of Plasmas* 2.1 (Jan. 1995), pp. 310–318. DOI: 10.1063/1.871107 (cit. on p. 24).

[105] G. Shvets and J. S. Wurtele. "Instabilities of Short-Pulse Laser Propagation through Plasma Channels". In: *Physical Review Letters* 73.26 (Dec. 1994), pp. 3540–3543. DOI: 10.1103/physrevlett.73.3540 (cit. on p. 24).

[106] N. E. Andreev et al. "Structure of the wake field in plasma channels". In: *Physics of Plasmas* 4.4 (Apr. 1997), pp. 1145–1153. DOI: 10.1063/1.872186 (cit. on p. 24).

[107] W. P. Leemans et al. "GeV electron beams from a centimetre-scale accelerator". In: *Nature Physics* 2.10 (Sept. 2006), pp. 696–699. DOI: 10.1038/nphys418 (cit. on p. 24).

[108] Xiangkun Li, Phu Anh Phi Nghiem, and Alban Mosnier. "Toward low energy spread in plasma accelerators in quasilinear regime". In: *Physical Review Accelerators and Beams* 21.11 (Nov. 2018), p. 111301. DOI: 10.1103/physrevaccelbeams.21.111301 (cit. on p. 25).

[109] Alexander Debus et al. “Circumventing the Dephasing and Depletion Limits of Laser-Wakefield Acceleration”. In: *Physical Review X* 9.3 (Sept. 2019), p. 031044. DOI: 10.1103/physrevx.9.031044 (cit. on p. 25).

[110] M. Sedaghat, S. Barzegar, and A. R. Niknam. “Quasi-phase-matched laser wakefield acceleration of electrons in an axially density-modulated plasma channel”. In: *Scientific Reports* 11.1 (July 2021). DOI: 10.1038/s41598-021-94751-y (cit. on p. 25).

[111] Kyle G. Miller et al. “Dephasingless laser wakefield acceleration in the bubble regime”. In: *Scientific Reports* 13.1 (Dec. 2023). DOI: 10.1038/s41598-023-48249-4 (cit. on p. 25).

[112] B. A. Shadwick, C. B. Schroeder, and E. Esarey. “Nonlinear laser energy depletion in laser-plasma accelerators”. In: *Physics of Plasmas* 16.5 (May 2009). DOI: 10.1063/1.3124185 (cit. on p. 25).

[113] Wim Leemans and Eric Esarey. “Laser-driven plasma-wave electron accelerators”. In: *Physics Today* 62.3 (Mar. 2009), pp. 44–49. DOI: 10.1063/1.3099645 (cit. on p. 25).

[114] J. Luo et al. “Multistage Coupling of Laser-Wakefield Accelerators with Curved Plasma Channels”. In: *Physical Review Letters* 120.15 (Apr. 2018), p. 154801. DOI: 10.1103/physrevlett.120.154801 (cit. on p. 25).

[115] Norman P. Barnes. “Solid-State Lasers From an Efficiency Perspective”. In: *IEEE Journal of Selected Topics in Quantum Electronics* 13.3 (2007), pp. 435–447. DOI: 10.1109/jstqe.2007.895280 (cit. on p. 26).

[116] Jay W. Dawson et al. “High average power lasers for future particle accelerators”. In: *AIP Conference Proceedings*. AIP, 2013. DOI: 10.1063/1.4773687 (cit. on p. 26).

[117] Frank Trager. “Springer Handbook of Lasers and Optics”. In: Springer Berlin, Heidelberg, 2012. Chap. 11 (cit. on p. 26).

[118] P A P Nghiem et al. “Eupraxia, A Step Toward A Plasma-Wakefield Based Accelerator With High Beam Quality”. In: *Journal of Physics: Conference Series* 1350.1 (Nov. 2019), p. 012068. DOI: 10.1088/1742-6596/1350/1/012068 (cit. on p. 26).

[119] O. Jakobsson, S. M. Hooker, and R. Walczak. “Gev-Scale Accelerators Driven by Plasma-Modulated Pulses from Kilohertz Lasers”. In: *Physical Review Letters* 127.18 (Oct. 2021), p. 184801. DOI: 10.1103/physrevlett.127.184801 (cit. on pp. 26, 142, 153, 154).

[120] J. J. van de Wetering, S. M. Hooker, and R. Walczak. “Multi-GeV wakefield acceleration in a plasma-modulated plasma accelerator”. In: *Physical Review E* 109.2 (Feb. 2024), p. 025206. DOI: 10.1103/physreve.109.025206 (cit. on p. 26).

[121] Hongshan Chen et al. “High-efficiency 100-W Kerr-lens mode-locked Yb:YAG thin-disk oscillator”. In: *Frontiers in Physics* 11 (Apr. 2023). DOI: 10.3389/fphy.2023.1191010 (cit. on p. 26).

[122] Weijian Sha, Jean Christophe Chanteloup, and Gerard Mourou. “Ultrafast Fiber Technologies for Compact Laser Wake Field in Medical Application”. In: *Photonics* 9.6 (Jan. 2022), p. 423. DOI: 10.3390/photonics9060423 (cit. on p. 26).

[123] Simon Nagel et al. “Thin disk laser system operating above 10 kW at near fundamental mode beam quality”. In: *Optics Letters* 46.5 (Feb. 2021), p. 965. DOI: 10.1364/ol.416432 (cit. on p. 26).

[124] Charles Babbage. "Reflections on the decline of science in England, and on some of its causes". In: London; Printed for B. Fellowes, Ludgate Street; and J. Booth, Duke Street, Portland Place, 1830, p. 167 (cit. on p. 28).

[125] T. Robinson et al. "Simple technique for generating trains of ultrashort pulses". In: *Optics Letters* 32.15 (July 2007), p. 2203. DOI: 10.1364/ol.32.002203 (cit. on pp. 29, 35).

[126] Bahaa E. A. Saleh and Malvin Carl Teich. "Fundamentals of Photonics". In: John Wiley and Sons, Inc., 1991. Chap. 2, p. 59 (cit. on p. 34).

[127] Andrew M. Weiner. "Ultrafast Optics". In: John Wiley and Sons, Inc., 2008. Chap. 4, pp. 162–163 (cit. on p. 34).

[128] Rick Trebino. "Frequency-resolved optical gating : the measurement of ultrashort laser pulses". In: Springer Science+Business Media New Yor, 2000. Chap. 2 (cit. on p. 36).

[129] Andrew M. Weiner. "Ultrafast Optics". In: John Wiley and Sons, Inc., 2008. Chap. 3 (cit. on pp. 36, 61, 62).

[130] Andrew M. Weiner. "Ultrafast Optics". In: John Wiley and Sons, Inc., 2008. Chap. 3, pp. 88–91 (cit. on p. 37).

[131] H. P. Weber. "Method for Pulsewidth Measurement of Ultrashort Light Pulses Generated by Phase-Locked Lasers using Nonlinear Optics". In: *Journal of Applied Physics* 38.5 (Apr. 1967), pp. 2231–2234. DOI: 10.1063/1.1709859 (cit. on p. 38).

[132] Evgeni Sorokin, Gabriel Tempea, and Thomas Brabec. "Measurement of the root-mean-square width and the root-mean-square chirp in ultrafast optics". In: *Journal of the Optical Society of America B* 17.1 (Jan. 2000), p. 146. DOI: 10.1364/josab.17.000146 (cit. on p. 38).

[133] Andrew M. Weiner. "Ultrafast Optics". In: John Wiley and Sons, Inc., 2008. Chap. 3, p. 92 (cit. on p. 38).

[134] S. M. Hooker. "Phase retrieval algorithm of multi-pulse trains". In: *Internal communication (Unpublished)* (2020) (cit. on p. 39).

[135] Rick Trebino. "Frequency-resolved optical gating : the measurement of ultrashort laser pulses". In: Springer Science+Business Media New Yor, 2000. Chap. 3, p. 87 (cit. on p. 41).

[136] K. Naganuma, K. Mogi, and H. Yamada. "General method for ultrashort light pulse chirp measurement". In: *IEEE Journal of Quantum Electronics* 25.6 (June 1989), pp. 1225–1233. DOI: 10.1109/3.29252 (cit. on p. 41).

[137] Jung-Ho Chung and A.M. Weiner. "Ambiguity of ultrashort pulse shapes retrieved from the intensity autocorrelation and the power spectrum". In: *IEEE Journal of Selected Topics in Quantum Electronics* 7.4 (2001), pp. 656–666. DOI: 10.1109/2944.974237 (cit. on p. 41).

[138] J. A. Armstrong. "MEASUREMENT OF PICOSECOND LASER PULSE WIDTHS". In: *Applied Physics Letters* 10.1 (Jan. 1967), pp. 16–18. DOI: 10.1063/1.1754787 (cit. on p. 41).

[139] J. P. Heritage, A. M. Weiner, and R. N. Thurston. "Picosecond pulse shaping by spectral phase and amplitude manipulation". In: *Optics Letters* 10.12 (Dec. 1985), p. 609. DOI: 10.1364/ol.10.000609 (cit. on p. 41).

[140] Joshua E. Rothenberg and D. Grischkowsky. "Measurement of optical phase with subpicosecond resolution by time-domain interferometry". In: *Optics Letters* 12.2 (Feb. 1987), p. 99. DOI: 10.1364/ol.12.000099 (cit. on p. 41).

[141] K. W. DeLong and Junji Yumoto. "Chirped light and its characterization using the cross-correlation technique". In: *Journal of the Optical Society of America B* 9.9 (Sept. 1992), p. 1593. DOI: 10.1364/josab.9.001593 (cit. on p. 41).

[142] Rick Trebino and Daniel J. Kane. "Using phase retrieval to measure the intensity and phase of ultrashort pulses: frequency-resolved optical gating". In: *Journal of the Optical Society of America A* 10.5 (May 1993), p. 1101. DOI: 10.1364/josaa.10.001101 (cit. on pp. 42, 45, 53, 54).

[143] Edwin J. Akutowicz. "On the determination of the phase of a Fourier integral. I". In: *Transactions of the American Mathematical Society* 83.1 (1956), pp. 179–192. DOI: 10.1090/s0002-9947-1956-0080802-2 (cit. on p. 42).

[144] Richard Barakat and Garry Newsam. "Necessary conditions for a unique solution to two-dimensional phase recovery". In: *Journal of Mathematical Physics* 25.11 (Nov. 1984), pp. 3190–3193. DOI: 10.1063/1.526089 (cit. on p. 42).

[145] J. R. Fienup. "Phase retrieval algorithms: a comparison". In: *Applied Optics* 21.15 (Aug. 1982), p. 2758. DOI: 10.1364/ao.21.002758 (cit. on p. 42).

[146] R. W. Gerchberg and W. O. Saxton. "A Practical Algorithm for the Determination of Phase from Image". In: 35.237 (1972) (cit. on pp. 42, 53).

[147] R. P. Millane. "Phase retrieval in crystallography and optics". In: *Journal of the Optical Society of America A* 7.3 (Mar. 1990), p. 394. DOI: 10.1364/josaa.7.000394 (cit. on p. 42).

[148] Rick Trebino. "Frequency-resolved optical gating : the measurement of ultrashort laser pulses". In: Springer Science+Business Media New Yor, 2000. Chap. 3, p. 102 (cit. on p. 43).

[149] Rick Trebino. "Frequency-resolved optical gating : the measurement of ultrashort laser pulses". In: Springer Science+Business Media New Yor, 2000. Chap. 3, p. 104 (cit. on p. 43).

[150] Y. Ishida, K. Naganuma, and T. Yajima. "Self-phase modulation in hybridly mode-locked CW dye lasers". In: *IEEE Journal of Quantum Electronics* 21.1 (Jan. 1985), pp. 69–77. DOI: 10.1109/jqe.1985.1072530 (cit. on p. 45).

[151] Akira Watanabe et al. "Microcomputer-based spectrum-resolved second-harmonic generation correlator for fast measurement of ultrashort pulses". In: *Review of Scientific Instruments* 56.12 (Dec. 1985), pp. 2259–2262. DOI: 10.1063/1.1138360 (cit. on p. 45).

[152] K. W. DeLong et al. "Frequency-resolved optical gating with the use of second-harmonic generation". In: *Journal of the Optical Society of America B* 11.11 (Nov. 1994), p. 2206. DOI: 10.1364/josab.11.002206 (cit. on p. 45).

[153] Daniel J. Kane and Rick P. Trebino. "Single-shot measurement of the intensity and phase of a femtosecond laser pulse". In: *Proceedings of SPIE* 1861.1 (June 1993). Ed. by Timothy R. Gosnell et al., pp. 150–160. DOI: 10.1117/12.147045 (cit. on pp. 45, 48).

[154] E. Zeek et al. "Simultaneous automatic calibration and direction-of-time removal in frequency-resolved optical gating". In: *Applied Physics B* 74.S1 (June 2002), s265–s271. DOI: 10.1007/s00340-002-0900-1 (cit. on pp. 46, 60).

[155] Dorine Keusters et al. "Relative-phase ambiguities in measurements of ultrashort pulses with well-separated multiple frequency components". In: *Journal of the Optical Society of America B* 20.10 (Oct. 2003), p. 2226. DOI: 10.1364/josab.20.002226 (cit. on p. 46).

[156] Birger Seifert, Heinrich Stolz, and Manfred Tasche. "Nontrivial ambiguities for blind frequency-resolved optical gating and the problem of uniqueness". In: *Journal of the Optical Society of America B* 21.5 (May 2004), p. 1089. DOI: 10.1364/josab.21.001089 (cit. on p. 46).

[157] Thomas Tsang et al. "Frequency-resolved optical-gating measurements of ultrashort pulses using surface third-harmonic generation". In: *Optics Letters* 21.17 (Sept. 1996), p. 1381. DOI: 10.1364/ol.21.001381 (cit. on p. 46).

[158] Rebecca Chadwick et al. "Fringe-free, background-free, collinear third-harmonic generation frequency-resolved optical gating measurements for multiphoton microscopy". In: *Optics Letters* 31.22 (Oct. 2006), p. 3366. DOI: 10.1364/ol.31.003366 (cit. on p. 46).

[159] John Kerr. "XL. A new relation between electricity and light: Dielectrified media birefringent". In: *The London, Edinburgh, and Dublin Philosophical Magazine and Journal of Science* 50.332 (Nov. 1875), pp. 337–348. DOI: 10.1080/14786447508641302 (cit. on p. 46).

[160] Tracy Sharp Clement, Daniel J. Kane, and A. J. Taylor. "Single-shot measurement of the amplitude and phase of ultrashort laser pulses in the violet". In: *Optics Letters* 20.1 (Jan. 1995), p. 70. DOI: 10.1364/ol.20.000070 (cit. on p. 46).

[161] Tsz Chun Wong and Rick Trebino. "Single-frame measurement of complex laser pulses tens of picoseconds long using pulse-front tilt in cross-correlation frequency-resolved optical gating". In: *Journal of the Optical Society of America B* 30.11 (Oct. 2013), p. 2781. DOI: 10.1364/josab.30.002781 (cit. on p. 49).

[162] John N. Sweetser, David N. Fittinghoff, and Rick Trebino. "Transient-grating frequency-resolved optical gating". In: *Optics Letters* 22.8 (Apr. 1997), p. 519. DOI: 10.1364/ol.22.000519 (cit. on p. 49).

[163] Vadim V. Lozovoy, Igor Pastirk, and Marcos Dantus. "Multiphoton intrapulse interference. IV. Ultrashort laser pulse spectral phase characterization and compensation". In: *Optics Letters* 29 (2004), pp. 775–777. DOI: https://doi.org/10.1364/OL.29.000775 (cit. on p. 49).

[164] Miguel Miranda et al. "Simultaneous compression and characterization of ultrashort laser pulses using chirped mirrors and glass wedges". In: *Optics Express* 20.1 (Dec. 2011), p. 688. DOI: 10.1364/oe.20.000688 (cit. on p. 49).

[165] Gil Ilan Haham et al. "V-FROG—single-scan vectorial FROG". In: *Journal of Physics: Photonics* 3.3 (Jan. 2021), p. 034017. DOI: 10.1088/2515-7647/ac0541 (cit. on p. 49).

[166] O. Chekhlov et al. "Development of petawatt laser amplification systems at the Central Laser Facility". In: *Conference paper* (Jan. 2007). Ed. by Vladislav Panchenko et al. DOI: 10.1117/12.753222 (cit. on p. 50).

[167] Klaus Ertel et al. "ASE suppression in a high energy Titanium sapphire amplifier". In: *Optics Express* 16.11 (May 2008), p. 8039. DOI: 10.1364/oe.16.008039 (cit. on p. 50).

[168] Chris Hooker et al. "Improving coherent contrast of petawatt laser pulses". In: *Optics Express* 19.3 (Jan. 2011), p. 2193. DOI: 10.1364/oe.19.002193 (cit. on p. 50).

[169] Peter E. Powers and Joseph W. Haus. "Fundamentals of nonlinear optics". In: Taylor and Francis Group, LLC., 2017. Chap. 4 (cit. on p. 51).

[170] Andrew M. Weiner. "Ultrafast Optics". In: John Wiley and Sons, Inc., 2008. Chap. 5 (cit. on p. 51).

[171] Peter E. Powers and Joseph W. Haus. "Fundamentals of nonlinear optics". In: Taylor and Francis Group, LLC., 2017. Chap. 2 (cit. on p. 51).

[172] Bahaa E. A. Saleh and Malvin Carl Teich. "Fundamentals of Photonics". In: John Wiley and Sons, Inc., 1991. Chap. 1 (cit. on p. 52).

[173] Rick Trebino. "Frequency-resolved optical gating : the measurement of ultrashort laser pulses". In: Springer Science+Business Media New Yor, 2000. Chap. 7 (cit. on p. 53).

[174] W. O. Saxton. *Computer techniques for image processing in electron microscopy.png*. Ed. by Claire Marton L. Marton. New York : Academic Press, 1978 (cit. on p. 53).

[175] Rick Trebino. "Frequency-resolved optical gating : the measurement of ultrashort laser pulses". In: Springer Science+Business Media New Yor, 2000. Chap. 8 (cit. on pp. 54, 76).

[176] Daniel J. Kane et al. "Simultaneous measurement of two ultrashort laser pulses from a single spectrogram in a single shot". In: *Journal of the Optical Society of America B* 14.4 (Apr. 1997), p. 935. DOI: 10.1364/josab.14.000935 (cit. on pp. 55, 174).

[177] D.J. Kane. "Real-time measurement of ultrashort laser pulses using principal component generalized projections". In: *IEEE Journal of Selected Topics in Quantum Electronics* 4.2 (1998), pp. 278–284. DOI: 10.1109/2944.686733 (cit. on pp. 55, 76, 174).

[178] Howard Anton and Chris Rorres. *Elementary Linear Algebra 11th edition*. John Wiley and Sons, Inc., 2014 (cit. on pp. 56, 57).

[179] Gilbert Strange. *Introduction To Linear Algebra 5th edition*. Wellesley Cambridge Press, 2016 (cit. on p. 56).

[180] P. D. Nellist, B. C. McCallum, and J. M. Rodenburg. "Resolution beyond the information limit in transmission electron microscopy". In: *Nature* 374.6523 (Apr. 1995), pp. 630–632. DOI: 10.1038/374630a0 (cit. on p. 57).

[181] J. M. Rodenburg and H. M. L. Faulkner. "A phase retrieval algorithm for shifting illumination". In: *Applied Physics Letters* 85.20 (Nov. 2004), pp. 4795–4797. DOI: 10.1063/1.1823034 (cit. on p. 57).

[182] Andrew M. Maiden and John M. Rodenburg. "An improved ptychographical phase retrieval algorithm for diffractive imaging". In: *Ultramicroscopy* 109.10 (Sept. 2009), pp. 1256–1262. DOI: 10.1016/j.ultramic.2009.05.012 (cit. on p. 58).

[183] Erich Rohwer et al. "Time-domain ptychography". en. In: *Preceedings* (2015). DOI: 10.7892/BORIS.74987 (cit. on p. 58).

[184] D. Spangenberg et al. "Ptychographic ultrafast pulse reconstruction". In: *Optics Letters* 40.6 (Mar. 2015), p. 1002. DOI: 10.1364/ol.40.001002 (cit. on pp. 58, 60, 76, 133).

[185] Pavel Sidorenko et al. "Ptychographic reconstruction algorithm for frequency-resolved optical gating: super-resolution and supreme robustness". In: *Optica* 3.12 (Nov. 2016), p. 1320. DOI: 10.1364/optica.3.001320 (cit. on pp. 58, 76).

[186] Alexander M. Heidt et al. "Improved retrieval of complex supercontinuum pulses from XFROG traces using a ptychographic algorithm". In: *Optics Letters* 41.21 (Oct. 2016), p. 4903. DOI: 10.1364/ol.41.004903 (cit. on p. 58).

[187] T. Witting et al. "Time-domain ptychography of over-octave-spanning laser pulses in the single-cycle regime". In: *Optics Letters* 41.18 (Sept. 2016), p. 4218. DOI: 10.1364/ol.41.004218 (cit. on p. 58).

[188] Matteo Lucchini and Mauro Nisoli. "Refined Ptychographic Reconstruction of Attosecond Pulses". In: *Applied Sciences* 8.12 (Dec. 2018), p. 2563. DOI: 10.3390/app8122563 (cit. on p. 58).

[189] Daniel J. Kane. "Comparison of the Ptychographic Inversion Engine to Principal Components Generalized Projections". In: *IEEE Journal of Selected Topics in Quantum Electronics* 25.4 (July 2019), pp. 1–8. DOI: 10.1109/jstqe.2019.2904414 (cit. on pp. 58, 133).

[190] Daniel J. Kane and Andrei B. Vakhtin. "A review of ptychographic techniques for ultrashort pulse measurement". In: *Progress in Quantum Electronics* 81 (Jan. 2022), p. 100364. DOI: 10.1016/j.pquantelec.2021.100364 (cit. on pp. 58, 133).

[191] Tamir Bendory, Pavel Sidorenko, and Yonina C. Eldar. "On the Uniqueness of FROG Methods". In: *IEEE Signal Processing Letters* 24.5 (May 2017), pp. 722–726. DOI: 10.1109/lsp.2017.2690358 (cit. on p. 58).

[192] Albert Fannjiang and Pengwen Chen. "Blind ptychography: uniqueness and ambiguities". In: *Inverse Problems* 36.4 (Feb. 2020), p. 045005. DOI: 10.1088/1361-6420/ab6504 (cit. on p. 58).

[193] Rick Trebino et al. "Measuring ultrashort laser pulses in the time-frequency domain using frequency-resolved optical gating". In: *Review of Scientific Instruments* 68.9 (Sept. 1997), pp. 3277–3295. DOI: 10.1063/1.1148286 (cit. on p. 60).

[194] K. W. DeLong, Rick Trebino, and Daniel J. Kane. "Comparison of ultrashort-pulse frequency-resolved-optical-gating traces for three common beam geometries". In: *Journal of the Optical Society of America B* 11.9 (Sept. 1994), p. 1595. DOI: 10.1364/josab.11.001595 (cit. on p. 60).

[195] N X Truong, J Tiggesbäumker, and T Döppner. "Shaper-assisted removal of the direction-of-time ambiguity in second-harmonic generation frequency-resolved optical gating". In: *Measurement Science and Technology* 21.8 (July 2010), p. 085303. DOI: 10.1088/0957-0233/21/8/085303 (cit. on p. 60).

[196] Birger Seifert, Heinrich Stolz, and Manfred Tasche. "Nontrivial ambiguities for blind frequency-resolved optical gating and the problem of uniqueness". In: *Journal of the Optical Society of America B* 21.5 (May 2004), p. 1089. DOI: 10.1364/josab.21.001089 (cit. on p. 61).

[197] K. C. Chu et al. "Direct measurement of the spectral phase of femtosecond pulses". In: *Optics Letters* 20.8 (Apr. 1995), p. 904. DOI: 10.1364/ol.20.000904 (cit. on p. 62).

[198] L. Cohen. "Time-frequency distributions-a review". In: *Proceedings of the IEEE* 77.7 (July 1989), pp. 941–981. DOI: 10.1109/5.30749 (cit. on p. 62).

[199] Susan Ratcliffe. "Popular Lectures and Addresses vol. 1 (1889) 'Electrical Units of Measurement', delivered 3 May 1883". In: *Oxford Essential Quotations (6 ed.)* Oxford University Press, 2018, p. 107. DOI: 10.1093/acref/9780191866692.001.0001 (cit. on p. 65).

[200] Bahaa E. A. Saleh and Malvin Carl Teich. "Fundamentals of Photonics". In: John Wiley and Sons, Inc., 1991. Chap. 18 (cit. on p. 82).

[201] Gerald C. Holst and Terrence S. Lomheim. "CMOS CCD sensors and camera systems". In: SPIE Press and JCD Publishing, 1991. Chap. 6 (cit. on pp. 82, 83, 86, 155).

[202] Ursula Keller. *Ultrafast Lasers A Comprehensive Introduction to Fundamental Principles with Practical Applications*. Springer, 2022. DOI: https://doi.org/10.1007/978-3-030-82532-4 (cit. on p. 82).

[203] Richard E. Woods and Rafael C. Gonzalez. "Digital Image Processing Global Edition 4th". In: Pearson, 2017. Chap. 5 (cit. on p. 82).

[204] Rick Trebino. "Frequency-resolved optical gating : the measurement of ultrashort laser pulses". In: Springer Science+Business Media New Yor, 2000. Chap. 9 (cit. on p. 82).

[205] Bahaa E. A. Saleh and Malvin Carl Teich. "Fundamentals of Photonics". In: John Wiley and Sons, Inc., 1991. Chap. 12 (cit. on p. 83).

[206] NumPy Developers. "numpy.random.poisson". Accessed 08/03/2024. url:https://numpy.org/doc/stable/reference/random/generated/numpy.random.poisson.html. 2024 (cit. on p. 83).

[207] NumPy Developers. "numpy.random.normal". Accessed 08/03/2024. url:https://numpy.org/doc/stable/reference/random/generated/numpy.random.normal.html. 2024 (cit. on p. 83).

[208] Eksma Optics. *Crystals Selection Guide*. Tech. rep. Dvarcioniu st. 2B LT-10233 Vilnius, Lithuania: Eksma Optics (cit. on pp. 90, 91).

[209] Eksma Optics. *BBO, LBO, KDP, LiIO3, AgGaS2, GaSe – ULTRATHIN NONLINEAR CRYSTALS*. Tech. rep. Dvarcioniu st. 2B LT-10233 Vilnius, Lithuania: Eksma Optics (cit. on pp. 90, 91).

[210] Rick Trebino. "Frequency-resolved optical gating : the measurement of ultrashort laser pulses". In: Springer Science+Business Media New Yor, 2000. Chap. 10 (cit. on p. 95).

[211] Joseph W. Goodman. "Introduction to Fourier optics". In: Englewood, Co. Roberts and Company, 2005. Chap. 2 (cit. on p. 95).

[212] Wilfried Neumann. "Fundamentals of dispersive optical spectroscopy systems". In: Society of Photo-Optical Instrumentation Engineers, 2014. Chap. 3 (cit. on p. 98).

[213] Naftaly Menn. "Practical Optics". In: Elsevier Academic Press, 2004. Chap. 5 (cit. on p. 99).

[214] Ibsen Photonics. *Spectrometer Design Guide*. Tech. rep. Ryttermarken 17, DK-3520 Farum, Denmark: Ibsen Photonics (cit. on p. 99).

[215] Bertrand Russell. "The Scientific Outlook". In: Taylor and Francis, 2008. Chap. 2, p. 42 (cit. on p. 102).

[216] Inc. Thorlabs. *1951 USAF Targetsn*. 2024. URL: https://www.thorlabs.com/newgrouppage9.cfm?objectgroup_id=4338 (visited on 03/18/2024) (cit. on p. 107).

[217] Oiel Instruments. *Typical spectra of spectral calibration lamps*. Tech. rep. 250 Long Beach Boulevard, Stratford, CT 06497-0872 U.S.A.: Oiel Instruments (cit. on p. 108).

[218] Wilfried Neumann. "Fundamentals of dispersive optical spectroscopy systems". In: Society of Photo-Optical Instrumentation Engineers, 2014. Chap. 2 (cit. on p. 108).

[219] Rick Trebino. "Frequency-resolved optical gating : the measurement of ultrashort laser pulses". In: Springer Science+Business Media New Yor, 2000. Chap. 11 (cit. on pp. 109, 110).

[220] Inc. Thorlabs. *Cylindrical Achromatic Doublets, AR Coating 650 to 1050 nm.* 2024. URL: https://www.thorlabs.com/newgrouppage9.cfm?objectgroup_id=5528 (visited on 03/21/2024) (cit. on p. 116).

[221] Inc. Thorlabs. *1-inch Zero-Order Half-Wave Plates, SM1-Threaded Mounts.* 2024. URL: https://www.thorlabs.com/newgrouppage9.cfm?objectgroup_id=711 (visited on 03/21/2024) (cit. on p. 116).

[222] S. M. Hooker et al. "Resonant Down-ramp Injection in Multi-Pulse Laser Wakefield Accelerators". In: *Experimental proposal for an experiment in Gemini target area 3 at Central Laser Facility* (2022) (cit. on p. 125).

[223] S. Bulanov et al. "Particle injection into the wave acceleration phase due to nonlinear wake wave breaking". In: *Physical Review E* 58.5 (Nov. 1998), R5257–R5260. DOI: 10.1103/physreve.58.r5257 (cit. on p. 125).

[224] G. Fubiani et al. "Improvement of electron beam quality in optical injection schemes using negative plasma density gradients". In: *Physical Review E* 73.2 (Feb. 2006), p. 026402. DOI: 10.1103/physreve.73.026402 (cit. on pp. 125, 126).

[225] C. G. R. Geddes et al. "Plasma-Density-Gradient Injection of Low Absolute-Momentum-Spread Electron Bunches". In: *Physical Review Letters* 100.21 (May 2008), p. 215004. DOI: 10.1103/physrevlett.100.215004 (cit. on p. 125).

[226] A. Martinez de la Ossa et al. "Optimizing density down-ramp injection for beam-driven plasma wakefield accelerators". In: *Physical Review Accelerators and Beams* 20.9 (Sept. 2017), p. 091301. DOI: 10.1103/physrevaccelbeams.20.091301 (cit. on p. 125).

[227] R. J. Shalloo et al. "Hydrodynamic optical-field-ionized plasma channels". In: *Physical Review E* 97.5 (May 2018), p. 053203. DOI: 10.1103/physreve.97.053203 (cit. on p. 127).

[228] R. J. Shalloo et al. "Low-density hydrodynamic optical-field-ionized plasma channels generated with an axicon lens". In: *Physical Review Accelerators and Beams* 22.4 (Apr. 2019), p. 041302. DOI: 10.1103/physrevaccelbeams.22.041302 (cit. on p. 127).

[229] A. Picksley et al. "Meter-scale conditioned hydrodynamic optical-field-ionized plasma channels". In: *Physical Review E* 102.5 (Nov. 2020), p. 053201. DOI: 10.1103/physreve.102.053201 (cit. on p. 127).

[230] John S. Nodvick and David S. Saxon. "Suppression of Coherent Radiation by Electrons in a Synchrotron". In: *Physical Review* 96.1 (Oct. 1954), pp. 180–184. DOI: 10.1103/physrev.96.180 (cit. on p. 127).

[231] M. Heigoldt et al. "Temporal evolution of longitudinal bunch profile in a laser wakefield accelerator". In: *Physical Review Special Topics - Accelerators and Beams* 18.12 (Dec. 2015), p. 121302. DOI: 10.1103/physrevstab.18.121302 (cit. on p. 127).

[232] Matthias Heigoldt. "Temporal dynamics of the longitudinal bunch profile in a laser wakefield accelerator". PhD thesis. Ludwig Maximilian University of Munich, 2017 (cit. on p. 127).

[233] A. Buck et al. "Absolute charge calibration of scintillating screens for relativistic electron detection". In: *Review of Scientific Instruments* 81.3 (Mar. 2010), p. 033301. DOI: 10.1063/1.3310275 (cit. on p. 127).

[234] Y. Glinec et al. "Absolute calibration for a broad range single shot electron spectrometer". In: *Review of Scientific Instruments* 77.10 (Oct. 2006), p. 103301. DOI: 10.1063/1.2360988 (cit. on p. 127).

[235] Gavin Cheung. "X-Ray Powder Diffraction as a Non-Destructive Tool for Characterising Laser Wakefield Betatron". PhD thesis. University of Oxford, 2018 (cit. on p. 127).

[236] Jason Mark Coles. "Diagnosis and Application of Laser Wakefield Accelerators". PhD thesis. Imperial College of London, 2016 (cit. on p. 127).

[237] U Schramm et al. "First results with the novel petawatt laser acceleration facility in Dresden". In: *Journal of Physics: Conference Series* 874 (July 2017), p. 012028. DOI: 10.1088/1742-6596/874/1/012028 (cit. on p. 127).

[238] James Clerk Maxwell. "General considerations concerning Scientific Apparatus". In: *Cambridge University Press* (Jan. 1890), pp. 505–522. DOI: 10.1017/cbo9780511710377.053 (cit. on p. 140).

[239] Martin Kaumanns et al. "Spectral broadening of 112 mJ, 1.3 ps pulses at 5 in a 10 multipass cell with compressibility to 37 fs". In: *Optics Letters* 46.5 (Feb. 2021), p. 929. DOI: 10.1364/ol.416734 (cit. on pp. 141, 153).

[240] S. Nawab, T. Quatieri, and Jae Lim. "Signal reconstruction from short-time Fourier transform magnitude". In: *IEEE Transactions on Acoustics, Speech, and Signal Processing* 31.4 (Aug. 1983), pp. 986–998. DOI: 10.1109/tassp.1983.1164162 (cit. on p. 147).

[241] D.J. Kane and R. Trebino. "Characterization of arbitrary femtosecond pulses using frequency-resolved optical gating". In: *IEEE Journal of Quantum Electronics* 29.2 (1993), pp. 571–579. DOI: 10.1109/3.199311 (cit. on p. 147).

[242] C. Iaconis and I. A. Walmsley. "Spectral phase interferometry for direct electric-field reconstruction of ultrashort optical pulses". In: *Optics Letters* 23.10 (May 1998), p. 792. DOI: 10.1364/ol.23.000792 (cit. on p. 148).

[243] Ellen M. Kosik et al. "Interferometric technique for measuring broadband ultrashort pulses at the sampling limit". In: *Optics Letters* 30.3 (Feb. 2005), p. 326. DOI: 10.1364/ol.30.000326 (cit. on p. 150).

[244] T. Oksenhendler et al. "Self-referenced spectral interferometry". In: *Applied Physics B* 99.1-2 (Feb. 2010), pp. 7–12. DOI: 10.1007/s00340-010-3916-y (cit. on p. 150).

[245] N. Minkovski et al. "Polarization rotation induced by cascaded third-order processes". In: *Optics Letters* 27.22 (Nov. 2002), p. 2025. DOI: 10.1364/ol.27.002025 (cit. on p. 150).

[246] N. Minkovski et al. "Nonlinear polarization rotation and orthogonal polarization generation experienced in a single-beam configuration". In: *Journal of the Optical Society of America B* 21.9 (Sept. 2004), p. 1659. DOI: 10.1364/josab.21.001659 (cit. on p. 150).

[247] A. Moulet et al. "Single-shot, high-dynamic-range measurement of sub-15 fs pulses by self-referenced spectral interferometry". In: *Optics Letters* 35.22 (Nov. 2010), p. 3856. DOI: 10.1364/ol.35.003856 (cit. on p. 150).

[248] Dorine Keusters et al. "Relative-phase ambiguities in measurements of ultrashort pulses with well-separated multiple frequency components". In: *Journal of the Optical Society of America B* 20.10 (Oct. 2003), p. 2226. DOI: 10.1364/josab.20.002226 (cit. on p. 150).

[249] Pamela Bowlan et al. "Crossed-beam spectral interferometry: a simple, high-spectral-resolution method for completely characterizing complex ultrashort pulses in real time". In: *Optics Express* 14.24 (2006), p. 11892. DOI: 10.1364/oe.14.011892 (cit. on p. 150).

[250] Thomas Nubbemeyer et al. "1 kW, 200 mJ picosecond thin disk laser system". In: *Optics Letters* 42.7 (Mar. 2017), p. 1381. DOI: 10.1364/ol.42.001381 (cit. on p. 153).

[251] Reimund Martin Kaumanns. "Generation of Energetic Femtosecond Pulses at High Average Power". PhD thesis. Ludwig Maximilians Universitat, 2020 (cit. on p. 153).

[252] Andrew M. Weiner. "Ultrafast Optics". In: John Wiley and Sons, Inc., 2008. Chap. 6 (cit. on p. 153).

[253] Sony Semiconductor Solutions Corporation. *IMX249LLJ/IMX249LQJ*. Tech. rep. 4-14-1 Asahi-cho, Atsugi-shi, Kanagawa, 243-0014 Japan: Sony Semiconductor Solutions Corporation (cit. on p. 155).

[254] George Henry Lewes. "The Physical Basis of Mind". In: *Mind* 2.8 (Oct. 1878), pp. 565–568 (cit. on p. 169).

[255] R. Aboushelbaya et al. "Single-shot frequency-resolved optical gating for retrieving the pulse shape of high energy picosecond pulses". In: *Review of Scientific Instruments* 89.10 (Oct. 2018). DOI: 10.1063/1.5044526 (cit. on p. 174).

[256] J. R. Fienup and C. C. Wackerman. "Phase-retrieval stagnation problems and solutions". In: *Journal of the Optical Society of America A* 3.11 (Nov. 1986), p. 1897. DOI: 10.1364/josaa.3.001897 (cit. on p. 175).

[257] Tom Zahavy et al. "Deep learning reconstruction of ultrashort pulses". In: *Optica* 5.5 (May 2018), p. 666. DOI: 10.1364/optica.5.000666 (cit. on p. 175).

[258] Rana Jafari, Travis Jones, and Rick Trebino. "100 percent reliable algorithm for second-harmonic-generation frequency-resolved optical gating". In: *Optics Express* 27.3 (Jan. 2019), p. 2112. DOI: 10.1364/oe.27.002112 (cit. on p. 175).

[259] Christoffer Krook and Valdas Pasiskevicius. "Eliminating local convergences in FROG retrieval algorithms". In: *EPJ Web of Conferences* 287 (2023). Ed. by B. Kibler, G. Millot, and P. Segonds, p. 08001. DOI: 10.1051/epjconf/202328708001 (cit. on p. 175).

[260] Pablo Gabolde and Rick Trebino. "Single-shot measurement of the full spatio-temporal field of ultrashort pulses with multi-spectral digital holography". In: *Optics Express* 14.23 (2006), p. 11460. DOI: 10.1364/oe.14.011460 (cit. on p. 176).

[261] Elizabeth Grace et al. "Single-shot complete spatiotemporal measurement of terawatt laser pulses". In: *Journal of Optics* 23.7 (July 2021), p. 075505. DOI: 10.1088/2040-8986/ac0e1b (cit. on p. 176).

[262] D. E. Leaird and A. M. Weiner. "Femtosecond optical packet generation by a direct space-to-time pulse shaper". In: *Optics Letters* 24.12 (Jan. 1999), p. 853. DOI: 10.1364/ol.24.000853 (cit. on p. 176).

[263] A. Jullien et al. "Nonlinear spectral cleaning of few-cycle pulses via cross-polarized wave (XPW) generation". In: *Applied Physics B* 96.2–3 (Apr. 2009), pp. 293–299. DOI: 10.1007/s00340-009-3503-2 (cit. on p. 177).

[264] Jaismeen Kaur et al. "Simultaneous nonlinear spectral broadening and temporal contrast enhancement of ultrashort pulses in a multi-pass cell". In: *Journal of Physics: Photonics* 6.1 (Nov. 2023), p. 015001. DOI: 10.1088/2515-7647/ad078a (cit. on p. 177).

[265] R. DeSalvo et al. "Self-focusing and self-defocusing by cascaded second-order effects in KTP". In: *Optics Letters* 17.1 (Jan. 1992), p. 28. DOI: 10.1364/ol.17.000028 (cit. on p. 177).

[266] B. B. Zhou et al. "Ultrafast and Octave-Spanning Optical Nonlinearities from Strongly Phase-Mismatched Quadratic Interactions". In: *Physical Review Letters* 109.4 (July 2012), p. 043902. DOI: 10.1103/physrevlett.109.043902 (cit. on p. 177).

[267] Thomas Young. "A Course of Lectures on Natural Philosophy and the Mechanical Arts". In: London, Printed for J. Johnson, 1807, 1807. Chap. On the nature of light and colours, p. 457. DOI: https://doi.org/10.5962/bhl.title.22458 (cit. on p. 179).

[268] Andrew M. Weiner. “Ultrafast Optics”. In: John Wiley and Sons, Inc., 2008. Chap. 4 (cit. on pp. 181, 183).

[269] A. M. Turing. “Programmers’ Handbook (1st Edition) for the Manchester Electronic Computer Mark II”. In: 1951, p. 59 (cit. on p. 184).